# The Design and Development of a Planar Coil Sensor for Angular Displacements

A thesis submitted for the degree of

Doctor of Philosophy

Gregory M. Moreton

Wolfson Centre for Magnetics

School of Engineering

Cardiff University

May 2018

# Declaration

This work has not been submitted in substance for any other degree or award at this or any other university or place of learning, nor is being submitted concurrently in candidature for any degree or other award.

Signed ……..…….…… (candidate)  Date ……

**Statement 1**

This thesis is being submitted in partial fulfillment of the requirements for the degree of Doctor of Philosophy.

Signed ……..…….…… (candidate)  Date ……

**Statement 2**

This thesis is the result of my own independent work/investigation, except where otherwise stated, and the thesis has not been edited by a third party beyond what is permitted by Cardiff University's Policy on the Use of Third Party Editors by Research Degree Students. Other sources are acknowledged by explicit references. The views expressed are my own.

Signed ……..…….…… (candidate)  Date ……

**Statement 3**

I hereby give consent for my thesis, if accepted, to be available online in the University's Open Access repository and for inter-library loan, and for the title and summary to be made available to outside organisations.

Signed ……..…….…… (candidate)  Date ……

# Acknowledgements

The work was carried out at the Wolfson Centre for Magnetics, Cardiff School of Engineering, Cardiff University.

I am grateful to my supervisor Dr. T. Meydan for his guidance, advice, encouragement and support throughout this study. I would also like to thank Dr. P. Williams for his valuable input during many discussions we shared, and guidance throughout this study.

I wish to thank all of my friends and colleagues for their support throughout the years. I would also like to thank the Engineering and Physical Sciences Research Council for its support through a Doctoral Training Grant (Ref EP/M50631X/1), without which this research would not have been possible.

Finally, I would like to express my deepest gratitude to my family, especially my parents, for their continued support throughout my studies. Your help and encouragement have driven me throughout this study.

# Abstract

The increased prevalence of wearable sensing devices is accelerating the development of personalised medical devices for monitoring the human condition. The measurement of joint posture and kinematics is particularly relevant in areas of physiotherapy and in the management of diseases. Existing sensors for performing these tasks are however, either inaccurate or too technically complex and obtrusive. A novel approach has been taken to develop a new type of sensor for angular displacement sensing.

This thesis describes the development of a series of novel inductive planar coil sensors for measuring angular displacement. The small profile of these sensors makes them ideal for integration into garments as part of wearable devices.

The main objective of this work was to design a planar coil topology, based on an inductive methodology, suitable for measuring angular displacements typically observed in finger articulation.

Finite Element Method software was initially employed to determine the feasibility of various coil topologies. The planar coils were subsequently manufactured on several types of substrate including rigid printed circuit boards and flexible polyester films incorporating an iron-based amorphous ribbon as the inductive element. A series of experimental investigations involving inductance and stray field measurements, were performed on a range of coil topologies and layered configurations. The resulting data provided information relating sensor performance to positioning of the amorphous element and its overall angular displacement.

The main findings showed that inductance change was not frequency dependent in the range (20 – 100) kHz but decreased by up to 15% for large angular displacements when utilising a figure-of-eight coil design. The sensors developed in this work provide significantly better accuracy than current resistive-based flexible sensors. Further refinements to coil design and optimisation of the inductive element's magnetic properties is expected to yield further improvements in sensor performance providing an excellent platform for future wearable technologies.

# Nomenclature

SI units

| **Quantity** | **Unit Name** | **Unit Symbol** |
|---|---|---|
| Length | Meter | m |
| Frequency | Hertz | Hz |
| Force | Newton | N |
| Pressure | Pascal | Pa |
| Energy | Joule | J |
| Electric charge | Coulomb | C |
| Electric current | Ampere | A |
| Electric potential | Volt | V |
| Resistance | Ohm | Ω |
| Capacitance | Farad | F |
| Electric displacement | Coulomb/meter$^2$ | C/m$^2$ |
| Inductance | Henry | H |
| Magnetic flux | Weber | Wb |
| Magnetic flux density | Tesla | T |

Initialisms

| | |
|---|---|
| *AC* | Alternating current |
| *AD* | Angular displacement |
| *B* | Boron |
| *Co* | Cobalt |
| *Dy* | Dysprosium |
| *DC* | Direct current |
| *e.m.f.* | Electro-motive force |
| *Fe* | Iron |
| *FEM* | Finite element modelling |
| *FOE* | Figure-of-eight |
| *Ni* | Nickel |
| *PCB* | Printed circuit board |
| *Si* | Silicon |
| *Tb* | Terbium |
| *TMR* | Tunnel Magnetoresistance |

Greek letters

| | **Description** | **Units** |
|---|---|---|
| $\theta$ | Angle of rotation | rad |
| $\lambda$ | Magnetostriction | - |
| $\lambda_0$ | Spontaneous magnetostriction | - |
| $\lambda_s$ | Saturation magnetostriction | - |
| $\mu$ | Permeability | H/m |
| $\mu_0$ | Permeability of free space | H/m |
| $\mu_r$ | Relative permeability | - |
| $\rho$ | Free electric charge density | C /m$^3$ |
| $\Phi$ | Magnetic flux | Wb |
| $\tau$ | Torque | N.m |
| $\chi$ | Magnetic susceptibility | - |
| $\omega$ | Angular frequency | rad/s |

Roman letters

| | **Description** | **Units** |
|---|---|---|
| $A$ | Area | m$^2$ |
| $B$ | Magnetic flux density (Magnetic induction) | T |
| $C$ | Capacitance | F |
| $D$ | Electric displacement field | C/m$^2$ |
| $E$ | Electric field | V/m |
| $E'$ | Young's modulus | Pa |
| $E_m$ | Magnetic energy | J |
| $e$ | Spontaneous strain | - |
| $f$ | Frequency | Hz |
| $H$ | Magnetic field | A/m |
| $HV$ | Vicker's hardness | - |
| $I$ | Electric current | A |
| $j$ | Free current density | A/m$^2$ |
| $L$ | Inductance | H |
| $M$ | Magnetisation | A/m |
| $m$ | Magnetic moment | A.m$^2$ |
| $N$ | Number of turns of a coil | - |
| $p$ | Magnetic pole strength | A.m |
| $R$ | Resistance | Ω |
| $R_p$ | Tensile strength | N/mm$^2$ |
| $T_c$ | Curie temperature | $^o$C |
| $V$ | Volume | m$^3$ |

# Publications

**Articles:**

**Moreton, G.**, Meydan, T. and Williams, P. (2016). A Novel Magnetostrictive Curvature Sensor Employing Flexible, Figure-of-Eight Sensing Coils. IEEE Transactions on Magnetics, 52(5), pp.1-4.

**Moreton, G.**, Meydan, T. and Williams, P. (2018). Using finite element modelling and experimental methods to investigate planar coil sensor topologies for inductive measurement of displacement. AIP Advances, 8(4), p.047503.

Gibbs, R., **Moreton, G.**, Meydan, T. and Williams, P. (2018). Comparison between Modelled and Measured Magnetic Field Scans of Different Planar Coil Topologies for Stress Sensor Applications. Sensors, 18(4), p.931.

**Conference papers:**

**Moreton, G.**, Meydan, T. and Williams, P. (2017). Investigation and characterization of a planar figure-of-eight coil as a curvature sensor. *In the proceedings of 2017 IEEE SENSORS*.

# Table of Contents

# List of Figures

# List of Tables

# Chapter 1. Introduction

In recent years, the demand for sensors which can be used for angular displacement sensing has increased significantly [1]. This demand is driven by many industries, including the health care sector in areas such as monitoring, rehabilitation and medical instrumentation, and robotics for motion control including the mapping and translation of human movements into robotic actions [2-3]. The increase in demand has seen many types of sensing technology developed, however the majority are too cumbersome to be used in a clinical setting [1, 4]. Current sensors can be found employing a wide range of sensing principles, such as capacitive, resistive, and piezoelectric sensing [1]. These sensors have various disadvantages including high complexity and cost, poor ease of use and low accuracy [1, 5].

The aim of this research is to develop a flexible angular displacement sensor that is accurate, small in size, and easy to use. The proposed sensor design utilises the Villari effect, where the magnetic permeability of the sensing element, in this case amorphous ferromagnetic ribbon, is affected by the applied stress. A coil is used to detect this change in permeability, which results in an inductance change in the coil. The inductance change is then used to determine the angle induced through bending. For this research, planar coils will be used in favour of traditional wound coils, as planar coils have the advantage of a low profile, high reproducibility, and ease of manufacturing [6].

Recently, there has been increasing interest in planar coils, partly due to the growing need for miniaturised sensors, and also the need for batch-produced sensors without the need for sophisticated coil winding machinery [7]. The advances in manufacturing have increased the track density of planar coils, allowing for a larger number of turns given the same dimensions. A further advance, is the ability to produce planar coils on to flexible substrates. Other advantages include the ability to stack multiple planar coils to further reduce the dimensions of the sensor and the possibility for multi-parameter sensing [8-9]. These advantages present opportunities for planar coils to be implemented in applications where wound coils were previously unsuitable due to size or cost restraints [10-11].

The development of the inductive planar coil sensor is divided into three distinct investigations. The first investigation aims to characterise different planar coil topologies, and investigate the effect of distance separation between the ferromagnetic ribbon and the planar coil surface. The second investigation involves assessing the response of different planar coil topologies to the Villari effect as part of a stress sensing experiment. This provides insight into which coil topology is best for stress sensing applications, and forming the basis for the flexible bend sensor design. The third and final investigation involves characterising a series of flexible bend sensors with differing layer configurations. An optimised sensor construction is presented under different conditions of bending.

The literature review is split into two parts. Chapter 2 outlines the fundamental principles of magnetism relevant to the sensor operation and the amorphous magnetic sensing element used. Chapter 3 includes a review of the advances in planar coil design and technology, and its subsequent implementation in sensing devices. The literature review also contains the developments in fields which are applicable to the sensors designed in this thesis, such as wearable devices and motion-sensing. Chapter 4 covers the experimental methodology undertaken for Chapters 5, 6, and 7.

Chapter 5 details the study of different planar coil topologies, and investigates the effects of distance separation between the magnetic ribbon used in the study and the planar coil. The usage of 3D finite element modelling (FEM) was investigated to validate whether FEM can be used for planar coil design. For this, the FEM findings were coupled with experimental findings of planar coils manufactured on printed circuit boards (PCB). Chapter 6 details the experimental studies of planar coil topologies for stress sensing. Chapter 5 and Chapter 6 have been carried out to aid in the design of a flexible bend sensor. Chapter 7 investigates the design of a flexible figure-of-eight coil, which is coupled with magnetostrictive ribbon to form an angular displacement sensor. Different configurations were examined and the optimisation of the sensor was investigated. The flexible angular displacement sensor was comprehensively tested for two different directions of bending.

Chapter 8 contains the conclusions of this investigation followed by Chapter 9 which contains future work identified for furthering the sensor developed and presented in this work.

## 1.1 References for Chapter 1


[1] Szelitzky, E., Kuklyte, J., Mândru, D., O'Connor, N. (2014). Low cost angular displacement sensors for biomechanical applications—A review. *Journal of Biomedical Engineering and Technology*, 2(2), pp.21–28.

[2] Saggio, G., Riillo, F., Sbernini, L. and Quitadamo, L. (2015). Resistive flex sensors: a survey. *Smart Materials and Structures*, 25(1), pp.013001.

[3] Patel, S., Park, H., Bonato, P., Chan, L. and Rodgers, M. (2012). A review of wearable sensors and systems with application in rehabilitation. *Journal of NeuroEngineering and Rehabilitation*, 9(1), pp.21.

[4] Wong, W., Wong, M. and Lo, K. (2007). Clinical Applications of Sensors for Human Posture and Movement Analysis: A Review. *Prosthetics and Orthotics International*, 31(1), pp.62-75.

[5] Jeong, U. and Cho, K. (2016). A Novel Low-Cost, Large Curvature Bend Sensor Based on a Bowden-Cable. *Sensors*, 16(7), pp.961.

[6] Dixon, L. (n.d.). *Designing Planar Magnetics*. [online] Ti.com. Available at: http://www.ti.com/download/trng/docs/seminar/Topic4LD.pdf [Accessed 25 Nov. 2017].

[7] Jow, U. and Ghovanloo, M. (2007). Design and Optimization of Printed Spiral Coils for Efficient Transcutaneous Inductive Power Transmission. *IEEE Transactions on Biomedical Circuits and Systems*, 1(3), pp.193-202.

[8] Dong, L., Wang, L., Ren, Q. and Huang, Q. (2014). Mutual inductance suppressed stacked inductors for passive wireless multi-parameter sensors. *In proceedings of IEEE SENSORS 2014*, pp.926-929.

[9] Jow, U. and Ghovanloo, M. (2013). Geometrical Design of a Scalable Overlapping Planar Spiral Coil Array to Generate a Homogeneous Magnetic Field. *IEEE Transactions on Magnetics*, 49(6), pp.2933-2945.

[10] Nopper, R., Niekrawietz, R. and Reindl, L. (2010). Wireless Readout of Passive LC Sensors. *IEEE Transactions on Instrumentation and Measurement*, 59(9), pp.2450-2457.

[11] Chang, H., Liao, S., Hsieh, H., Lin, S., Lai, C., Chen, R. and Fang, W. (2013). A novel inverse-magnetostrictive type pressure sensor with planar sensing inductor. *In the proceedings of the 2013 IEEE 26th International Conference on Micro Electro Mechanical Systems (MEMS)*, pp.685-688.

# Chapter 2. Fundamentals of Magnetism and Magnetostriction

## 2.1 Fundamentals of Magnetics

This chapter introduces basic principles of magnetism and the derivation of fundamental magnetic equations. Magnetostriction, an intrinsic property of ferromagnetic materials is also discussed, relating the effects of stress on magnetism and vice versa. Finally, an overview of amorphous metallic alloys is presented, including its characteristics and the manufacturing techniques.

### 2.1.1 Maxwell's equations

The properties of electric and magnetic fields can be summarised in the following four differential equations, known as the Maxwell equations:

$$\nabla \cdot D = \rho \tag{2-1}$$

$$\nabla \cdot B = 0 \tag{2-2}$$

$$\nabla \times E = -\frac{dB}{dt} \tag{2-3}$$

$$\nabla \times H = j + \frac{dD}{dt} \tag{2-4}$$

Equation (2-1) describes the relationship between electric charge, $\rho$, and the resulting electric displacement field, $D$; this equation is based on Gauss's law. Equation (2-2) describes an important property of all magnetic fields, where the magnetic flux density $B$ must have a divergence of zero, therefore stating that magnetic monopoles do not exist; this equation is based on Gauss's law for magnetism. Equation (2-3) states that a time varying magnetic field, $B$, induces a voltage in a conductor, with $E$ being the electric field; this equation is based on Faraday's law of induction. Equation (2-4) provides the relationship of the magnetic field, $H$, around a closed loop and the electric current, $j$, passing through the loop, with the addition of the curl generated by a varying electric displacement field $D$. This equation is based on Ampère's circuital law. [1]

### 2.1.2 Magnetic field of a solenoid

A magnetic field, *H*, is produced whenever there is electrical charge in motion. This can be due to an electrical current, *I*, flowing through a conductor, for example. A magnetic field can also be produced by a permanent magnet. In this case the magnetic field is not generated by conventional electric current, but rather the orbital motions and spins of electrons, also known as Ampèrian currents, within the permanent magnetic material. This phenomenon leads to a magnetisation within the material and a magnetic field generated outside of the material. Magnetic fields exert a force on both permanent magnets and current-carrying conductors.

The simplest way of producing a uniform magnetic field is in a thin long solenoid. Assuming an infinitely long solenoid with *N* turns wound to a length of *L* and carrying a current of *I* Amperes the field generated within the solenoid will be

$$H = \frac{NI}{L} \tag{2-5}$$

The magnetic field lines flowing through and around a solenoid is shown in Figure 2.1.

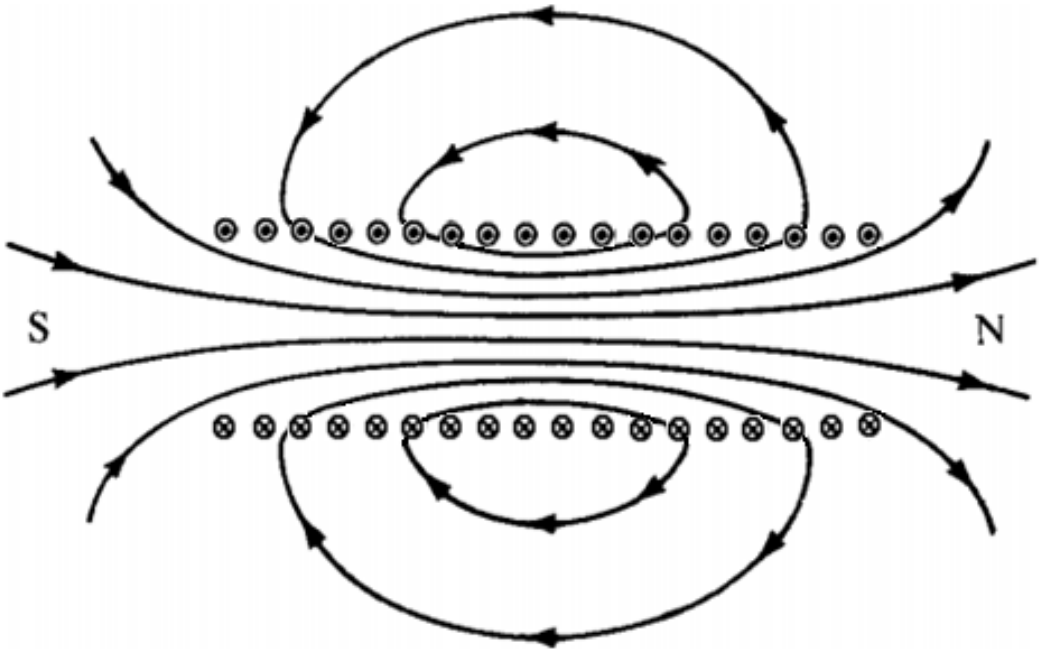


Figure 2.1 – Magnetic field lines of a solenoid. [2]

### 2.1.3 Magnetic flux

When current passes around a conductor loop there is a magnetic field generated, and a certain amount of energy associated with the conductor loop. This magnetic energy created by the current-carrying loop is defined as

$$E_m = \frac{1}{2} I \Phi \tag{2-6}$$

where $I$ is the current flowing around the loop, and $\Phi$ is the amount of magnetic flux generated by this current. Through this relationship it can be seen how the magnetic flux is related with the energy. A magnetic flux will be present whenever there is a magnetic field in free space. The unit which magnetic flux is measured in is Webers.

The magnetic flux density $B$, also known as the magnetic induction, is commonly described in terms of the force on a moving electric charge or electric current. $B$ can be expressed by the value of $\Phi$ passing through a unit area, A, as

$$B = \frac{\Phi}{A} \tag{2-7}$$

The magnetic flux density of 1 Tesla can be described by the force of 1 $Nm^{-1}$ on a conductor carrying a current of 1 A, which is placed perpendicular to the direction of the induction. In free space $B$ can be written as

$$B = \mu_0 H \tag{2-8}$$

with $\mu_0$ being the permeability of free space, which is a universal constant with a value of

$$\mu_0 = 4\pi \text{ x } 10^{-7} H\, m^{-1} \tag{2-9}$$

If either value of $B$ or $H$ in free space is known, the counterpart can be immediately known due to this relationship.

However, this relationship is not representative for $B$ in other media, such as ferromagnetic materials, hence the previous linear function cannot be applied. The two terms are still related by permeability, $\mu$, through the equation

$$B = \mu H \tag{2-10}$$

It is important to note that μ is no longer necessarily a constant. The permeability term μ can be described as

$$\mu = \mu_r \mu_0 \tag{2-11}$$

with $\mu_r$ being the relative permeability. In ferromagnetic materials, the relative permeability varies rapidly with $H$, and cannot be assumed to be constant. The relative permeability is a dimensionless quantity, and is defined as the ratio of the permeability of a specific medium $\mu$, compared to the permeability of free space $\mu_0$.

### 2.1.4 Magnetisation

The effect a magnetic material has on the magnetic induction $B$ when a field passes through it can be represented by the magnetisation. The properties of the material can alter $B$ by making it larger or smaller. The relative permeability of the material indicates how it affects the magnetic induction compared with the observed $B$ in free space.

The magnetic moment can be used as a measure of a magnetic object's tendency to align with an applied magnetic field. The torque on a magnetic dipole τ, of moment $m$ in a magnetic induction $B$ can be written as

$$\tau = m \times B \tag{2-12}$$

and in free space

$$\tau = \mu_0 m \times H \tag{2-13}$$

As shown in (2-6) the energy associated with a conductor loop carrying a current is dependent on the product of the current with the magnetic flux. Using the magnetic flux, it is possible to define a pole strength *p*, where

$$p = \frac{\Phi}{\mu_0} \tag{2-14}$$

The magnetic moment of a dipole consisting of two opposite poles, each of strength *p*, separated by length *l*, is

$$m = pl \tag{2-15}$$

and therefore

$$m = \frac{\Phi l}{\mu_0} \tag{2-16}$$

This definition of magnetic moment can be used to define another quantity, the magnetisation *M*, which is the magnetic moment per unit volume of a solid *V*.

$$M = \frac{m}{V} \tag{2-17}$$

Assuming a bar magnet of dipole length *l*, with flux density Φ at the center, and a cross-sectional area of *A*, the magnetic moment *m* can be given by (2-16). The magnetisation can therefore be written as

$$M = \frac{\Phi}{\mu_0 A} \tag{2-18}$$

and by substituting (2-7) into (2-18), it can be further simplified to

$$B = \mu_0 M \tag{2-19}$$

If both the magnetic field and magnetisation are present then their contribution to the magnetic induction can be summed. It can be concluded that the magnetic induction in free space is $\mu_0 H$ and the magnetisation of a material contributes $\mu_0 M$ to the magnetic induction. The magnetic induction can therefore be simplified to be the vector sum of these,

$$B = \mu_0(H + M) \tag{2-20}$$

where $H$ and $M$ are in Amperes per meter and $B$ is in Tesla.

When a material is converted to a single magnetic domain, magnetic saturation $M_s$ has been achieved. However, at higher fields this magnetisation increases very slowly beyond the point of saturation; this slow increase of magnetisation at high fields is due to the increase in spontaneous magnetisation within a single domain, this is known as forced magnetisation.

The response of a magnetic material to a magnetic field can therefore be defined, using the permeability $\mu$ and susceptibility $\chi$. The permeability is defined as

$$\mu = \frac{B}{H} \tag{2-21}$$

and the susceptibility is defined as

$$\chi = \frac{M}{H} \tag{2-22}$$

Due to the nature of $M$ and $B$, they cannot be assumed to be linear functions of $H$, depending on the material or medium, therefore the permeability and susceptibility cannot be assumed to be constant.

Another term that is often used is relative permeability, denoted as $\mu_r$, and is defined as

$$\mu_r = \frac{\mu}{\mu_0} \tag{2-23}$$

where $\mu_0$ is the permeability of free space. Using this relationship the relative permeability of free space is 1. The relative permeability is also related to the susceptibility by the following equation

$$\mu_r = \chi + 1 \tag{2-24}$$

### 2.1.5 Self-inductance

An example of self-inductance can be realised through a solenoid, of length much greater than its diameter, which has an air core. Consider the solenoid to be of length *l*, composed of *N* turns, which carries a current *I*. The magnetic field, *B*, can be approximated to be uniform within the solenoid, following the equation

$$B = \mu_0 \frac{NI}{l} \tag{2-25}$$

The magnetic flux, Φ, through each turn of the solenoid coil is defined as

$$\Phi = \mu_0 \frac{NI}{l} \pi r^2 \tag{2-26}$$

with *r* being the radius of the coil. The equation can be further simplified, with the cross-sectional area $\pi r^2$ abbreviated as *A*. By combining this abbreviation, and accounting for the *N* turns of the complete solenoid, the total magnetic flux through the solenoid is

$$\Phi = \mu_0 \frac{N^2 IA}{l} \tag{2-27}$$

When the solenoid's current changes there will be a voltage induced in the solenoid coil, this voltage opposes the change of current. The voltage is referred to as the electromotive force, e.m.f. Using Faraday's law of induction, the e.m.f. voltage can be expressed as

$$V = -\frac{d\Phi}{dt} \tag{2-28}$$

The equation can be further expanded

$$V = -\frac{d\Phi}{dI} \cdot \frac{dI}{dt}$$

$$V = -\mu_0 \frac{N^2 A}{l} \cdot \frac{dI}{dt} \tag{2-29}$$

This equation for e.m.f can be written as

$$V = -L\frac{dI}{dt} \tag{2-30}$$

where

$$L = \frac{d\Phi}{dI} \tag{2-31}$$

$$L = \mu_0 \frac{N^2 A}{l} \tag{2-32}$$

## 2.2 Magnetostriction

### 2.2.1 Principles of magnetostriction

The magnetisation of a ferromagnetic material is nearly always accompanied by changes in dimensions. This resulting strain is referred to as magnetostriction, $\lambda$. This phenomenon can be categorised into two main types, the spontaneous magnetostriction which arises from the ordering of magnetic moments into domains at the Curie temperature, $T_c$, and the magnetostriction induced by an external magnetic field. [3]

In both cases the magnetostriction, $\lambda$, is defined as the fractional change in length,

$$\lambda = \triangle l/l \tag{2-33}$$

Where $l$ is the length of the material in the absence of an external magnetic field $H$ and $\Delta l$ being the change in length under the application of $H$. In most materials, $\Delta l$ is a very small value [2]. $\Delta l$ can also be positive or negative depending on whether the material increases or decreases in respect to its length as a result of an applied magnetic field.

Magnetostriction was first discovered by Joule in the 19$^{th}$ century, by observing a rod of iron. [4] Spontaneous magnetostriction occurs due to the creation of domains within the ferromagnetic material as it is cooled below $T_c$. Above this temperature, a paramagnetic state exists with a completely random alignment of magnetic moments. These magnetic moments become ordered over volumes containing a vast quantity of atoms (typically $10^{12}$-$10^{18}$), these volumes are referred to as domains. In these domains all of the moments lie parallel, thus leaving the domain with an overall magnetic moment. In the demagnetised state, these magnetic domains are aligned in such a way to ensure that the bulk magnetisation of the material is zero, as shown in Figure 2.2(a).

Field-induced magnetostriction occurs when the domains are reoriented by a magnetic field. The saturation magnetostriction, $\lambda_s$, is the fractional change in length between a ferromagnetic specimen which is demagnetised and the same specimen in a magnetic field with a magnitude sufficiently large to saturate the magnetisation along the field direction. In this scenario, there will be a change in the shape of the material as the applied field generates a preferred direction for the magnetic domains. The gradual effects of an applied magnetic field to domain magnetisation can be seen in Figure 2.2 (b, c), and the saturation magnetisation in Figure 2.2 (d).

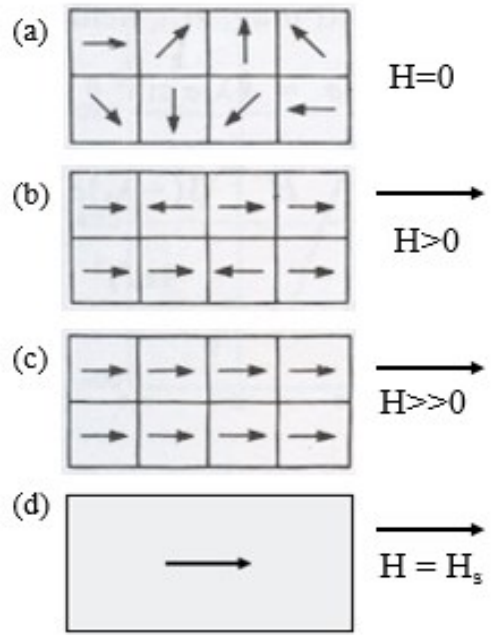


Figure 2.2 – A simplified representation of domain magnetisation due to an external applied field. [5]

Magnetostriction is greatly dependent on the internal structure of the material. When the domains are parallel or antiparallel to the applied field it can be said that they are in an easy axis with the field, as they experience no rotational force. However, should the domains intersect the applied field at a certain angle, they will start to rotate towards the field direction, shown in Figure 2.2 (a, b). Given sufficient field strength these non-parallel domains will become parallel or antiparallel with the applied field, and by increasing the field further all of the domains will eventually become parallel at saturation magnetisation, this transition is seen in Figure 2.2 (c, d). The magnetisation of domains which are at an angle to the easy axis will require larger fields to attain saturation magnetisation, and therefore higher amounts of energy. This is due to the directional dependence of the magnetic material's properties, and is known as anisotropy. This energy is referred to as the magnetic anisotropy energy.

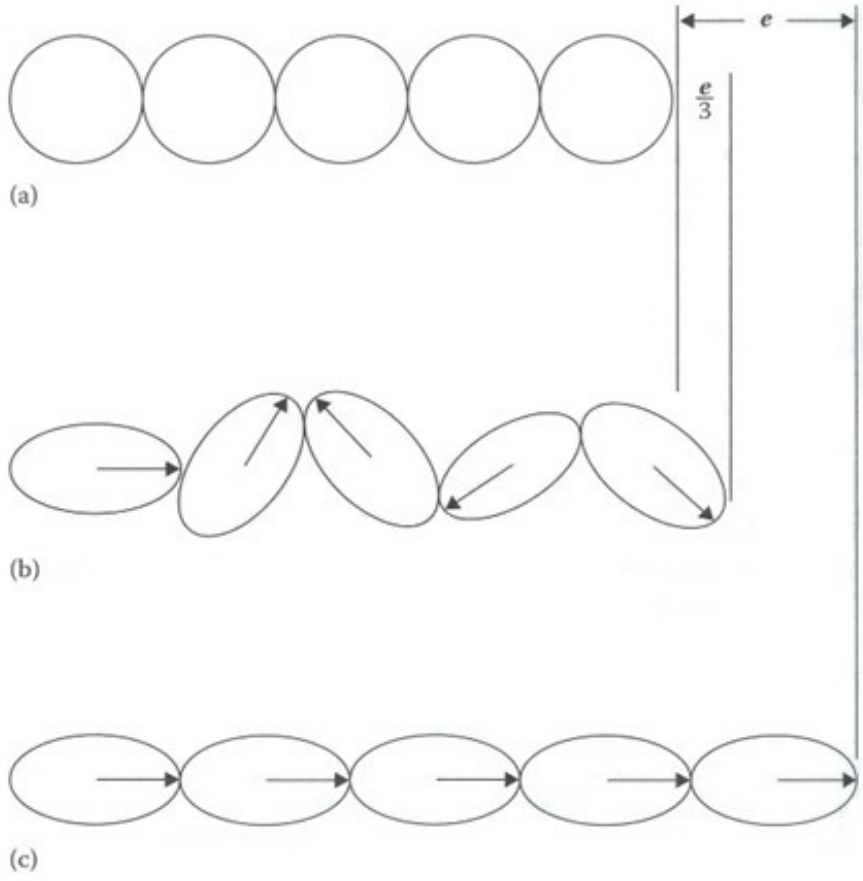


Figure 2.3 – Schematic diagram demonstrating magnetostriction. (a) Magnetostriction in a disordered regime; (b) magnetostriction in a demagnetised ferromagnetic regime; (c) magnetostriction in a ferromagnetic regime, magnetised to saturation. [3]

Considering an isotropic material with unstrained, disordered, spherical volumes above $T_c$, as seen in Figure 2.3(a). When the material is cooled below $T_c$ it becomes ferromagnetic, and spontaneous magnetisation appears within the newly formed domains. With this magnetisation, an associated spontaneous strain $e$, also known as spontaneous magnetostriction $\lambda_0$, is generated as shown in Figure 2.3 (b).

For this isotropic example the amplitudes of the spontaneous magnetostrictions are independent of the crystallographic direction. Within each of these domains the strain varies with angle $\theta$ from the direction of the spontaneous magnetisation according to the following relation

$$e(\theta) = e\cos^2\theta \tag{2-34}$$

The average deformation throughout this isotropic solid due to the spontaneous magnetostriction can therefore be obtained through integration assuming that the domains are oriented randomly so all directions are equally likely.

$$\lambda_0 = \int_{-\pi/2}^{\pi/2} e \cos^2\theta \sin\theta \, \mathrm{d}\theta \qquad (2\text{-}35)$$
$$= e/3$$

This is the spontaneous magnetostriction caused by the ordering of magnetic moments due to the onset of ferromagnetism.

By using the isotropic model, the ordered but demagnetised state is transformed to the ordered and saturated state through the application of an external magnetic field. In this saturated state the magnetic moments, and therefore the strains, within each domain will all be aligned parallel to the field. This can be seen in Figure 2.3 (c). It is possible to calculate the saturation magnetostriction as it is the difference between the saturation magnetostriction, and the spontaneous magnetostriction,

$$\lambda_s = e - \lambda_0$$
$$\lambda_s = \frac{2}{3}e \qquad (2\text{-}36)$$

When the magnetic field applied exceeds the strength required for saturation magnetostriction, forced magnetostriction occurs. This effect is much like the forced magnetisation process discussed in Chapter 2, where the material has been converted to a single domain, however it is a very small change in magnetostriction as the field is increased. This phenomenon is caused by the increase in the ordering of individual atomic magnetic moments within the single domain. Figure 2.4 shows the effects of an applied magnetic field on a magnetostrictive material.

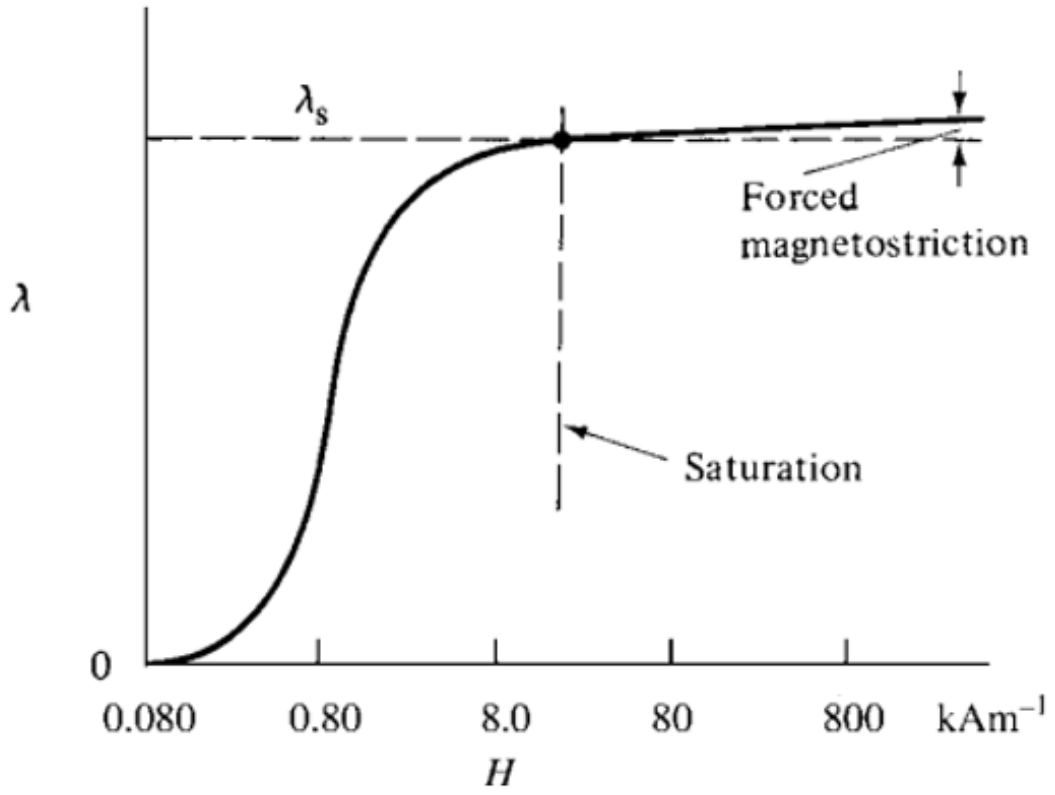


Figure 2.4 – Variation of magnetostriction with magnetic field. [2]

### 2.2.2 Inverse magnetostriction

In 1864 Villari discovered that when a stress is applied, the direction of domain magnetisation changes due to the externally induced magnetostriction. This phenomenon is known as inverse magnetostriction, or the Villari effect. The applied stresses affect magnetic properties, most importantly the permeability, of the material. For example, a material with a positive $\lambda$ will elongate when magnetised; or by applying a tensile stress increases the ease of magnetisation in the strain direction. Applying a compressive stress has the opposite effect. These conclusions are valid whether or not a field is acting, as long as the magnetisation is not zero, as no changes in $H$ will take place if the material is stressed in a demagnetised state [2]. An example of this phenomenon can be seen in Figure 2.5.

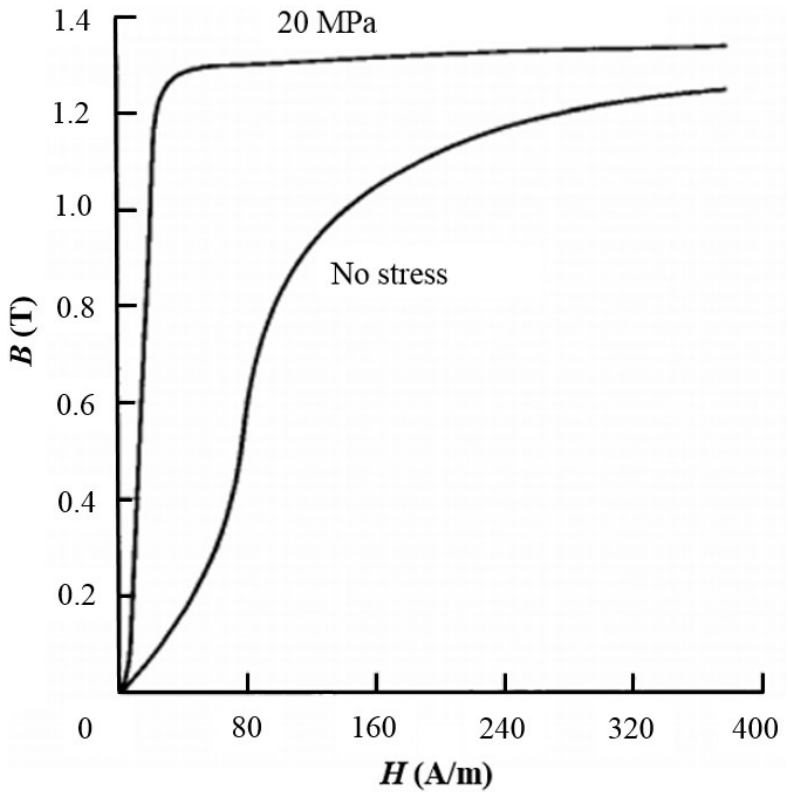


Figure 2.5 – Effect of applied tensile stress on the magnetisation curve of 68 Permalloy. [5]

## 2.3 Properties of Ferromagnetic Materials

### 2.3.1 Ferromagnets

Bulk susceptibility can be used to classify different groups of magnetic materials. If a material has a susceptibility which is small and negative it is classified as a diamagnetic material, with a typical susceptibility of $\approx -10^{-5}$. Diamagnetic materials' magnetic response opposes an applied magnetic field, as the susceptibility is negative.

If a material has a susceptibility which is positive and small, they are classified as a paramagnetic material. A paramagnetic material has a typical susceptibility of $\approx 10^{-3}$ to $10^{-5}$. The magnetisation of paramagnets are weak, however they align parallel with the direction of an applied magnetic field.

Ferromagnetic materials are the most widely recognised magnetic materials, which possess a positive susceptibility that is much greater than 1. Typical susceptibility values are $\approx$ 50 to 10000 [3].

### 2.3.2 Hysteresis

The most common way of representing bulk magnetic properties of a ferromagnetic material is by a plot of magnetic flux density, *B*, for varying magnetic field strengths, *H*. An example of a hysteresis loop of a ferromagnetic material is shown in Figure 2.6.

A ferromagnetic material retains the magnetisation when the external applied field is removed. To return the material back to its zero magnetisation state an external applied field in the opposite direction must be applied. A hysteresis loop such as Figure 2.6 will be traced if an alternating magnetic field is applied to the material, this is due to the presence of magnetic domains in the material. If the magnetic domains are oriented, additional energy is required to return them to their previous state.

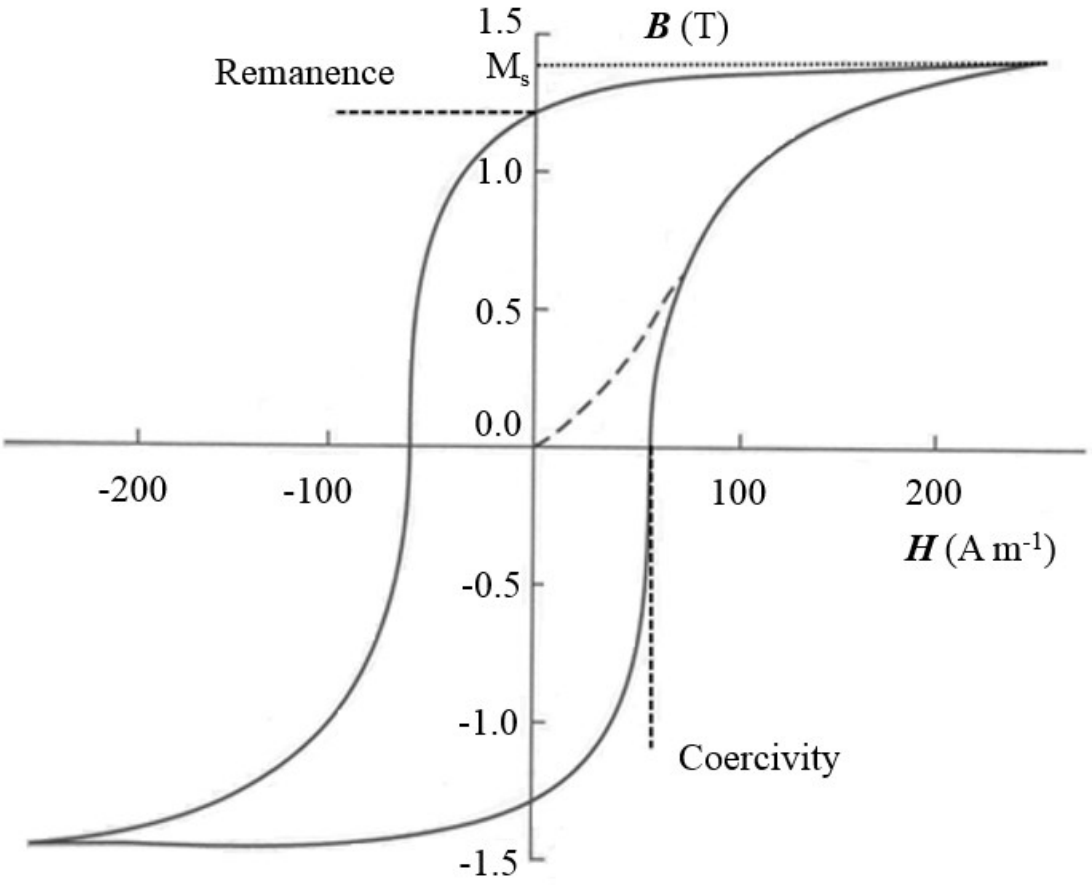


Figure 2.6 – Hysteresis loop of a ferromagnetic material, showing coercivity, remanence, and the saturation magnetisation, $M_s$. [3]

### 2.3.3 Saturation magnetisation

It can be seen in Figure 2.6 that the ferromagnetic material is not magnetised in its initial state, and that due to the application of an external magnetic field the magnetic induction increases in the direction of the applied field. If the applied magnetic field is increased to a point where all the magnetic dipoles within the material are aligned in the direction of the applied field, the value of the magnetic field at this point is the saturation magnetisation, $M_s$.

### 2.3.4 Remanence

When an external applied field is reduced to zero after magnetising a ferromagnetic material the remaining magnetic induction is defined as the remanent induction, $B_R$, and the remaining magnetisation is defined as the remanent magnetisation, $M_R$.

$$B_R = \mu_0 M_R \tag{2-37}$$

Along with remanent induction, remanence is used as a term which describes the value of the induction remaining in the ferromagnetic material after the applied field is removed after saturation magnetisation has been reached. Whereas the remanent induction term is used to describe scenarios where a field is removed before reaching saturation magnetisation. The remanence can therefore be thought of as the upper limit of remanent induction for the material [3].

### 2.3.5 Coercivity

The magnetic induction of a ferromagnetic material can be reduced to zero through the application of a magnetic field strength in the opposite direction of strength $H_c$. This field strength is known as the coercivity. As with remanence, there is a distinction drawn between the coercive field and coercivity. The coercive field describes the magnetic field required to reduce the magnetisation to zero from an arbitrary level. Coercivity describes the magnetic field required to reduce the magnetisation to zero from saturation. The coercivity can therefore be thought of as the upper limit of coercive force for the material [3].

## 2.4 Amorphous Metallic Alloys

Amorphous metals are solid metallic materials with a disordered structure on the atomic-scale. These amorphous metals are often alloys. The majority of metals are crystalline in their solid state, meaning the structure of the atoms are highly ordered. The absence of lattice ordering and therefore non-crystalline structure is shown in Figure 2.7.

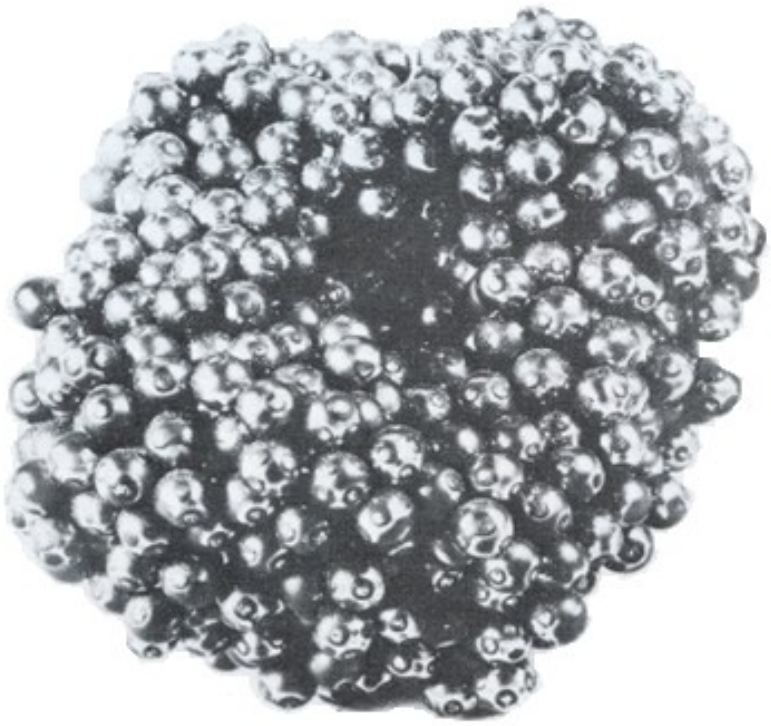

Figure 2.7 – A lab-constructed random close-packing of hard spheres, demonstrating an absence of lattice ordering. [6]

Amorphous magnetic ribbons, also known as metallic glasses, are produced by the process of rapid cooling (quenching) of magnetic alloys containing iron, nickel and/or cobalt together with one or more of the following elements: boron, silicon, phosphorous and sometimes carbon [6]. In the as cast condition the alloys have very soft magnetic properties however by annealing these alloys these properties are enhanced for soft magnetic material applications.

The annealing process relieves stresses within the material, field annealing can also be employed for domain alignment to create an easy axis. The molten alloy is continuously sprayed in a high pressure jet on to a rapidly moving cold surface, often a rotating metal wheel. This process of quenching produces a thin ribbon of the material.

Due to the quenching process the materials do not form a crystalline structure but rather a solid with only short-range order with otherwise random microstructural properties. These materials can therefore be considered to have a random structure [3]. In general, a magnetically soft alloy, which is easily magnetisable, will be mechanically soft. In contrast magnetically hard alloys are normally mechanically hard. Amorphous metallic alloys are extremely useful as they combine magnetic softness with mechanical hardness, lending themselves to many applications where crystalline alloys are unsuitable [7].

In amorphous metallic alloys, the absence of a long-range ordered atomic structure leads to a wide range of characteristics and features which makes these alloys favourable in a variety of applications. Table 2.1 presents a survey of crystalline and amorphous magnetic alloys, detailing their magnetic and mechanical properties. In this table the mechanical properties listed are the Vicker's Hardness, HV, the Young's modulus, E', and the tensile strength, $R_p$.

Table 2.1. Materials used for magnetoelastic sensors. [7, 8]

| *Type* | *Alloy* | $\lambda_s$ $\cdot 10^{-6}$ | $H_c$ A/cm | $B_s$ T | HV | $R_p$ N/mm$^2$ | $E$ GPa |
|---|---|---|---|---|---|---|---|
| Crystalline | 50 Co, 50 Fe | +70 | 1.4 | 2.35 | 200 | 400 | 230 |
| | 50 Ni, 50 Fe | +25 | 0.05 | 1.55 | 110 | 140 | 140 |
| | 97 Fe, 3 Si | +9 | 0.1 | 2.0 | 180 | 350 | 150 |
| | Ni | -35 | 1.5 | 0.6 | 75 | 120 | 210 |
| Amorphous | $Fe_{80}$ $B_{14}$ $Si_6$ | +30 | 0.04 | 1.5 | 950 | | 150 |
| | $Co_{75}$ $Si_{15}$ $B_{10}$ | -3.5 | 0.025 | 0.7 | 1000 | 1500 ~ | 150 |
| | $Co_{68}$ $Ni_{10}$ $B_{14}$ $Si_8$ | -8 | 0.025 | 0.85 | ~1000 | 2000 | 150 |
| | Metglas 2605S3A | 20 | 0.16 | 1.41 | 860 | | ~100 |
| Crystalline | (Tb Dy) $Fe_2$ | +2000 | 50 | 1.0 | 460 | 700 | 30 |

It can be seen that amorphous metallic alloys are easily magnetisable, they also exhibit magnetostriction comparable with crystalline alloys with similar coercivity values. At the macroscopic level, the magnetostriction of amorphous alloys is isotropic and the magnetocrystalline anisotropy is nearly zero, which allows for easy magnetisation rotation [7]. Mechanically they exhibit high tensile strength, yield strength, and hardness, compared with crystalline alloys. In addition, their homogeneity and lack of microstructural discontinuities make them highly resistant to corrosion [6].

A brief overview has been provided on the theory of magnetism in this chapter. The effects of magnetostriction has been described, as well as the inverse magnetostrictive effect. Amorphous materials were also described, and how they can be preferable in certain applications, due to their properties. This will provide the basic understanding required for some concepts described in later chapters.

## 2.5 References for Chapter 2


[1] Stöhr, J. and Siegmann, H. (2006). *Magnetism*. Berlin: Springer.

[2] Cullity, B. and Graham, C. (2011). *Introduction to Magnetic Materials*. Somerset: Wiley.

[3] Jiles, D. (1998). *Introduction to magnetism and magnetic materials*. 2nd ed. London: Chapman & Hall.

[4] Joule, J. (1847). *On the effects of magnetism upon the dimensions of iron and steel bars*.

[5] Bozorth, R. (2003). *Ferromagnetism*. Hoboken, N.J.: Wiley.

[6] Luborsky, F. (1983). *Amorphous metallic alloys*. London: Butterworths.

[7] Göpel, W., Hesse, J., Zemel, J., Boll, R. and Overshott, K. (1989). *Sensors: A comprehensive survey, Volume 5, Magnetic Sensors*. Weinheim: VCH.

[8] Metglas. (n.d.). Magnetic Alloy 2605S3A(Iron-based) Technical Bulletin. [online] Metglas.com. Available at: https://metglas.com/wp-content/uploads/2016/12/2605S3A-Technical-Bulletin.pdf. [Accessed 16 Dec. 2017]

# Chapter 3. Planar Coil Technology and Sensors

## 3.1 Introduction to Planar Coil Technology

The purpose of this research is to investigate and develop inductive planar coil sensors. This chapter aims to provide a background on the inception of planar coils and the development of planar coil technology through time, including design considerations and fabrication methods. The many different algorithms and modelling methods used to characterise and predict the parameters and performance of different planar coils is described. A wide range of planar coil applications have also been discussed, varying from wireless power transmission systems to nondestructive testing (NDT) and evaluation (NDE). As part of this research focuses on developing a wearable flexible planar coil sensor, wearable sensor technology has also been presented in this chapter, with a focus on hand motion sensing.

### 3.1.1 Development of planar coils

Planar coils were investigated in the early 1900s due to their applications as radio coils and wound inductor alternatives. Many studies investigating planar coils were conducted, in an attempt of deriving the characteristics of the coils, such as the inductor values which will aid the design of the coils [1-8]. The self-inductance of planar coils was first investigated by Rosa [3-4], whose work was further developed by Grover [5-7].

Their work pioneered the concepts of self-inductance of each individual segment within the planar coil, and the mutual inductance between two segments. The mutual inductance of a coil segment interacts with neighboring segments of the coils, and the value of the mutual inductance is dependent on the direction of the current flow within the segments. These principles became imperative in the calculation of the inductance of planar coils, as the planar coils were divided into individual segments, and their respective self-inductance and mutual inductance were calculated and summed to provide an inductance value of the coil. Whilst Grover's work focused predominantly on solving inductance calculations for rectangular spiral coils, Wheeler proposed an approximate calculation for spiral-shaped inductors [1-2].

Both Wheeler's and Grover's models for calculating spiral coil inductances were used as the basis to improve inductance formulae, with Greenhouse developing a method based on Grover's model which is considered as the most comprehensive and accurate method [8].

### 3.1.2 Development of applications for planar coils

Planar inductors were first developed for use in IC (integrated circuit) applications by Soohoo [9], who designed and fabricated spiral planar coils specifically for replacing wound coils in IC applications. This work was followed up by Kawabe et al., who investigated various topologies and their inductive and resistive characteristics over a large span of frequency of up to 100 MHz [10]. It was found that the inductance value remains largely unaffected by frequency, up to a frequency of approximately 10 MHz. The analysis of various coil topologies showed that spiral coil topologies possessed the largest inductance value, and the lowest resonance frequency, indicating that the spiral topology may not be suitable for applications exceeding the high frequency band. This work of designing planar coils suitable for magnetic IC applications was continued by Oshiro et al. [11-12], who developed a planar inductor with an improved frequency response. Oshiro et al. also developed a bifilar configuration, which includes a parallel planar coil which was additionally manufactured as shown in Figure 3.1 and Figure 3.2, to change the inductor's performance. It was observed that by configuring the parallel planar coil differently, the coupling factor of the segments were influenced. With a positive coupling factor, the inductance of the coil became much larger, and vice versa.

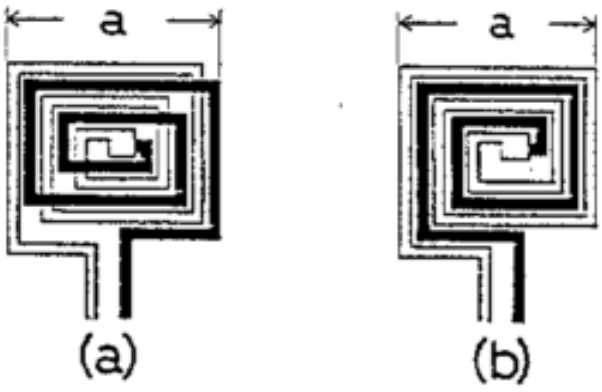


Figure 3.1 – Schematics for the two 'bifiliar' planar inductors. (a) Outer type; (b) inner type. [11]

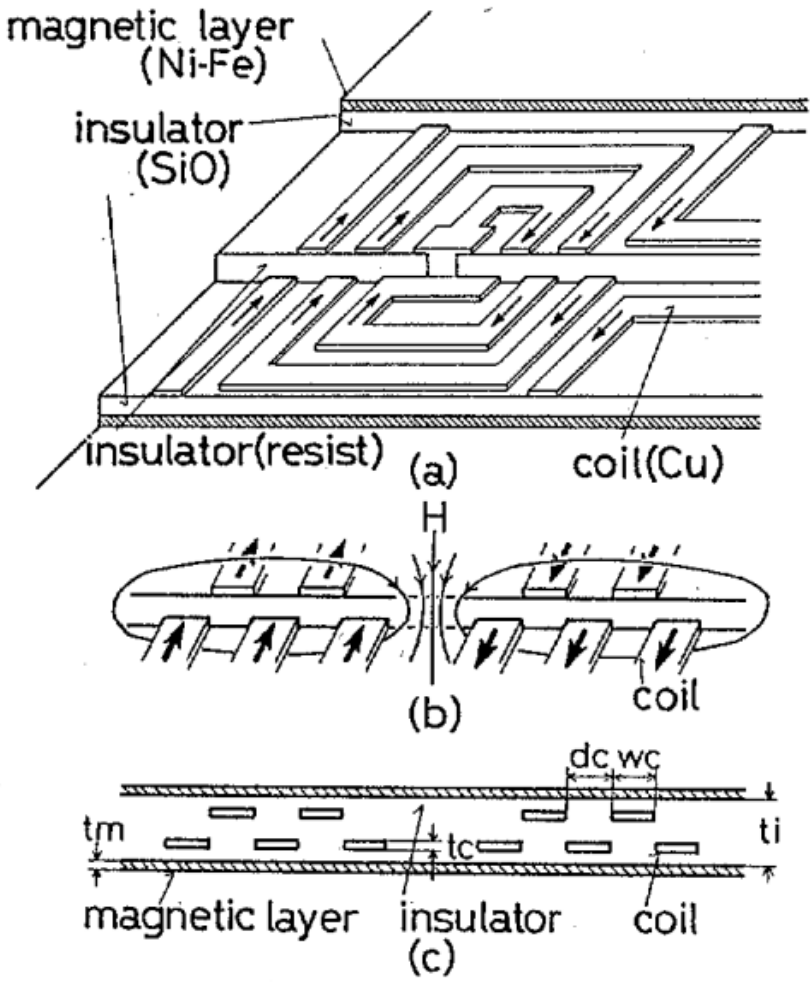


Figure 3.2 – An overview of the outer type configuration, with an Iron-Nickel alloy (Ni-Fe) magnetic layer, a silicon oxide (SiO) insulator layer, and copper (Cu) tracks. (a) Schematic view; (b) magnetic field distribution due to coil current; (c) cross-sectional view of the coil, with dc being the distance between tracks, wc being the width of the tracks, tc being the thickness of the tracks, tm being the thickness of the magnetic layer, and ti being the thickness of the insulator. [11]

As the demand for Si-based based RF circuits grew, the research into planar coils expanded, with a physical model for planar spiral inductors being developed [13]. The physical model considers the many various parameters which may affect the performance of planar spiral inductors in RF applications, with which the quality factor (Q-factor) of the inductor can be approximated. This physical model also investigated parasitics of the planar inductor, and hence its feasibility of implementation in high frequency applications. The model proposed can be seen in Figure 3.3.

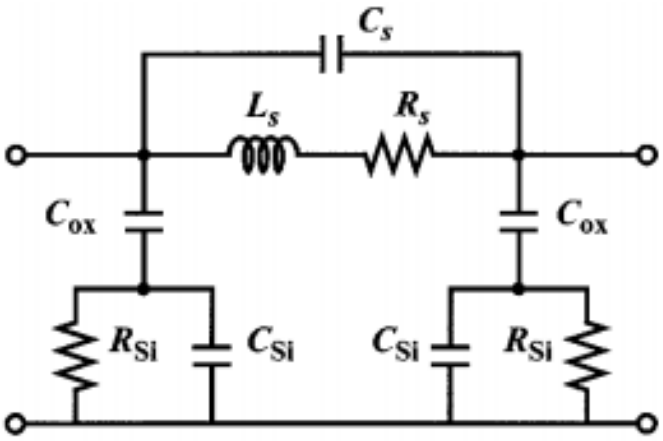


Figure 3.3 – Physical model of an inductor on silicon. With Ls representing the series inductance computed using Greenhouse's equation, Rs representing the series resistance of the coil, Cs representing the feed-forward capacitance, Cox representing the capacitance between the spiral and the silicon substrate. Rsi and Csi are used to model the silicon substrate. [13]

Interest in planar coils has increased due to developments in implant technologies. Due to the need to miniaturise the size of the implants, an alternative to a conventional battery was required. This encouraged researchers to investigate wireless power transfer using paired coils, the receiver coils had to have a very small size profile due to the application. Neagu et al. [14] investigated planar coils designed for telemetry systems for wireless power transfer to implantable microsystems, shown in Figure 3.4. A model was developed based on their work, which described parasitics of planar coils over a range of frequencies, and predicting characteristics of the planar coil such as the resonant frequency, the quality factor, and the power transfer. The model was compared with experimental findings, and a good agreement was found between the two. Various parameters could be altered for an improved quality factor of the power transmission system, one of the parameters being the increased number of turns of the coil.

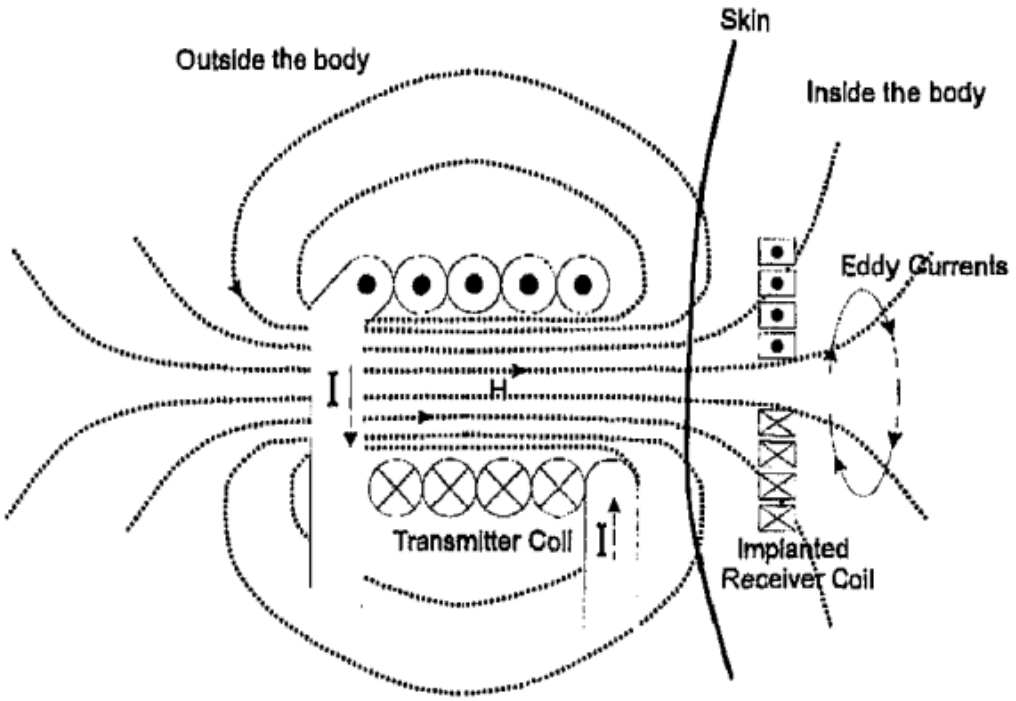


Figure 3.4 - Cross-section of proposed transmitter-receiver system, showing magnetic field linkage. [14]

Mohan et al. [15] presented several expressions for approximating the DC inductance of various spiral planar coils, ranging from the square to circular topology. The accuracy of the proposed expression was compared with the solutions of a 3D field solver ASITIC (Analysis and Simulation of Spiral Inductors and Transformers for ICs), measurements made through experimental means, and previously published data. The proposed expression matches the field solver solution better than previous published algorithms, it also matched the experimental measurements better. This proposed expression is thought to match typical inductor tolerance levels, and can be considered as an expression accurate enough for the design and optimisation of planar inductors.

Planar coil topologies have since then been employed in many applications, as both inductive and electromagnetic sensors [16]. The modelling and optimisation of planar coils continued being an area of great interest [17-18], with developments in miniaturisation of the coil and the environment in which the coil was to be used. Reissman et al. [19] demonstrated the possibility of manufacturing multilayer stacked coils using single-level lithography, as opposed to multi-level approach previously employed, thus reducing the cost of fabrication. Through stacking multiple planar

coils, the inductance value can be increased greatly, which is a requirement for certain applications, such as DC-DC power converters.

Ortego et al. [20] demonstrated the possibility of fabricating planar coils through a combination of additive manufacturing and sintering. A planar coil antenna was printed using the Dimatix inkjet printer using silver conductive ink. An advantage of this fabrication method is the ability to modify the inkjet print drop volume and the number of layers, this allows for the characteristics of the coil to be finely tuned to the designer's specifications. An overview of the sintering process is shown in Figure 3.5, and a prototype of the printed antenna is shown in Figure 3.6.

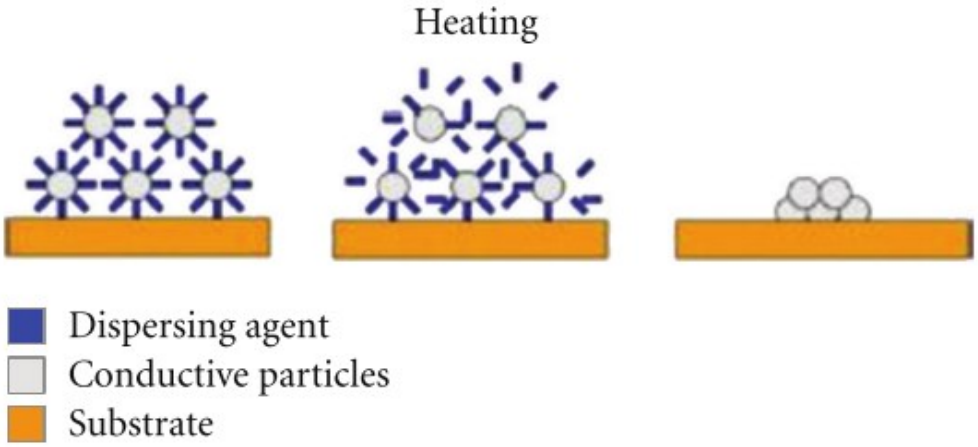


Figure 3.5 – Sintering process of the inkjet printed silver track. [21]

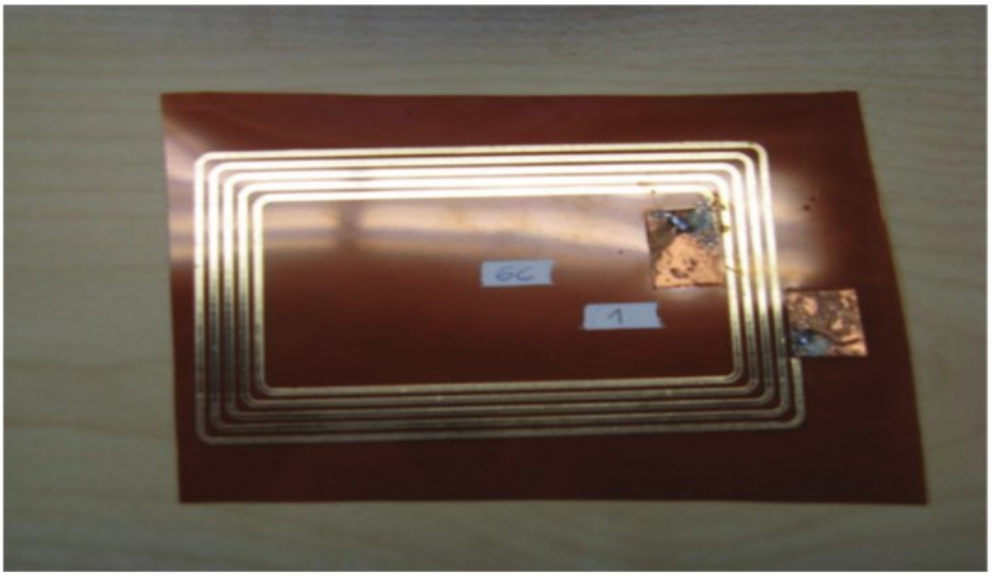

Figure 3.6 – Printed antenna prototype. [20]

Further investigations were conducted for Coreless Printed Spiral Winding (CPSW) inductors, by observing the changes to the characteristics of the inductor caused by modifying the hollowness of the coil. The hollowness parameter is defined as a relationship between the innermost radii and outermost radii of the coil, the ratio between these two are defined as the hollowness [22]. The quality factor can be improved greatly along with a reduction in power loss if optimal hollowness is achieved, which depends on the ratio between conductor width to the skin depth at the operating frequency. Figure 3.7 shows a full spiral coil and a hollow spiral coil.

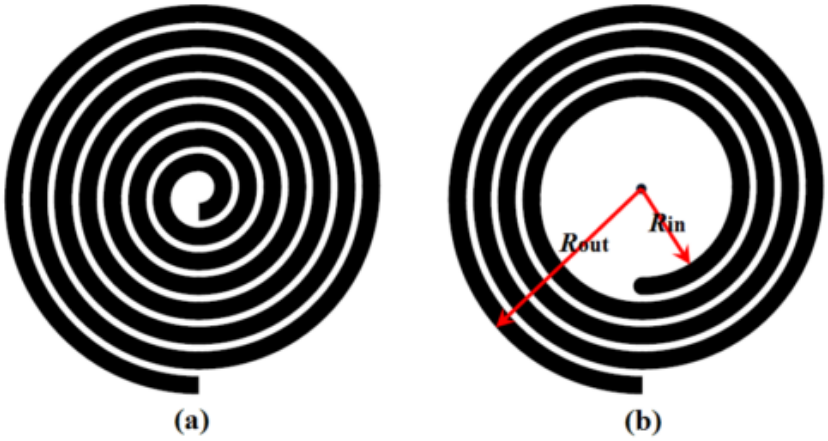


Figure 3.7 – Spiral coil types. (a) Full spiral coil; (b) hollow spiral coil. [22]

One of the characteristics that have also been investigated is the self-resonance of the spiral coils, this is important for wireless power transfer systems based on resonant coupling. A faster computation was achieved by utilising a transmission line model, however stray capacitances were neglected at the ends along with the radial component of the tracks. It is reported that the frequency error is about 1%, whilst reducing solving times to under a second. This is a significant improvement, however it should be noted that it only applies to almost rotationally symmetric structures, such as the circular spiral coil [23].

### 3.1.3 General planar coil design considerations and constraints

There are many parameters which will affect the characteristic of a planar coil, and its performance in the application it has been designed for. Design constraints are often centered on the limits of the fabrication technique, and other application specific constraints such as size and inductance.

There have been many investigations on the various parameters and how they affect planar coils in different applications, based on these findings planar spiral coil (PSC) design methodologies for specific applications have been proposed [24-29]. A combination of calculations and commercial software have been used to investigate how parameters such as fill ratio and track width affects PSC characteristics, and how they can be optimised for wireless power transfer (WPT) in specific environments [18, 24]. Sophisticated algorithms have also been used to aid optimisation of PSC characteristics given parameter limits and requirements, it was demonstrated that the algorithm based design method proposed is effective for both single layer planar coil design and double stacked planar coil design, with the Method of Assigning Priority Levels (MAPLE) being particularly efficient [26]. In addition to MAPLE, the Self-Organising Migrating Algorithm (SOMA) was also used, displaying the possibility of using artificial neural networks for planar coil design and optimisation.

An optimisation on coil size ratios have been made for WPT applications, a simplified equation is given for the calculation of parasitics in spiral coils for WPT systems, and a design procedure which can maximise coil ratios for maximum WPT efficiency given operating distance constraints [27]. Utilising the modified Wheeler's equation, high inductance planar coils were designed given a size constraint. These high inductance coils were optimised for the largest inductance possible, by changing the number of turns, which is a common method of increasing self-inductance of a PSC. It was presented that the modified Wheeler's equation could be used to optimise PSCs, with good agreement between experimentally measured parameters and approximated values [28].

## 3.2 Planar Coil Sensors

PSCs have been used in conjunction with capacitors to create inductor-capacitor (LC) tank circuits. These LC tanks have been used widely in many applications, due to the passive nature and versatility of these circuits. Both the inductive and capacitive elements of the tank can be used as sensing elements, in capacitive sensing scenarios the planar coil serves as a pick-up coil in addition to an inductor. A wide range of RFID based solutions have been proposed, due to the wireless nature of these sensors, the low costs of manufacturing, unobtrusiveness, and accessibility [29-30]. A general overview of sensors with planar coil integration will be discussed.

Food quality control is an area where the RFID tag sensors can be implemented, as tags are commonly placed on the packaging for foodstuffs, the capacitive element interacts with the foodstuffs under investigation and a dielectric constant shift can be detected should certain bacteria be produced [31-35]. An example of food quality monitoring using RFID can be seen in Figure 3.8.


Figure 3.8 – Milk cartons with RFID sensors attached. [32]

Wireless pH sensor based on LC tank circuits have been proposed, with mutual inductance coupling and a varactor-based sensing element. The variable capacitive property of the varactor provides a shift in the resonant frequency of the LC tank, however if implanted for gastric pH monitoring the signal will be weaker than magnetic alternatives, due to lower attenuation of magnetic fields compared to

electromagnetic fields [36]. Capacitive sensing elements using electrodes have been proposed for corrosion sensing for the remote monitoring of structures, and for the use in a smart-cap for detecting degradation of milk [35, 37].

The interdigital configuration is commonly used for capacitive sensing, an example is shown in Figure 3.9. Such configurations have been widely used in many sensing applications, such as dielectric constant and conductivity sensors, gas sensors, and RFID food quality sensors [32, 38-39]. The interdigital configuration generates electric fields which interact with its surroundings, when the dielectric constant of its surroundings changes a change in the capacitance can be detected.

Figure 3.9 – A planar interdigital sensor. [38]

An interesting field of research is the development of multi-parameter sensors, using passive LC sensors for monitoring multiple parameters. A multi-parameter sensor based on a stacked inductor configuration has been proposed [40-41]. One of the proposed designs relies on three sensors for temperature, pressure, and relative humidity, each connected to a coil. The mutual inductance between the stacked inductors is suppressed through configuring the windings in a specific way such that mutual inductance between the inductors is minimised [40]. A similar implementation of stacked coils was also reported, with two sensors and two stacked coils [41].

A major improvement to this configuration can be seen in Figure 3.10, where a single planar inductor is required for the sensing of two parameters, made possible through the relay switch. The relay switch operates through the voltage induced by the planar inductor when it is coupled with the readout coil [42]. This demonstrates the versatility of LC circuits as multiple parameters can be passively and wirelessly monitored

through the coupling of just one planar inductor. To accommodate increasing applications of stacked coils a variable inductance inductor has been developed by implementing a MOSFET switch control and stacked planar coils, as shown in Figure 3.11 [43]. By fabricating stacked inductors, chip area can be conserved, and the proposed design demonstrates comparable quality factor at high frequencies, with large quality factor degradation being contributed through the losses in the switch.

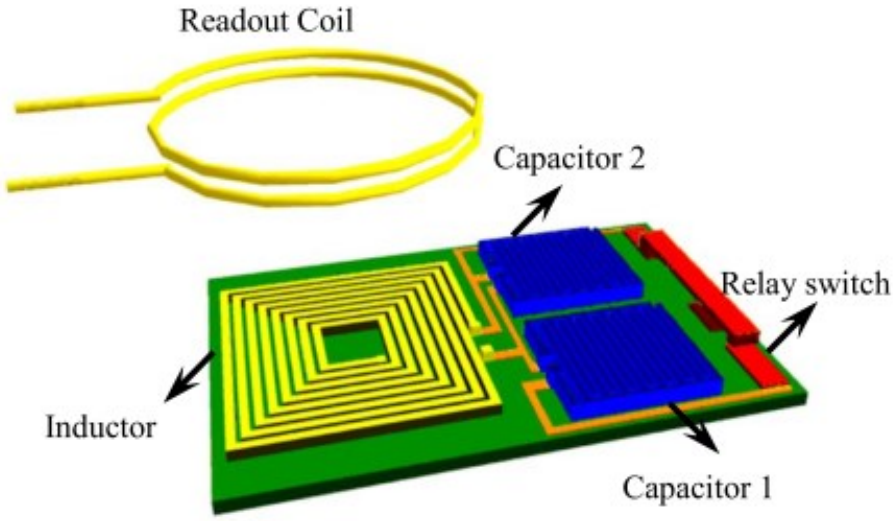


Figure 3.10 – Double parameter sensor based on LC tank with relay switch integrated. [42]

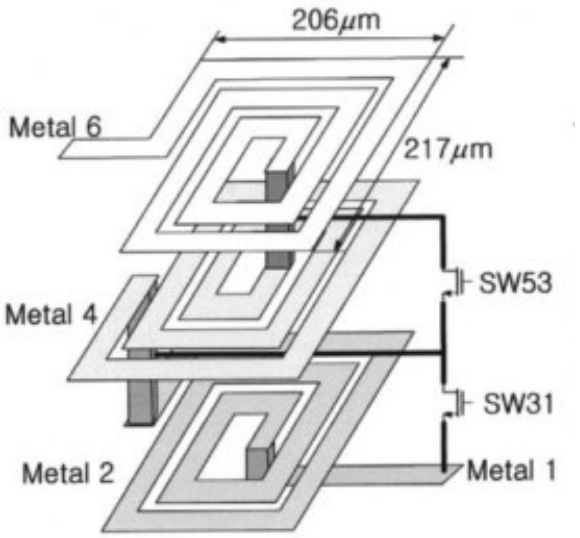


Figure 3.11 – Variable monolithic stacked inductor. [43]

Due to the increased interest and development of sensors employing planar coil as a means of interrogating the sensor, improvements of the readout technique of such LC sensors have been proposed [44-45], with mutual coupling between planar coils displaying promising results for the wireless interrogation of passive LC circuitry.

In addition to being a vital component of capacitive sensing LC circuitry, planar coils have been implemented as inductive sensing devices in many applications [46-50]. Much like capacitive sensing, inductive sensing relies on the change in inductance when certain physical phenomena changes. The development of sensors employing planar coils in the following categories will be discussed further – humidity, displacement, pressure, strain, and temperature.

### 3.2.1 Humidity sensing

Humidity sensing using LC circuitry relies predominantly on detecting impedance changes due to electric field interaction with changes in humidity. Planar coils are used to create the LC circuitry, which is favorable as this configuration accommodates a passive wireless sensor design. Humidity sensing is important in a wide range of applications, ranging from healthcare [47, 51], food quality monitoring [34], and water content of various materials and environments [52-53]. A sensor die or an interdigital capacitor configuration are often the sensing element, a few designs of such humidity sensors are shown in Figure 3.12

The versatility in fabrication method allows for a wide range of materials to be used, there are designs which are rigid and robust due to the FR-4 PCB substrate they are fabricated on [52,54], there are also flexible designs manufactured on flexible PCB substrates [51] or even paper and foil [34,55]. Due to the disposable nature of the items which the sensors are designed for, such as diapers [47, 51], and food packaging [34], low cost sensors which are easily disposed of are ideal. Humidity is one of the parameters which are often investigated in multi-parameter sensors [40, 42, 56], due to the importance of the parameter in many sensor networks.

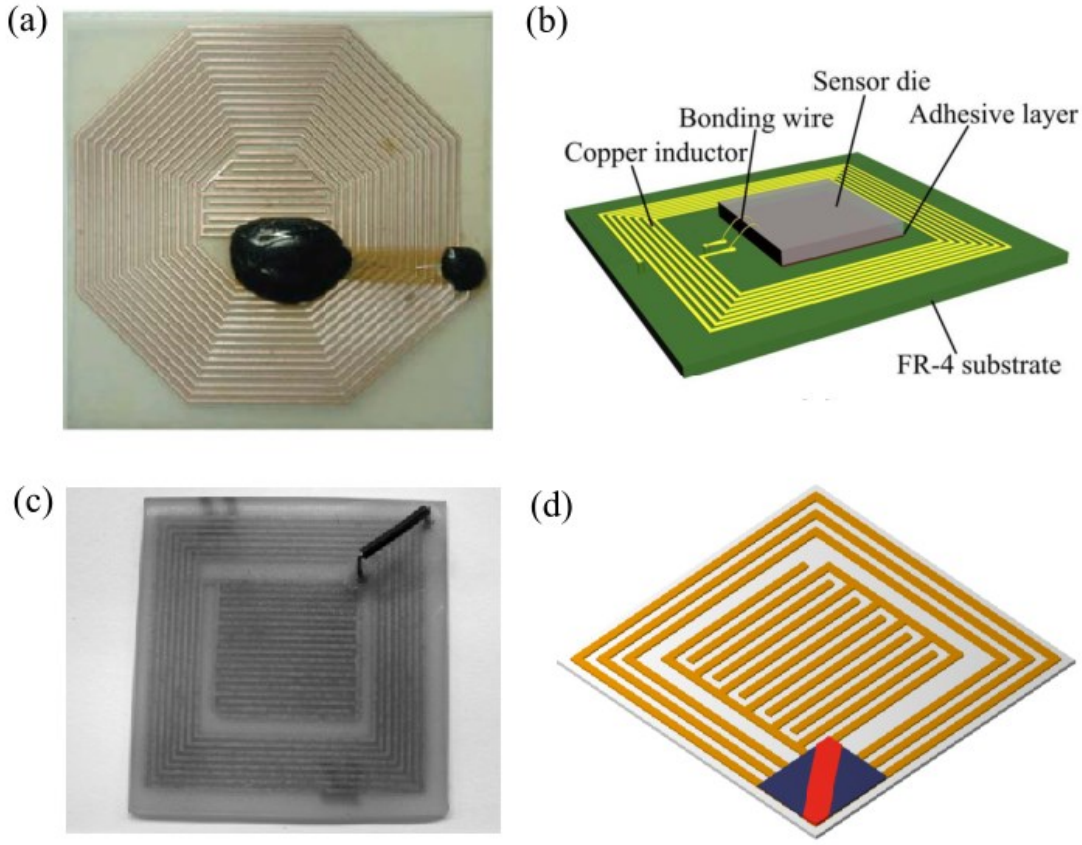


Figure 3.12 – Various humidity sensor designs. (a) Flexible RFID wetness sensor; (b) LC type wetness sensor with sensor die; (c) rigid LC wetness sensor; (d) wireless LC wetness sensor tag design to be printed on paper. [51, 54, 52, 34]

### 3.2.2 Displacement sensing

Displacement is an important parameter for sensor systems, it is used in many complex systems, from robotics to micro electromechanical systems (MEMS). Planar coils have small size profiles, can be manufactured easily with low costs, and are very robust [57-65, 77]. These sensors can be used in many environments, with little interference from the environmental conditions, should the sensor be operating at frequencies where the parasitics are minimal, and can be compensated for [66]. Unlike humidity sensing, many displacement sensors have been realised through inductive sensing, a simple solution is to incorporate mutual coupling between planar coils to determine displacement and position, which can be wired [67] or wirelessly implemented [68-70].

Displacement sensing for thermally actuated planar coil microactuators have also been reported, incorporating the variable inductance of an out-of-plane planar coil which changes via thermally induced deformation, demonstrating the versatility of planar coil sensor design [71]. Position sensors have also been proposed, and can be realised through the coupling of planar coils or the interaction between magnetic fields and ferromagnetic materials [72-73]. Several topologies have been proposed for displacement sensing and absolute position sensing, some examples are shown in Figure 3.13.

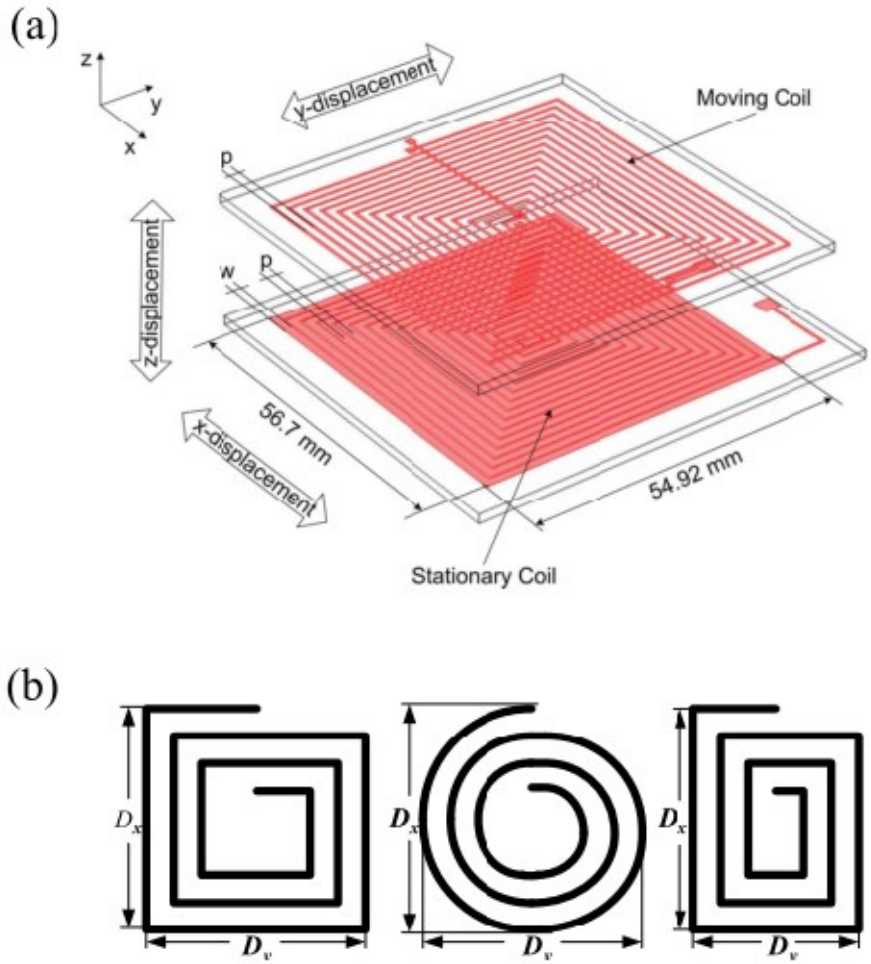


Figure 3.13 – Planar coil topologies for displacement sensing. (a) Square coil topology utilising wireless mutual coupling; (b) position sensor based on Square coil topology, circular coil topology, and rectangular coil topology, from left to right. [69, 72]

### 3.2.3 Pressure sensing

LC circuitry is also commonly used for pressure sensor design, both capacitive [74-79] and inductive [80-83] sensing elements have been implemented and reported. Pressure sensors with planar coil integration have been designed for many applications, ranging from automotive [82], medical [75], to harsh environment sensing [77]. The pressure sensors using inductive sensing elements have been demonstrated to operate with magnetic films [80], ferrofluids [81], ferrites [82], and mutual inductance effect [83].

The magnetic film based pressure sensor relies on changes in inductance due to the inverse magnetostrictive effect of the magnetic film, to induce a change in inductance. The other examples of inductive sensing rely on applied pressure to cause a displacement of a stimuli relative to the sensing element, thus changing the inductance and therefore the resonance. The pressure sensors incorporating capacitive sensing elements operate similarly, with interdigital capacitive designs and small sensor dies being used. Figure 3.14 illustrates a couple of proposed pressure sensors utilising inductive sensing elements.

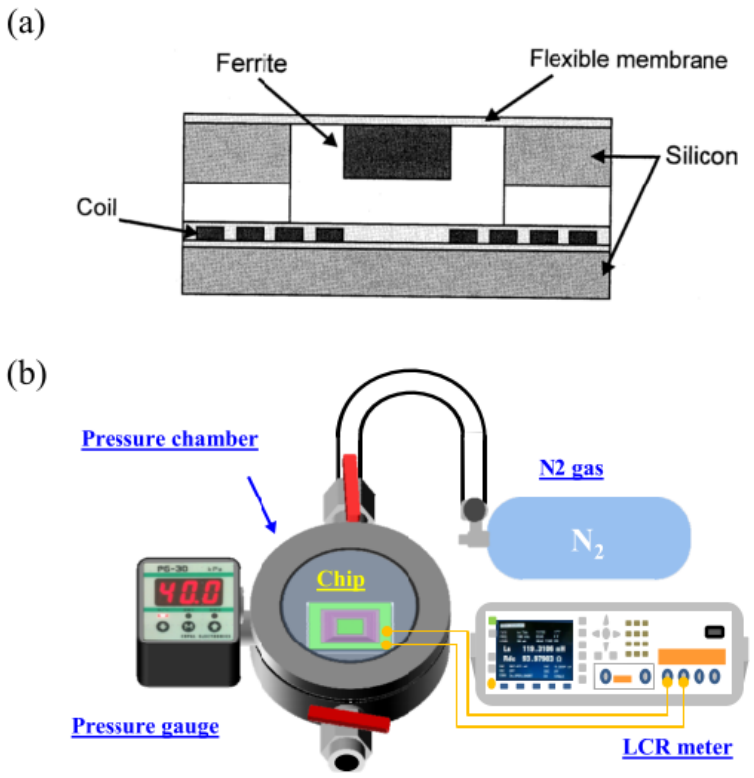


Figure 3.14 – Inductive pressure sensors. (a) Ferrite core inductive pressure sensor; (b) inverse magnetostrictive inductive pressure sensor schematic. [82, 80]

### 3.2.4 Strain sensing

Strain sensors have also been proposed based on planar coil integration, finding applications in fields such as medical care research [84] and automotive research [85-86]. Interdigital capacitive sensing elements are mainly used [85-87], but inductive strain sensors have also been reported [84]. By harnessing the properties of magnetostrictive materials, the bone healing process has been indirectly measured through strain sensing. Figure 3.15 shows the proposed sensor schematic, where bone growth stimulated strains induce changes to the permeability via the inverse magnetostrictive effect. Magnetic principles can be utilised in sensors for noninvasive monitoring of implanted devices, this is a huge advantage for automotive and medical applications.

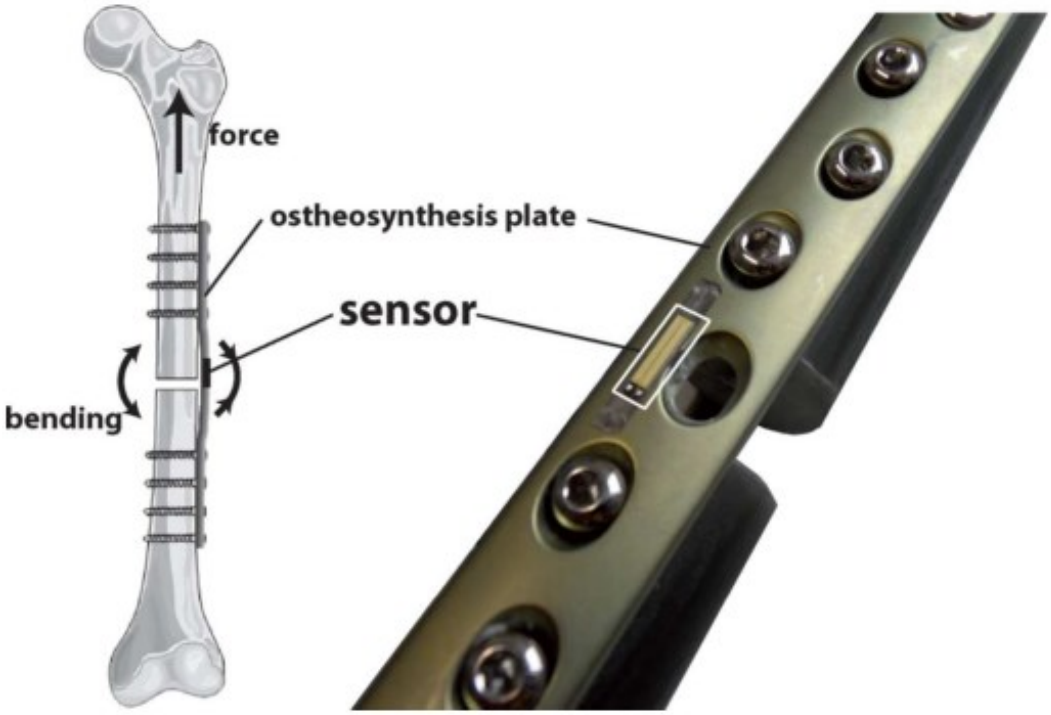


Figure 3.15 – Bone healing monitoring through strain sensor employing a planar coil inductor. [84]

### 3.2.5 Temperature sensing

Temperature sensing has also been achieved through LC tank circuitry, through the predominant usage of temperature sensitive capacitors, with planar coils used for LC tank and wireless interrogation purposes [56-57, 79, 88]. A temperature sensor based on a resistive sensing element has also been proposed, with temperature sensitive resistance variations, the proposed sensor design is shown in Figure 3.16 [89].

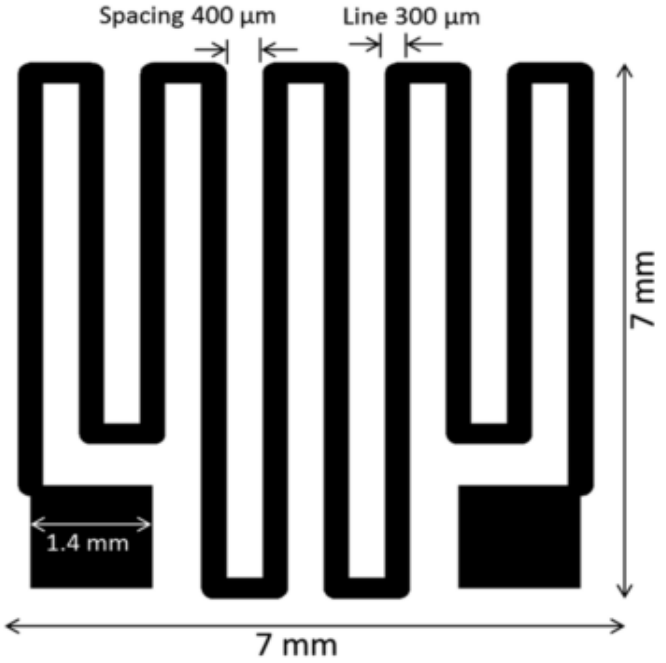


Figure 3.16 – Single-sided planar temperature sensor based on meander topology. [89]

## 3.3 Planar Coils in NDT and NDE Applications

Due to the wide variety of sensors which can constructed based on the robust LC circuitry, there has been many advances in the integration of planar coil designs in many NDT/NDE applications. Many electromagnetic sensors, including both capacitive and inductive sensing types, based on various topologies have been proposed and characterised [90-101], for applications ranging from the noninvasive inspection of meat [33, 90-91], quality monitoring of various food items for potential harmful bacteria [31, 92-93], and the quality inspection of electroplated materials [94-96].

Figure 3.17 shows a couple of sensors designed for NDT applications. One of the main advantages of planar coil based sensors is the low cost, compared with its conventional counterpart, along with comparable, if not improved, measurement speed and accuracy [91-93].

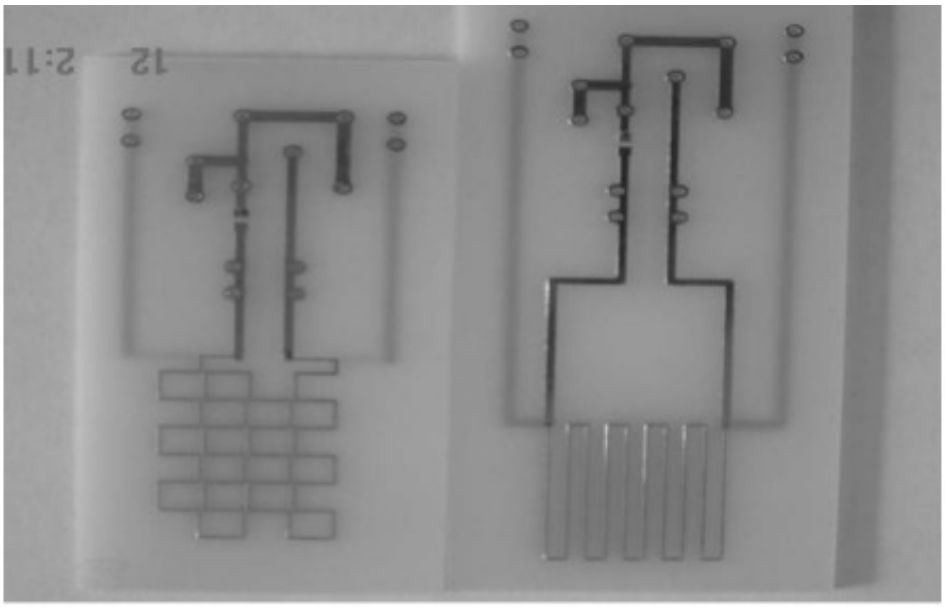

Figure 3.17 – Planar electromagnetic sensors designed for quality monitoring of dairy products, based on the mesh topology and the meander topology, from left to right. [92]

A prevalent field of research is the usage of planar coils for eddy current testing (ECT). ECT probes composed of planar coils were reported in 1995 [102], and due to the promising results of this proposed ECT probe with its greater output signal clarity, it has received research interests. The report demonstrated the usage of planar coils for both the excitation and sensing components of an ECT probe, shown in Figure 3.18. Many NDT investigations rely on ECT; therefore, much progress has been reported in this field, with new topologies, simulations, coil configurations, and applications being investigated [103-109]. Designs of planar coil usage in electromagnetic acoustic transducers (EMATS) have also been investigated, as guided waves are used in a variety of NDE applications, including the inspection of pipes, rails, and plates [110-112]. A schematic of a planar coil integrated in an EMATS system is shown in Figure 3.19.

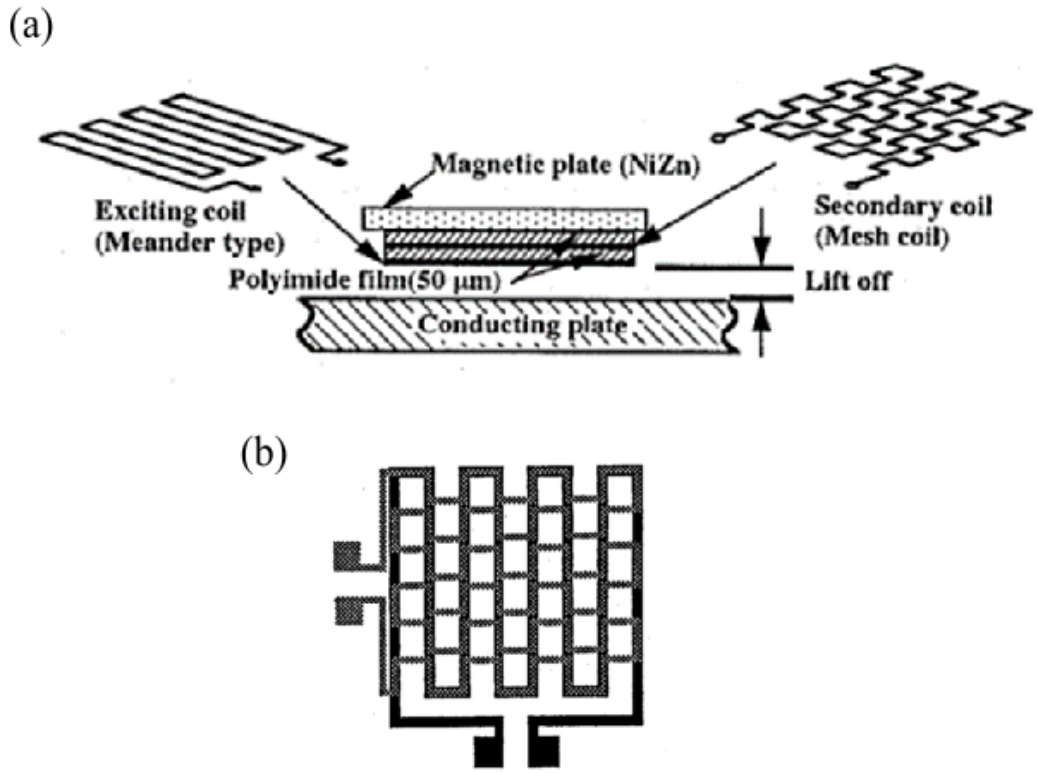


Figure 3.18 – Planar coil based ECT probe. (a) Schematic of proposed probe design, utilising both mesh and meander topologies; (b) overview of stacked exciting coil and sensing coil. [102]

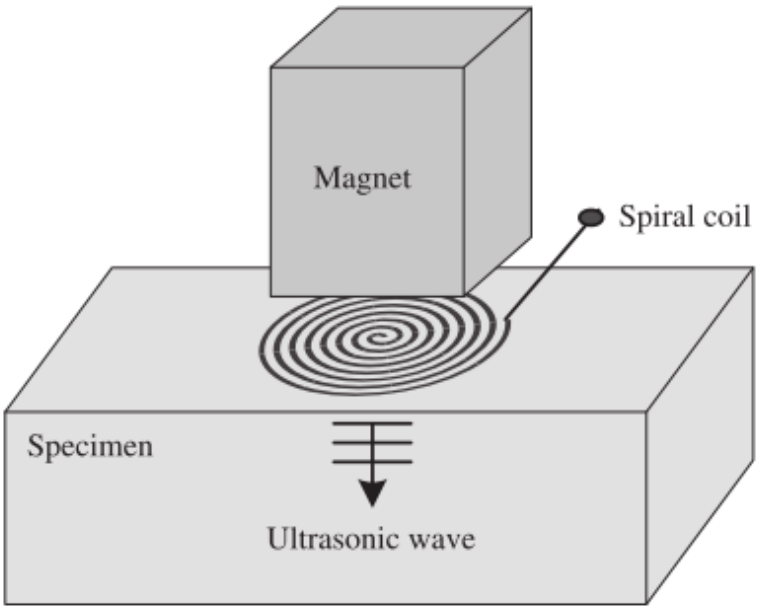


Figure 3.19 – Configuration of planar coil in EMATS system. [111]

## 3.4 Wearable Sensors, Implantable Devices, and Hand Motion Sensing

Planar coil sensors are ideal for wearable sensors and implantable devices, as they are passive in nature and can be interrogated wirelessly, this is very attractive for applications where noninvasive methods are preferred, such as medical sensors. There has been much research into wireless medical devices, there are many reasons how wireless medical devices will benefit us, examples such as remote monitoring of patients and noninvasive monitoring of patient recovery will greatly improve quality of care [113-123]. The possibilities of manufacturing sensors using different materials have also encouraged the design of several sensors, for example flexible sensors and biodegradable sensors have been proposed [115-119]. Sensors have been proposed for the sensing of parameters such as skin conductance, skin temperature, and pressure, for medical monitoring [115-116,122].

Figure 3.20 shows a proposed wireless pressure monitoring system, fabricated on flexible polyamide substrates. Magnetoelastic curvature sensors for biomedical applications have also been proposed, using soft magnetostrictive materials in a bilayer configuration to detect deformities in the material caused by bending [124-126]. The principle in these investigations are based on a wound coil which is used to detect changes in permeability of a magnetostrictive ribbon, which is configured as a bilayer. The proposed application of a skin curvature sensor was proposed, for usage on different parts of the body. The proposed bilayer is nonintrusive and thin; however, this does not consider the wound coil, which adds considerable bulk to the sensor design, relative to the size of the bilayer.

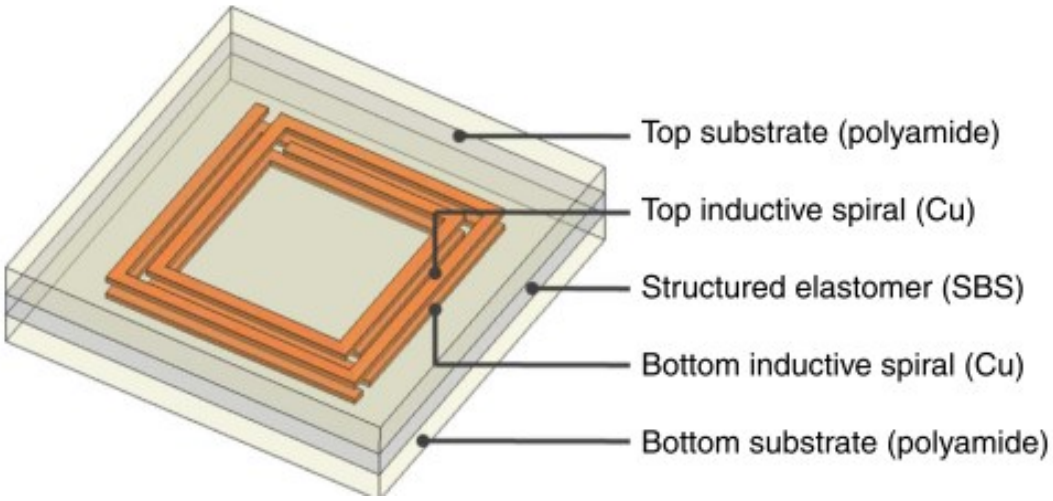


Figure 3.20 – structure overview of proposed pressure sensor. [115]

Intraocular pressure (IOP) monitoring is one of the fields of research which has seen a high number of proposed sensors with planar coil integration, for conditions such as glaucoma long-term measurement of the IOP is of great importance for both diagnosis and treatment purposes [127-131]. Planar coils are chiefly integrated to form LC tank circuitry and for wireless telemetric purposes, with a capacitive sensing element that varies with stress. Examples of proposed sensors for IOP monitoring are shown in Figure 3.21.

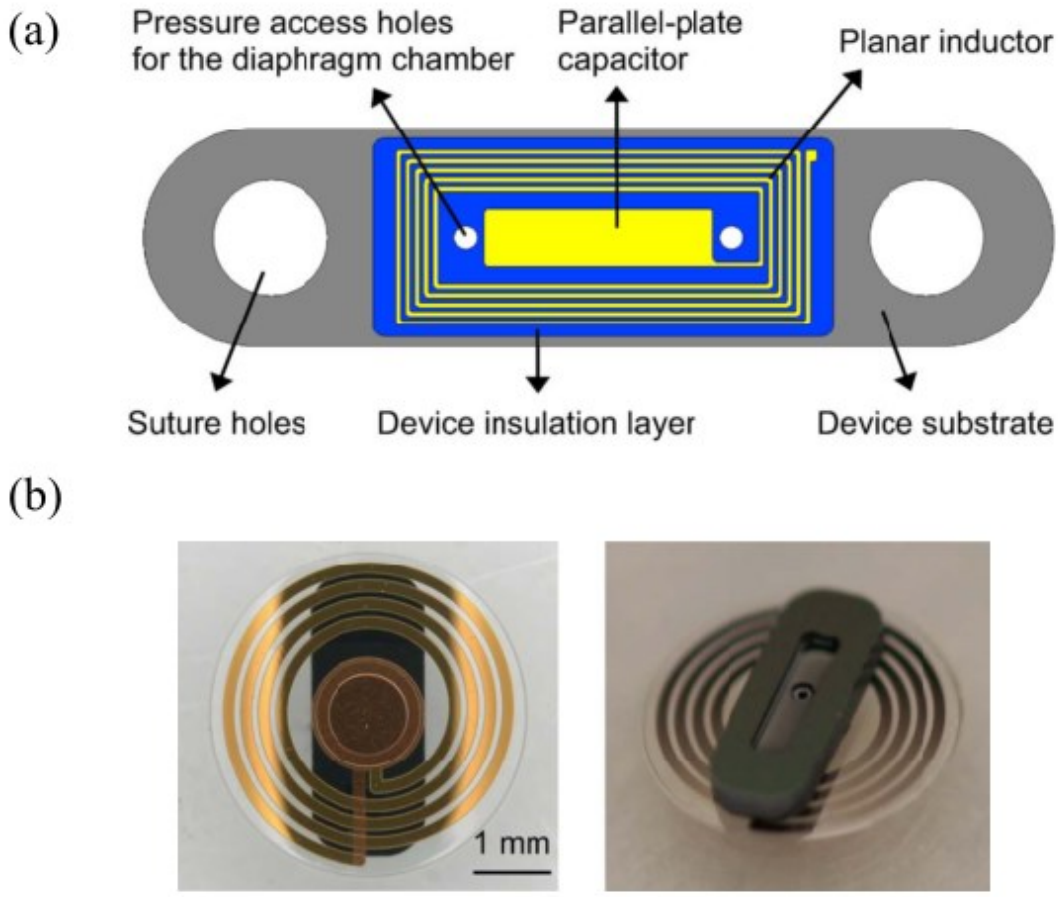


Figure 3.21 – Examples of IOP sensors. (a) Rectangular planar coil based design; (b) circular planar coil based design, top view and bottom view from left to right. [128, 129]

Hand motion sensing can be achieved through many means. The importance of this field is great, due to the hands being the primary method of physical interaction. Hand motion sensing can be utilised in simulations, virtual reality (VR), and medical

purposes. Hand motion sensing solutions have been proposed in the form of resistive sensing, optical sensing, and inertial measurement unit (IMU) sensing [132-136]. Sensor designs that can be miniaturised and fabricated on flexible substrates are ideal for hand motion sensing, it is preferable for the sensor to also be mechanically passive [133, 135-136]. The most widely available bend sensors are resistive based, however capacitive based and optic based bend sensors have also been proposed, a capacitive based bend sensor schematic diagram can be seen in Figure 3.22 [137-139].

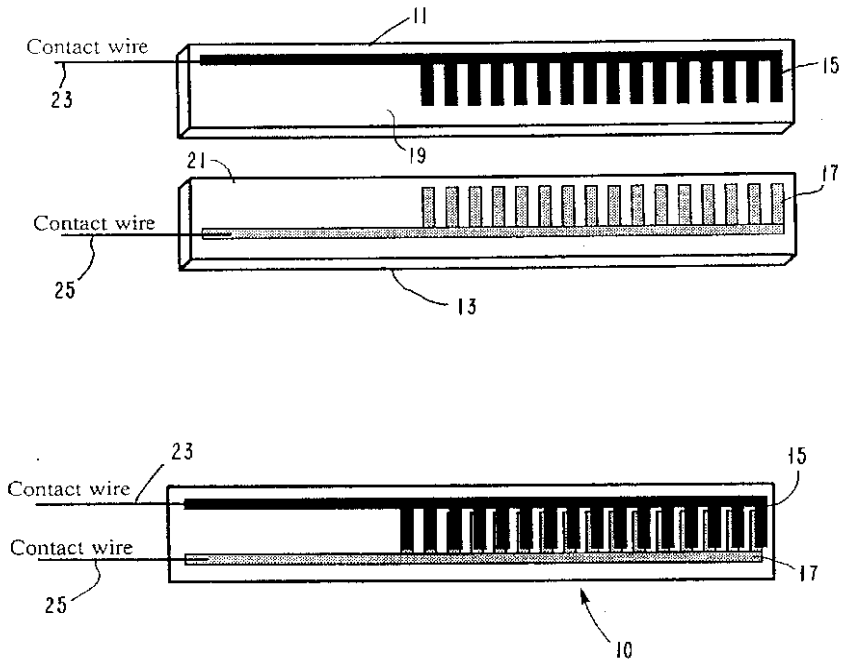


Figure 3.22 – Patent of capacitive based sensor, composed of stacked comb like conductor strips. [137]

Resistive flex sensors are widely available and can be obtained cheaply, an example can be seen in Figure 3.23. The flex sensors are fabricated with a resistive element on a substrate. The conductive element is often carbon based, and can be in the form of powder, ink, particles, nanoparticles, and nanotubes [138]. These sensors are often manufactured on many different materials, primarily polymers. Elastomers are often selected for their elastic properties, and polyesters are also a popular choice [138]. The flex sensors operate through the principle of a change in the electrical properties of the sensor when it is bent, as the conductive material is physically deformed. In the case of an ink-based flex sensor, cracks are formed in the ink surface, and as these cracks form the resistance of the sensor increases.

Figure 3.23 – Examples of resistive flex sensors, by Flexpoint Inc. [138]

Table 3.1 shows the thickness and tolerance levels of a few commercially available flex sensors, the sensors are thin, however there is a large tolerance rating, which must be compensated for through calibration and further circuitry design. This is a major disadvantage as the large tolerances mean that the sensors must be individually integrated to a sensor system, which is time consuming and adds further complexity to the design of a sensor system based on these flex sensors. The large tolerance is mainly due to the randomness within the conductive surface, and presents a real problem.

Table 3.1. Flex sensor thickness and tolerance levels

| Flex Sensor | *Thickness (μm)* | *Tolerance (%)* |
|---|---|---|
| Flexpoint flex sensor [140] | Typ. <130 | ±25 |
| Spectrasymbol flex sensor [141] | ≤430 | ±30 |
| Brewer Science InFlect flex sensor [142] | 175 | ±20 |

## 3.5 Further Research in Inductive Sensing Using Planar Coils

The chapter has covered a plethora of applications where planar coils have been integrated, either as the sensing element or part of an LC tank circuit. In this review the vast majority of sensor development relies on capacitive sensing in the form of interdigital capacitors or variable capacitive sensor dies. There are, however, exceptions, such as the development in ECT probes and EMATS systems. This presents a large opportunity to develop inductive planar coil based sensors to replace conventional sensors, as many of the sensors discussed have demonstrated characteristics and performances comparable to conventionally used sensors. There are many additional advantages to utilising planar coils in sensor design, such as the low costs of fabrication, possibilities in sensor design and manufacturing, and robustness of the sensor.

There is still a need for inductive planar coil sensor design, through the inductive coupling of magnetic materials and the planar coils. This research aims to investigate the design and characteristics of various inductive planar coil topologies for several applications, including stress, displacement, and to develop a flexible bend sensor for human joint angle monitoring with lower tolerance ratings than alternative solutions.

## 3.6 References for Chapter 3


[1] Wheeler, H. (1928). Simple Inductance Formulas for Radio Coils. *In the proceedings of the IRE*, 16(10), pp.1398-1400.

[2] Wheeler, H. (1982). Inductance formulas for circular and square coils. *In the proceedings of the IEEE*, 70(12), pp.1449-1450.

[3] Rosa, E. (1906). Calculation of the self-inductance of single-layer coils. *Bulletin of the Bureau of Standards*, 2(2), p.161-187.

[4] Rosa, E. (1907). On the geometrical mean distances of rectangular areas and the calculation of self-inductance. *Bulletin of the Bureau of Standards*, 3(1), p.1-41.

[5] Grover, F. (1922). Formulas and tables for the calculation of the inductance of coils of polygonal form. *Scientific Papers of the Bureau of Standards*, 18, p.737-762.

[6] Grover, F. (1929). The Calculation of the Inductance of Single-Layer Coils and Spirals Wound with Wire of Large Cross Section. *In the proceedings of the IRE*, 17(11), pp.2053-2063.

[7] Grover, F. (1962). *Inductance Calculations: Working Formulas and Tables*. NY, Dover Publications.

[8] Greenhouse, H. (1974). Design of Planar Rectangular Microelectronic Inductors. *IEEE Transactions on Parts, Hybrids, and Packaging*, 10(2), pp.101-109.

[9] Soohoo, R. (1979). Magnetic thin film inductors for integrated circuit applications. *IEEE Transactions on Magnetics*, 15(6), pp.1803-1805.

[10] Kawabe, K., Koyama, H. and Shirae, K. (1984). Planar inductor. *IEEE Transactions on Magnetics*, 20(5), pp.1804-1806.

[11] Oshiro, O., Tsujimoto, H. and Shirae, K. (1987). A novel miniature planar inductor. *IEEE Transactions on Magnetics*, 23(5), pp.3759-3761.

[12] Oshiro, O., Kawabe, K., Tsujimoto, H. and Shirae, K. (1987). A Wide Frequency Planar Inductor. *IEEE Translation Journal on Magnetics in Japan*, 2(4), pp.331-332.

[13] Yue, C. and Wong, S. (2000). Physical modeling of spiral inductors on silicon. IEEE Transactions on Electron Devices, 47(3), pp.560-568.

[14] Neagu, C., Jansen, H., Smith, A., Gardeniers, J. and Elwenspoek, M. (1997). Characterization of a planar microcoil for implantable microsystems. *Sensors and Actuators A: Physical*, 62(1-3), pp.599-611.

[15] Mohan, S., del Mar Hershenson, M., Boyd, S. and Lee, T. (1999). Simple accurate expressions for planar spiral inductances. *IEEE Journal of Solid-State Circuits*, 34(10), pp.1419-1424.

[16] Mukhopadhyay, S. (2005). Novel Planar Electromagnetic Sensors: Modeling and Performance Evaluation. *Sensors*, 5(12), pp.546-579.

[17] Beyzavi, A. and Nguyen, N. (2008). Modeling and optimization of planar microcoils. *Journal of Micromechanics and Microengineering*, 18(9), p.095018.

[18] Jow, U. and Ghovanloo, M. (2009). Modeling and Optimization of Printed Spiral Coils in Air, Saline, and Muscle Tissue Environments. *IEEE Transactions on Biomedical Circuits and Systems*, 3(5), pp.339-347.

[19] Reissman, T., Park, J. and Garcia, E. (2012). Multilayer, Stacked Spiral Copper Inductors on Silicon with Micro-Henry Inductance Using Single-Level Lithography. *Active and Passive Electronic Components*, 2012, pp.1-8.

[20] Ortego, I., Sanchez, N., Garcia, J., Casado, F., Valderas, D. and Sancho, J. (2012). Inkjet Printed Planar Coil Antenna Analysis for NFC Technology Applications. *International Journal of Antennas and Propagation*, 2012, pp.1-6.

[21] Mancosu, R., Quintero, J. and Azevedo, R. (2010). Sintering, in different temperatures, of traces of silver printed in flexible surfaces. *In the proceedings of the 2010 11th International Thermal, Mechanical & Multi-Physics Simulation, and Experiments in Microelectronics and Microsystems (EuroSimE)*, 4(9), pp.1804-1812.

[22] Yipeng Su, Xun Liu, Chi Kwan Lee and Hui, S. (2012). On the relationship of quality factor and hollow winding structure of coreless printed spiral winding (CPSW) inductor. *IEEE Transactions on Power Electronics*, 27(6), pp.3050-3056.

[23] Breitkreutz, B. and Henke, H. (2013). Calculation of Self-Resonant Spiral Coils for Wireless Power Transfer Systems With a Transmission Line Approach. *IEEE Transactions on Magnetics*, 49(9), pp.5035-5042.

[24] Jow, U. and Ghovanloo, M. (2007). Design and Optimization of Printed Spiral Coils for Efficient Transcutaneous Inductive Power Transmission. *IEEE Transactions on Biomedical Circuits and Systems*, 1(3), pp.193-202.

[25] Jow, U. and Ghovanloo, M. (2013). Geometrical Design of a Scalable Overlapping Planar Spiral Coil Array to Generate a Homogeneous Magnetic Field. *IEEE Transactions on Magnetics*, 49(6), pp.2933-2945.

[26] Pospisilik, M., Kouril, L., Motyl, I. and Adamek, M. (2011). Single and double layer spiral planar inductors optimisation with the aid of self-organising migrating algorithm. *In the proceedings of the 2011 Recent Advances in Signal Processing, Computational Geometry and Systems Theory*, pp.272-277.

[27] Waters, B., Mahoney, B., Lee, G. and Smith, J. (2014). Optimal coil size ratios for wireless power transfer applications. *2014 IEEE International Symposium on Circuits and Systems (ISCAS)*, 1(1), pp.2045-2048.

[28] Poliakine, J., Civet, Y. and Perriard, Y. (2016). Design and Manufacturing of High Inductance Planar Coils for Small Scale Sensing Applications. *Procedia Engineering*, 168, pp.1127-1130.

[29] Cook, B., Vyas, R., Kim, S., Thai, T., Le, T., Traille, A., Aubert, H. and Tentzeris, M. (2014). RFID-Based Sensors for Zero-Power Autonomous Wireless Sensor Networks. *IEEE Sensors Journal*, 14(8), pp.2419-2431.

[30] Huang, Q., Dong, L. and Wang, L. (2016). LC Passive Wireless Sensors toward a Wireless Sensing Platform: Status, Prospects, and Challenges. *IEEE Journal of Microelectromechanical Systems*, 25(5), pp. 822-841.

[31] Ong, K., Bitler, J., Grimes, C., Puckett, L. and Bachas, L. (2002). Remote Query Resonant-Circuit Sensors for Monitoring of Bacteria Growth: Application to Food Quality Control. *Sensors*, 2(6), pp.219-232.

[32] Potyrailo, R., Nagraj, N., Tang, Z., Mondello, F., Surman, C. and Morris, W. (2012). Battery-free Radio Frequency Identification (RFID) Sensors for Food Quality and Safety. *Journal of Agricultural and Food Chemistry*, 60(35), pp.8535-8543.

[33] Mohebi, E. and Marquez, L. (2014). Intelligent packaging in meat industry: An overview of existing solutions. *Journal of Food Science and Technology*, 52(7), pp.3947-3964.

[34] Tan, E., Ng, W., Shao, R., Pereles, B. and Ong, K. (2007). A Wireless, Passive Sensor for Quantifying Packaged Food Quality. *Sensors*, 7(9), pp.1747-1756.

[35] Wu, S., Yang, C., Hsu, W. and Lin, L. (2015). RF wireless lc tank sensors fabricated by 3D additive manufacturing. *In the proceedings of the 2015 18th International Conference on Solid-State Sensors, Actuators and Microsystems (TRANSDUCERS)*, pp.2208-2211.

[36] Horton, B., Schweitzer, S., DeRouin, A. and Ong, K. (2011). A Varactor-Based, Inductively Coupled Wireless pH Sensor. *IEEE Sensors Journal*, 11(4), pp.1061-1066.

[37] Perveen, K., Bridges, G., Bhadra, S. and Thomson, D. (2014). Corrosion Potential Sensor for Remote Monitoring of Civil Structure Based on Printed Circuit Board Sensor. *IEEE Transactions on Instrumentation and Measurement*, 63(10), pp.2422-2431.

[38] Zhang, S., Pasupathy, P. and Neikirk, D. (2011). Microfabricated self-resonant structure as a passive wireless dielectric constant and conductivity sensor. *Microsystem Technologies*, 18(7-8), pp.885-891.

[39] Ma, M., Liu, Z., Shan, W., Li, Y., Kalantar-zadeh, K. and Wlodarski, W. (2015). Passive wireless gas sensors based on the LTCC technique. *In the proceedings of the 2015 IEEE MTT-S International Microwave Workshop Series on Advanced Materials and Processes for RF and THz Applications (IMWS-AMP)*, 1(3), pp.3-5.

[40] Dong, L., Wang, L., Ren, Q. and Huang, Q. (2014). Mutual inductance suppressed stacked inductors for passive wireless multi-parameter sensors. *In the proceedings of IEEE SENSORS 2014*, pp.926-929.

[41] Dong, L., Wang, L. and Huang, Q. (2015). Implementation of multiparameter monitoring by an LC-Type passive wireless sensor through specific winding stacked inductors. *IEEE Internet of Things Journal*, 2(2), pp.168–174.

[42] Dong, L., Wang, L. and Huang Q. (2016). An LC passive wireless multifunctional sensor using a relay switch. *IEEE Sensors Journal*, 16(12), pp.4968–4973.

[43] Park, P., Kim, C., Park, M., Kim, S. and Yu, H. (2004). Variable Inductance Multilayer Inductor With MOSFET Switch Control. *IEEE Electron Device Letters*, 25(3), pp.144-146.

[44] Nopper, R., Niekrawietz, R. and Reindl, L. (2010). Wireless Readout of Passive LC Sensors. *IEEE Transactions on Instrumentation and Measurement*, 59(9), pp.2450-2457.

[45] Jacquemod, G., Nowak, M., Colinet, E., Delorme, N. and Conseil, F. (2010). Novel architecture and algorithm for remote interrogation of battery-free sensors. *Sensors and Actuators A: Physical*, 160(1-2), pp.125-131.

[46] Neudorff, L. (2006). *Freeway management and operations handbook*. Washington, D.C.: Federal Highway Administration.

[47] Yambem, L., Yapici, M. and Zou, J. (2008). A New Wireless Sensor System for Smart Diapers. *IEEE Sensors Journal*, 8(3), pp.238-239.

[48] Sridhar, V. and Takahata, K. (2009). A hydrogel-based passive wireless sensor using a flex-circuit inductive transducer. *Sensors and Actuators A: Physical*, 155(1), pp.58-65.

[49] Song, S., Park, J., Chitnis, G., Siegel, R. and Ziaie, B. (2014). A wireless chemical sensor featuring iron oxide nanoparticle-embedded hydrogels. *Sensors and Actuators B: Chemical*, 193, pp.925-930.

[50] Kisic, M., Blaz, N., Babkovic, K., Maric, A., Radosavljevic, G., Zivanov, L. and Damnjanovic, M. (2015). Passive Wireless Sensor for Force Measurements. *IEEE Transactions on Magnetics*, 51(1), pp.1-4.

[51] Yang, C., Chien, J., Wang, B., Chen, P. and Lee, D. (2007). A flexible surface wetness sensor using a RFID technique. *Biomedical Microdevices*, 10(1), pp.47-54.

[52] Ong, J., You, Z., Mills-Beale, J., Tan, E., Pereles, B. and Ong, K. (2008). A Wireless, Passive Embedded Sensor for Real-Time Monitoring of Water Content in Civil Engineering Materials. *IEEE Sensors Journal*, 8(12), pp.2053-2058.

[53] Marioli, D., Sardini, E. and Serpelloni, M. (2008). An inductive telemetric measurement system for humidity sensing. *Measurement Science and Technology*, 19(11), p.115204.

[54] Zhang, C., Wang, L., Huang, J. and Huang, Q. (2015). An LC-type passive wireless humidity sensor system with portable telemetry unit. *Journal of Microelectromechanical Systems*, 24(3), pp.575–581.

[55] Wang, X., Larsson, O., Platt, D., Nordlinder, S., Engquist, I., Berggren, M. and Crispin, X. (2012). An all-printed wireless humidity sensor label. *Sensors and Actuators B: Chemical*, 166-167, pp.556-561.

[56] Ren, Q., Wang, L., Huang, J., Zhang, C. and Huang, Q. (2015). Simultaneous Remote Sensing of Temperature and Humidity by LC-Type Passive Wireless Sensors. *Journal of Microelectromechanical Systems*, 24(4), pp.1117-1123.

[57] Tan, Q., Luo, T., Xiong, J., Kang, H., Ji, X., Zhang, Y., Yang, M., Wang, X., Xue, C., Liu, J. and Zhang, W. (2014). A Harsh Environment-Oriented Wireless Passive Temperature Sensor Realized by LTCC Technology. *Sensors*, 14(3), pp.4154-4166.

[58] Marioli, D., Sardini, E. and Serpelloni, M. (2010). Passive Hybrid MEMS for High-Temperature Telemetric Measurements. *IEEE Transactions on Instrumentation and Measurement*, 59(5), pp.1353-1361.

[59] Fonseca, M., English, J., von Arx, M. and Allen, M. (2002). Wireless micromachined ceramic pressure sensor for high-temperature applications. *Journal of Microelectromechanical Systems*, 11(4), pp.337-343.

[60] Chen Li, Qiulin Tan, Wendong Zhang, Chenyang Xue and Jijun Xiong (2015). An Embedded Passive Resonant Sensor Using Frequency Diversity Technology for High-Temperature Wireless Measurement. *IEEE Sensors Journal*, 15(2), pp.1055-1060.

[61] Birdsell, E. and Allen, M. (2006). Wireless Chemical Sensors for High Temperature Environments. *In the proceedings of the 2006 Solid-State Sensors, Actuators, and Microsystems Workshop*, pp.212-215.

[62] Wilson, W. and Juarez, P. (2014). Emerging Needs for Pervasive Passive Wireless Sensor Networks on Aerospace Vehicles. *Procedia Computer Science*, 37, pp.101-108.

[63] Li, C., Tan, Q., Jia, P., Zhang, W., Liu, J., Xue, C. and Xiong, J. (2015). Review of Research Status and Development Trends of Wireless Passive LC Resonant Sensors for Harsh Environments. *Sensors*, 15(6), pp.13097-13109.

[64] Rocznik, M., Henrici, F. and Has, R. (2012). ASIC for a resonant wireless pressure-sensing system for harsh environments achieving ±2% error between -40 and 150ºC using Q-based temperature compensation. *In the proceedings of the 2012 IEEE International Solid-State Circuits Conference*, pp.202-204.

[65] Knobloch, A., Ahmad, F., Sexton, D. and Vernooy, D. (2013). Remote Driven and Read MEMS Sensors for Harsh Environments. *Sensors*, 13(10), pp.14175-14188.

[66] Vogel, J., Chaturvedi, V. and Nihtianov, S. (2017). Humidity Sensitivity and Coil Design of a High-Precision Eddy-Current Displacement Sensor. *Proceedings*, 1(5), p.283.

[67] Coskun, M., Thotahewa, K., Ying, Y., Yuce, M., Neild, A. and Alan, T. (2013). Nanoscale displacement sensing using microfabricated variable-inductance planar coils. *Applied Physics Letters*, 103(14), p.143501.

[68] Djuric, S., Nad, L., Biberdzic, B., Damnjanovic, M. and Zivanov, L. (2008). Planar inductive sensor for small displacement. *In the proceedings of the 2008 26th International Conference on Microelectronics*, pp.11-14.

[69] Djuric, S. (2014). Performance Analysis of a Planar Displacement Sensor With Inductive Spiral Coils. *IEEE Transactions on Magnetics*, 50(4), pp.1-4.

[70] Damnjanovic, M., Zivanov, L., Nagy, L., Djuric, S. and Biberdzic, B. (2008). A Novel Approach to Extending the Linearity Range of Displacement Inductive Sensor. *IEEE Transactions on Magnetics*, 44(11), pp.4123-4126.

[71] Ali, M., AbuZaiter, A., Schlosser, C., Bycraft, B. and Takahata, K. (2014). Wireless Displacement Sensing of Micromachined Spiral-Coil Actuator Using Resonant Frequency Tracking. *Sensors*, 14(7), pp.12399-12409.

[72] He, N., Long, Z. and Xue, S. (2013). Modeling and optimal design of relative position detection sensor for high speed maglev train. *Sensors and Actuators A: Physical*, 189, pp.24-32.

[73] Jeranče, N., Vasiljević, D., Samardžić, N. and Stojanović, G. (2012). A Compact Inductive Position Sensor Made by Inkjet Printing Technology on a Flexible Substrate. *Sensors*, 12(12), pp.1288-1298.

[74] Zhai, J., How, T. and Hon, B. (2010). Design and modelling of a passive wireless pressure sensor. *CIRP Annals*, 59(1), pp.187-190.

[75] Park, E., Yoon, J. and Yoon, E. (1998). Hermetically Sealed Inductor-Capacitor (LC) Resonator for Remote Pressure Monitoring. *Japanese Journal of Applied Physics*, 37(Part 1, No. 12B), pp.7124-7128.

[76] Shin, K., Moon, C., Lee, T., Lim, C. and Kim, Y. (2005). Flexible wireless pressure sensor module. *Sensors and Actuators A: Physical*, 123-124, pp.30-35.

[77] Fonseca, M., English, J., von Arx, M. and Allen, M. (2002). Wireless micromachined ceramic pressure sensor for high-temperature applications. *Journal of Microelectromechanical Systems*, 11(4), pp.337-343.

[78] Akar, O., Akin, T. and Najafi, K. (2001). A wireless batch sealed absolute capacitive pressure sensor. *Sensors and Actuators A: Physical*, 95(1), pp.29-38.

[79] Nabipoor, M. and Majlis, B. (2006). A new passive telemetry LC pressure and temperature sensor optimized for TPMS. *Journal of Physics: Conference Series*, 34, pp.770-775.

[80] Chang, H., Liao, S., Hsieh, H., Lin, S., Lai, C., Chen, R. and Fang, W. (2013). A novel inverse-magnetostrictive type pressure sensor with planar sensing inductor. *In the proceedings of the 2013 IEEE 26th International Conference on Micro Electro Mechanical Systems (MEMS)*, pp.685-688.

[81] Chitnis, G. and Ziaie, B. (2013). A ferrofluid-based wireless pressure sensor. *Journal of Micromechanics and Microengineering*, 23(12), p.125031.

[82] Baldi, A., Woohyek Choi and Ziaie, B. (2003). A self-resonant frequency-modulated micromachined passive pressure transensor. *IEEE Sensors Journal*, 3(6), pp.728-733.

[83] Djuric, S., Nagy, L., Damnjanovic, M., Djuric, N. and Zivanov, L. (2011). A novel application of planar-type meander sensors. *Microelectronics International*, 28(1), pp.41-49.

[84] Sauer, S., Marschner, U., Adolphi, B., Clasbrummel, B. and Fischer, W. (2012). Passive Wireless Resonant Galfenol Sensor for Osteosynthesis Plate Bending Measurement. *IEEE Sensors Journal*, 12(5), pp.1226-1233.

[85] Matsuzaki, R. and Todoroki, A. (2007). Wireless flexible capacitive sensor based on ultra-flexible epoxy resin for strain measurement of automobile tires. *Sensors and Actuators, A: Physical*, 140(1), pp.32-42.

[86] Matsuzaki, R. and Todoroki, A. (2006). Passive wireless strain monitoring of actual tire using capacitance–resistance change and multiple spectral features. *Sensors and Actuators A: Physical*, 126(2), pp.277-286.

[87] Jia, Y., Sun, K., Agosto, F. and Quiñones, M. (2006). Design and characterization of a passive wireless strain sensor. *Measurement Science and Technology*, 17(11), pp.2869-2876.

[88] Ren, Q., Huang, J., Wang, L., Wan, S., Sun, L. and Huang, Q. (2014). Temperature sensing properties of the passive wireless sensor based on graphene oxide films. *In the proceedings of IEEE SENSORS 2014*, pp.3-6.

[89] Ali, S., Hassan, A., Bae, J., Lee, C. and Kim, J. (2016). All-Printed Differential Temperature Sensor for the Compensation of Bending Effects. *Langmuir*, 32(44), pp.11432-11439.

[90] Gooneratne C., Mukhopadhyay S., Purchas R., Sen Gupta G. (2005). Interaction of planar electromagnetic sensors with pork belly cuts. *In the proceedings of the 1st International Conference on Sensing* Technology, pp.519-526.

[91] Mukhopadhyay, S. and Gooneratne, C. (2007). A Novel Planar-Type Biosensor for Noninvasive Meat Inspection. *IEEE Sensors Journal*, 7(9), pp.1340-1346.

[92] Mukhopadhyay, S., Gooneratne, C., SenGupta, G. and Demidenko, S. (2006). A Low-Cost Sensing System for Quality Monitoring of Dairy Products. *IEEE Transactions on Instrumentation and Measurement*, 55(4), pp.1331-1338.

[93] Mohd Syaifudin, A., Jayasundera, K. and Mukhopadhyay, S. (2009). A low cost novel sensing system for detection of dangerous marine biotoxins in seafood. *Sensors and Actuators B: Chemical*, 137(1), pp.67-75.

[94] Mukhopadhyay, S. (2002). Quality inspection of electroplated materials using planar type micro-magnetic sensors with post-processing from neural network model. *IEE Proceedings - Science, Measurement and Technology*, 149(4), pp.165-171.

[95] Mukhopadhyay, S.; Yamada, S.; Iwahara, M. (2002) Inspection of electroplated materials – performance comparison with planar meander and mesh type magnetic sensor. *International journal of Applied Electromagnetics and Mechanics*, 15(4), pp.323–329.

[96] Mukhopadhyay, S., Sen Gupta, G., Woolley, J. and Demidenko, S. (2007). Saxophone Reed Inspection Employing Planar Electromagnetic Sensors. *IEEE Transactions on Instrumentation and Measurement*, 56(6), pp.2492-2503.

[97] Mukhopadhyay, S. (2004). A Novel Planar Mesh-Type Microelectromagnetic Sensor—Part I: Model Formulation. *IEEE Sensors Journal*, 4(3), pp.301-307.

[98] Mukhopadhyay, S. (2004). A Novel Planar Mesh-Type Microelectromagnetic Sensor—Part II: Estimation of System Properties. *IEEE Sensors Journal*, 4(3), pp.308-312.

[99] Mukhopadhyay, S., Gooneratne, C., Gupta, G. and Yamada, S. (2005). Characterization and comparative evaluation of novel planar electromagnetic sensors. *IEEE Transactions on Magnetics*, 41(10), pp.3658-3660.

[100] Mamishev, A., Sundara-Rajan, K., Fumin Yang, Yanqing Du and Zahn, M. (2004). Interdigital sensors and transducers. *Proceedings of the IEEE*, 92(5), pp.808-845.

[101] Mukhopadhyay, S., Yamada, S. and Iwahara, M. (2002). Experimental determination of optimum coil pitch for a planar mesh-type micromagnetic sensor. *IEEE Transactions on Magnetics*, 38(5), pp.3380-3382.

[102] Yamada, S., Katou, M., Iwahara, M. and Dawson, F. (1995). Eddy current testing probe composed of planar coils. *IEEE Transactions on Magnetics*, 31(6), pp.3185-3187.

[103] Yamada, S., Fujiki, H., Iwahara, M., Mukhopadhyay, S. and Dawson, F. (1997). Investigation of printed wiring board testing by using planar coil type ECT probe. *IEEE Transactions on Magnetics*, 33(5), pp.3376-3378.

[104] Theodoulidis, T. and Kriezis, E. (2002). Impedance evaluation of rectangular coils for eddy current testing of planar media. *NDT & E International*, 35(6), pp.407-414.

[105] Fava, J., Lanzani, L. and Ruch, M. (2009). Multilayer planar rectangular coils for eddy current testing: Design considerations. *NDT & E International*, 42(8), pp.713-720.

[106] Fava, J. and Ruch, M. (2006). Calculation and simulation of impedance diagrams of planar rectangular spiral coils for eddy current testing. *NDT & E International*, 39(5), pp.414-424.

[107] Fava, J. and Ruch, M. (2004). Design, construction and characterisation of ECT sensors with rectangular planar coils. *Insight - Non-Destructive Testing and Condition Monitoring*, 46(5), pp.268-274.

[108] Postolache, O., Ribeiro, A. and Ramos, H. (2013). GMR array uniform eddy current probe for defect detection in conductive specimens. *Measurement*, 46(10), pp.4369-4378.

[109] Ditchburn, R. and Burke, S. (2005). Planar rectangular spiral coils in eddy-current non-destructive inspection. *NDT & E International*, 38(8), pp.690-700.

[110] Wilcox, P., Lowe, M. and Cawley, P. (2005). The excitation and detection of Lamb waves with planar coil electromagnetic acoustic transducers. *IEEE Transactions on Ultrasonics, Ferroelectrics and Frequency Control*, 52(12), pp.2370-2383.

[111] Hao, K., Huang, S., Zhao, W., Wang, S. and Dong, J. (2011). Analytical modelling and calculation of pulsed magnetic field and input impedance for EMATs with planar spiral coils. *NDT & E International*, 44(3), pp.274-280.

[112] Seher, M. and Challis, R. (2015). The electrical properties of a planar coil electromagnetic acoustic transducer and their implications for noise performance. *Measurement Science and Technology*, 27(2), p.025102.

[113] Mukhopadhyay, S. (2015). Wearable Sensors for Human Activity Monitoring: A Review. *IEEE Sensors Journal*, 15(3), pp.1321-1330.

[114] Mahfouz, M., Kuhn, M. and To, G. (2013). Wireless medical devices: A review of current research and commercial systems. *In the proceedings of the 2013 IEEE Topical Conference on Biomedical Wireless Technologies, Networks, and Sensing Systems*, pp.16-18.

[115] Chen, L., Tee, B., Chortos, A., Schwartz, G., Tse, V., J. Lipomi, D., Wong, H., McConnell, M. and Bao, Z. (2014). Continuous wireless pressure monitoring and mapping with ultra-small passive sensors for health monitoring and critical care. *Nature Communications*, 5, p.5028.

[116] Fonseca M., Allen M., Kroh J., and White J. (2006). Flexible wireless passive pressure sensors for biomedical applications. *In the proceedings of the 12th Solid-state Sensors, Actuators, and Microsystems Workshop*, pp.37–42.

[117] Boutry, C., Chandrahalim, H., Streit, P., Schinhammer, M., Hanzi, A. and Hierold, C. (2012). Towards biodegradable wireless implants. *Philosophical Transactions of the Royal Society A: Mathematical, Physical and Engineering Sciences*, 370(1967), pp.2418-2432.

[118] Boutry, C., Chandrahalim, H., Streit, P., Schinhammer, M., Hänzi, A. and Hierold, C. (2013). Characterization of miniaturized RLC resonators made of biodegradable materials for wireless implant applications. *Sensors and Actuators A: Physical*, 189, pp.344-355.

[119] Yong-Lae Park, Bor-Rong Chen and Wood, R. (2012). Design and Fabrication of Soft Artificial Skin Using Embedded Microchannels and Liquid Conductors. *IEEE Sensors Journal*, 12(8), pp.2711-2718.

[120] Black, R. (2011). Recent Advances in Translational Work on Implantable Sensors. *IEEE Sensors Journal*, 11(12), pp.3171-3182.

[121] Klaric Felic, G., Ng, D. and Skafidas, E. (2013). Investigation of Frequency-Dependent Effects in Inductive Coils for Implantable Electronics. *IEEE Transactions on Magnetics*, 49(4), pp.1353-1360.

[122] Ahn, D. and Ghovanloo, M. (2016). Optimal Design of Wireless Power Transmission Links for Millimeter-Sized Biomedical Implants. *IEEE Transactions on Biomedical Circuits and Systems*, 10(1), pp.125-137.

[123] Yoon, S., Sim, J. and Cho, Y. (2014). On-chip flexible multi-layer sensors for Human stress monitoring. *In the proceedings of IEEE SENSORS 2014*, pp.851-854.

[124] Kaniusas, E., Pfutzner, H., Meydan, T., Vazquez, M., and Varoneckas, G. (2013). Magnetoelastic Bilayer Sensors: From Technology to Application. *Sensor Letters*, 11(1), pp.164-169.

[125] Kaniusas, E., Pfutzner, H., Mehnen, L., Kosel, J., Tellez-Blanco, C., Varoneckas, G., Alonderis, A., Meydan, T., Vazquez, M., Rohn, M., Merlo, A. and Marquardt, B. (2006). Method for continuous nondisturbing monitoring of blood pressure by magnetoelastic skin curvature sensor and ECG. *IEEE Sensors Journal*, 6(3), pp.819-828.

[126] Katranas, G., Meydan, T., Ovari, T. and Borza, F. (2008). Applications of the bi-layer thin film sensor system for registering cardio-respiratory activity. *Sensors and Actuators A: Physical*, 142(2), pp.455-458.

[127] Puers, R., Vandevoorde, G., Bruyker, D., Puers, R. and Vandevoorde, G. (2000). Electrodeposited copper inductors for intraocular pressure telemetry. *Journal of Micromechanics and Microengineering*, 10(2), pp.124-129.

[128] Po-Jui Chen, Rodger, D., Saati, S., Humayun, M. and Yu-Chong Tai (2008). Microfabricated Implantable Parylene-Based Wireless Passive Intraocular Pressure Sensors. *Journal of Microelectromechanical Systems*, 17(6), pp.1342-1351.

[129] Chen, P., Saati, S., Varma, R., Humayun, M. and Tai, Y. (2010). Wireless Intraocular Pressure Sensing Using Microfabricated Minimally Invasive Flexible-Coiled LC Sensor Implant. *Journal of Microelectromechanical Systems*, 19(4), pp.721-734.

[130] Xue, N., Chang, S. and Lee, J. (2012). A SU-8-Based Microfabricated Implantable Inductively Coupled Passive RF Wireless Intraocular Pressure Sensor. *Journal of Microelectromechanical Systems*, 21(6), pp.1338-1346.

[131] Chitnis, G., Maleki, T., Samuels, B., Cantor, L. and Ziaie, B. (2013). A Minimally Invasive Implantable Wireless Pressure Sensor for Continuous IOP Monitoring. *IEEE Transactions on Biomedical Engineering*, 60(1), pp.250-256.

[132] Jentoft, L., Dollar, A., Wagner, C. and Howe, R. (2014). Intrinsic Embedded Sensors for Polymeric Mechatronics: Flexure and Force Sensing. *Sensors*, 14(3), pp.3861-3870.

[133] Kramer, R., Majidi, C., Sahai, R. and Wood, R. (2011). Soft curvature sensors for joint angle proprioception. *In the proceedings of the 2011 IEEE/RSJ International Conference on Intelligent Robots and Systems*, pp.1919-1926.

[134] Orengo G., Sbernini L., Di Lorenzo N., Lagati A., and Saggio G. (2013). Curvature characterization of flex sensors for human posture recognition. *Universal Journal of Biomedical Engineering*, 1, pp.10–15.

[135] Vogt, D. and Wood, R. (2014). Wrist angle measurements using soft sensors. *In the proceedings of IEEE SENSORS 2014*, pp.1631-1634.

[136] Eshkeiti, A., Joyce, M., Narakathu, B., Emamian, S., Avuthu, S., Joyce, M. and Atashbar, M. (2014). A novel self-supported printed flexible strain sensor for monitoring body movement and temperature. *In the proceedings of IEEE SENSORS 2014*, pp.1615-1618.

[137] International Business Machines Corporation (1997). *Capacitive Bend Sensor*. US5610528 A.

[138] Saggio, G., Riillo, F., Sbernini, L. and Quitadamo, L. (2015). Resistive flex sensors: a survey. *Smart Materials and Structures*, 25(1), p.013001.

[139] Orengo, G., Saggio, G., Bocchetti, S. and Giannini, F. (2010). Advanced characterization of piezoresistive sensors for human body movement tracking. *In the*

*proceedings of 2010 IEEE International Symposium on Circuits and Systems*, pp.1181-1184.

[140] Flexpoint.com. *Flexpoint Bend Sensor Technology Mechanical Application Design Guide*. [online] Available at: http://www.flexpoint.com/wp-content/uploads/2015/10/Mechanical-Design-Guide_151001.pdf [Accessed 15 Nov. 2017].

[141] Sparkfun.com. *Spectra Symbol Flex Sensor Data Sheet*. [online] Available at: https://www.sparkfun.com/datasheets/Sensors/Flex/flex22.pdf [Accessed 15 Nov. 2017].

[142] Brewerscience.com. *Brewer Science InFlect Flex Sensor Data Sheet*. [online] Available at: https://www.brewerscience.com/wp-content/uploads/2015/06/Flex-Data-Sheet-1.pdf [Accessed 15 Nov. 2017].

# Chapter 4. Modelling Procedures and Experimental Methods

## 4.1 Introduction

In this chapter, the experimental methodologies used for the research area presented. These experiments have been designed to provide valuable data which may be used to aid the design of the angular displacement (AD) sensor. Firstly, the planar coils are described, and their inductive properties defined. The effects of distance separation between the planar coil and the magnetic ribbon is also investigated. Secondly the different planar coil topologies are examined in a stress sensing setting, where their capabilities are investigated. Finally, the AD sensor is fabricated and characterised.

## 4.2 Planar Coil Characterisation and Distance Separation Investigation

### 4.2.1 3D modelling procedures

3D Finite Element Modelling (FEM) was conducted to obtain a better understanding of field distribution and inductance values of various topologies. The planar coil topologies studied were chosen to be square, circular, meander, and mesh. These coils have various parameters which can be changed to modify coil characteristics and performance, such as the track width, track thickness, and track gap. The track width and thickness are often limited by the manufacturing process, resulting in the track gap being the parameter which is commonly altered, this is commonly referred to as the pitch value.

These different topologies and their respective pitches are shown in Figure 4.1. The square and circular coil designs represent spiral topologies, where the coil expands in a spiral manner. There are many variations of spiral based topologies, hexagonal and octagonal spirals for example, however for simplification these variations have been omitted. The meander and mesh coil represent non-spiral topologies, and have been chosen for comparison against spiral topologies and due to their prevalence in planar coil sensor design. There are other planar topologies which rely on capacitive sensing such as interdigital configurations, however only inductive coil topologies have been considered for this investigation.

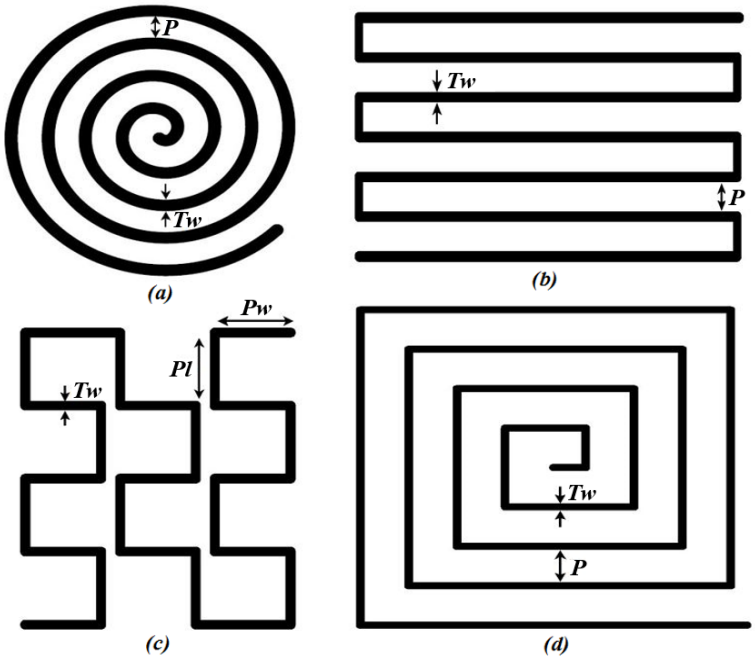


Figure 4.1 - Examples of coil topologies, with *P* being the pitch and *Tw* being the track width. (a) Circular coil; (b) Meander coil; (c) Mesh coil, for simplification *Pw* and *Pl* have been designed to be equal in all mesh coils; (d) Square coil.

The sensor was modelled using a constraint of 25 mm x 25 mm, it was necessary to model the coils in three dimensions, due to the asymmetry of the mesh and meander coil topologies and the geometrical arrangement of the coil relative to the ribbon element. Table 4.1 lists the pitch values of various topologies which were used in this study, three pitch values were chosen for each topology, with a total of 12 planar coil configurations. A boundary volume of 40 mm x 40 mm x 20 mm was applied to the models based on a preliminary investigation where the response range of the square planar coil was approximately 10 mm. Pitch values were chosen to conform to the area constraint and populate the area efficiently. Due to the limitation of the fabrication method, the pitch values chosen for the mesh topology are larger than those for the other coil types, they have also been selected to efficiently populate the area constraint.

Table 4.1. List of topologies and respective pitch values.

| Topology | *Pitch 1 (mm)* | *Pitch 2 (mm)* | *Pitch 3 (mm)* |
|---|---|---|---|
| Square Coil | 0.5 | 0.75 | 1.0 |
| Circular Coil | 0.5 | 0.75 | 1.0 |
| Meander Coil | 0.5 | 0.75 | 1.0 |
| Mesh Coil | 1.0 | 2.5 | 3.5 |

Firstly, the field distribution generated by the planar coils were investigated using a 3D magnetostatic simulation, using the ANSYS Maxwell 3D FEM software. The magnetic field formulation of this software is founded on Maxwell's equations, in particular equations (2.2), (2.3), and (2.4) [1]. The coils were excited with a current of 0.4 A, and were positioned in the center of the boundary volume. The z-component ($H_z$) was evaluated for each model listed in Table 4.1, as this field is the main field which will interact with the magnetic ribbon in displacements which are perpendicular to the surface of the coil.

Secondly, the displacement separation characteristics of the different topologies were investigated. Inductance changes were modelled using material parameters based on a Metglas 2605S3A amorphous ribbon with dimensions of 25 mm x 25 mm, 18 μm thickness, and relative permeability of 20000, the upper limit for the permeability of as cast 2605S3A ribbon [2]. Inductance as a function of distance between the ribbon and the planar coil was modelled using a parametric sweep. The software computes the inductance of the planar coil through an incremental energy analysis, which requires less computations and is more efficient [3]. The ribbon was displaced using a decade sweep so the displacement was not linear, this was integrated to increase number of data points in the region of small displacements. A displacement of 10 mm was applied to the ribbon. This was sufficient to model sensor performance for later comparison with experimental data. A percentage error of 2% was applied to all the simulations, after this threshold has been reached the simulation would terminate.

### 4.2.2 Planar coil fabrication

The planar coils used in the experiment are milled from a 54 mm x 30 mm FR4 PC board, with a 35μm copper thickness, a track width of 0.5 mm, and varying track gaps according to the desired pitch value, an example of the fabricated coils can be seen in Figure 4.2. The PCBs have holes drilled on both sides for the holder pins, which are used to secure the PCBs. The magnetic ribbon used in this experiment was as cast Metglas 2605S3A (i.e. no annealing treatments), with a thickness of 23 μm and dimensions of 25.4 mm x 30 mm. The ribbon used in the experiment was slightly longer than the model in the FEM, due to the need of securing the ribbon to the holder. As connections were required to be soldered on to the coil, there is slight protrusion on the surface of the coil. These protrusions have been filed to reduce the dimension, and to minimise the effect it has on the investigations.

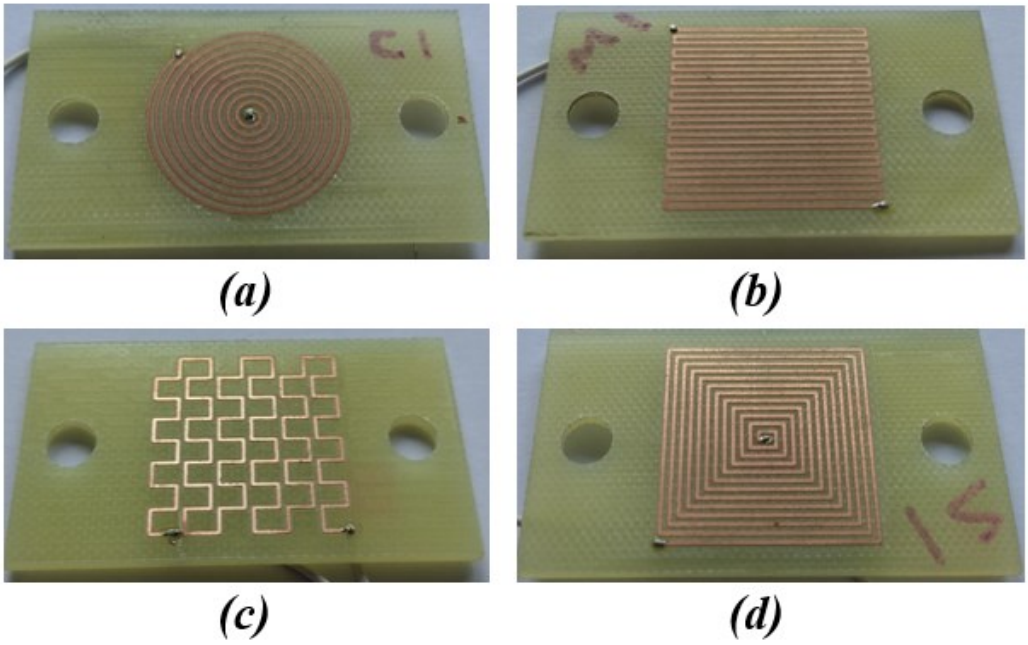


Figure 4.2 - Examples of fabricated coils on PCB, with holes for 3D printed support structures. (a) Circular coil topology. (b) Meander coil topology. (c) Mesh coil topology. (d) Square coil topology.

### 4.2.3 Planar coil measurement system

The measuring system consists of a computer with a LabVIEW program written for control and data acquisition purposes, a KDC101 DC servo motor, and an Agilent 4294A impedance analyser, with the 16089B Kelvin clip attachment. The key specifications for the 4294A are shown in Table 4.2. The servo motor was connected to the PC through USB connection, and the impedance analyser was connected to the PC through an Ethernet connection with a USB adapter. The servo motor controls a single axis translation stage, PT1/M-Z8, which moves along the same axis as the stationary stage, the stationary stage was not controlled but used as a point of reference for the experiments. The stages are configured so the motorised stage displacements are towards the stationary stage. A block diagram of the measurement system is shown in Figure 4.3, and a system diagram is shown in Figure 4.4. Due to the solder protrusion on the surface of the coil, there is a slight distance kept between the ribbon and the coil, to prevent any deformation to the ribbon. The data acquired does not begin at 0 mm due to this.

Table 4.2. Agilent 4294A key specifications. [4]

| Parameter | *Parameter specification* |
|---|---|
| Operating frequency | 40 Hz to 110 MHz, 1 mHz resolution |
| Basic impedance accuracy | ±0.08% |
| Q accuracy | ±3% (typical) @ Q = 100, f ≤ 10 MHz |
| Impedance range | 3 mΩ to 500 MΩ[*1] |
| Measurement time | 3 msec/point @ f ≥ 500 kHz, BW = 1 (fast) |
| Number of points per sweep | 2 to 801 points |

([*1]) 30% typical accuracy range: 3 mΩ (100 Hz to 110 MHz), 500 MΩ (100 Hz to 200 kHz)

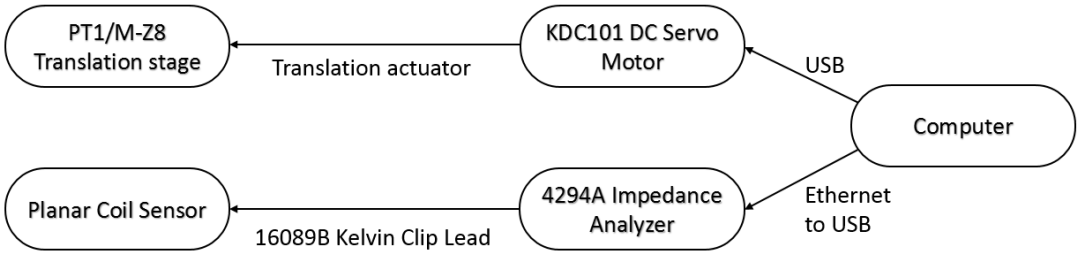


Figure 4.3 – Block diagram of measurement system for planar coil characterisation.

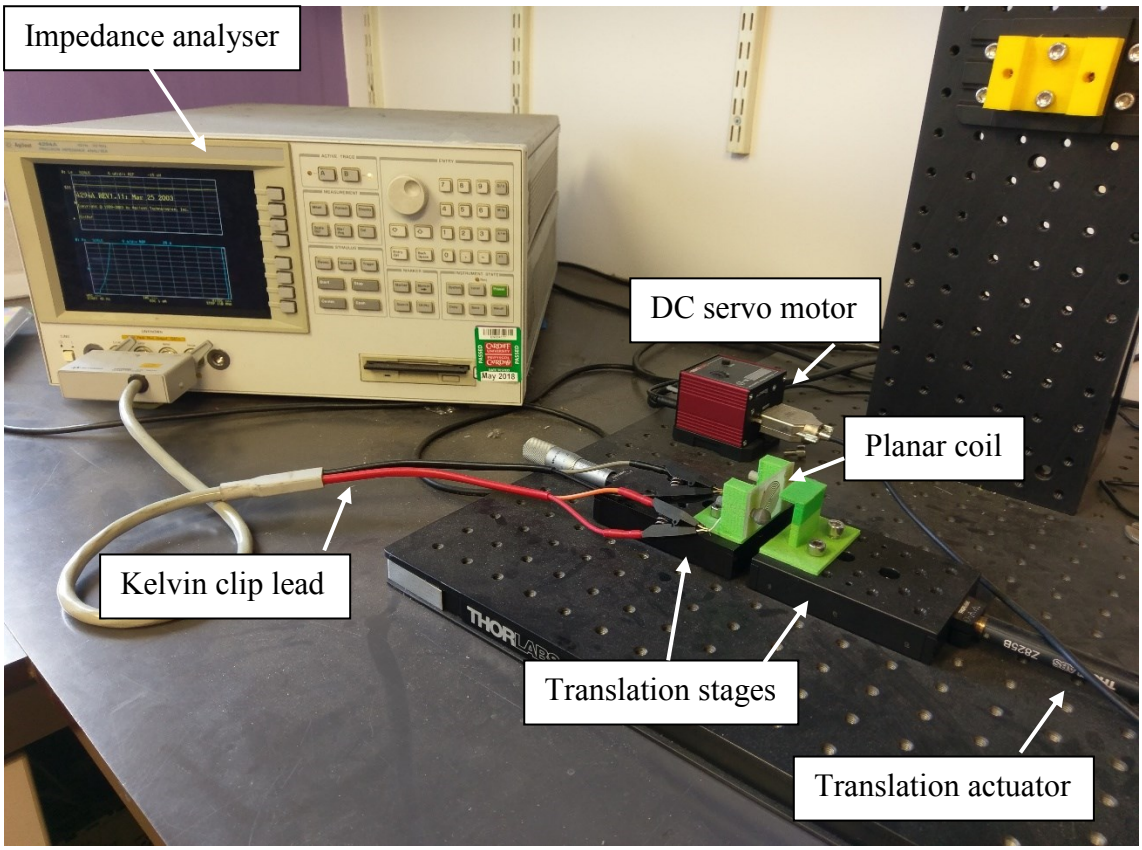


Figure 4.4 – System diagram of measurement system for planar coil characterisation.

LabVIEW is a graphical programming language which has a high level of modularity, and through the computer it can be used to create custom written software. The use of the LabVIEW package provides many features, such as interfacing with different hardware devices, acquiring and processing large amounts of data, and automating the various stages of the experiment. The LabVIEW software is laid out in two main views, the front panel interface and the block diagram. The front panel interface is where the user can control the program and can also be used to display data and additional information. The block diagram is, for this investigation, composed of elements used to acquire and process signals.

To evaluate the effects of separation displacement between the coil and ribbon, the translation stage will be displaced and a measurement will be made by the impedance analyser. The software has been written to automate the process of moving the displacement stage and acquiring the data, conditional loops have been used to add further automation in the form of repeating measurements given certain control parameters, such as the total displacement and the number of steps for that displacement. The software will acquire impedance data after each displacement, and after the stage reaches the final displacement value it returns to the starting position whilst travelling through the same number of steps. The data collected from each repetition of the experiment was stored in an excel spreadsheet.

For the experiment a pair of 3D structures were printed using a rubber filament, these structures serve the purpose of supporting the sensor and the ribbon in the displacement separation experiments. The 3D structures were designed to be secured on the translation stages, with the sensor being on the stationary stage and the ribbon being on the controlled stage. The 3D models of these structures can be seen in Figure 4.5. For the magnetic ribbon holder, a two-part design had to be implemented due to difficulties in the manufacturing process. The planar coil was secured to the 3D structure by printed holder pins, which are printed with polylactic acid, PLA. Figure 4.6 shows the planar coil and ribbon attached to their support structures.

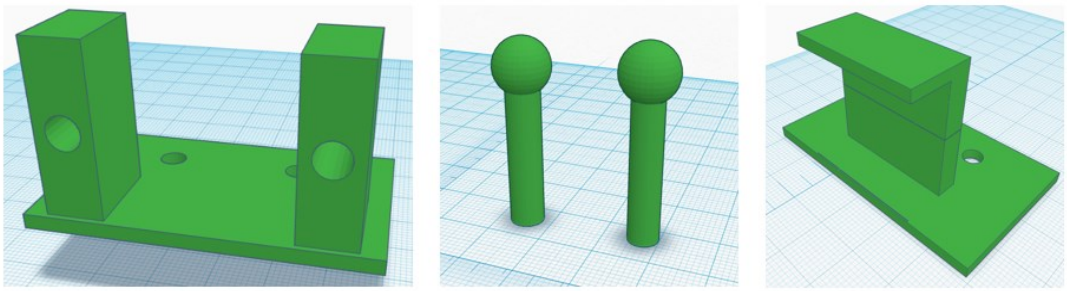


Figure 4.5 - 3D models of supporting structures. (a) Planar coil holder. (b) Holder pins for securing planar coil to the coil holder (c) Magnetic ribbon holder.

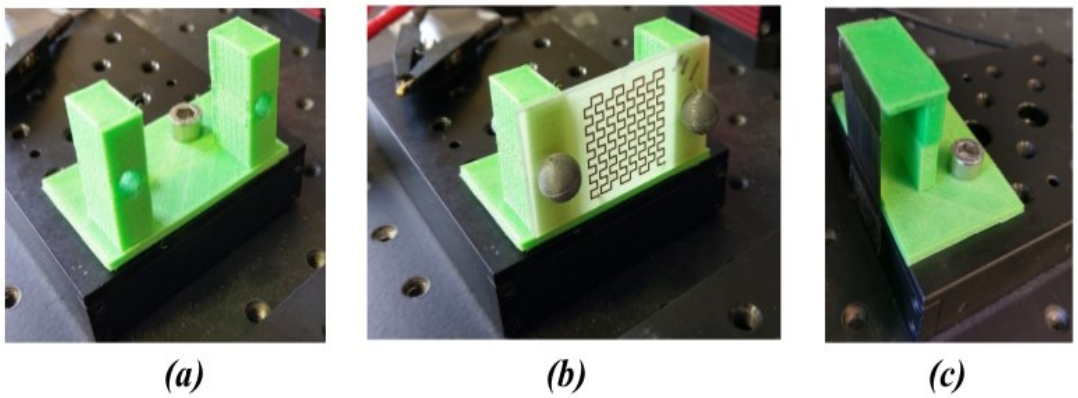


Figure 4.6 - Printed 3D structures secured on displacement stage. (a) Planar coil holder with no coil attached. (b) Planar coil holder with mesh coil attached. (c) Magnetic ribbon holder with ribbon attached.

The LabVIEW program was set to displace the stage from 0 mm with respect to the coil and finishing at 10 mm. The step size was set to 200 μm and measurements over the whole measurement range were repeated ten times for each coil. A sweep of 201 points between 40 Hz and 100 kHz was performed for each displacement step. This frequency range limitation was imposed by the attachment used on the impedance analyser.

To better evaluate the field profiles of different topologies, a surface scan of the sensor was performed using a Micromagnetics® STJ-020 tunnel magnetoresistance (TMR) sensor. The TMR sensor was attached to a custom 3D-printed enclosure, which was attached to a Parker Automation based 3-axis positioning arm, the system overview is shown in Figure 4.7 [5]. The positioning arm was controlled by LabVIEW, which also acquired and processed the data obtained from the sensor. This system was developed internally within the department. Each planar coil was excited with a current of 0.4 A, and scanned at varying distances above the surface of the coil, limited by protrusion of surface solder. The scanning heights ranged from 0.15 mm to 0.25 mm. The $H_z$ component generated by the planar coils was obtained and compared with the findings from the 3D FEM simulations. The $H_z$ component has been extracted specifically as it will be the primary field interacting with the magnetic ribbon, in this configuration of the experiment.

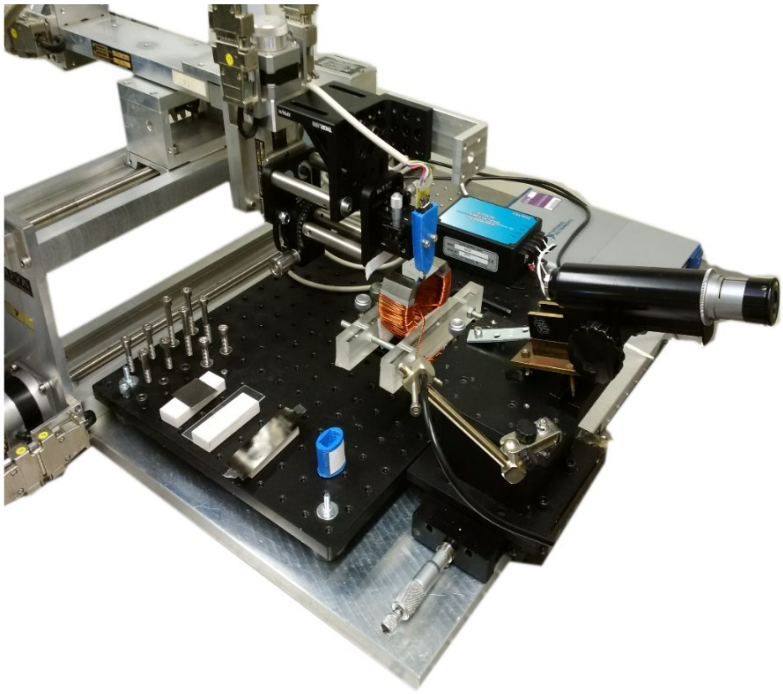

Figure 4.7 – TMR scanning system overview. [5]

## 4.3 Planar Coil Stress Sensing Measurement System

To analyse the performance of the various planar coil topologies in a stress sensing application a vertical suspension set-up was designed and constructed. This experiment uses both machined components and 3D printed parts in the construction. The non-printed components were made from TUFNOL sheets, a laminated plastic material which is non-metallic, rigid, and light weight. Figure 4.8 shows the vertical suspension experimental set-up.

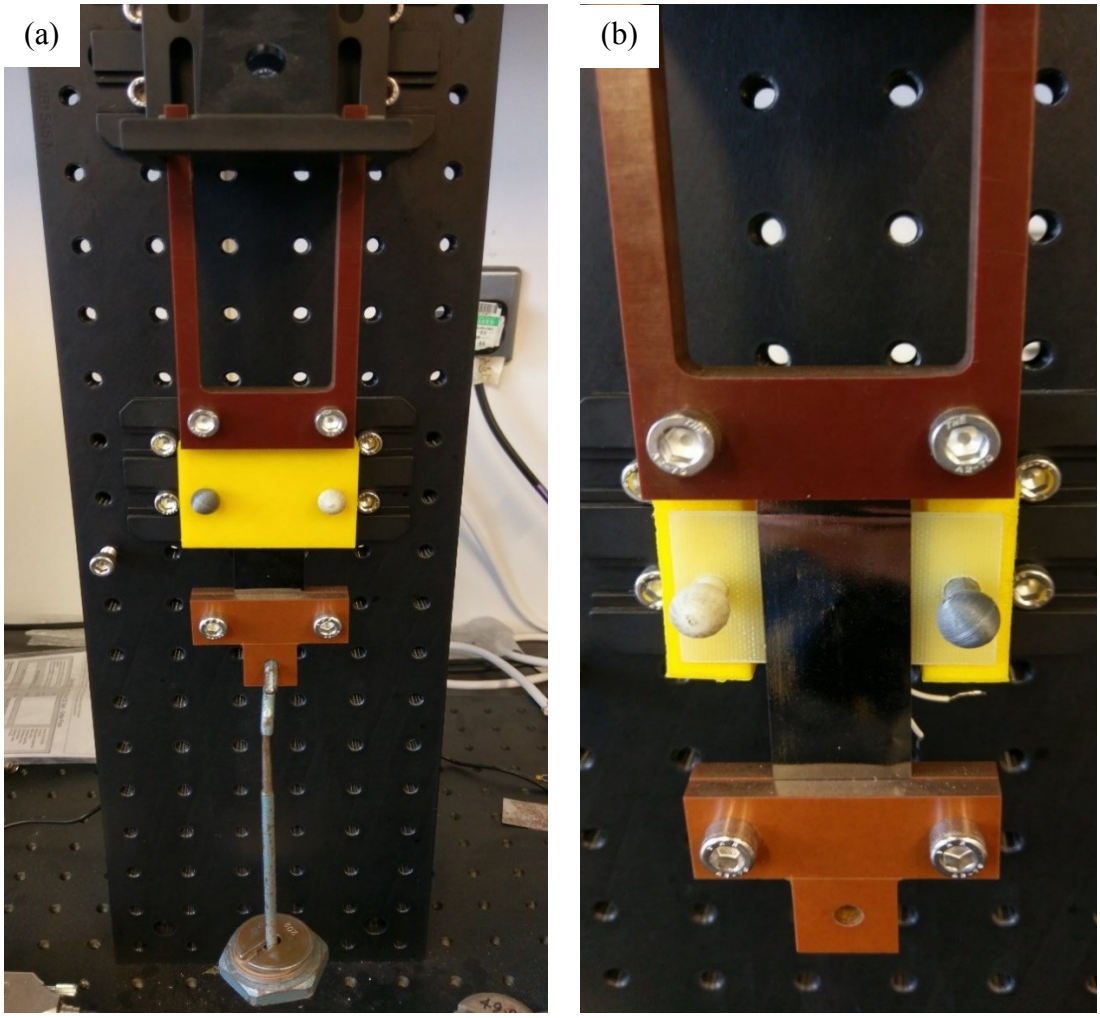


Figure 4.8 – Vertical suspension for stress sensing. (a) System overview; (b) system overview without 3D printed boundary layer.

One end of the TUFNOL suspension component was secured by 3D printed pins to an angle bracket, and the other end secures the top of the magnetic ribbon, this was done by additional TUFNOL pieces which were secured using non-magnetic screws and nuts. One of the TUFNOL pieces used in securing the bottom of the magnetic ribbon has been manufactured to accommodate a weight holder. The planar coil was secured to lie flat against the suspended magnetic ribbon via a 3D printed coil holder. The planar coil was held in place by 3D printed pins and a 3D printed boundary layer, the 3D models are shown in Figure 4.9. The purpose of the layer is to minimise the gap between the magnetic ribbon and the coil. Inserting the pins fully through both the boundary layer and the coil holder, the distance of the gap will be minimised for each coil.

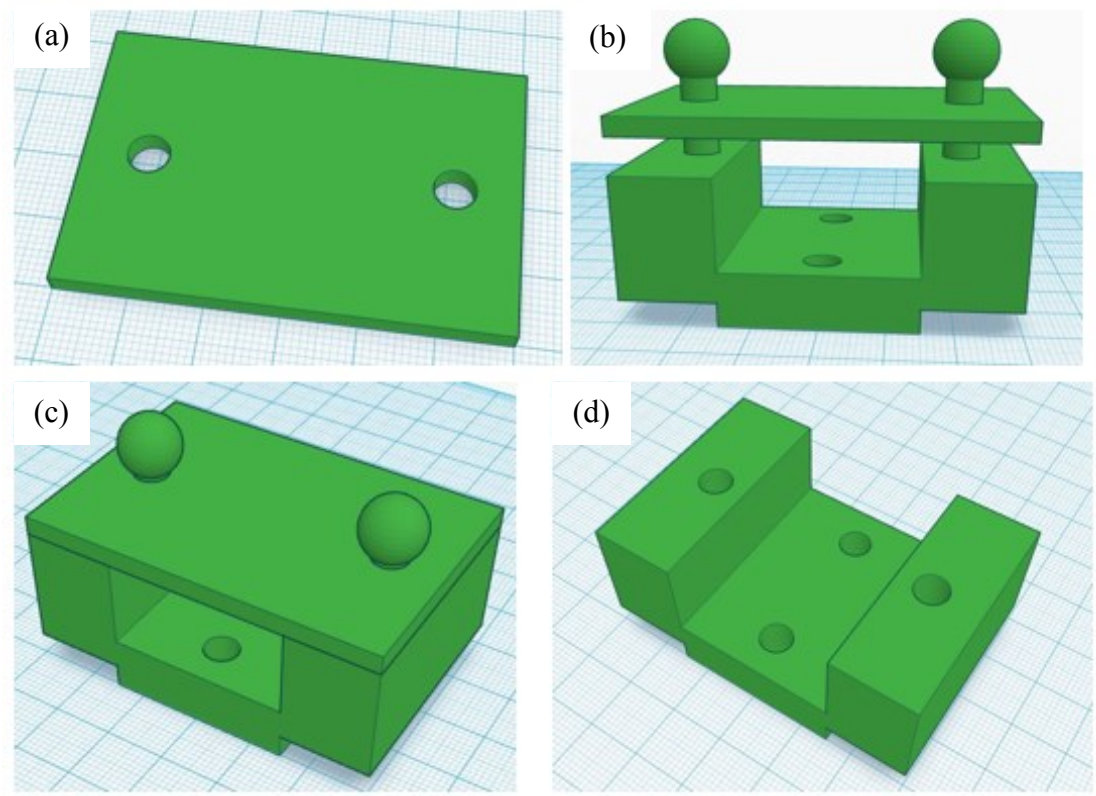


Figure 4.9 – 3D printed components for the vertical suspension configuration. (a) Boundary layer; (b) schematic of the coil holding system; (c) coil holding system with pins fully inserted; (d) 3D printed coil holder.

A weight holder was inserted to the TUFNOL piece, and slotted weights are placed on it, as shown in Figure 4.8. This exerts vertical stress on the magnetostrictive ribbon, Metglas 2605S3A. The applied stress translates into a change in the permeability, and by analysing the inductance value of the coil it was possible to compare how different topologies respond to changes in the ribbon's permeability.

For this investigation the planar coils were treated with an insulating spray for electrical insulation, due to the proximity between the ribbon and the coil. After the coils have been treated they were placed on the measurement system, and after it has been secured the measurements were taken. The measurements were taken after the addition of each new weight and repeated for the removal of weights.

A LabVIEW program was written to assist in the data acquisition and storage. Through LabVIEW the impedance analyser has been programmed to obtain impedance data, however due to the manual procedure of adding and removing weights, the trigger for the data acquisition has been replaced with a manual switch in the LabVIEW program. This allows for the weight holder and weight to settle down and avoiding excessive motion of the ribbon. This swinging could affect measurement results and was minimised to ensure vertical stress was applied.

For each planar coil the loading and unloading cycle was repeated 5 times, and the applied force ranged from approximately 0.3 N to 4.0 N. The same strip of ribbon was used for all the coils tested in this experiment, and had dimensions of 60 mm x 25 mm.

In addition to the planar coils, a wound coil was also tested for comparison. It consisted of a 40 turn coil wound around a former with dimensions of 45 mm x 30 mm x 1 mm. The ribbon was slotted through the former before investigating the coil's impedance characteristics. The wound coil was subject to the same experimental procedures of the planar coils. In addition to these measurements, the inductance response of the wound coil without a magnetic ribbon core was also investigated, to identify how the two types of coils differ.

## 4.4 Figure-of-eight Coil Angular Displacement Measurement System

### 4.4.1 Angular displacement sensor fabrication

The AD sensor design consists of two square coil segments which generated fields in opposite polarities, the two square coil segments are configured in a series connection. A top down view of the sensor design is shown in Figure 4.10. The sensor was fabricated through etching, a layer of solder mask was applied over the entirety of the sensor on both sides, except two solder pads on the bottom side of the sensor where external connections are made. The track width of the sensor was limited by the machinery in the manufacturing process, which was 150 µm, this was also the limit of the gap between each track. This limitation can be reduced through the usage of more sophisticated machinery in the manufacturing process. The sensors were fabricated by Quick-Teck electronics, which specialise in PCB manufacturing. The gap between the two square coil segments can be lengthened or shortened to suit specific applications, as can the dimensions of the coil segments. The gap between the coil segments is the area which will be positioned over the region of flexion, therefore it is important to have minimal resistance to any bending motion in this area.

The gap between the coil segments have been left largely unpopulated for this purpose. Ribbon samples with dimension of 30±1 mm x 7.5±1 mm x 23 µm were attached to the sensor in different configurations, which are detailed in Chapter 7. The dimension of these ribbon samples cover the two coil segments shown in Figure 4.10 entirely.

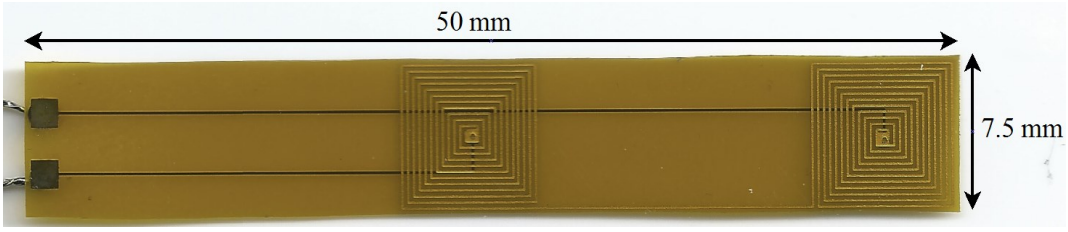


Figure 4.10 – Top down view of the top side of flexible figure-of-eight sensing coil.

The design of the sensor coil is referred to as the figure-of-eight (FOE) configuration, as the design resembles the shape of the number eight; such design principles were used in transcranial magnetic stimulation (TMS) applications. An example of a conventional FOE coil can be seen in Figure 4.11, the conventional FOE coil was designed such that each half of the coil produces a field of opposite polarity, to reinforce the field at the coil's centre.

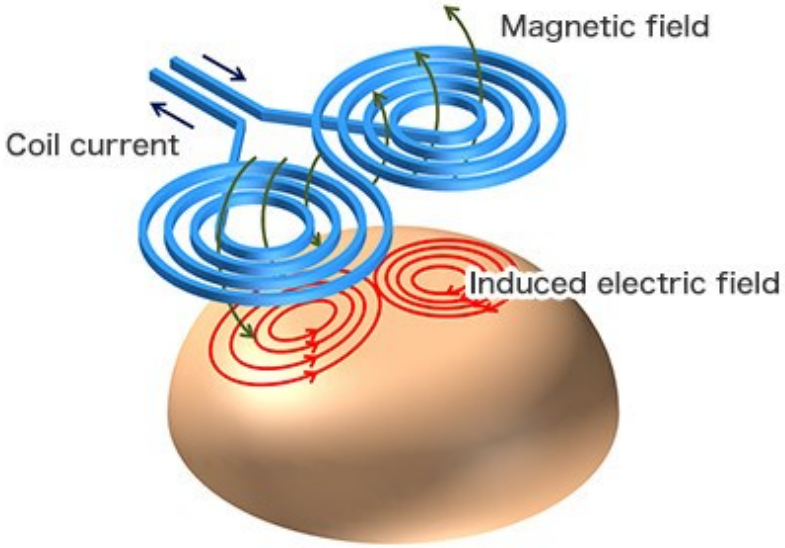


Figure 4.11 – Figure-of-eight coil configuration in TMS application. [6]

Figure 4.12 shows the schematic diagram of the sensor, including the magnetic sensing element. To fabricate the sensor prototype, a piece of magnetic ribbon was cut to the dimensions that match the sensing area including the entirety of both coil segments and the gap between the segments, which is 30 mm x 7.5 mm. The magnetic ribbon was then attached to the top surface of the sensor by an adhesive layer, which was approximately 25 μm thick.

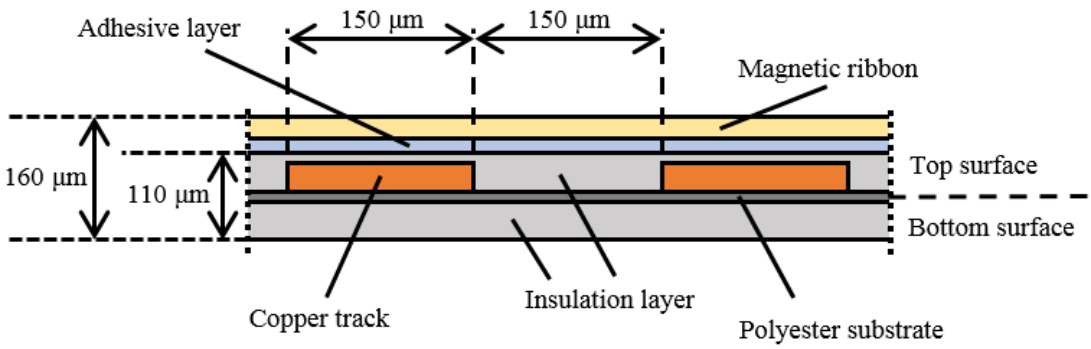


Figure 4.12 – Schematic diagram of sensor in its basic configuration, showing the cross-section image of two copper tracks, omitting tracks that are perpendicular to the tracks shown. (Image not to scale; measurements to the closest 10 µm)

To investigate the characteristics of the sensor, additional sensors were fabricated using different configurations of adhesive layers and magnetic ribbon layers. Additional adhesive layers were used to increase the displacement between the magnetic ribbon layer and the top surface of the sensor, for this investigation two additional sensors were fabricated with 2 and 3 layers of adhesive respectively. Additional magnetic ribbon layers were introduced to investigate the effects of multiple magnetic ribbon layers on the sensor's performance. In order to add extra ribbon layers a layer of adhesive had to be used between each layer of ribbon, to bond them together. For this investigation two sensors were fabricated with 2 and 3 layers of magnetic ribbon respectively, all being on the top surface of the sensor. In addition, a sensor was fabricated with a magnetic ribbon layer attached on both sides of the sensor, resulting in a configuration where the sensor was sandwiched by the magnetic ribbon layers.

### 4.4.2 Figure-of-eight coil measurement system for angular sensing

The measuring system closely resembles the measurement system described in 4.2.3, a block diagram can be seen in Figure 4.13. The measurement system for the AD sensor consists of the same equipment in the same configuration, however no 3D printed components are used in this experiment. The bottom surface of the sensor was bonded on top of a Kapton layer, which was used as a reference surface and provides a support for the sensor. The Kapton layer was important so the sensing region of the sensor, both coil segments and the area between them, could be placed directly over the gap between the displacement stages, without affecting the size of the sensing region. The Kapton layer was secured on both a stationary stage and the controlled stage, shown in Figure 4.14, the distance between these two stages was 30 mm. The LabVIEW program was written to displace the controlled stage towards the stationary stage, and returning to its original position. This will cause a curvature to develop in the sensor, which can be used to extrapolate an approximate bend angle, before returning to an unbent state.

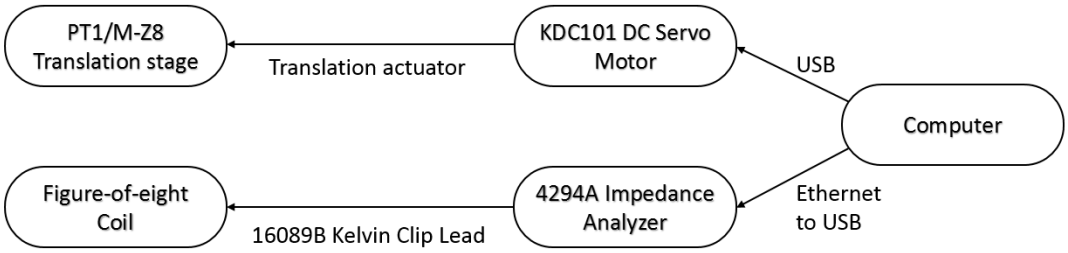


Figure 4.13 – Block diagram of measurement system for angular displacement sensor.

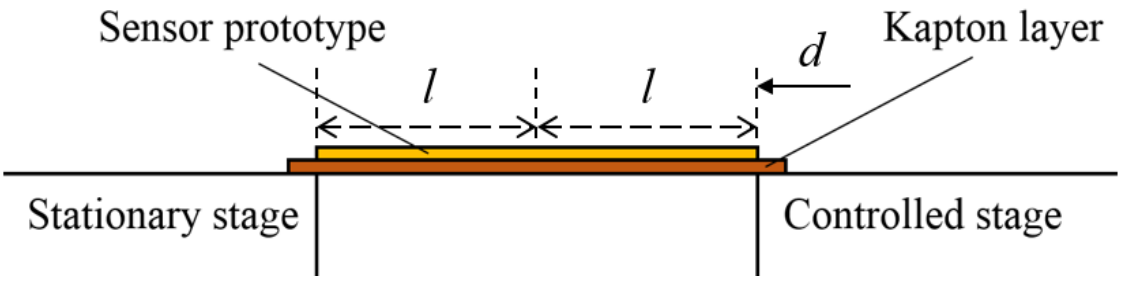


Figure 4.14 – Measurement system configuration of the angular displacement sensor and displacement stages.

The controlled stage was programmed to displace 15 mm in 30 steps, and to return to its original position in 30 steps. The frequency range observed was from 40 Hz – 100 kHz, a limit imposed by the attachment used on the impedance analyser. The inductance response was taken after each displacement, and a sweep of 201 points was made over the observed frequency range. The measurements are repeated 10 times for each sensor configuration. For each different sensor a new adhesive layer was used to bond the sensor prototype to the Kapton layer, which was unchanged throughout this investigation.

As the experiment relies on displacing stages to induce a bend angle, an approximate relationship between displacement and bend angle had to be developed. To extrapolate bend angle from the arc, induced through displacement, the following equation has been devised.

$$Angle = 180 - (2 \times \theta)$$
$$Angle = 180 - (2 \times sin^{-1}\left(1 - \frac{3d}{2l}\right)) \quad (4\text{-}1)$$

The equation is based on approximations of the changing dimensions due to displacement and the trigonometric relationship between them. Figure 4.15 shows the method of extrapolation and the different parameters used in (4-1). The equation is limited by the assumption that the arc can be fitted to a circle with a radius much larger than the displacement. The equation also assumes that the tangential lines used to extrapolate the joint angle is of length $l$, which is a simplification of a complex relationship between the displacement and the length of the tangents. Another limitation of the equation is that the displacement is not too large, as the extrapolated tangents will be much larger than $l$. Displacements should not overly exceed length $l$, as this will induce arcs where the tangential lines become too long for the assumptions made.

Two different directions of bending have also been investigated, as shown in Figure 4.16. Each sensor configuration was tested in the two directions of bending, to investigate which direction of bending produced a more significant response.

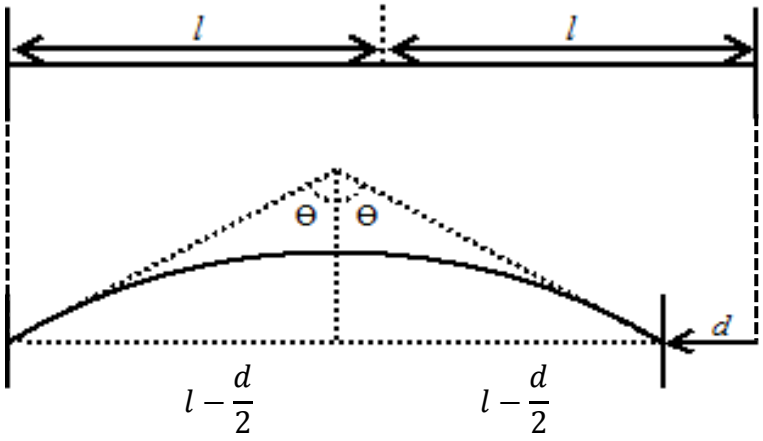


Figure 4.15 – Schematic diagram for the proposed method of bend angle extrapolation, induced through displacement.

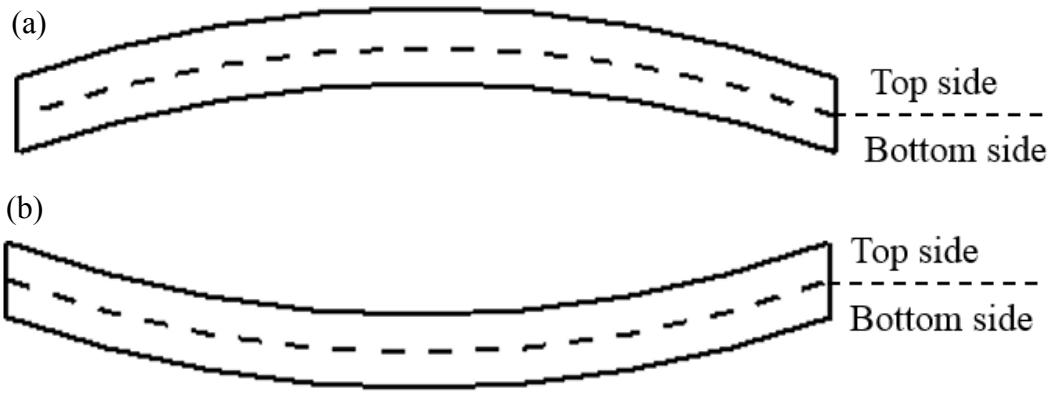


Figure 4.16 – Schematic diagram for the two types of bending investigated, with respect to the top surface. (a) Convex bending; (b) concave bending.

The experimental and modelling methodologies have been designed to provide a good understanding of various coil topologies, which will aid the design of the AD sensor. The experiments for the AD sensor have been devised to provide a comprehensive study on the sensor's properties and capabilities. The AD sensor was constructed with several different configurations in an attempt to find an optimal configuration for the sensor, and it was subject to two different styles of bending to identify how this affects the sensor's performance.

## 4.5 References for Chapter 4

[1] ANSYS. (2013). *ANSYS Maxwell Magnetic Field Formulation*. [online] Ansys.com. Available at: http://www.ansys.com/-/media/ansys/corporate/resourcelibrary/techbrief/tb-ansys-maxwell-magnetic-field-formulation.pdf. [Accessed 16 Dec. 2017].

[2] Metglas. (n.d.). *Magnetic Alloy 2605S3A(Iron-based) Technical Bulletin*. [online] Metglas.com. Available at: https://metglas.com/wp-content/uploads/2016/12/2605S3A-Technical-Bulletin.pdf. [Accessed 16 Dec. 2017]

[3] Kohnke, P. (1999). *ANSYS theory reference*. Canonsburg, PA: ANSYS.

[4] Agilent Technologies. (2008). *Agilent 4294A Precision Impedance Analyzer 40 Hz to 110 MHz Technical Overview*. USA: Agilent Technologies.

[5] Gibbs, R., Moreton, G., Meydan, T. and Williams, P. (2018). Comparison between Modelled and Measured Magnetic Field Scans of Different Planar Coil Topologies for Stress Sensor Applications. *Sensors*, 18(4), p.931.

[6] Department of Neuromodulation and Neurosurgery, Osaka University. *Development of Highly-efficient magnetic stimulators for home care medical device*. [online] Available at: http://www.neuromod.med.osaka-u.ac.jp/en/project/ [Accessed 19 Jan. 2018].

# Chapter 5. Investigation and Characterisation of Planar Coil Topologies, and the effect of Planar Coil and Magnetic Ribbon Separation

## 5.1 Introduction

In this chapter, planar coil topologies were characterised and the effect of planar coil and magnetic ribbon separation was examined. The investigation on coil-ribbon separation will provide crucial data which will indicate limitations for planar coil technology and restraints for the design of the angular displacement sensor. Different topologies were tested in both 3D FEM and experiments, to confirm the usage of 3D FEM as a tool in aiding planar coil sensor design and development. The planar coils were tested experimentally using a 3D printed set-up and LabVIEW controlled components. A Metglas soft amorphous ribbon was used as the magnetic component of this investigation. The planar coils were configured to be parallel with the magnetic ribbon and to detect displacements of the magnetic component, controlled by a displacement stage. In addition, the $H_z$ field generated by different coil topologies have been investigated, using a tunneling-magnetoresistance (TMR) sensor, and compared with 3D FEM findings. This investigation provides an insight to how the field profiles of various topologies differ.

## 5.2 Results and Discussion

### 5.2.1 Inductance changes due to ribbon displacement as a function of frequency

The following graphs show the inductance change from zero displacement of the ribbon to the maximum displacement tested of 10 mm, for the four topologies tested. This displacement between the magnetic ribbon and the planar coil provides an understanding of how separation distance affects the inductance of the planar coils. The figures displayed in this section only include the data obtained for the planar coil with the smallest pitch for each respective topology, the figures of the other pitches are included in Appendix A.

Figure 5.1 shows the inductance response of the square planar coil against a 10 mm displacement of the ribbon sample. It was observed that displacing the ribbon away from the planar coil reduces the inductance of the planar coil, which is expected. It can also be seen that the trends of inductance over the frequencies tested are similar, even at the lower frequencies where measurement inaccuracy is high. The planar coil exhibits a good response over the frequency range tested, with a particularly stable inductance response between 30 kHz – 100 kHz. The frequency response of planar coils will be compared with a traditional wound coil in Chapter 6.

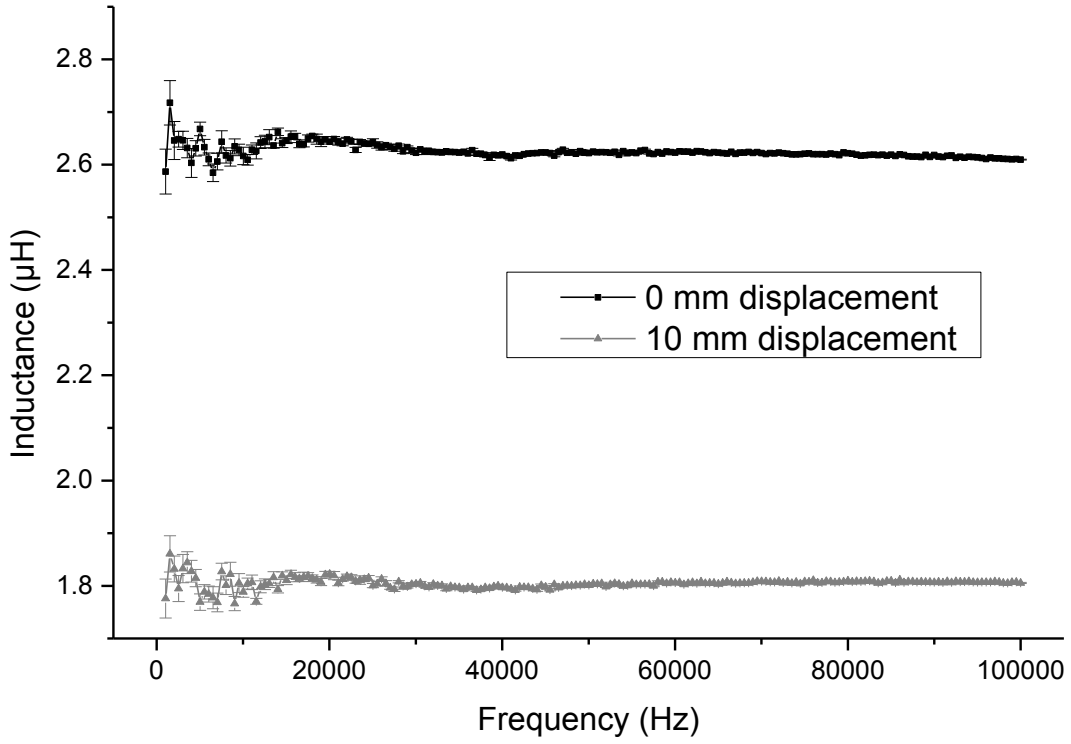


Figure 5.1 – Inductance change due to displacement over full span of observed frequencies for square topology with pitch of 0.5 mm.

Figure 5.2 shows the response of the circular coil topology. The low frequency response is different compared to the square topology, however the inductance response between 30 kHz – 100 kHz is comparable with that of the square topology. The circular coil topology has a lower inductance value than the square coil tested.

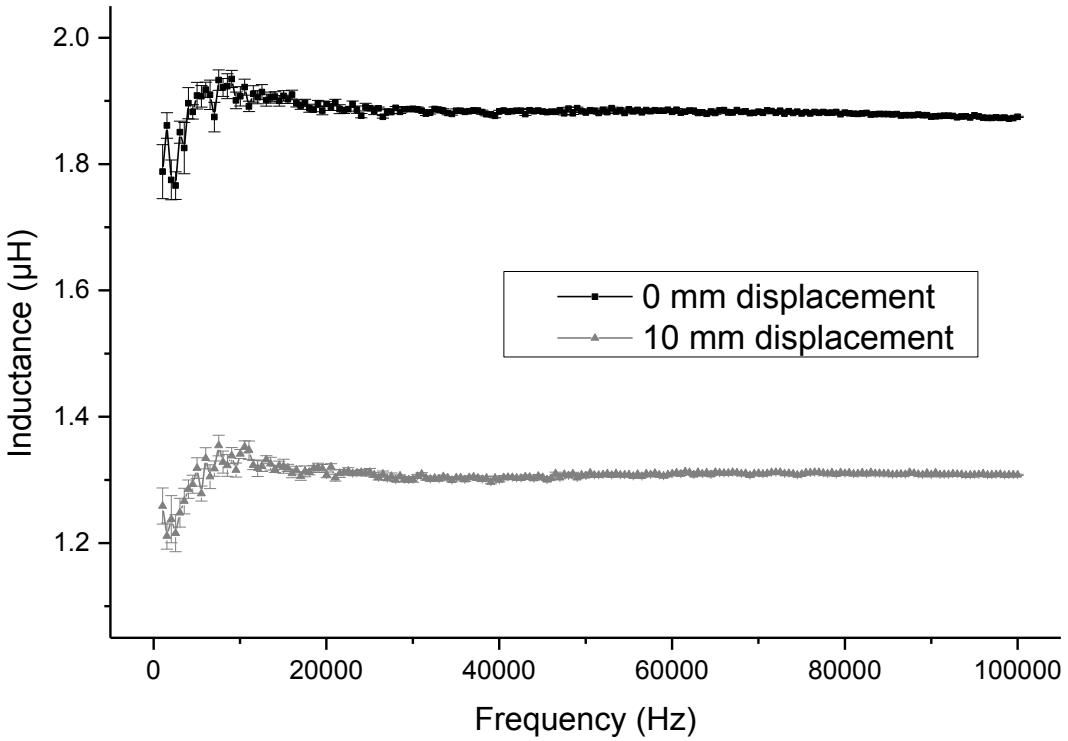


Figure 5.2 – Inductance change due to displacement over full span of observed frequencies for circular topology with pitch of 0.5 mm.

Figure 5.3 and Figure 5.4 show the response of the meander topology and the mesh topology, respectively. The inductance of these planar coils is much smaller, and the inductance change due to displacement of the magnetic ribbon is also smaller compared with the spiral topologies. The two non-spiral topologies also seem to exhibit similar trends for the entire frequency span of 40 Hz – 100 kHz. It can be seen from these figures, the difference in inductance between 0 and 10mm displacements is mostly independent of frequency. Each data point shown in the trace was obtained from averaging 10 measurements at each point in the frequency sweep. The standard error was then obtained for each mean data point. The standard error was dependent on frequency.

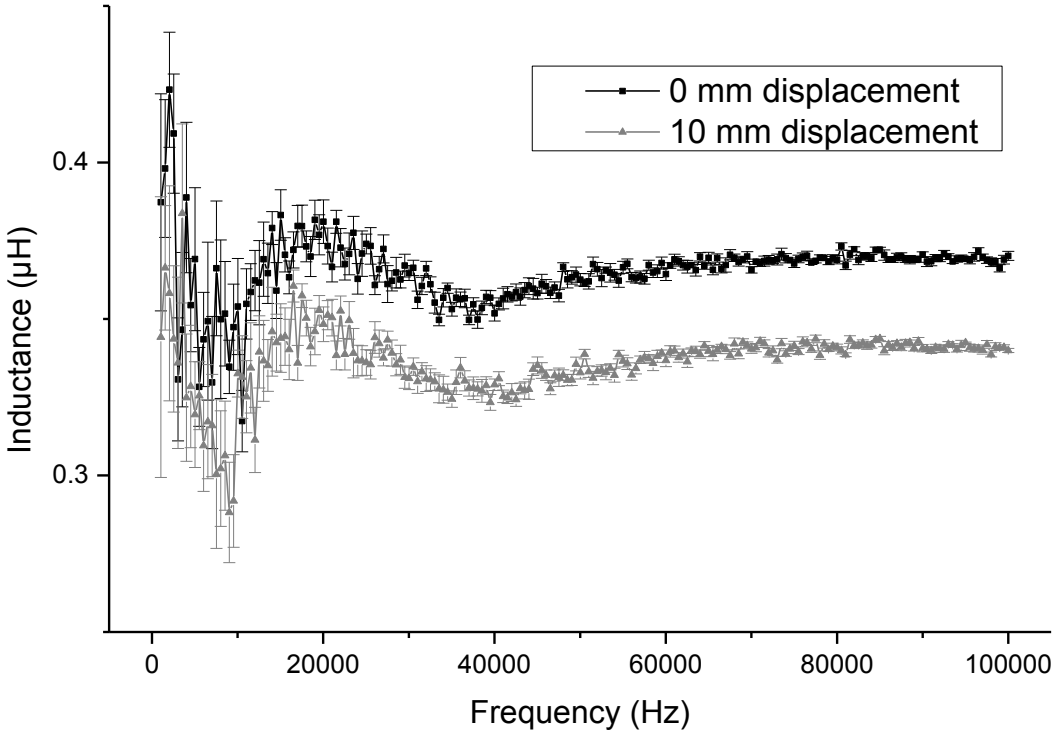


Figure 5.3 - Inductance change due to displacement over full span of observed frequencies for meander topology with pitch of 0.5 mm.

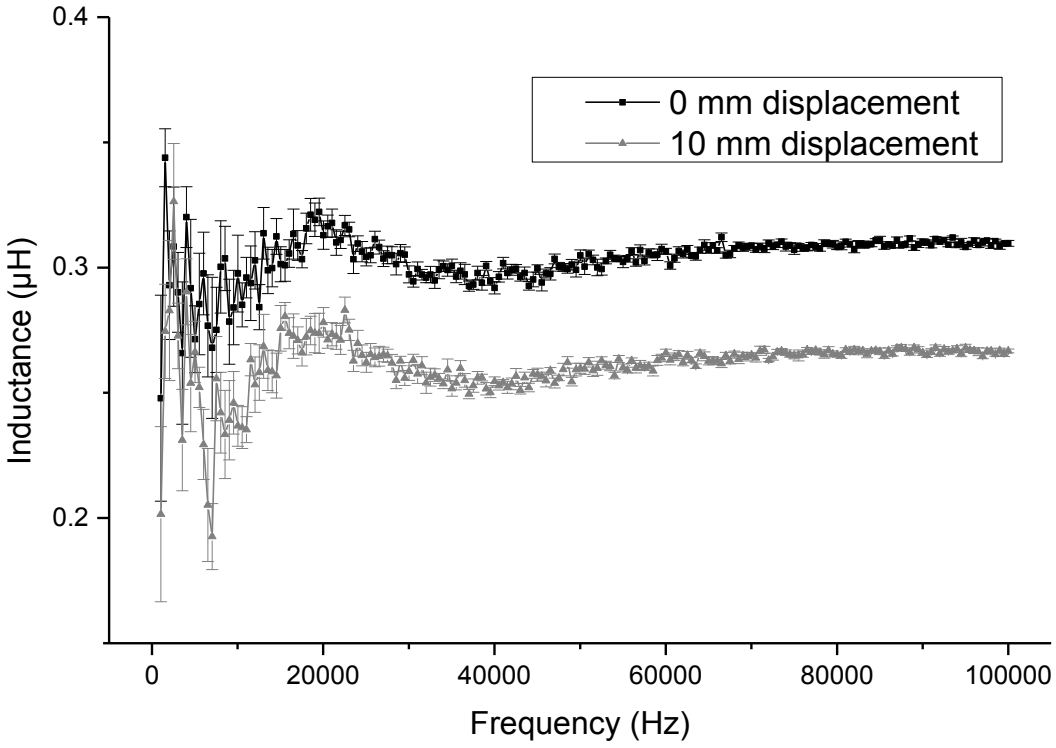


Figure 5.4 - Inductance change due to displacement over full span of observed frequencies for mesh topology with pitch of 1.0 mm.

Table 5.1. Standard error calculated for 2 frequency ranges.

| Topology | *Pitch (mm)* | *Averaged standard error for 40 Hz – 100 kHz (nH)* | *Averaged standard error for 30 kHz – 100 kHz (nH)* |
|---|---|---|---|
| Square Coil | 0.5 | 4 | 2 |
| Circular Coil | 0.5 | 3 | 2 |
| Meander Coil | 0.5 | 3 | 1 |
| Mesh Coil | 1.0 | 3 | 1 |

Table 5.1 shows the averaged standard error of all four topologies with measurement uncertainties larger at low frequencies. The noise at low frequencies was investigated by placing the planar coils into a magnetically shielded environment to eliminate external electromagnetic interference. The planar coils of each topology with the smallest pitch value were placed in a multilayered mu-metal box and characterised using the impedance analyser. The inductance of these coils were obtained 10 times and evaluated against the inductance response of these coils in an unshielded environment. No magnetic ribbon core was used as part of this investigation.

Figure 5.5 and Figure 5.6 show the response obtained from the spiral coil topologies. In both topologies, the low frequency noise has not been eliminated or reduced significantly. In general it can be seen that the uncertainties are large in the low frequency regions, under both shielded and unshielded conditions. There is a notable difference in the trend exhibited by the data traces. Comparing Figure 5.5 and Figure 5.6, it can be seen that the trends exhibited under shielded conditions are similar for both topologies. This similarity was not seen between the trends measured under unshielded conditions. The inductance value of the topologies changes slightly, however there is not a significant change to the frequency response of the inductor, other than at a low frequency.

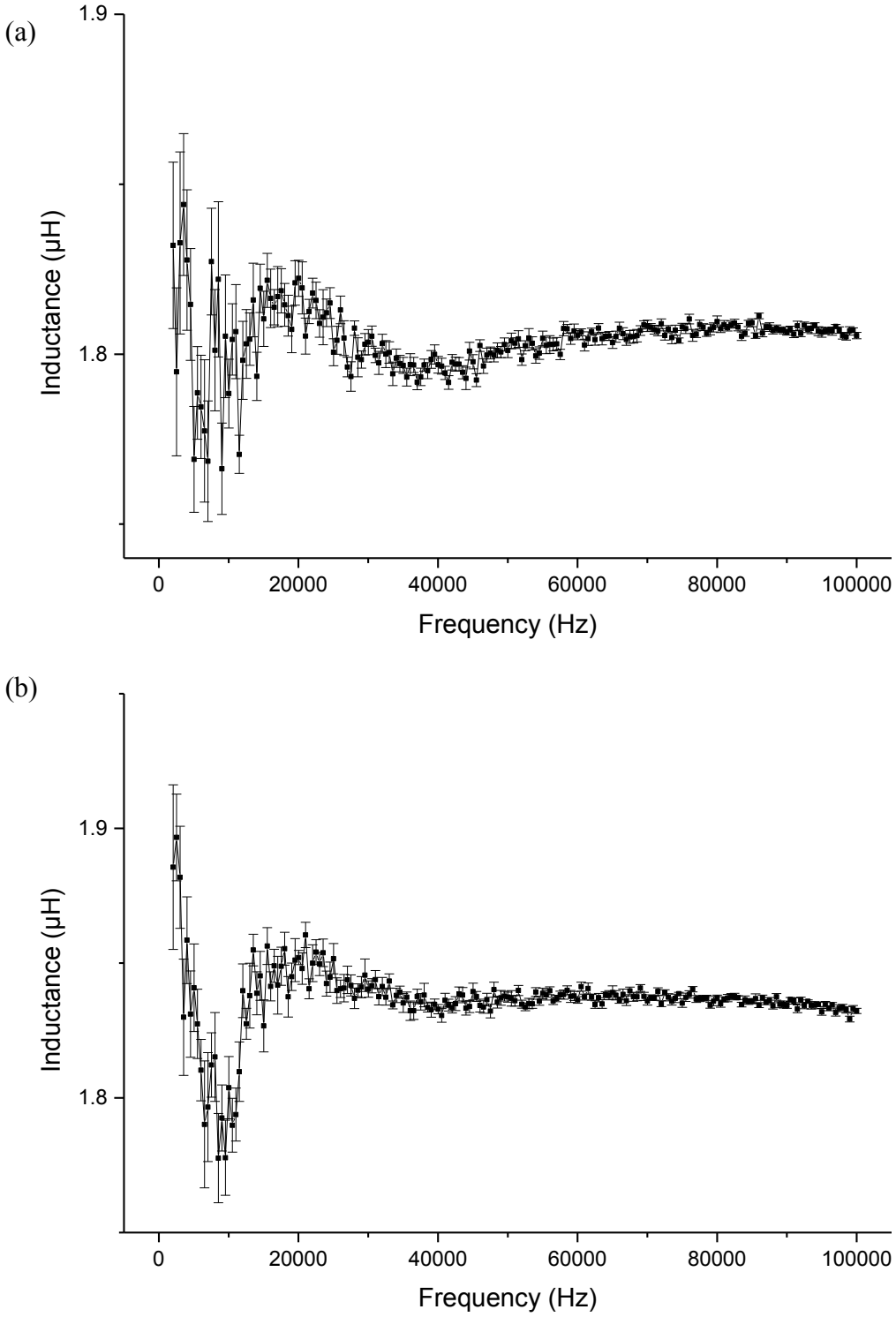


Figure 5.5 – Inductance response over span of observed frequencies for square topology with pitch of 0.5 mm. (a) In an unshielded environment; (b) in a shielded environment.

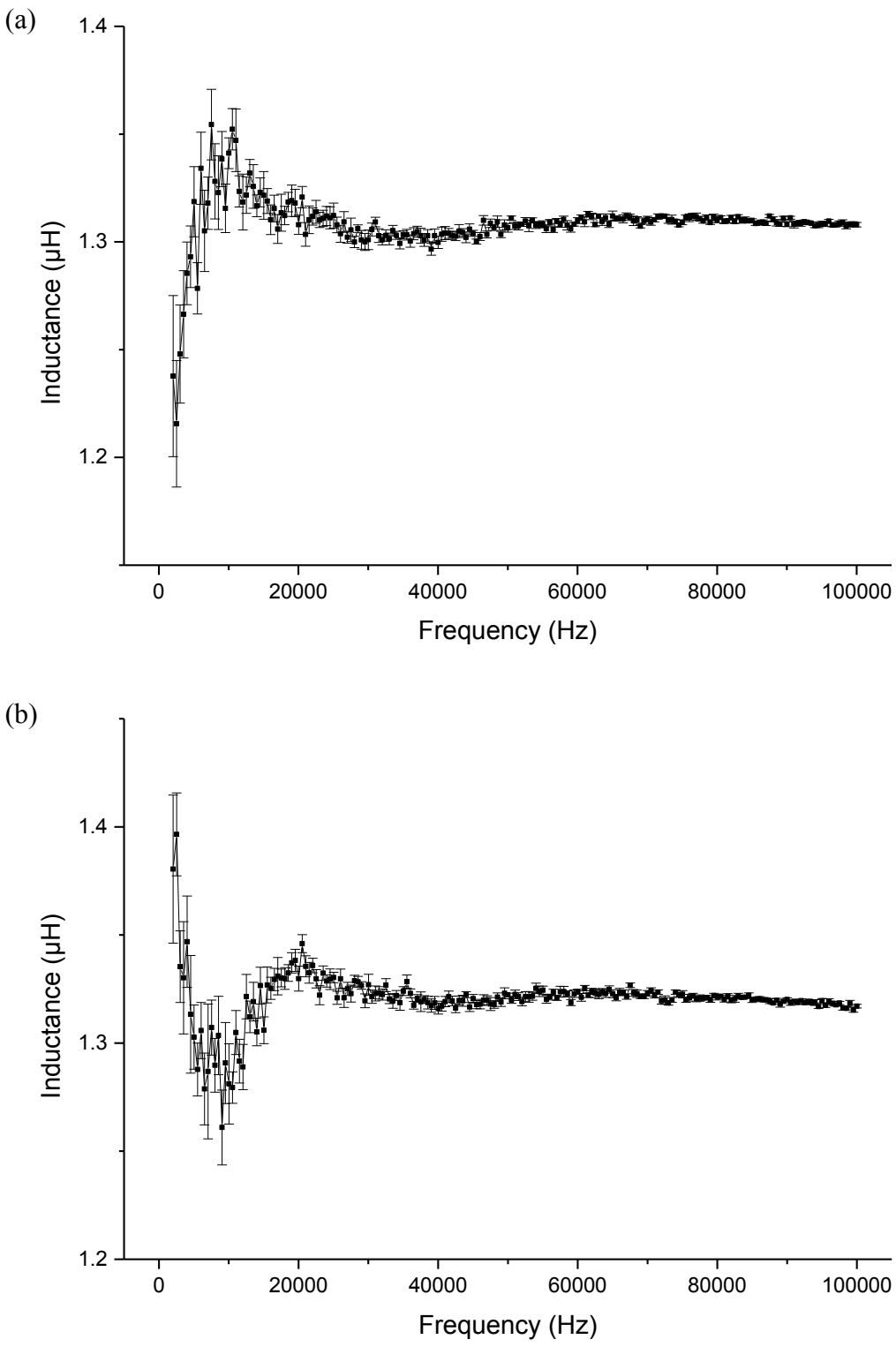


Figure 5.6 – Inductance response over span of observed frequencies for circular topology with pitch of 0.5 mm. (a) In an unshielded environment; (b) in a shielded environment.

Figure 5.7 and Figure 5.8 show the non-spiral coil topologies, which also show a lack of noise reduction. By comparing the shielded response to the response of their unshielded counterparts, placing the coils in a shielded environment has not benefitted the SNR at low frequencies greatly. The inductance-frequency response of both topologies have changed slightly, a minor change in inductance was also seen for both topologies.

By comparing the unshielded response and shielded response for each topology, shielding has had a minimal impact on reducing low frequency noise, and has not affected the frequency response of the planar coils by much, except for the region below 20 kHz where the circular coil was affected the most. It can also be seen that some topologies are affected more greatly than others, with the square, circular, and meander topologies showing a slight difference of the measured inductance at frequencies greater than 20 kHz, but the mesh coil exhibiting a minimal change in the measured inductance at frequencies greater than 20 kHz.

The findings from this experiment imply that the majority of the noise at low frequencies do not originate from external electromagnetic interference. By presenting measurements taken under a magnetically shielded condition, it can be seen that shielding had no impact on reducing low frequency noise.

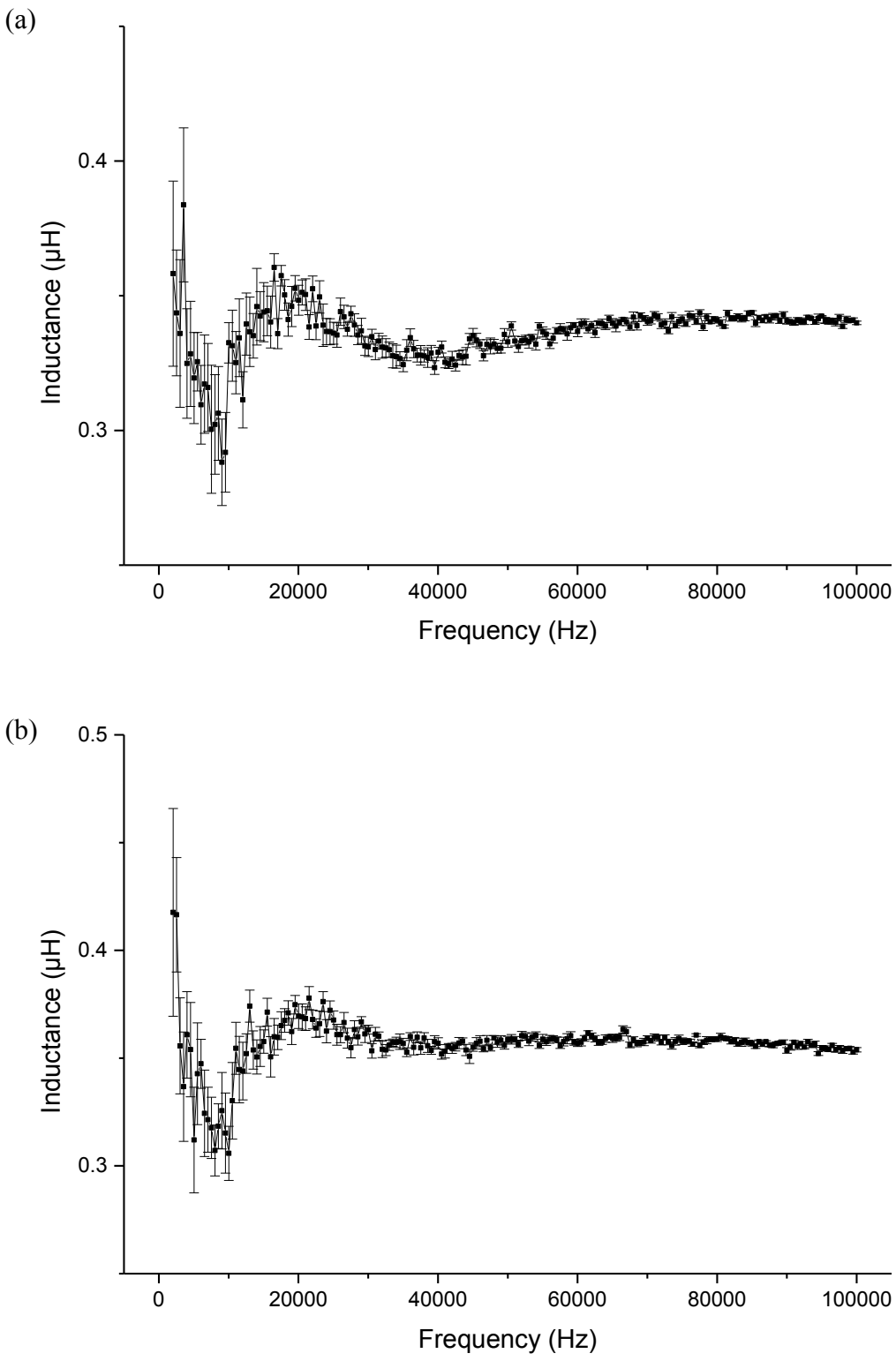


Figure 5.7 – Inductance response over span of observed frequencies for meander topology with pitch of 0.5 mm. (a) In an unshielded environment; (b) in a shielded environment.

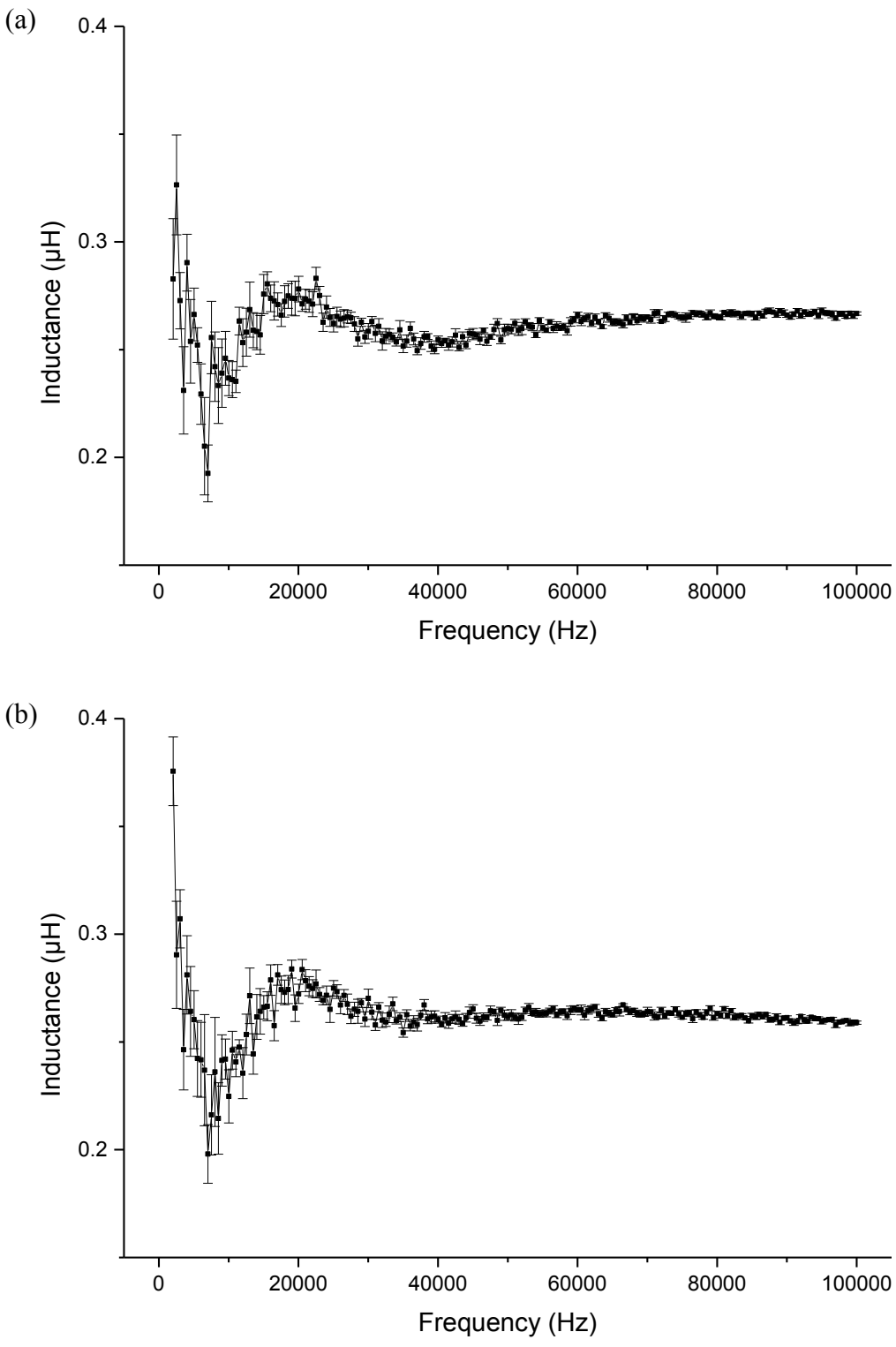


Figure 5.8 – Inductance response over span of observed frequencies for mesh topology with pitch of 1.0 mm. (a) In an unshielded environment; (b) in a shielded environment.

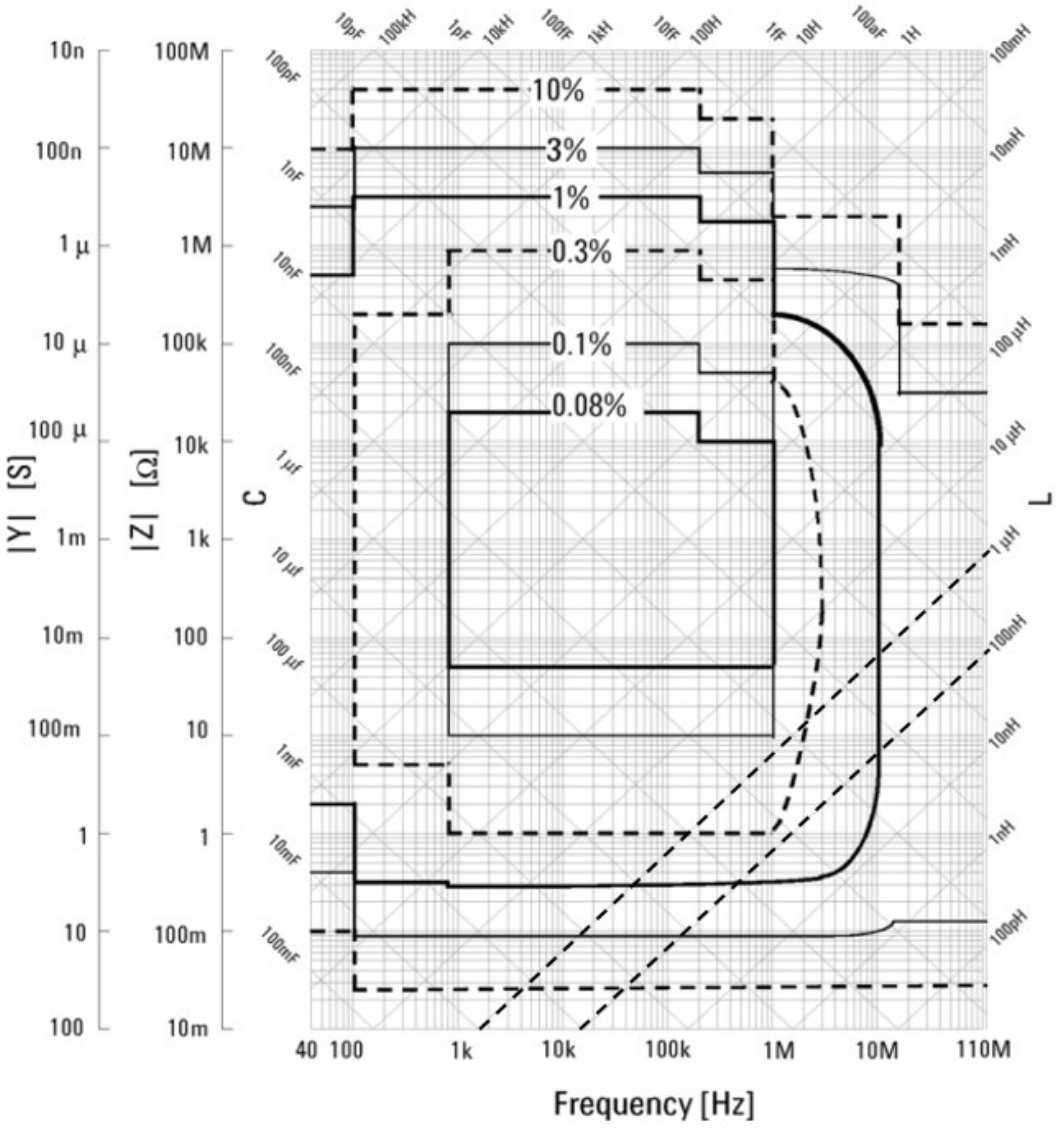


Figure 5.9 – Example of calculated impedance measurement inaccuracy at four-terminal pair port of the Agilent 4294A's front panel. [1]

Figure 5.9 was obtained from the manual for the impedance analyser used in these measurements. For measurements made between 1 μH and 100 nH, the frequency will affect measurement accuracy, with greater inaccuracy below 10 kHz. Two dotted lines have been superimposed over Figure 5.9, these two lines represent the measurement inaccuracy for measurements made in the respective inductance scale, of μH and 100 nH inductance values. By examining the intercept between the frequency and the dotted lines, the measurement inaccuracy can be represented by different zones. For example, using the dotted line for μH measurements, the inaccuracy is between 10% and 3% at 10 kHz. As the frequency is increased, the measurement accuracy improves,

approaching 0.3% at 100 kHz. By examining Figure 5.6 (b) as an example, the standard error at 10 kHz is approximately 3.5%, which corresponds well with 3% seen in Figure 5.9. The standard error at 100 kHz is approximately 1%, this also corresponds well with Figure 5.9, where the dotted line is shown to be in the measurement uncertainty range between 1% and 0.3%. Figure 5.9 shows that measurement accuracy improves vastly with frequency. Due to the superior measurement accuracy at higher frequencies, a frequency of 80 kHz was chosen for the analysis of the remaining datasets.

### 5.2.2 Investigation of $H_z$ profiles for different planar coil topologies

To better understand why inductance characteristics differ between topologies, especially between spiral and non-spiral planar coil designs, the $H_z$ field has been investigated. The $H_z$ field was chosen due to its importance in understanding why previous findings differed vastly between different topologies. The coil-ribbon separation is in the z-direction; therefore, it is important to examine the $H_z$ field. The magnetic ribbon used is a near square sample of an amorphous material, this means there is no magnetocrystalline anisotropy present within the material, and that shape anisotropy will be in plane with the ribbon, but not in a particular direction within the plane. With increased distance from the surface of the coil, the $H_z$ fields obtained through the scans and simulations will gain X and Y vector components, which will result in in-plane fields being applied to the ribbon. Another factor is the softness of the ribbon, which will influence the H field, considering all of its vector components, to warp its field lines to best interact with the magnetic ribbon. As the levels of coil-ribbon separation tested were quite large, the $H_x$ and $H_y$ components would not have been significant at further distances from the scan heights, therefore it can be assumed that $H_z$ will contribute the predominant excitation to the magnetic ribbon.

The $H_z$ field was modelled in the simulation software and measured experimentally using a TMR sensor integrated in a 3D scanning system [2]. The area scanned by the system was 25 mm x 25 mm at varying displacements above the surface of the coil. The output voltage of the TMR sensor was used to plot a 2D grayscale image of the $H_z$ field.

The coils were modelled in a 3D environment, excited by a current of 0.4A, and positioned in the center of the boundary volume, which had dimensions of 40 mm x 40 mm x 20 mm. The amorphous ribbon was modelled with dimensions of 25 mm x 25 mm with 18 μm thickness, and a relative permeability of 20000. A displacement of 10 mm was applied to the ribbon.

Figure 5.10 and Figure 5.11 show the simulated and scanned field profiles of the square planar coil respectively. The field reaches its maximum at the center of the coil, with an increased field strength at the corners of each turn, this can be due to the reinforcement of fields generated by the two track segments which make up the corner. At higher frequencies, this may also be due to current crowding effects occurring at the corners of the planar coils [3].

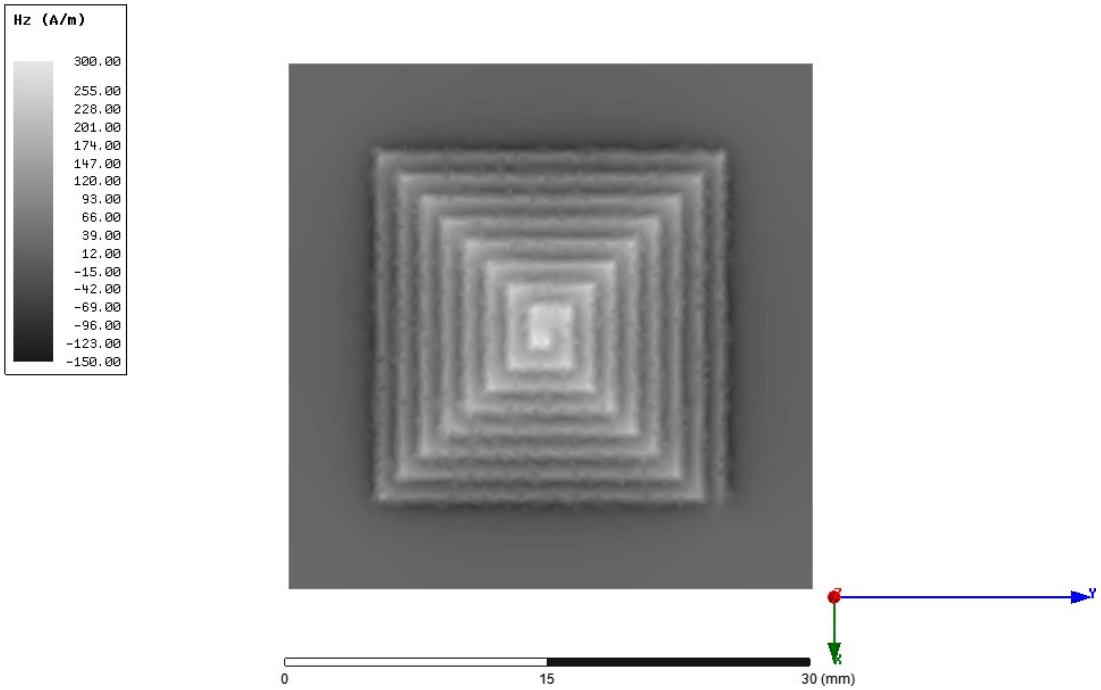


Figure 5.10 – 3D FEM analysis of the $H_z$ component for the square topology, with pitch of 0.75 mm. Distance of 0.15 mm from coil surface. [2]

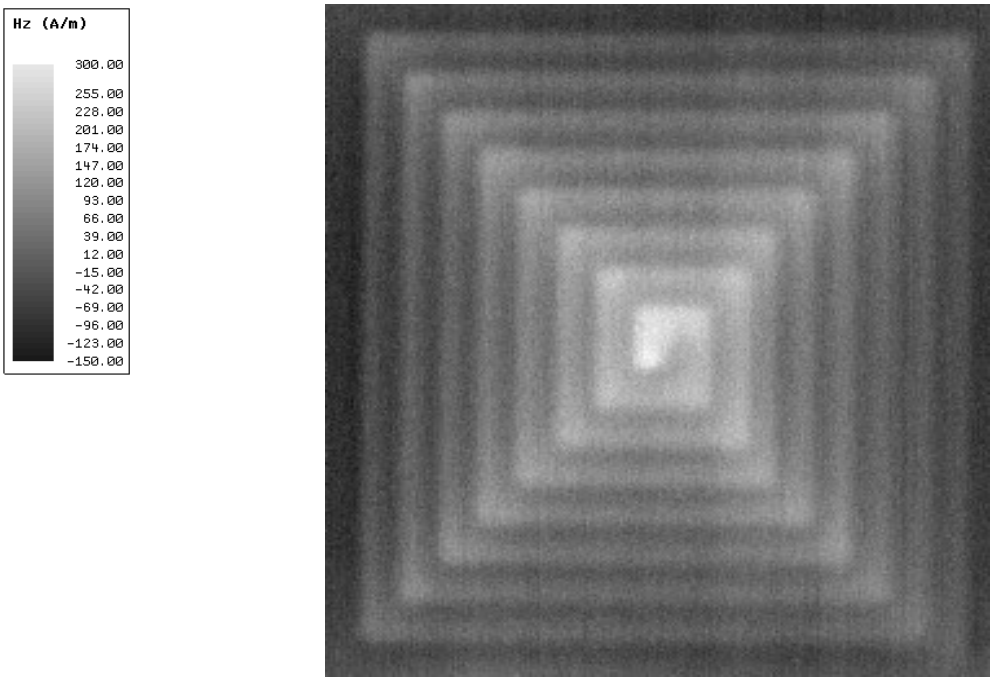


Figure 5.11 – Measured $H_z$ component for the square topology, dimensions of 25 mm x 25 mm, with pitch of 0.75 mm. Scan height of 0.15 mm. [2]

Figure 5.10 and Figure 5.11 show good agreement, the scanned image has the characteristics shown in the simulated image, such as the strength of the field being large at the corners and the large fields generated at the center of the coil. To quantify the agreement between the FEM and measured data a line scan has been carried out along the centre of the square coil, this is shown in Figure 5.12. The line scan demonstrates good agreement between the magnitude of the $H_z$ component and also the profiles of the $H_z$ component, especially the structures of rapid increases and decreases between each turn, resulting in many spikes. The simulated line scan result was within 10% of the measured line scan result.

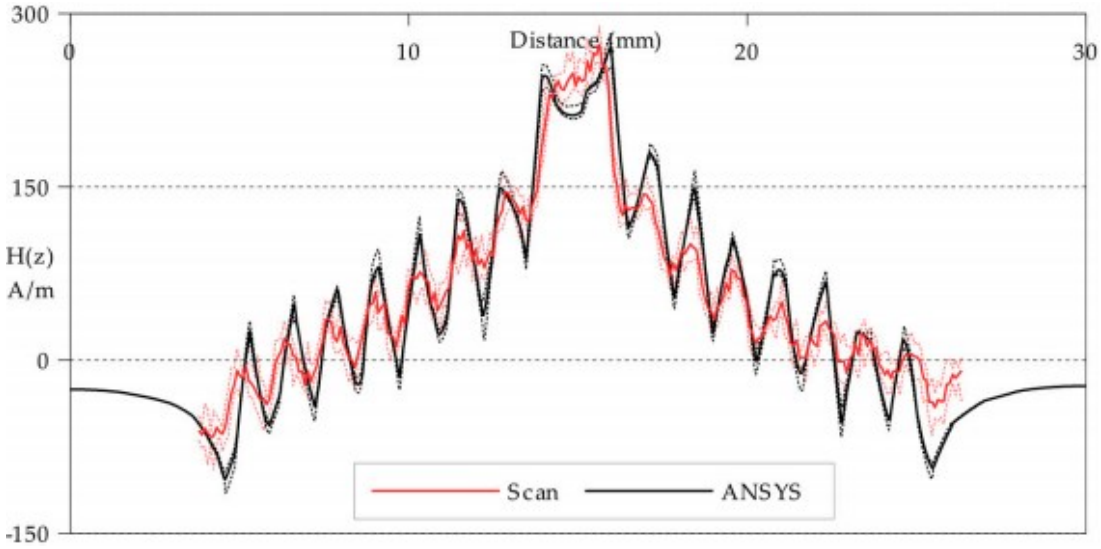


Figure 5.12 – Line scan of $H_z$ component along the centre of the square coil topology, dimensions of 25 mm x 25 mm, with pitch of 0.75 mm. Scan height of 0.15 mm. [2]

Figure 5.13 and Figure 5.14 show the simulated and scanned image for the circular topology, respectively. The circular coil also has a large field at the center of the coil, where the field generated by each turn is superpositioned in this region. The general field profile of spiral planar coils is a large field generated at the center of the coil, which diminishes towards its edges. In general, the field generated by planar spiral coils should resemble a shape similar to that of a cone. The magnetic field generated by each turn of the coil is being superpositioned at the center of the coil, as the current flows in the same direction. This is also why spiral planar coils have an inductance that is much larger than non-spiral coils, given the same area.

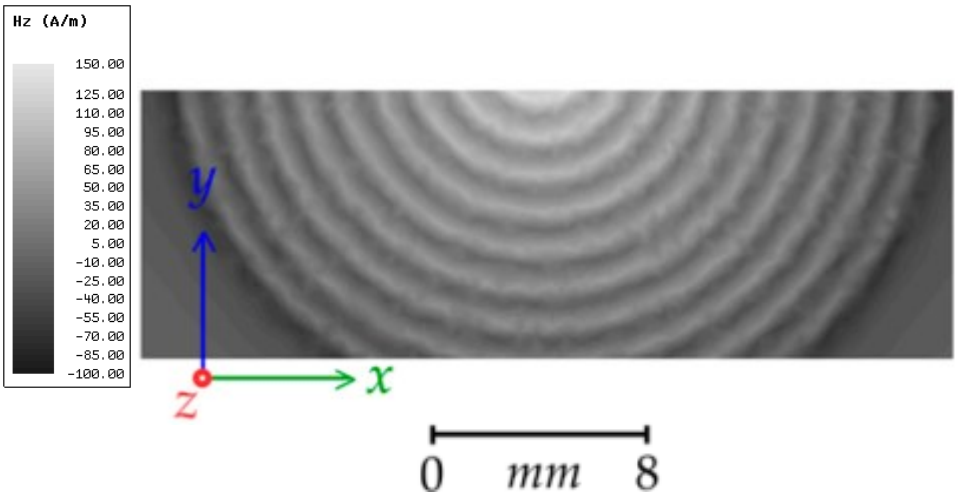


Figure 5.13 – 3D FEM analysis of the $H_z$ component for the circular topology, with pitch of 0.75 mm. Distance of 0.15 mm from coil surface. [2]

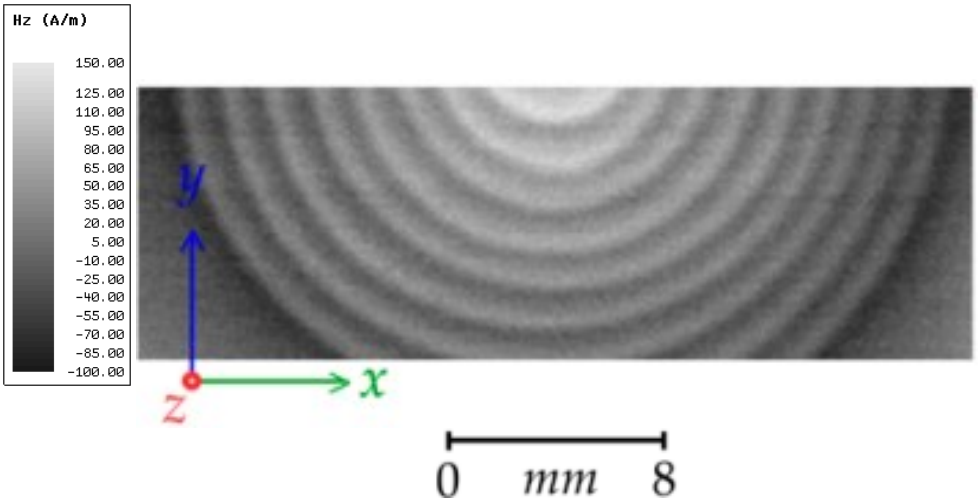


Figure 5.14 – Measured $H_z$ component for the circular topology, with pitch of 0.75 mm. Scan height of 0.15 mm. [2]

Artefacts were seen in the circular coil FEM solutions, as shown in Figure 5.13, small fluctuations in the uniform $H_z$ field can be clearly seen with the uneven pattern. This is due to the mesh size generated for this solution, the artifacts have been minimised by reducing mesh size, and applying a smoothing method to the plots. It should be noted that reducing mesh size too much leads to unacceptable increases in computation time.

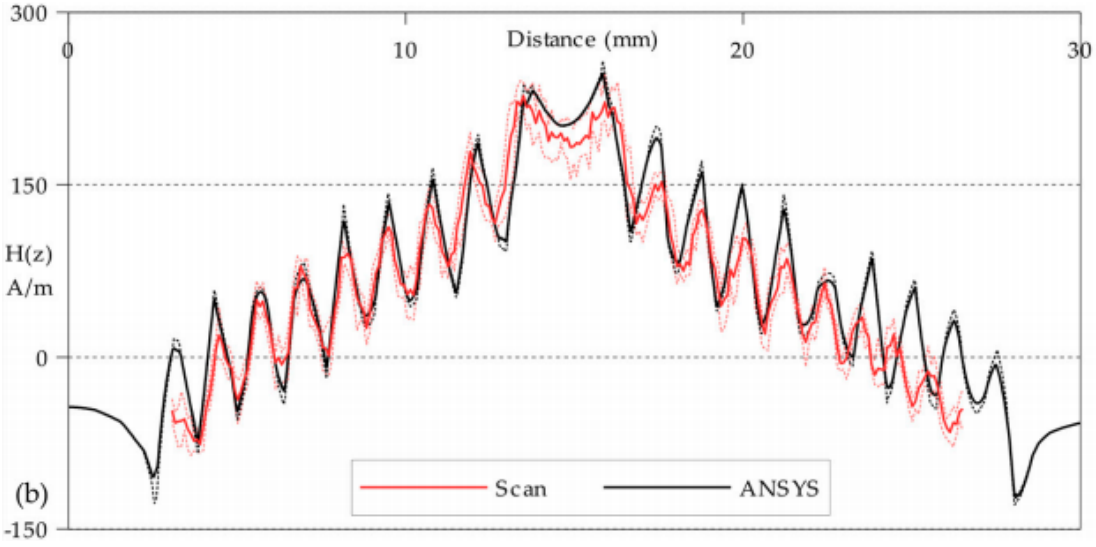


Figure 5.15 – Line scan of Hz component along a line which has been displaced from the centre of the circular coil topology by 2mm, dimensions of 25 mm x 25 mm, with pitch of 0.75 mm. Scan height of 0.15 mm. [2]

Figure 5.15 shows the line scan performed for the circular coil topology, and it also demonstrates good agreement between the simulated and measured results. It can be seen that the magnitude is in good agreement, and the spiked profile of the fields are in good agreement. Through these line scans it can be seen that FEM can be used to model planar coil field magnitudes and profiles with good agreement; the deviation of the simulated results is within 10% of the measured results.

Figure 5.16 and Figure 5.17 show the simulated and scanned field profiles for the meander topology, respectively. The field profile of the meander topology differs greatly from the field profile of the spiral coil topologies, due to the lack of uniformity in the current direction. The effect of superpositioned magnetic fields are not present due to the opposing direction of current flow between all tracks. Compared to the spiral coils, the strength of the field simulated and scanned also decreases, with the peak $H_z$ component halved in strength. With each turn the field generated by a track is opposing the field generated by the neighboring tracks, resulting in high contrast between each track, denoting regions of positive and negative $H_z$.

The direction of current flow in each track of the meander coil is opposite to the direction in its neighboring tracks. This lack of general field reinforcement may be why the inductance of the coil was significantly smaller than spiral base planar coils. In Figure 5.17, there was a reduced contrast seen in the image, this may be due to a change in the scanning height, possibly as a result of a physical distortion at the coil surface. It should be noted that difference in polarity between neighboring tracks was still visible.

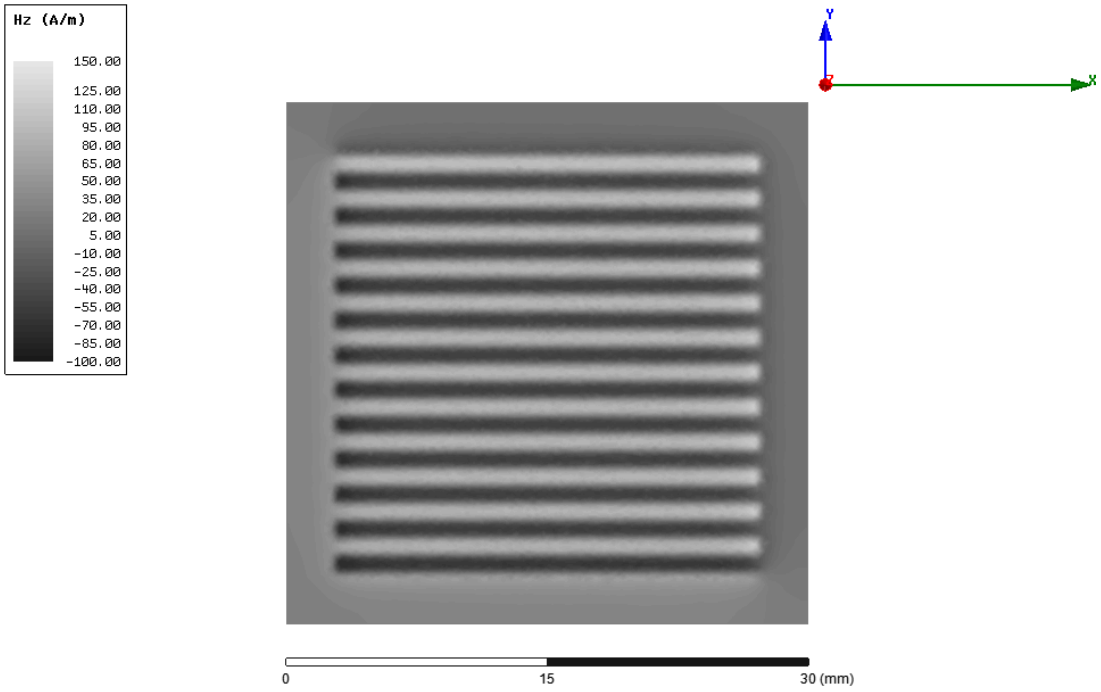


Figure 5.16 – 3D FEM analysis of the $H_z$ component for the meander topology, with pitch of 0.75 mm. Distance of 0.25 mm from coil surface. [2]

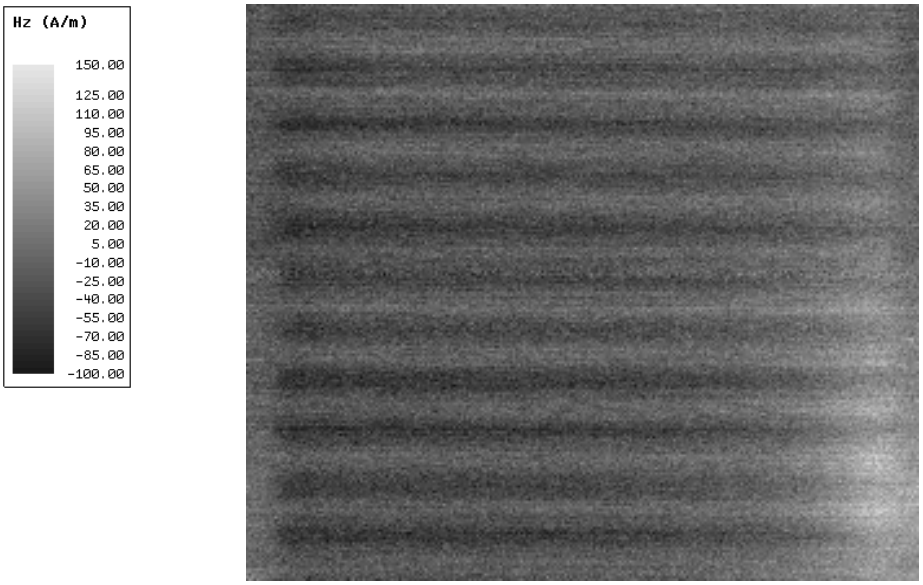


Figure 5.17 – Measured $H_z$ component for the meander topology, dimensions of 25 mm x 25 mm, with pitch of 0.75 mm. Scan height of 0.25 mm. [2]

Figure 5.18 and Figure 5.19 show the simulated field profile and scanned field profile for the mesh topology. A strong contrast like the meander coil's field profile can be seen, indicating that non-spiral coil topologies lack the positive reinforcement of field between each track. The decreased $H_z$ field strength was also observed, both non-spiral coils generate similar field strengths, and are presented with the same field intensity scale.

By analysing the results obtained from the $H_z$ field profiles, observations can be made that explain why different topologies have different characteristics, especially between spiral and non-spiral coils. The smaller inductance values of the non-spiral coils can be attributed to the opposing polarity of the field generated by neighboring tracks, the mutual inductance coefficient between these neighboring tracks can therefore be considered as negative, reducing the inductance of the coil. The low range of response to coil-ribbon separation is also due to the reduced field strength, caused by opposing current flow direction between neighboring tracks. The inductance of the spiral coil was larger due to the mutual inductance contribution between each neighboring track. The large range of response to coil-ribbon separation of spiral based coils could be due to the cone-like field generated, where a large $H_z$ was generated at a single point, this may aid in sensing the magnetic material at further distances.

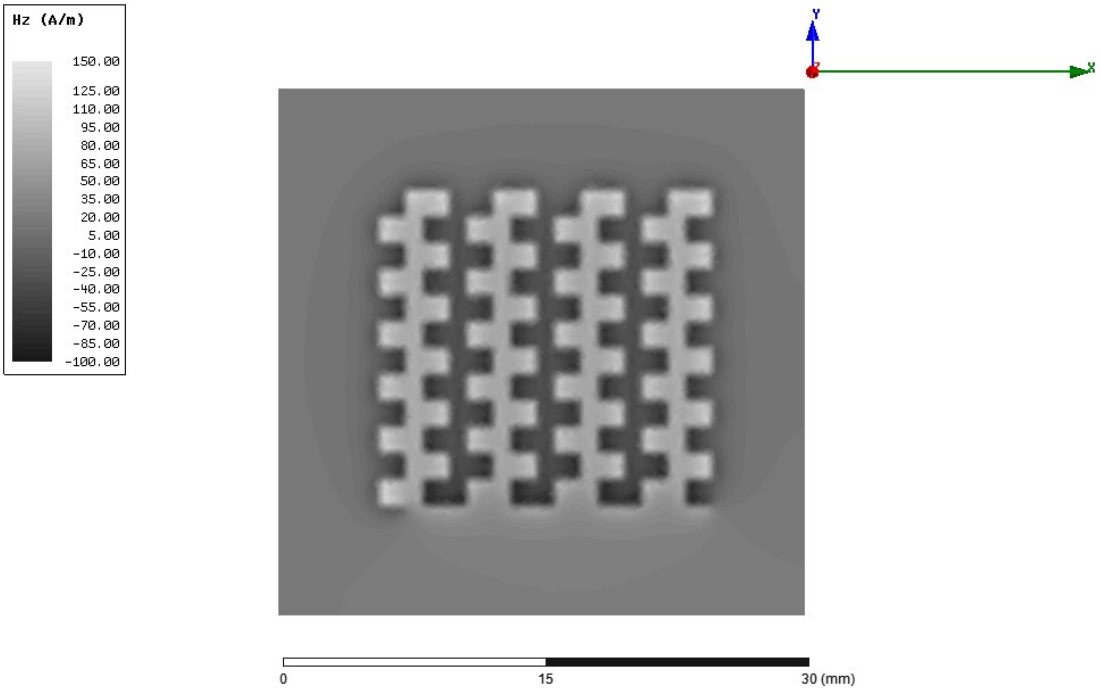


Figure 5.18 – 3D FEM analysis of the $H_z$ component for the mesh topology, with pitch of 0.75 mm. Distance of 0.25 mm from coil surface. [2]

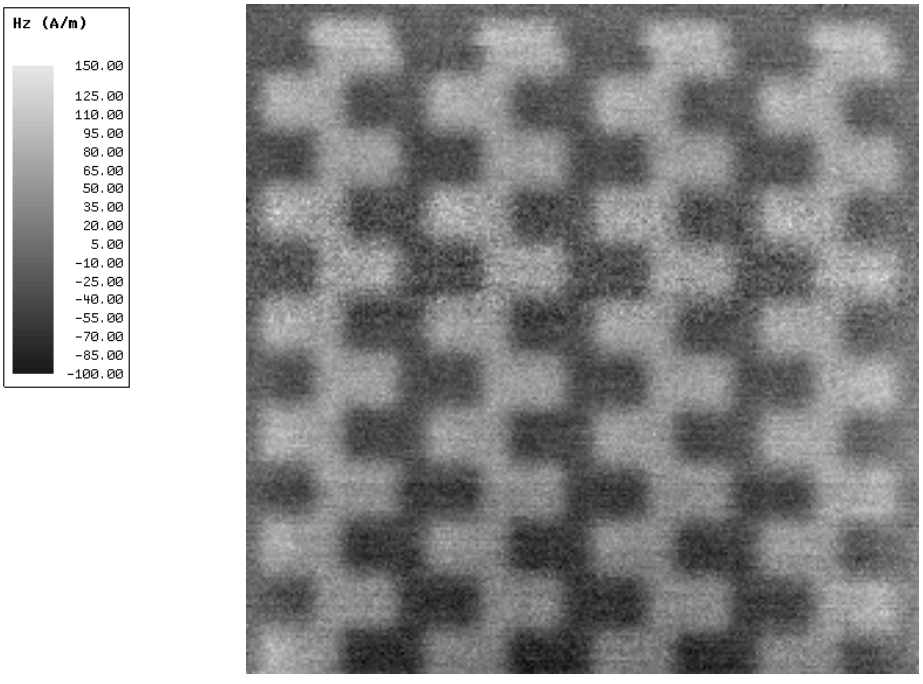


Figure 5.19 – Measured $H_z$ component for the mesh topology, dimensions of 25 mm x 25 mm, with pitch of 0.75 mm. Scan height of 0.25 mm. [2]

### 5.2.3 3D FEM analysis and experimental results of coil-ribbon separation with pitch variation

In this section, 3D FEM analysis of coil topology for various pitch values was compared to the response obtained experimentally for coil-ribbon separation. The FEM has been carried out as an investigation for alternative methods of planar coil design. If a good agreement between the two can be achieved it will be possible to design different planar coils without needing to construct physical prototypes. Error bars have been omitted from the following graphs to increase the clarity of the figures, the standard errors for the frequency range of 30 kHz – 100 kHz shown in Table 5.1 are in good agreement with the standard deviation of the data obtained for this experiment.

The response of the square topology to the displacement of the magnetic ribbon is shown in Figures 5.20 and 5.21 for the FEM model and the experiment respectively. In Figure 5.20 the inductance decreases consistently with the displacement of the ribbon. The square planar coil with the lowest pitch value has the highest inductance, this can be attributed to the increased number of turns. It can also be seen that the rate of change of the inductance was not constant, it decreases with increased displacement, and this indicates that the magnetic field generated by the planar coil which was interacting with the magnetic ribbon does not decrease linearly with displacement.

Figure 5.21 shows the inductance response obtained experimentally. The measured inductance values are slightly larger than the simulated values, and anomalies can be seen for the coils with 0.75 mm pitch and 1.0 mm pitch for small displacements, however the general response of these coils follows the response of the 0.5 mm pitch coil. The anomalies may be due to geometrical misalignment between the coil and the ribbon, i.e. the ribbon was misaligned with respect to the surface of the coil. The coil with 0.5 mm pitch has the best agreement with the simulated response, with a monotonic decrease in inductance with displacement. All coils tested reach an asymptote where the inductance no longer changes with displacement at approximately 10 mm.

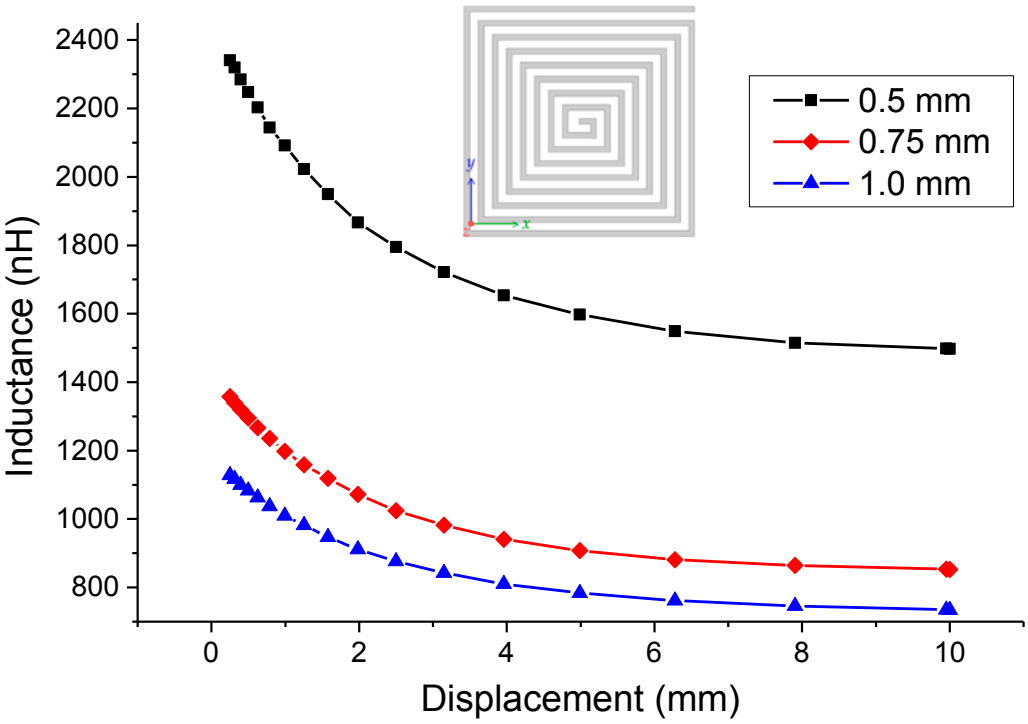


Figure 5.20 – 3D FEM inductance analysis for the square topology, with varying pitch.

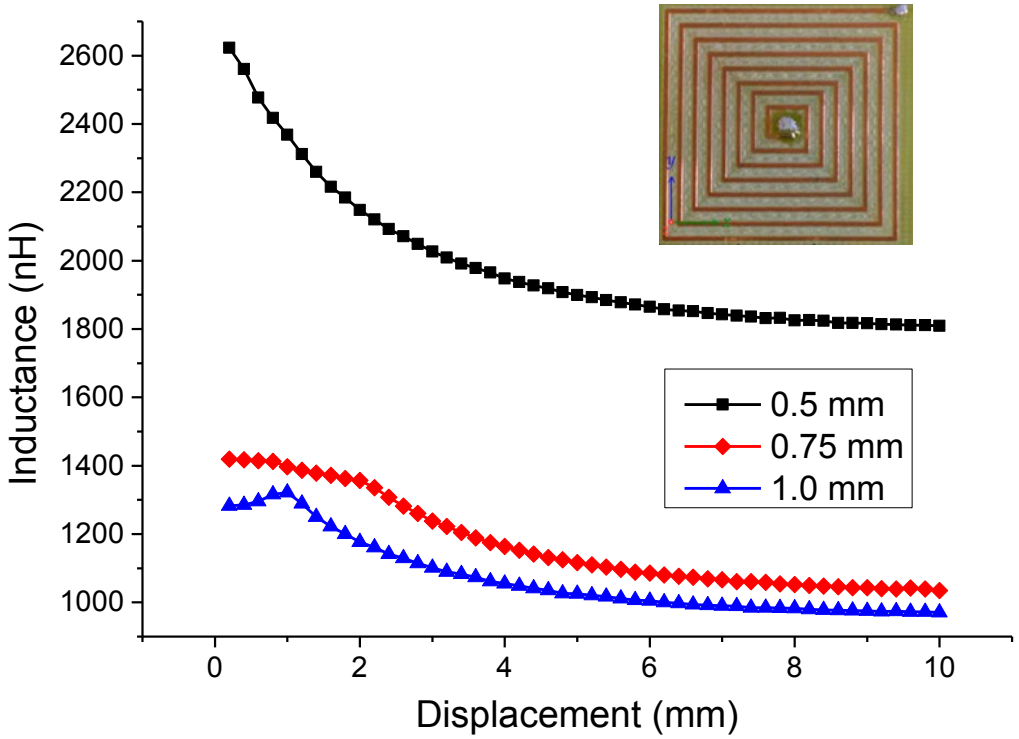


Figure 5.21 – Measured inductance values for the square topology, with varying pitch.

Figure 5.22 and Figure 5.23 show the response of the circular topology for FEM and experiment respectively. It can be seen comparing Figure 5.20 and Figure 5.22 that the square and circular topologies share very similar responses to ribbon displacement, a monotonic decrease with increased displacement, and an asymptote at approximately 10 mm. The circular topologies have smaller inductance values compared with the square planar coils of the same pitch value. The trends seen in the square coil topology is generally representative for the circular coil topology, where the coil with the smallest pitch has the largest inductance value, and an increasing pitch has a negative effect on the inductance for planar spiral coils.

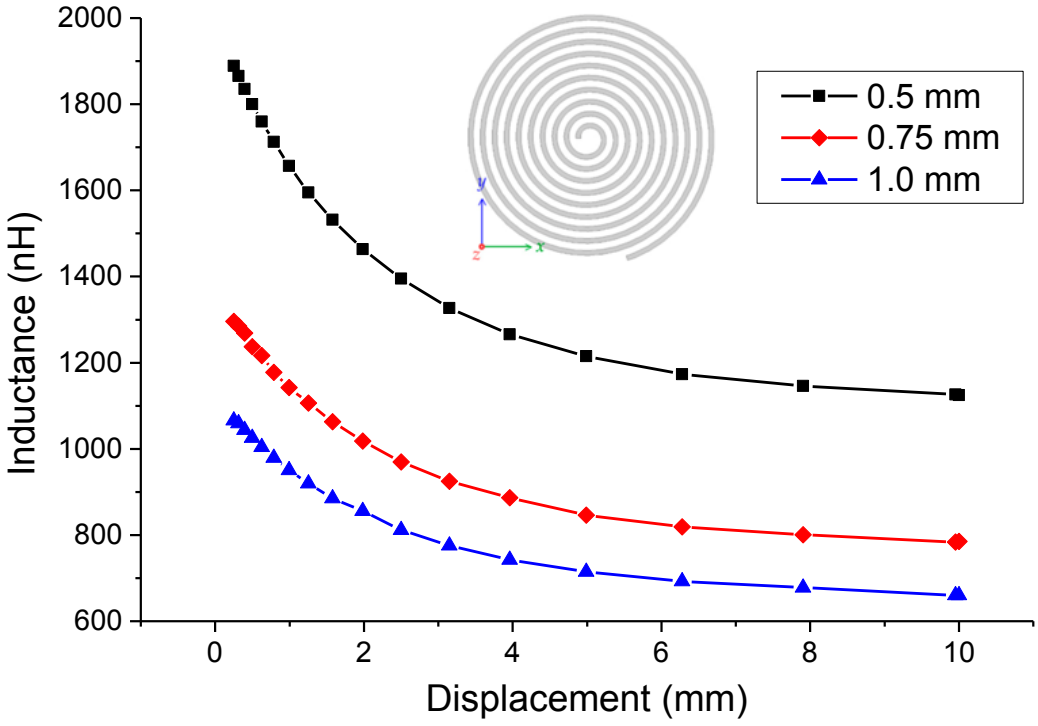


Figure 5.22 – 3D FEM inductance analysis for the circular topology, with varying pitch.

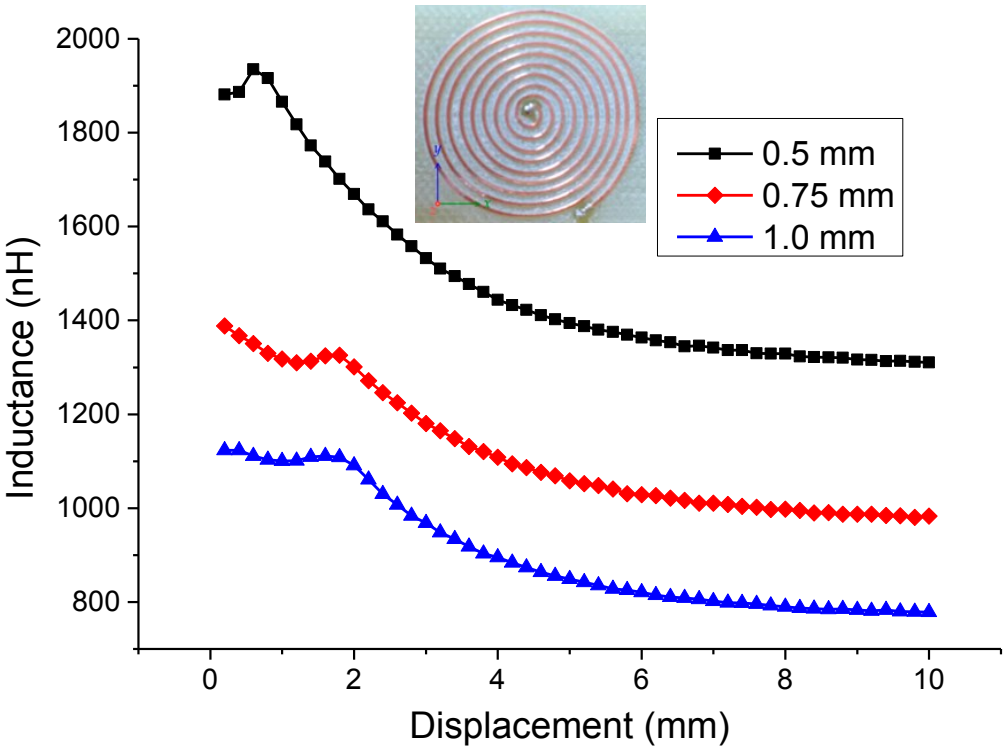


Figure 5.23 – Measured inductance values for the circular topology, with varying pitch.

Figure 5.23 shows the inductance response of the circular topologies obtained experimentally, there are anomalies in the region of small displacements, but overall the trend follows that of Figure 5.22. The anomalies in the region of small displacements (0 mm – 2 mm) are similar to those seen in Figure 5.21, and are possibly due to misalignment between the coil and the magnetic ribbon, or irregularities in the ribbon's surface. The measured inductance were slightly larger than simulated inductance values. It can be seen by comparing Figure 5.21 and Figure 5.23 that the spiral coil topologies share similar characteristics, such as the range of response and the decreasing rate of inductance change against increasing coil-ribbon separation. To analyse the anomalies at regions of small displacements, the experiment was repeated for the circular planar coil with pitch of 0.5 mm, with two samples of ribbon. Both of the ribbons are square, with different lengths. Ribbon sample #1 has side length equal to that of the coil's diameter. Ribbon sample #2 has side length equal to $\frac{1}{\sqrt{2}}$ of the coil's diameter, this was so that this ribbon sample will 'fit' within the coil.

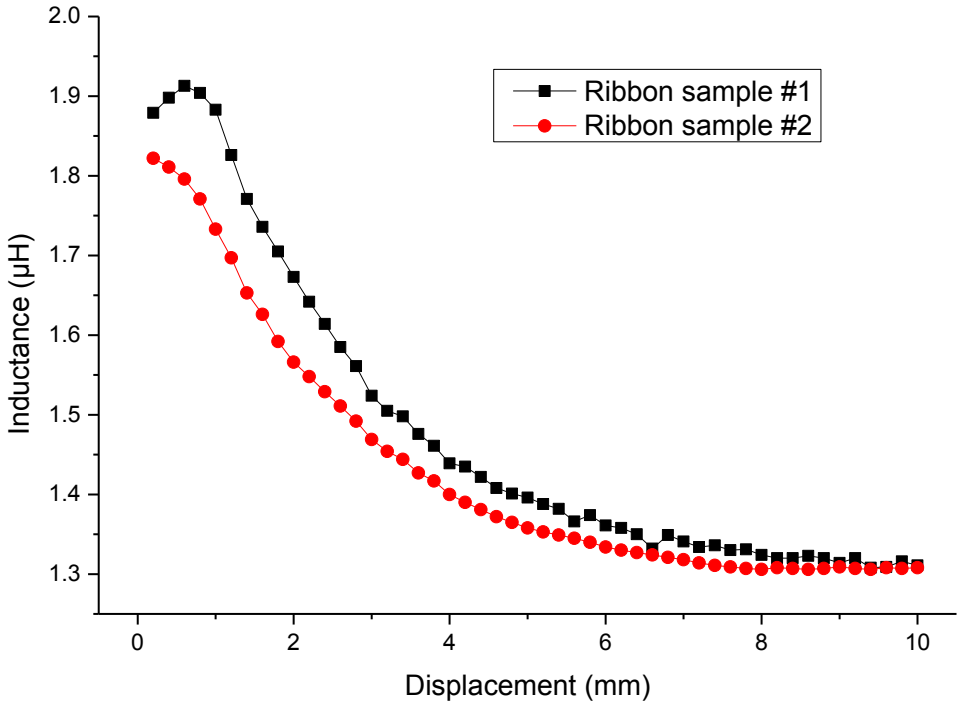


Figure 5.24 – Inductance response between ribbon samples of different sizes, for circular coil with pitch of 0.5 mm.

Figure 5.24 shows the inductance response obtained for both ribbon samples tested. The figure shows that for ribbon sample #1 the anomaly at small displacements was still present, however by decreasing the size of the ribbon sample the anomaly has been eliminated. The inductance response for ribbon sample #2 has a reduced inductance magnitude, and a reduced response range of approximately 7 mm. Figure 5.24 shows that the anomalies seen in Figure 5.23 may be attributed to a geometrical dependency between the coil and the ribbon, this may also be used to explain anomalies seen in Figure 5.20.

Figure 5.25 shows the inductance response of the meander topologies obtained in the 3D FEM simulation, and Figure 5.26 the experimentally obtained characteristics for the meander topologies. It can be seen in Figure 5.25 that the pitch value has a similar effect as it did on the spiral coil topologies, whereby increasing the pitch value the inductance of the coil decreases. It also shows that the meander coil has an effective response range of approximately 2 mm, as opposed to the spiral coils' response range of approximately 10 mm.

In Figure 5.26 the coil with the lowest pitch value has the highest measured inductance value. However, the inductance response shows that although the coil with the lowest pitch value has the highest inductance value, the inductance change measured was not the largest. The coils with 0.75 mm and 1.0 mm both have a larger inductance change compared to that observed in the 0.5 mm coil. This is in contrast with the spiral coil topologies' response, which indicate that the lower the pitch value the higher the inductance value and inductance change for an increased separation displacement between the ribbon and the coil.

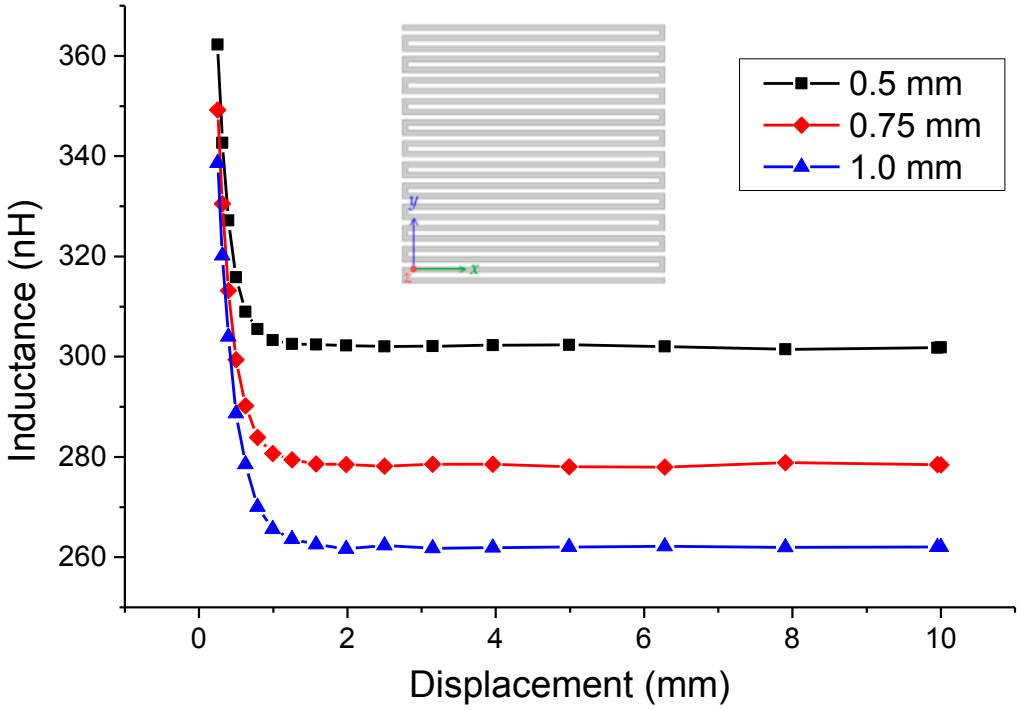


Figure 5.25 – 3D FEM inductance analysis for the meander topology, with varying pitch values.

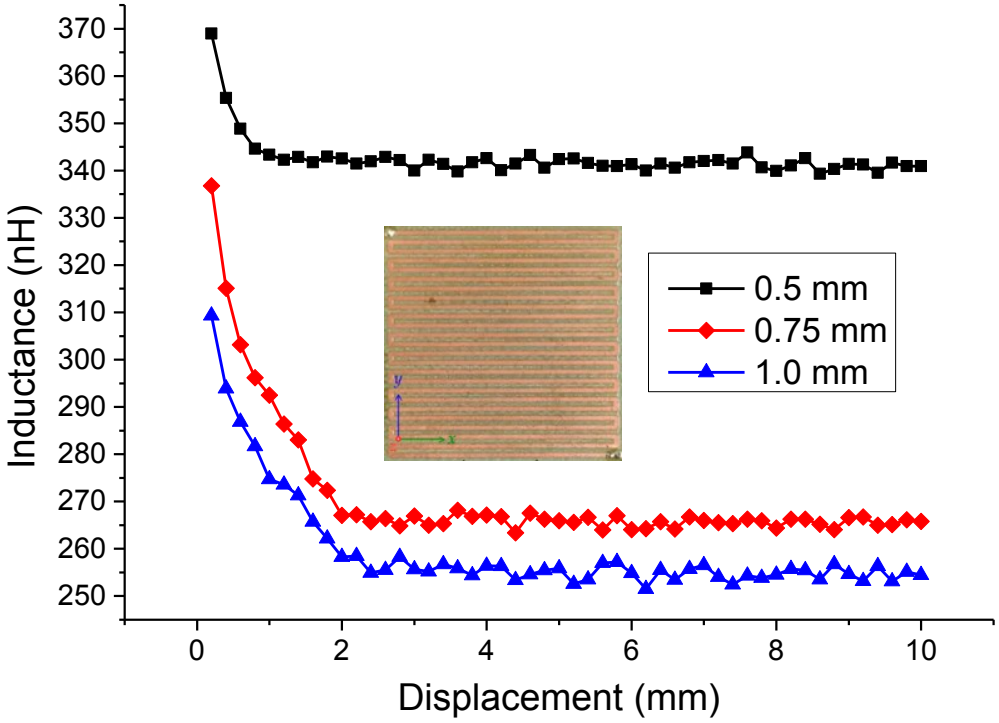


Figure 5.26 – Measured inductance values for the meander topology, with varying pitch.

Figure 5.27 and Figure 5.28 show the response obtained for the mesh topology through 3D FEM and experimental means respectively. Figure 5.27 shows that the mesh coil shows a similar response range to that of the meander coil. Figure 5.28 is in good agreement with Figure 5.27, with a response range of approximately 2 mm. The measured inductance response was generally in good agreement with the simulated response, however the 3.5 mm coil does not have the largest inductance change.

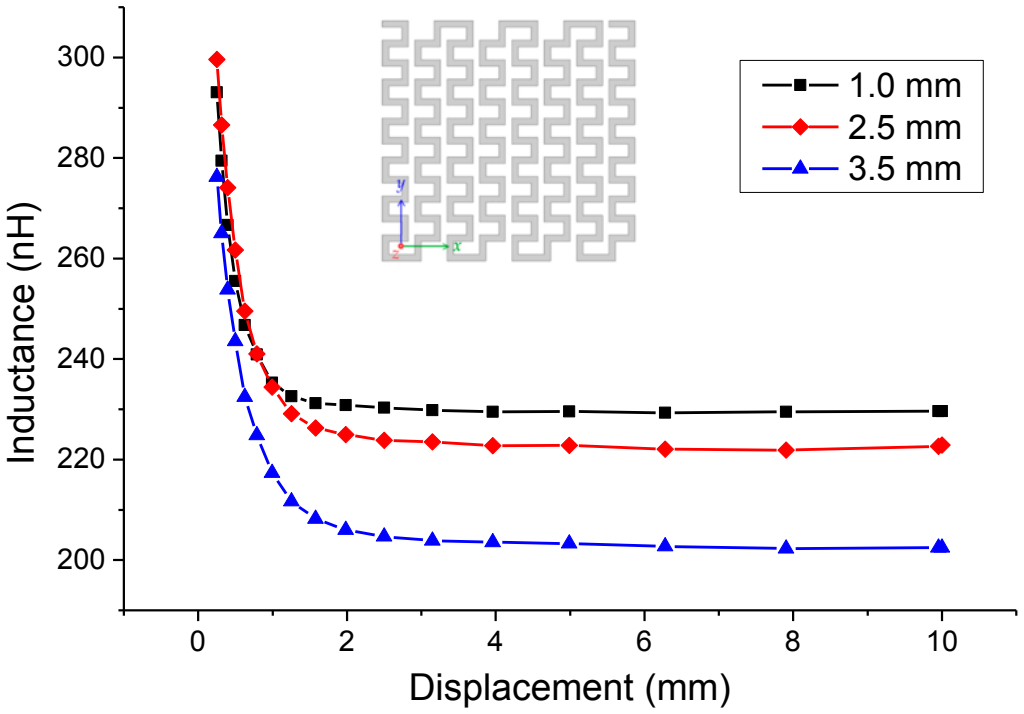


Figure 5.27 – 3D FEM inductance analysis for the mesh topology, with varying pitch values.

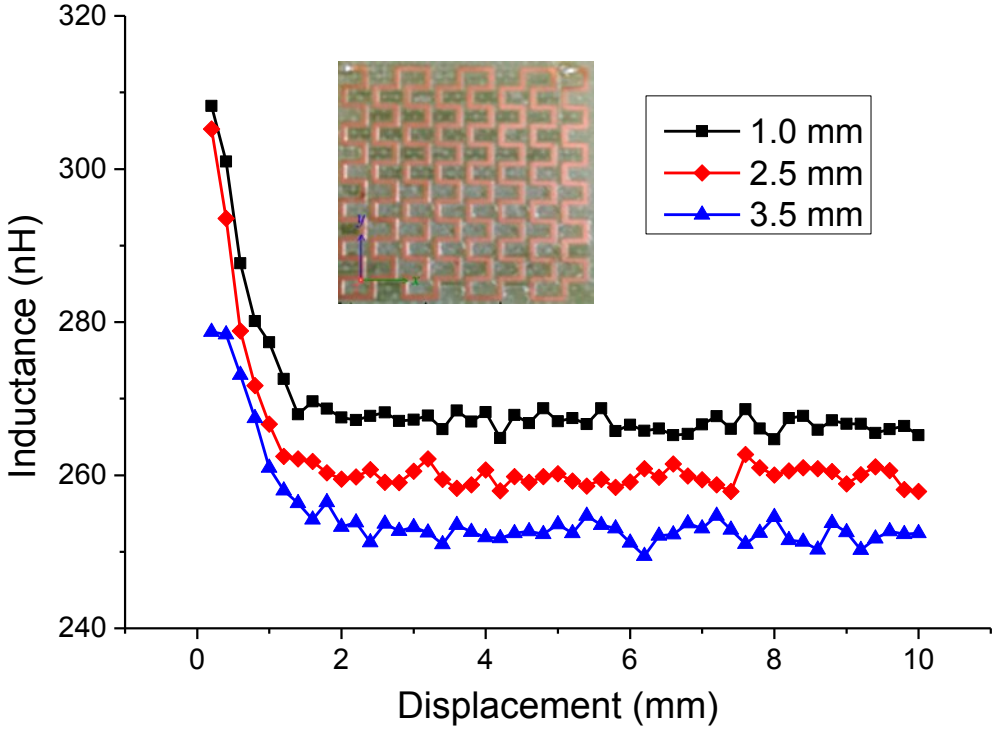


Figure 5.28 – Measured inductance values for the mesh topology, with varying pitch.

The trends seen in the FEM data deviate within a range of 10% of the experimental findings. The maximum change in inductance observed in both simulated and measured inductance responses have been calculated and are shown in Table 5.2. The largest inductance change observed was in the square coil topology, followed by the circular coil. In general, the inductance change observed in the 3D FEM are in good agreement with the inductance changes observed experimentally. The FEM has positively identified trends caused by varying pitch values for all topologies tested. This indicates that FEM may be used in designing planar coil sensors which operate through magnetic induction means with a soft magnetic material.

Table 5.2. Maximum change in inductance due to displacement, observed for each planar coil.

| Topology | *Pitch (mm)* | *Maximum change in inductance observed in simulation (μH)* | *Maximum change in inductance observed experimentally (μH)* |
|---|---|---|---|
| Square Coil | 0.5 | 0.844 | 0.813 |
| | 0.75 | 0.504 | 0.385 |
| | 1.0 | 0.394 | 0.352 |
| Circular Coil | 0.5 | 0.765 | 0.625 |
| | 0.75 | 0.511 | 0.405 |
| | 1.0 | 0.406 | 0.345 |
| Meander Coil | 0.5 | 0.061 | 0.028 |
| | 0.75 | 0.071 | 0.071 |
| | 1.0 | 0.064 | 0.055 |
| Mesh Coil | 1.0 | 0.064 | 0.043 |
| | 2.5 | 0.071 | 0.047 |
| | 3.5 | 0.074 | 0.027 |

The spiral coil topologies have demonstrated the largest inductance values and the biggest change in inductance. The non-spiral topologies have very small inductance values and do not change much.

Due to the nonlinear nature of the inductance response, the sensitivity is difficult to quantify by conventional linear fitting. Through non-linear fitting an exponential decay function was found to be the best fit for the inductance traces, the exponential decay function is described as

$$y = R \cdot e^{-\frac{x}{\tau}} + y_0 \tag{5-1}$$

In this equation R and $y_0$ represent constants. The exponential time constant, $\tau$, describes the properties of the decay function, focusing on how rapid the decay takes place. A small $\tau$ value indicates that the decay will occur rapidly, with most of the inductance change occurring over a small initial displacement range, and vice versa for a large $\tau$ value. The exponential decay fit was applied for each inductance response obtained experimentally, and the equation generated for each trace was differentiated to obtain the gradient. The sensitivity to coil-ribbon separation of each coil is its rate of inductance change, which was plotted over the span of observed displacement.

Figure 5.29 and Figure 5.30 show the rate of inductance change for the spiral coil topologies. For both topologies the highest sensitivity was observed in the smallest pitch value tested, of 0.5 mm. In Figure 5.29, it can be seen that the sensitivity for the coil with a pitch value of 0.75 mm was comparable to that of the coil with pitch value of 1.0 mm; this was also seen in Figure 5.30. The response range of all spiral coil topologies tested are comparable, at approximately 10 mm.

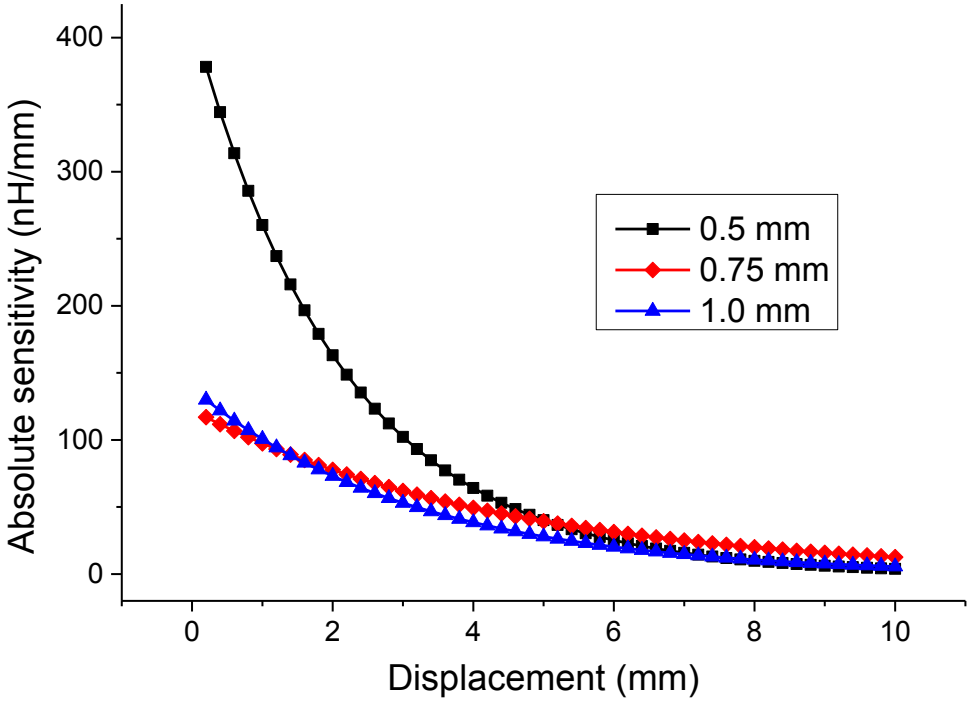


Figure 5.29 – Rate of inductance change for the square coil topology, with varying pitch.

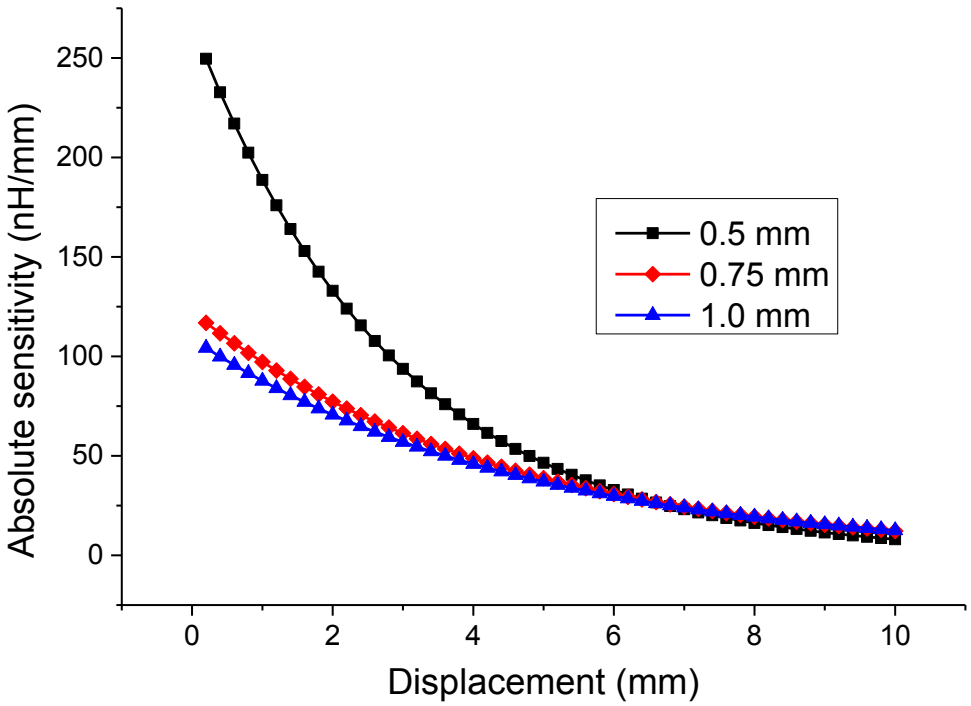


Figure 5.30 – Rate of inductance change for the circular coil topology, with varying pitch.

Figure 5.31 and Figure 5.32 show the rate of inductance change for the meander coil and mesh coil topologies respectively. Figure 5.31 shows that the meander coil with the smallest pitch value of 0.5 mm did not possess the greatest sensitivity to ribbon displacement. The largest sensitivity was observed in the coil with pitch of 0.75 mm pitch. The response range of the coil with a pitch of 0.5 mm was also the smallest, compared with the other two meander coils tested. The coils with pitch of 0.75 mm and 1.0 mm exhibit similar response ranges. Figure 5.32 shows that the response range of all mesh coils tested are similar. It can be seen that the maximum sensitivity was observed in the mesh coil with a pitch of 2.5 mm, not 1.0 mm, this is similar to the meander coil, where the coil with the smallest pitch didn't have the largest sensitivity.

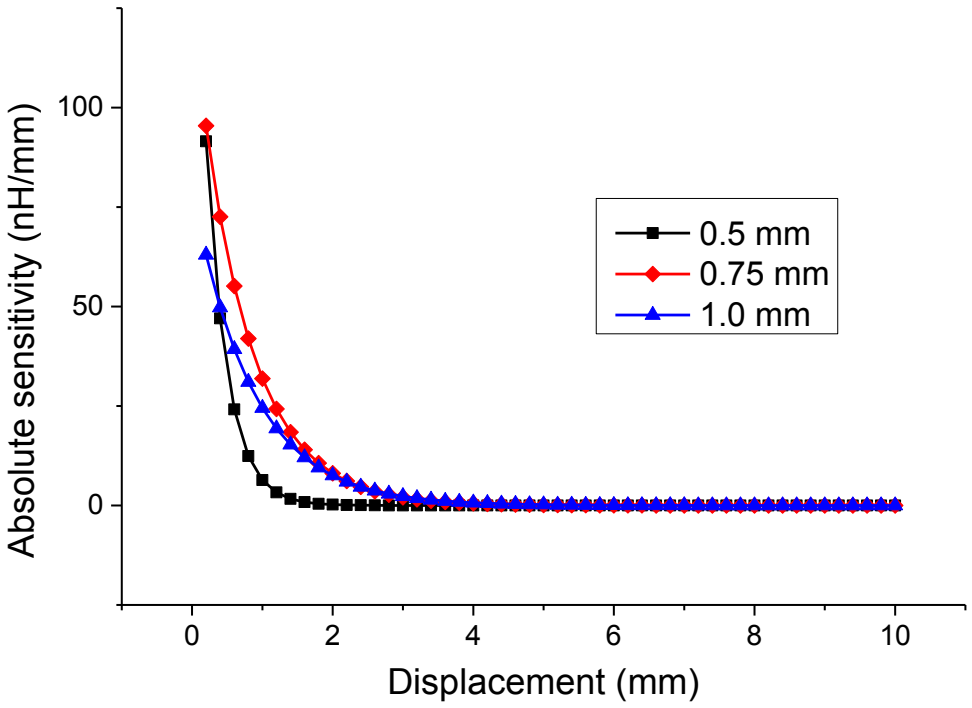


Figure 5.31 – Rate of inductance change for the meander coil topology, with varying pitch.

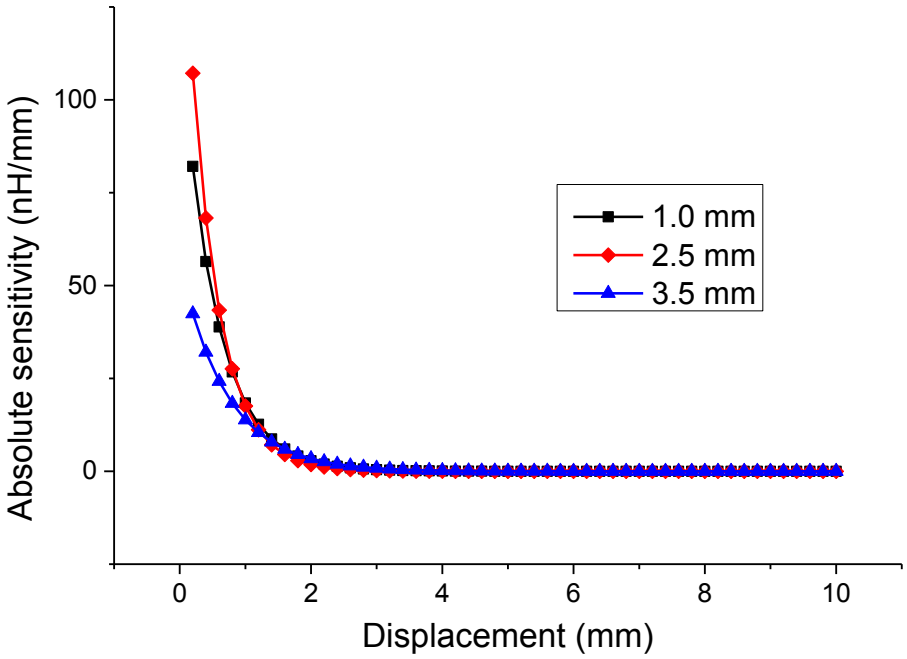


Figure 5.32 – Rate of inductance change for the mesh coil topology, with varying pitch.

Further analysis regarding the sensitivity response was carried out for the topologies, through normalising the change in sensitivity for the reported topologies. In the following figures an additional inset was included which focuses on small displacements up to 2 mm. This is due to the response range of the non-spiral topologies being smaller, and should provide a comprehensive comparison between the different coils for different sensing requirements.

Figure 5.33 and Figure 5.34 show the normalised rate of inductance change for the square coil topology and the circular coil topology respectively. Figure 5.33 shows that the coil with the smallest pitch had the largest change in sensitivity. In the inset of Figure 5.33, it can be seen that at 2 mm of displacement the sensitivity has changed by a large percentage of the initial value, especially for the coil with a pitch value of 0.5 mm. The square coil with pitch value of 0.75 mm has the most gradual decrease in sensitivity. Figure 5.34 shows that the circular coil topology exhibits similar responses, with the coil with pitch of 0.5 mm having the largest change in sensitivity. It can be seen in Figure 5.34 that the change in sensitivity is very similar for the coils with pitch of 0.75 mm and 1.0 mm. Figure 5.33 and Figure 5.34 show that the pitch affects the rate of sensitivity change differently for the two spiral topologies.

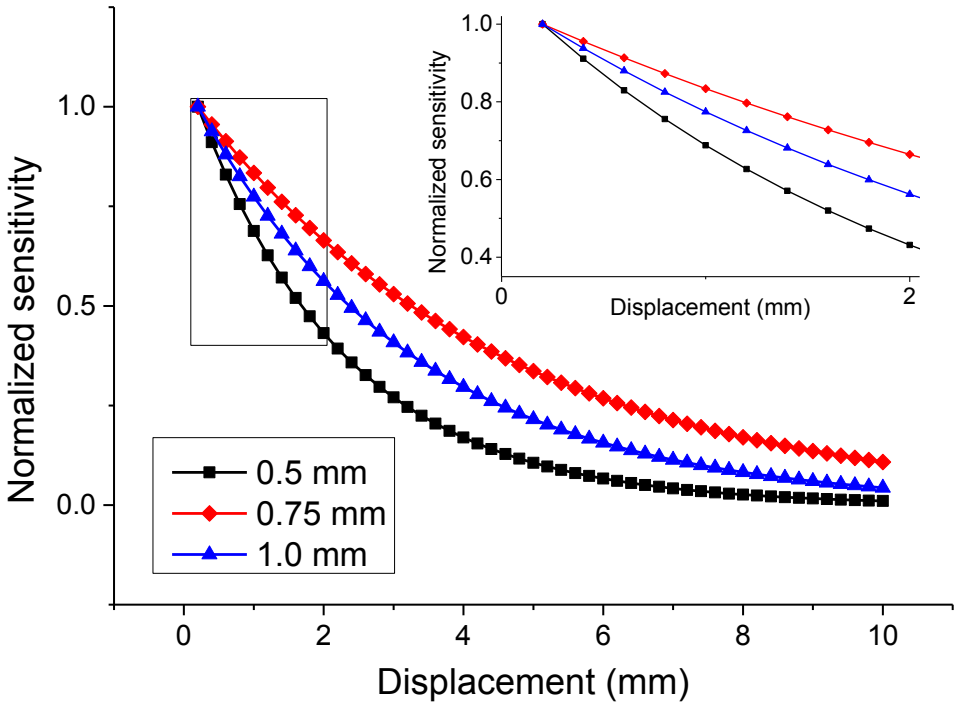


Figure 5.33 – Normalised sensitivity for the square coil topology, with varying pitch.

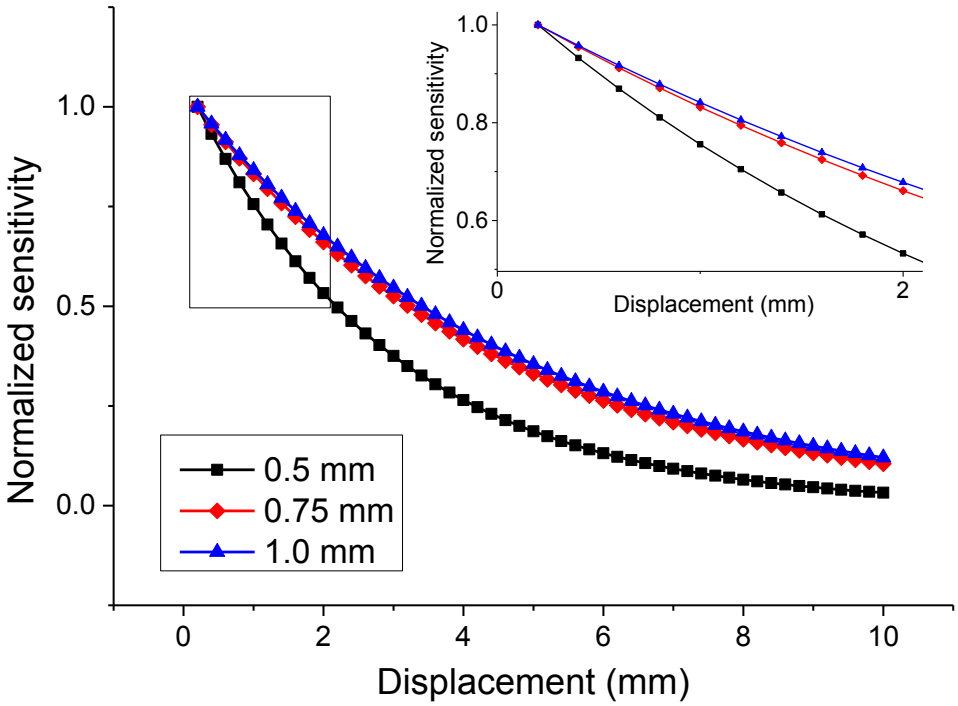


Figure 5.34 – Normalised sensitivity for the circular coil topology, with varying pitch.

Figure 5.35 and Figure 5.36 show the normalised sensitivity for the non-spiral coil topologies of the meander coil and the mesh coil respectively. Figure 5.35 shows that the change in sensitivity of the coil with the smallest pitch of 0.5 mm was the largest. The inset of Figure 5.35 shows that the sensitivity change over 2 mm of displacement is significant for all pitch values examined. Figure 5.36 shows that the change in sensitivity of all three mesh topologies tested is similarly drastic. The inset shows that the sensitivity change is near 0 for all mesh coils at approximately 2 mm of displacement. By comparing these normalised sensitivity responses, the spiral coil topologies are shown to have a more gradual decrease in sensitivity, the responses also appear quite linear over a small range, as shown in the insets of Figure 5.33 and Figure 5.34.

In general, the largest inductance was observed in the coil with the smallest pitch, along with the largest sensitivity, however by normalising the sensitivity it can be seen that the change in sensitivity rapidly decreases for the smallest pitch of all topologies. This is an important aspect to consider, as the intended operating environment may be more suitable for a particular topology.

For an AD sensor intended for a wearable sensor, external influences within 10 mm of displacement is not a large area for concern, therefore a spiral coil should be used, for its preferable inductance properties.

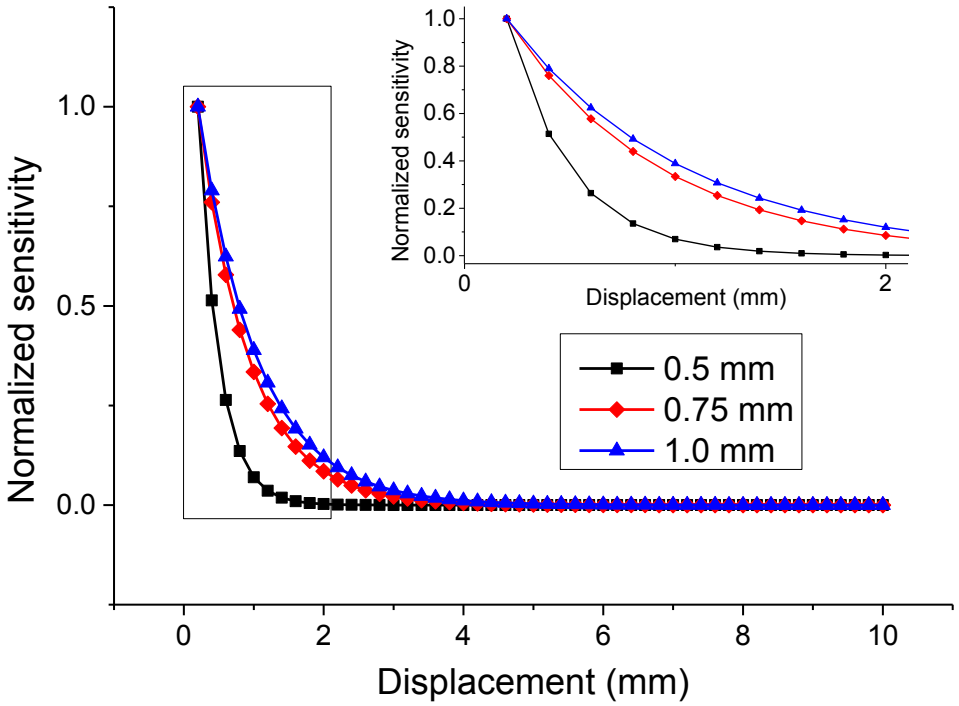


Figure 5.35 – Normalised sensitivity for the meander coil topology, with varying pitch.

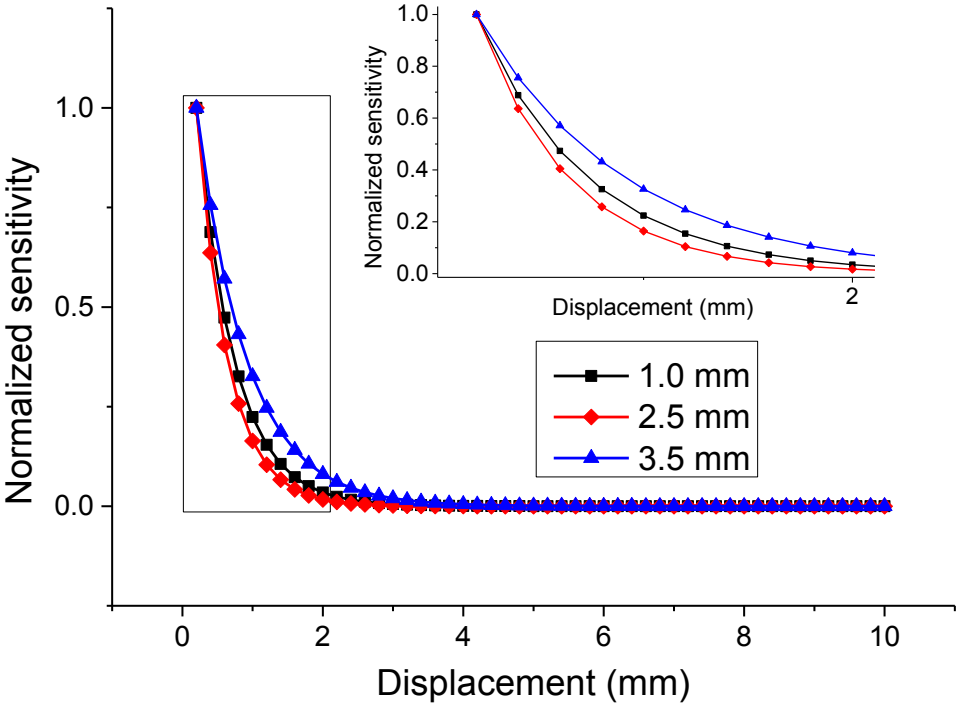


Figure 5.36 – Normalised sensitivity for the mesh coil topology, with varying pitch.

These results indicate that for designing an AD sensor, the coil-ribbon separation is an important aspect, and should be kept minimal, as magnetic induction between the coil and the ribbon weakens with increased displacement. A smaller pitch value increases the copper track density and increases the number of turns, which in turn increases the inductance of the coil hugely. In general, a 10 mm displacement is not significant for an AD sensor, and interference from neighboring sensors or other soft magnetic materials is unlikely. In this investigation the properties of different topologies have been presented. The non-spiral topologies have a very small response range with an extremely sharp inductance response, a smaller inductance value, and a lower sensitivity. The spiral coil alternatives have a much larger sensing range, inductance value, and sensitivity. Those are the general considerations when deciding what topology to use.

An AD sensor design was considered, which relied on a bend induced displacement of the ribbon from the coil, however this design was abandoned due to the significant displacements required, which would have been detrimental to the small size profile of the sensor, an important aspect of this work.

The interaction between the planar coil and the displaced ribbon indicate that the planar coil can also be employed as a displacement sensor. The work indicates that for such an application the square coil will be the most suitable topology. Planar coil displacement sensors have been proposed, using many principles, however many are designed for displacement sensing along the surface of the sensor [3-6]. An array of square planar coils have been demonstrated to operate by sensing a movable U-shaped magnetic core, however the movable core moves only along the surface [3, 4]. Another method of displacement sensing relies on mutual inductance measurements between two coils [5, 6]. This work reports on various planar coils with different pitch values, responding to displacements of ferromagnetic ribbon material perpendicular to the surface of the sensor. 3D FEM have previously been conducted for the interaction between planar coil and a soft magnetic material along the surface of the planar coil [7]. It was reported that the square coil and circular coil exhibited superior responses, however the meander topology also exhibited comparable results at higher turn numbers. By considering these findings with the findings reported in this study, the square spiral coil can be considered as the best design for a planar coil displacement sensor, in general.

## 5.3 Summary

An investigation into the characteristics of different topologies has been conducted, along with an investigation of coil-ribbon separation, for varying pitch values of each topology. The coils, two based on a spiral topology, and two based on a non-spiral topology, were simulated using 3D FEM software and experimentally tested. The inductance response for coil-ribbon separation indicate a good agreement between the results obtained from the 3D FEM software and experimentally. The spiral coils showed a larger range of response to the ribbon, they also exhibited larger inductance values than the non-spiral coils.

By analysing the $H_z$ component through 3D FEM and TMR scanning it was possible to observe the field profiles generated by different topologies, to better understand why the topologies varied so much in inductance value and their range of response. It was seen that the spiral coils, with identical current flow direction between neighboring tracks, generated larger fields and had superior operating ranges. In the non-spiral coils, the current flow was opposite between neighboring tracks, this results in regions of opposite polarity, shown by the greater contrast in the grayscale images. This also resulted in a general decreased field strength over the coil.

The investigation of pitch also showed that for the highest inductance value a spiral coil topology should be considered with the smallest pitch value. It appears that a small pitch value contributes to superior sensitivity and response range for planar coils in general.

The work has shown that external interference is unlikely to occur for the proposed AD sensor, due to the small range at which the planar coil no longer interacts with the ribbon. The topology used for the AD sensor design will be dependent on its performance in stress sensing, and inductance properties.

## 5.4 References for Chapter 5

[1] Agilent Technologies. (2003). *Agilent 4294A Precision Impedance Analyzer Data Sheet*. USA: Agilent Technologies.

[2] Gibbs, R., Moreton, G., Meydan, T. and Williams, P. (2018). Comparison between Modelled and Measured Magnetic Field Scans of Different Planar Coil Topologies for Stress Sensor Applications. Sensors, 18(4), p.931.

[3] Lin, C. and Kalkur, T. (2009). Modeling of current crowding for on-chip multi turn differential -spiral inductors. *In the proceedings of IEEE EUROCON 2009*, pp.178-182.

[4] Babu, A. and George, B. (2017). Design and Development of a New Non-Contact Inductive Displacement Sensor. *IEEE Sensors Journal*, pp.976-984.

[5] Djuric, S. (2014). Performance Analysis of a Planar Displacement Sensor With Inductive Spiral Coils. *IEEE Transactions on Magnetics*, 50(4), pp.1-4.

[6] Djuric, S., Nad, L., Biberdzic, B., Damnjanovic, M. and Zivanov, L. (2008). Planar inductive sensor for small displacement. *In the proceedings of the 2008 26th International Conference on Microelectronics*, pp.11-14.

[7] Misron, N., Ying, L., Firdaus, R., Abdullah, N., Mailah, N. and Wakiwaka, H. (2011). Effect of Inductive Coil Shape on Sensing Performance of Linear Displacement Sensor Using Thin Inductive Coil and Pattern Guide. *Sensors*, 11(12), pp.10522-10533.

# Chapter 6. Investigation of Planar Coil Topology for Stress Sensing Applications

## 6.1 Introduction

The interaction between planar coils and a changing permeability of the magnetic component is crucial for the design and development of planar coil based sensors which couple with a magnetic material. This investigation aims to look at how different planar coil topologies with various pitches respond to a change in permeability induced through stressing a highly magnetostrictive material. The planar coils reported in Chapter 5 are used in this study.

The outcome of this investigation will aid in the designing of an angular displacement sensor which relies on detecting stress induced variations in the permeability of the magnetic component. The optimal topology and pitch for the sensing of applied vertical stress will be determined, and will be the basis of the development of the AD sensor. Modelling was not used for this investigation, as ANSYS cannot perform such simulations involving the inverse magnetostrictive effect adequately. The modelling of this phenomenon in a sensing application was beyond the scope of this work.

## 6.2 Experimental Results and Discussion

### 6.2.1 Inductance response of the wound coil against tensile stress

A wound coil was characterised for comparison with the planar coils investigated, as a wound coil's response to a ribbon undergoing the Villari effect is well known. The inductance response of the wound coil is shown in Figures 6.1 and 6.2. Figure 6.1 shows the inductance response of the wound coil without a magnetic ribbon core, and Figure 6.2 shows the inductance response of the wound coil against stress applied to the magnetic ribbon. In Figure 6.2 only two data traces are displayed, the trace at the minimum stress applied to the magnetic ribbon core and the maximum amount of stress applied, for improved clarity of the data. It can be seen that the wound coils exhibit larger inductance values compared to the planar coils discussed in Chapter 5. It can also be seen that the frequency has a large effect on the inductance value of the wound coil, with an overall change of approximately 4.5 μH seen in Figure 6.1.

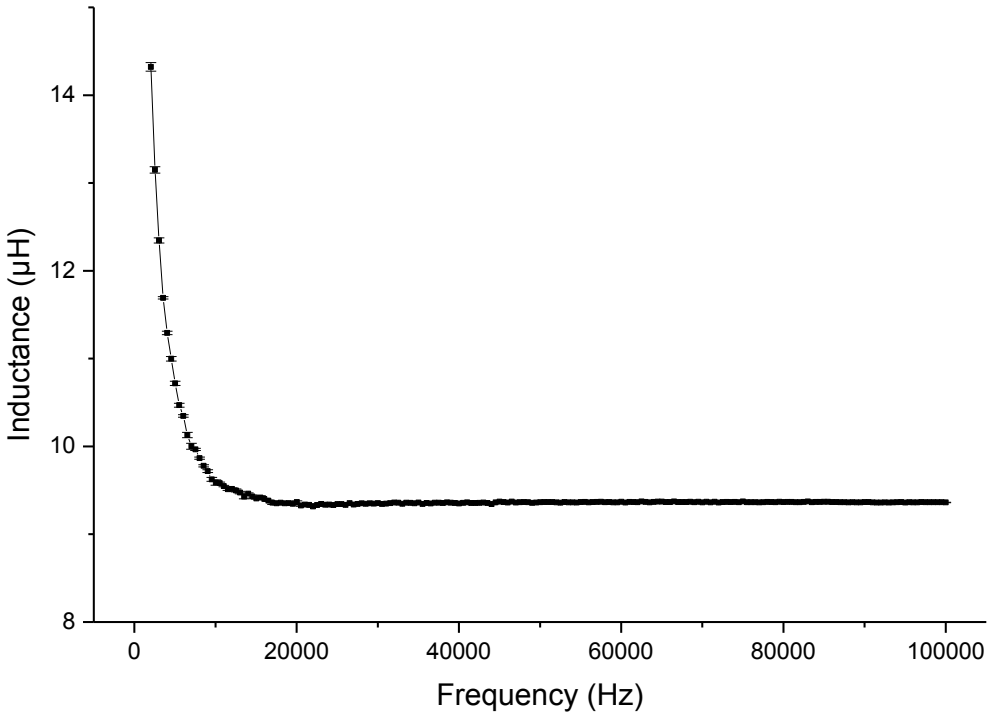


Figure 6.1 – Inductance response over the full span of observed frequencies for the wound coil without a magnetic ribbon core.

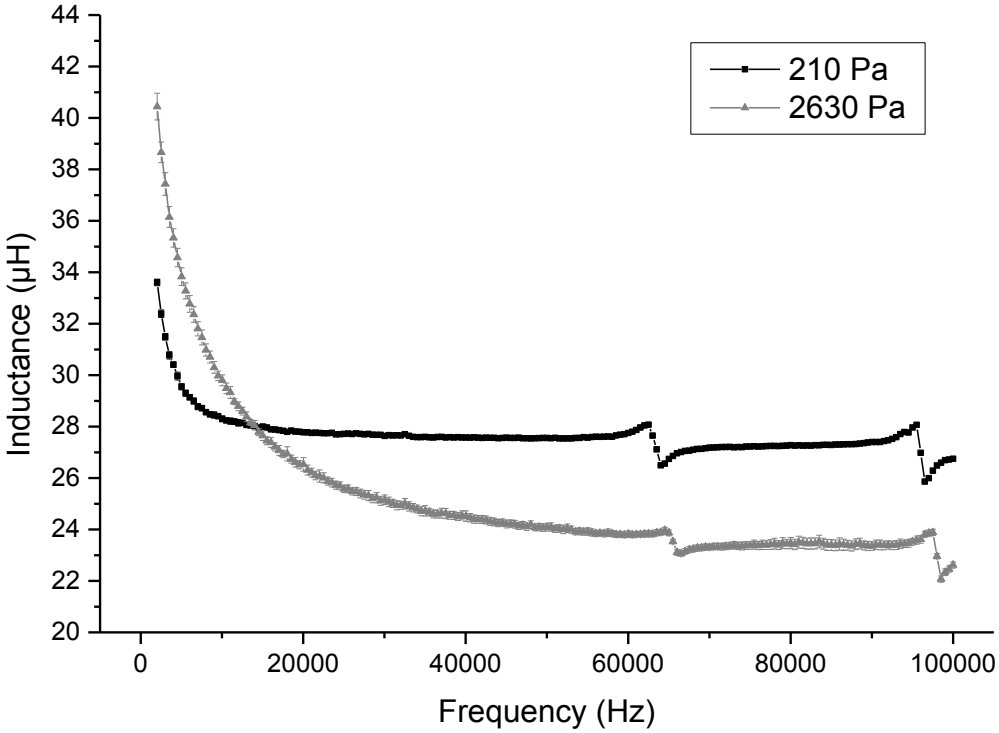


Figure 6.2 – Inductance response over the full span of observed frequencies for the wound coil with a magnetic ribbon core.

Figure 6.2 shows the inductance response of the wound coil with a magnetic ribbon core added under stresses of 210 Pa and 2630 Pa. Comparing the inductance of the 210 Pa trace with Figure 6.1, the inductance has increased due to the introduction of the magnetic ribbon. There are a couple of anomalies where the inductance fluctuates, at ~60 kHz and ~95 kHz, present in both the stressed and unstressed inductance response. These signatures are not present in Figure 6.1; therefore, it indicates that these anomalies have been caused by the introduction of the magnetic ribbon core. A possible explanation for this phenomenon could be the magnetoelastic resonance modes of the magnetic ribbon core; Metglas ribbon has been reported of having a freely oscillating magnetoelastic resonance at ~60 kHz, however this was dependent on the dimensions of the sample tested [1-2]. By comparing the two traces the fluctuations of inductance have shifted to higher frequencies through stressing of the ribbon.

By comparing both traces of Figure 6.2 the effects of tensile stress applied to the ribbon was seen to be frequency dependent, as the inductance of the 2630 Pa trace was seen to be larger and smaller than that of the 210 Pa trace, depending on the frequency. It was seen that in a lower frequency range (less than 17 kHz) the inductance is increased due to applied tensile stress, however in frequencies above this the inductance was seen to decrease due to applied tensile stress. This implies that the permeability change caused by stressing the ribbon is frequency dependent, and therefore so is the inductance response of the wound coil under stressed ribbon conditions.

In Figure 6.1 the inductance difference due to frequency was approximately one-third of the peak inductance value, seen at the lower frequencies. In Figure 6.2 the inductance difference over frequency differs greatly depending on whether the magnetic ribbon was under stress or not. If little stress was applied, the inductance change was approximately 6 μH, not considering the two anomalies, which was approximately 15% of the peak inductance value. Should further tensile stresses be applied, this difference in inductance increases greatly. Given an applied tensile stress of 2630 Pa to the magnetic ribbon, the inductance changes by approximately 18 μH, approximately 40% of the peak inductance value.

### 6.2.2 Inductance response of planar coils against tensile stress

The following figures are organised into two formats, the first set of graphs show the inductance response for each of the four topologies tested, however only the smallest pitch tested has been displayed in this section. The figures plotted with data obtained for the other pitches are included in Appendix B. The next set of graphs show the inductance response for each of the four topologies, with the whole span of applied stresses in their loading and unloading cycles. The latter set of graphs presents data obtained for all pitch values for each topology respectively.

Figure 6.3 shows the inductance response for the square planar coil against applied stresses of 210 Pa and 2630 Pa. Unlike the wound coil, there was minimal frequency dependency of the inductance response, and there are no anomalies where the inductance fluctuates. The stress induced inductance change was negative with a constant offset over the frequency range of 20 kHz – 100 kHz, unlike the wound coil where the inductance curves feature a cross-over point at approximately 14.5 kHz. The inductance of the planar coil was smaller, approximately 200 nH, this difference in inductance is approximately 8% of the inductance value at 210 Pa.

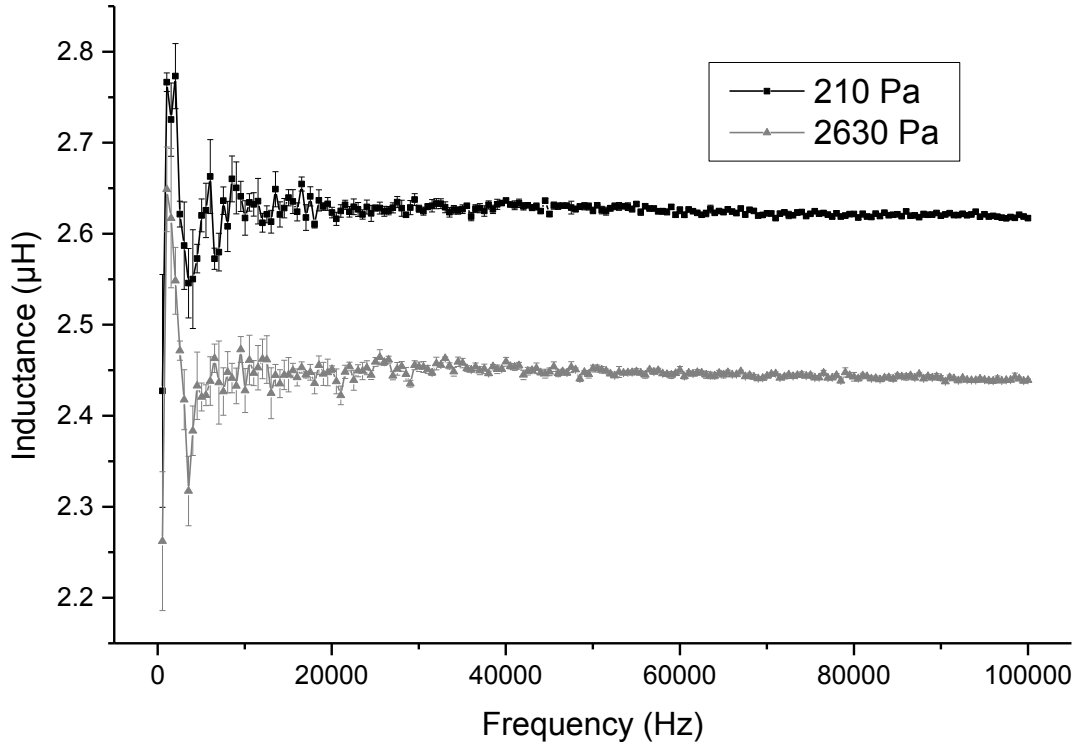


Figure 6.3 – Inductance response over the full span of observed frequencies for square topology with pitch of 0.5 mm.

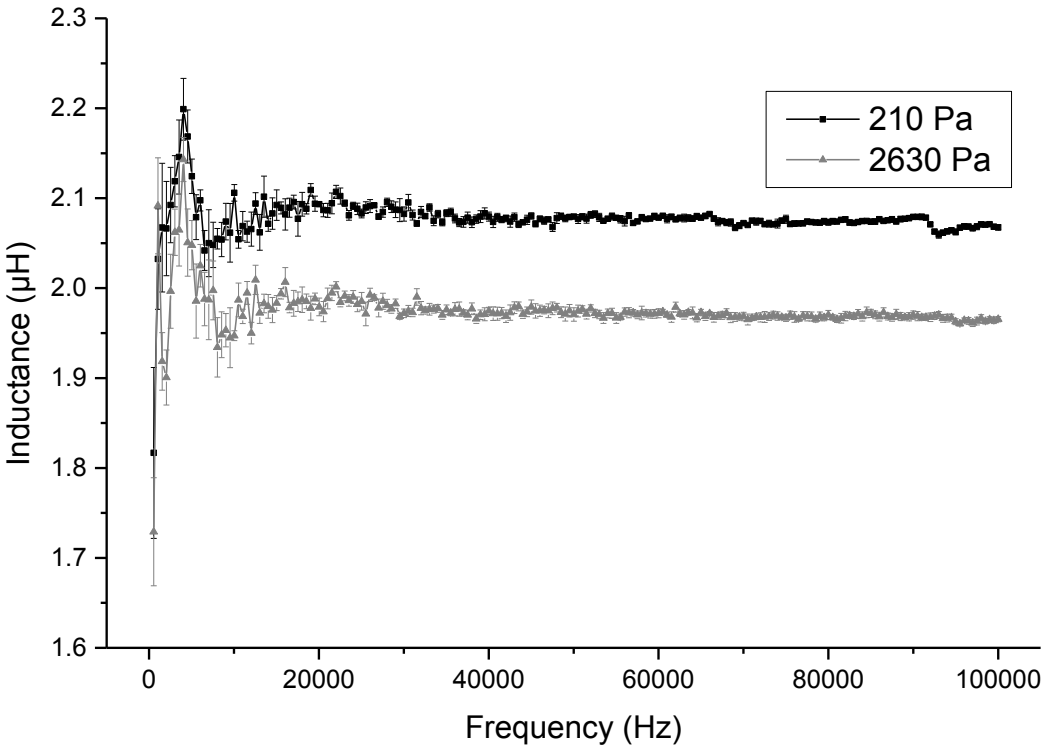


Figure 6.4 – Inductance response over the full span of observed frequencies for circular topology with pitch of 0.5 mm.

Figure 6.4 shows the inductance response for the circular planar coil against applied stresses. The response was similar to that of the square planar coil, with a frequency independent response and a constant inductance difference between the two stress plots over the frequency range of 20 kHz – 100 kHz. The inductance change was approximately 150 nH, which is approximately 7% of the inductance value at 210 Pa. By comparing the two topologies the square coil topology was better suited for tensile stress testing, due to the more stable frequency response, and a larger inductance change.

Figure 6.5 and Figure 6.6 show the inductance response for the meander coil and the mesh coil, respectively. It can be seen in Figure 6.5 that the inductance change was very small, compared to the spiral planar coils. For this meander coil the inductance change was approximately 50 nH, which is 10% of its inductance value at 210 Pa. The inductance response exhibits frequency independency like the spiral based topologies, and it also exhibits a constant negative inductance change in the range between 20 kHz – 100 kHz.

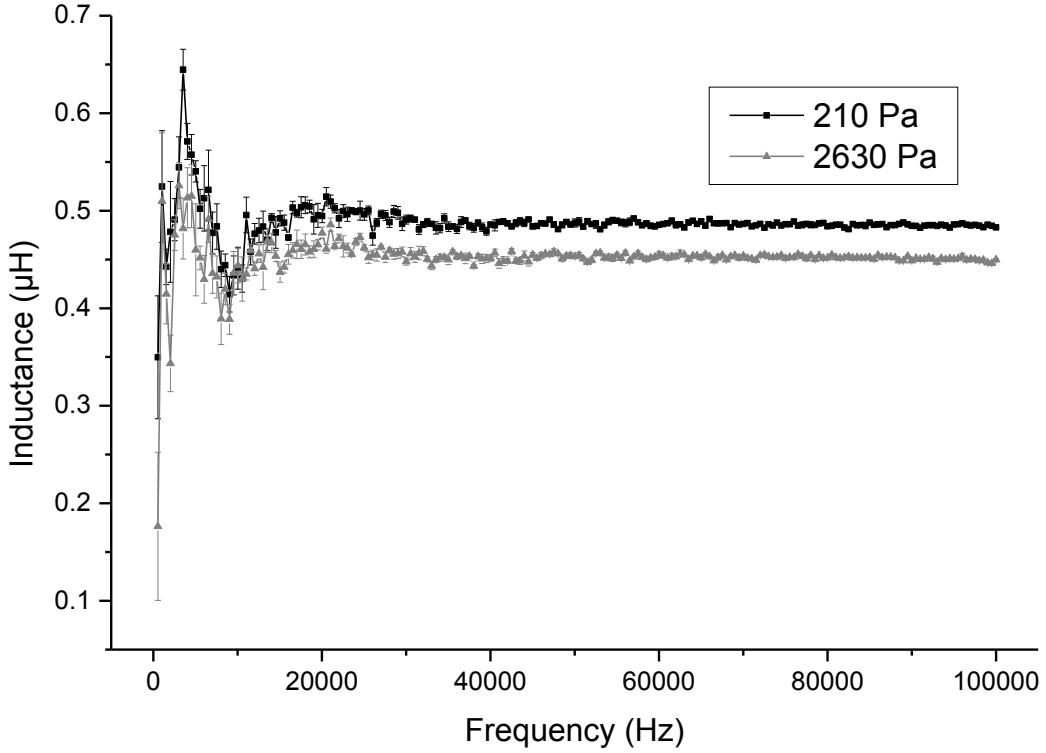


Figure 6.5 – Inductance response over the full span of observed frequencies for meander topology with pitch of 0.5 mm.

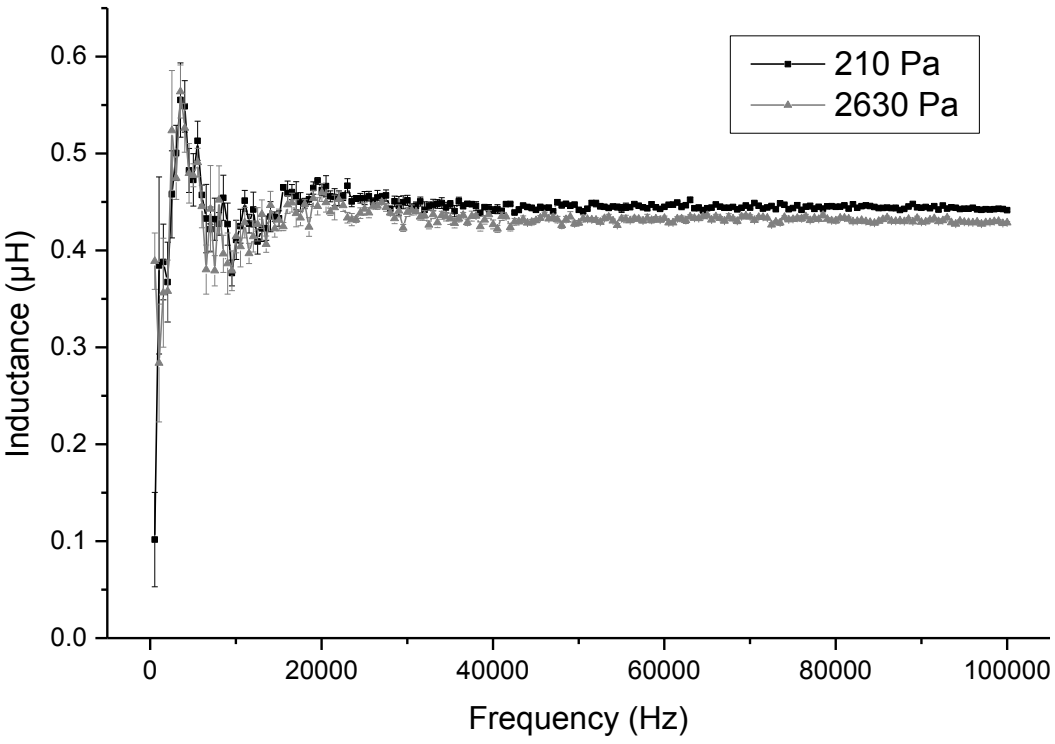


Figure 6.6 – Inductance response over the full span of observed frequencies for mesh topology with pitch of 1.0 mm.

By analysing Figure 6.6 it can be deduced that the smallest inductance change was present in the mesh topology, the inductance change was approximately 25 nH, a 5% change in inductance from its inductance value at 210 Pa. The mesh coil demonstrates a frequency independency, and shares the characteristic of a constant inductance change caused by increased tensile stress with the other planar coils.

By presenting the data in such a format it was possible to see the advantages a planar coil has over a wound coil. Frequency independency has been demonstrated for a large portion of the frequency range observed, as opposed to the wound coil, which demonstrated a large frequency dependency once a magnetic ribbon core was introduced. A constant negative inductance offset was seen for all planar coil topologies over a frequency range of 20 kHz – 100 kHz, which was superior when compared to the wound coil's response, with a varying inductance change over the entire span of observed frequency. The anomalies of the inductance response observed from the wound coil are not present in the planar coils' inductance response.

The differences between these coils could be due to the different field profiles produced by a wound coil and a planar coil. The planar coil creates a field that is perpendicular to the magnetic ribbon, whereas the wound coil creates a field that is largely parallel to the magnetic ribbon. The wound coil will also create a larger field, which could contribute to the anomalies, which may be certain magnetoelastic resonant modes of the magnetic ribbon. The lack of frequency dependency for the frequency range of 20 kHz – 100 kHz indicates that planar coils interact with the magnetic ribbon core differently, compared with wound coils. This may be advantageous, as frequency independency can decrease the complexity of sensor implementation in a system.

By analysing the planar coil topologies, the spiral coil topologies are superior, as the inductance changes are larger. However, as a percentage the meander coil's inductance change observed was the largest of the group, which indicates that should a smaller inductance be required, a meander coil could be used to substitute the spiral coils and still provide a strong performance, as a percentage change.

Figure 6.7 shows the inductance response of square planar coils to stress, the loading and unloading of the weights have been plotted separately, and a linear fit has been obtained for each of these cycles. It can be seen by comparing the different pitch values that the inductance of the coil with 0.5 mm pitch changes by the largest amount. For the other two pitch values tested the inductance change was similar, no large difference was exhibited. The figures show the trend of an increasing inductance value with a decrease in the pitch value, they also show the trend of a decreased inductance with increased tensile stress.

Figure 6.8 shows the inductance response of the circular coils to stress. The inductance values of all circular coils are smaller than their square coil counterparts of the same pitch value. By analysing the different inductance responses, the largest inductance change of the circular coils can be seen in the coil with the smallest pitch, of 0.5 mm. A line of best fit was used to analyse the overall sensitivity of the sensor, by linear fitting the data of both cycles combined. The sensitivities obtained for the spiral coils are shown in Table 6.1, which shows that the highest sensitivity was obtained with a square coil of 0.5 mm pitch, and the lowest sensitivity was for the circular coil of 0.75 mm pitch. It also shows that the sensitivity between the square coil of 0.75 mm pitch and 1.0 mm pitch are very similar, however this relationship was not seen for the circular coils of 0.75 mm pitch and 1.0 mm pitch.

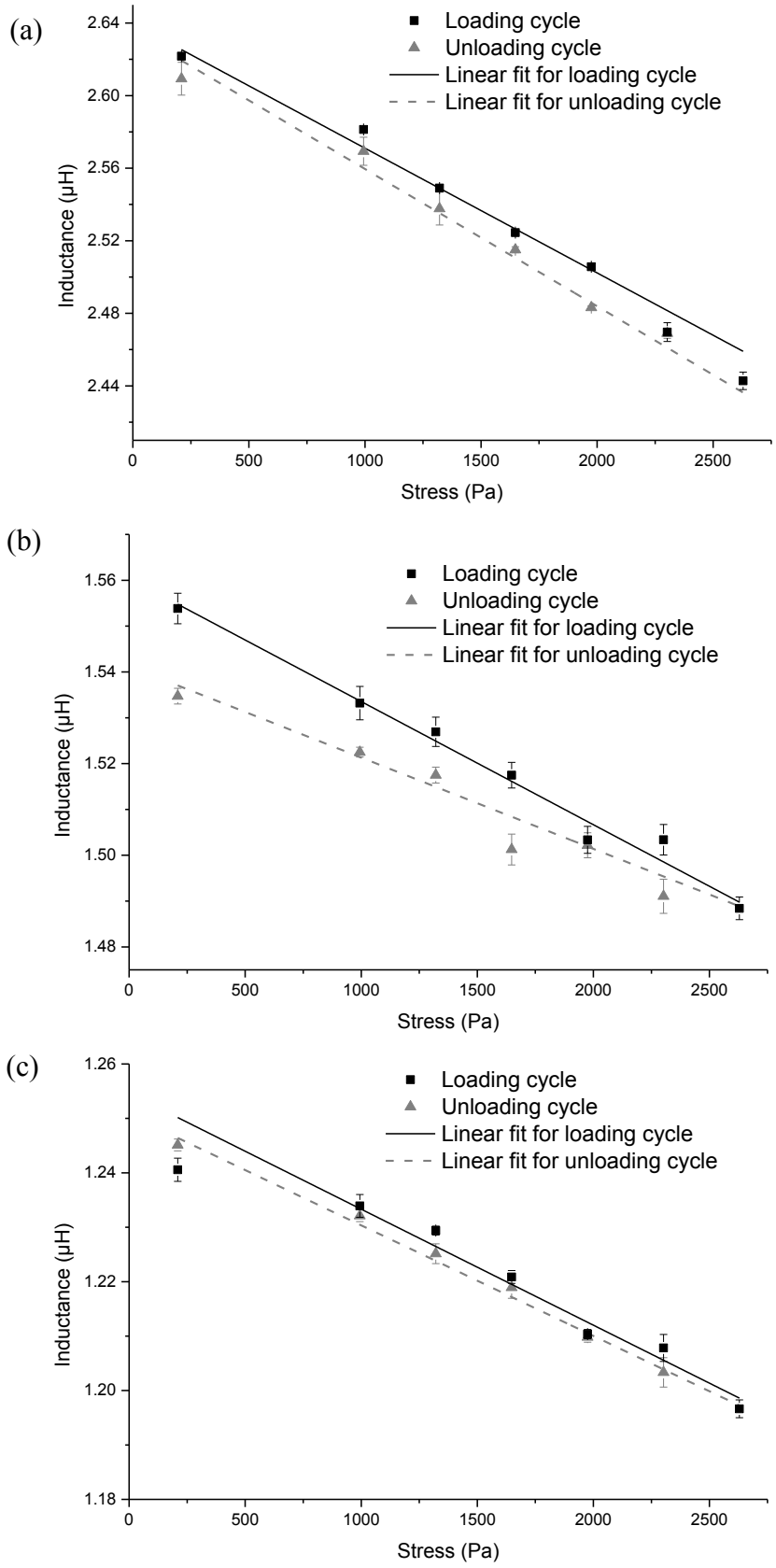


Figure 6.7 – Inductance response to stress for square topology at 80 kHz with pitch of (a) 0.5 mm; (b) 0.75 mm; (c) 1.0 mm.

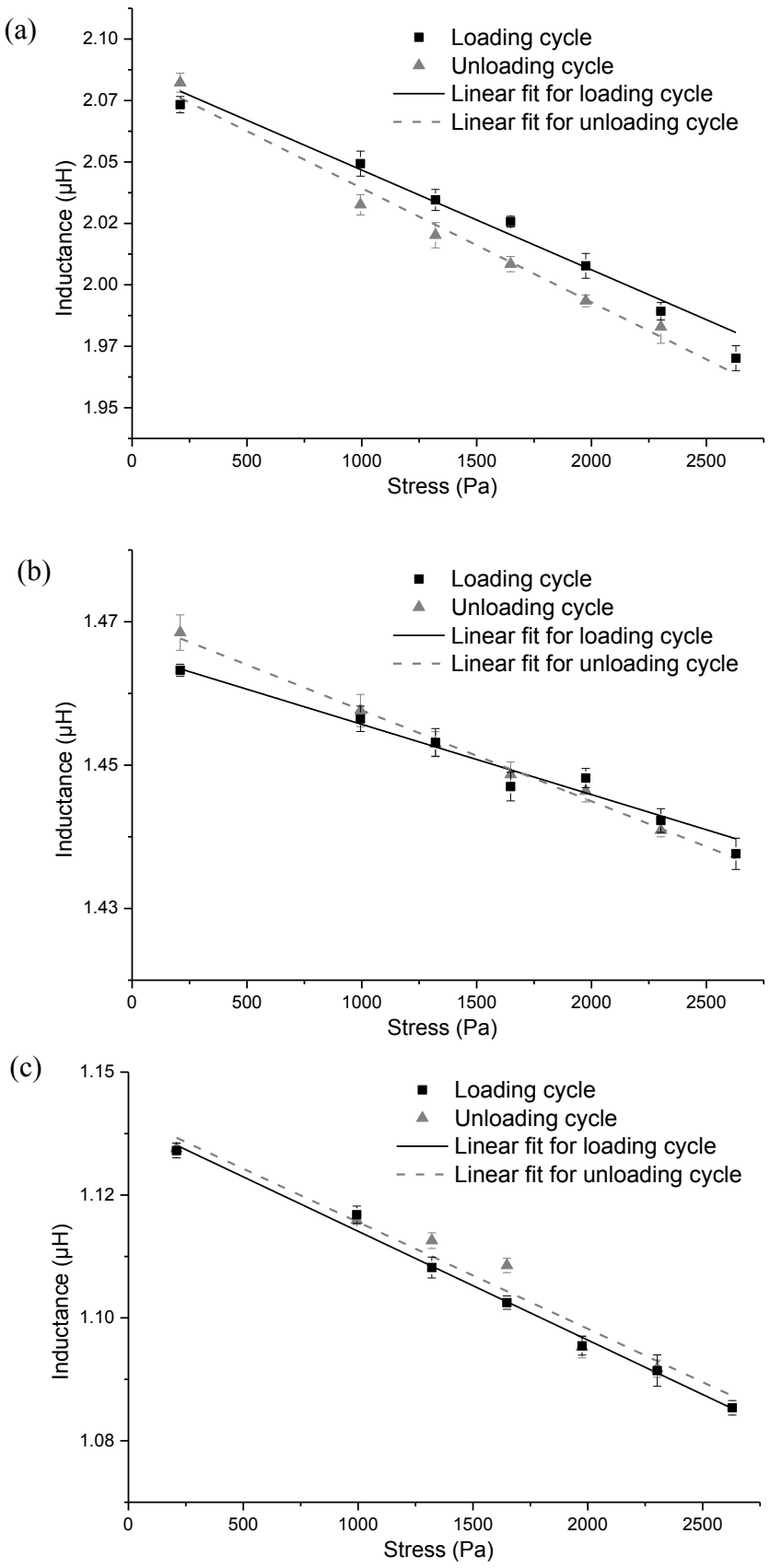


Figure 6.8 – Inductance response to stress for circular topology at 80 kHz with pitch of (a) 0.5 mm; (b) 0.75 mm; (c) 1.0 mm.

Table 6.1. Sensitivity of spiral planar coils extrapolated through linear fitting of data for loading and unloading cycles combined.

| Topology | *Pitch (mm)* | *Sensitivity of planar coil (nH/100 Pa)* |
|---|---|---|
| Square Coil | 0.5 | -7.63 |
| | 0.75 | -2.02 |
| | 1.0 | -2.00 |
| Circular Coil | 0.5 | -4.34 |
| | 0.75 | -1.32 |
| | 1.0 | -2.18 |

Figure 6.9 shows the inductance response of the meander coil to stress, the loading and unloading cycles have been plotted separately. The inductance change of the meander coil with 0.75 mm pitch was the largest, followed by the meander coil of 0.5 mm and 1.0 mm pitch. This was unlike the inductance response of the planar coils, where the largest inductance changes were exhibited by the lowest pitch value.

Figure 6.10 shows the inductance response of the mesh coil to stress. It shows that the mesh coil has the lowest inductance of all coils tested. The inductance change of the coil of 1.0 mm pitch and the coil of 2.5 mm pitch are very similar, the coil with the largest pitch of 3.5 mm has the smallest change in inductance. This implies a smaller pitch is favorable when using a mesh coil topology for a tensile stress sensing application.

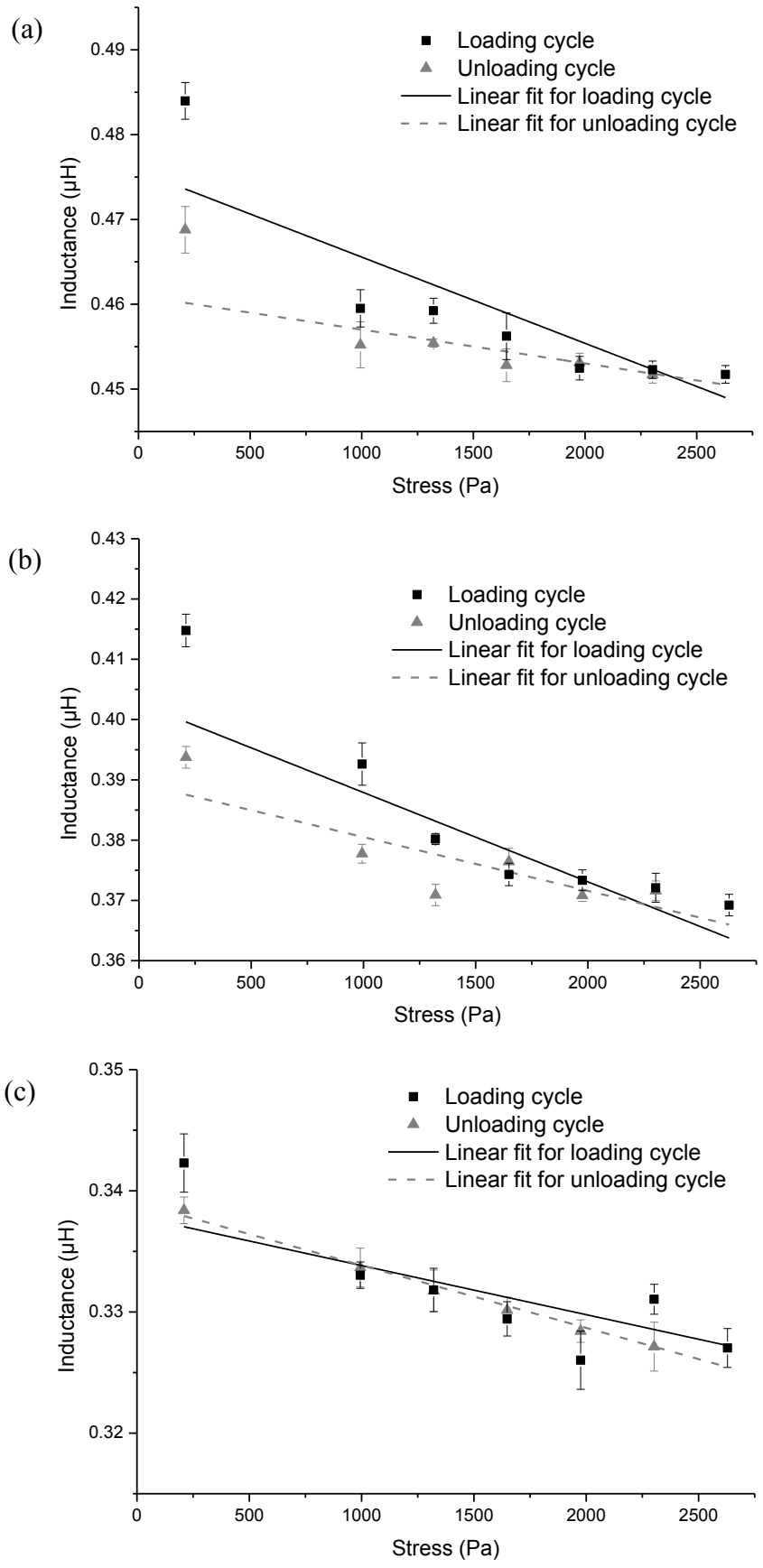


Figure 6.9 – Inductance response to stress for meander topology at 80 kHz with pitch of (a) 0.5 mm; (b) 0.75 mm; (c) 1.0 mm.

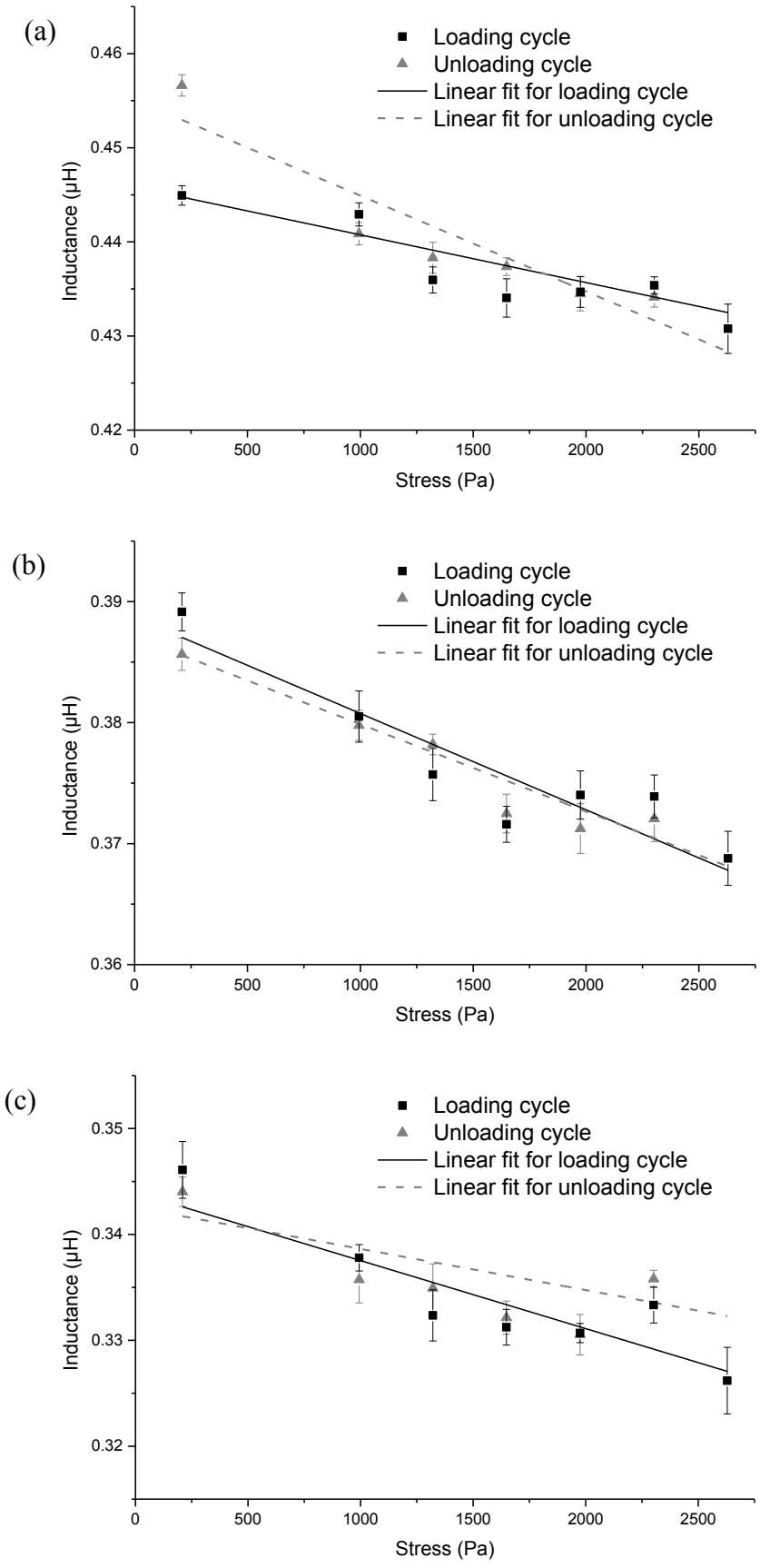


Figure 6.10 – Inductance response to stress for mesh topology at 80 kHz with pitch of (a) 1.0 mm; (b) 2.5 mm; (c) 3.5 mm.

Table 6.2. Sensitivity of non-spiral planar coils extrapolated through linear fitting of data for loading and unloading cycles combined.

| Topology | *Pitch (mm)* | *Sensitivity of planar coil (nH/100 Pa)* |
|---|---|---|
| Meander Coil | 0.5 | -0.65 |
| | 0.75 | -1.19 |
| | 1.0 | -0.48 |
| Mesh Coil | 1.0 | -0.74 |
| | 2.5 | -0.76 |
| | 3.5 | -0.45 |

A single set of data, combining the loading and unloading cycle, was analysed by linear fitting, to obtain the sensitivity of the non-spiral coils. The data obtained is shown in Table 6.2, and the non-spiral coils have lower inductance values and lower sensitivity compared with the spiral coils. By analysing the figures, the pitch value does not affect the linearity of the response. For the non-spiral coils, there is no general trend between pitch value and sensitivity, whereas the spiral coils exhibit the largest sensitivity for the coil with the smallest pitch tested, 0.5 mm. The general guideline for designing planar coils in a tensile stress sensing application with a maximum sensitivity is to incorporate a spiral coil with the smallest pitch possible.

This investigation has demonstrated the possibility of implementing planar coils for the detection of tensile stresses developed along a magnetostrictive ribbon. The possibility for planar coils to be manufactured on flexible substrates increases the possible applications and potential sensor designs. The findings are also useful in determining the best topology for tensile stress sensing, which are the spiral coil based topologies, especially the square coil topology with a small pitch value.

The applied stresses in this investigation acts on the magnetic ribbon core by aligning the domains in the direction in which the stresses are applied. This alignment of domains in the vertical direction causes the inductance to change, due to the Villari effect, as described in 2.2.2. The elongation of the ribbon should increase the ease of magnetisation in the longitudinal direction of the ribbon, as the Metglas 2605S3A has a positive magnetostrictive coefficient.

When using a wound coil, an increase in the inductance was observed for a low frequency region, however by increasing the frequency the inductance of the wound coil decreased with increased stresses. For all planar coils tested a constant negative inductance offset was observed, this may be due to the difference in the magnetic fields generated by two types of coils.

A wound coil will generate a magnetic field much like the field generated by a solenoid, shown in Figure 2.1. The magnetic field generated by the wound coil is aligned with the longitudinal direction of the ribbon, so the ease of magnetisation is increased, resulting in an increase in the inductance. As the frequency increases the AC permeability of the material decreases [3], Figure 6.2 indicates that the effective decrease in permeability could be affected by additional applied stresses.

Planar coils generate different magnetic field profiles compared to the wound coil, with $H_z$ being the majority component of the magnetic field generated, it is perpendicular to the direction of domain alignment. This may offer an explanation to the nature of the inductance responses obtained through this investigation. The response of a planar coil's inductance to a nearby amorphous ribbon undergoing the Villari effect is not well understood, and requires a substantial investigation which was beyond the scope of this work.

## 6.3 Summary

In this chapter an investigation into the inductance response of different planar coil topologies against tensile stress has been presented, and compared to the inductance response of a wound coil. The coils which have been fabricated were placed in a vertical suspension set-up, and a tensile stress was applied along the magnetic ribbon. The results obtained indicate that the spiral coil topologies with a small pitch value resulted in the largest sensitivity, whereas the non-spiral coils performed poorly in comparison. The spiral coils exhibit larger inductance values too.

By analysing the inductance response of the wound coil, the planar coil's inductance response was superior, by analysing the inductance response over the whole span of observed frequencies the wound coil exhibits large frequency dependency, whereas the planar coil's inductance response was independent of the frequency.

Through this investigation the square coil topology has been chosen as the basis for the design of a flexible AD sensor, due to its superior sensitivity compared to the other topologies and good frequency independency.

## 6.4 References for Chapter 6

[1] Grimes, C., Mungle, C., Zeng, K., Jain, M., Dreschel, W., Paulose, M. and Ong, K. (2002). Wireless Magnetoelastic Resonance Sensors: A Critical Review. *Sensors*, 2(12), pp.294-313.

[2] Huber, T., Bergmair, B., Vogler, C., Bruckner, F., Hrkac, G. and Suess, D. (2012). Magnetoelastic resonance sensor for remote strain measurements. *Applied Physics Letters*, 101(4), p.042402.

[3] Metglas. (n.d.). *Magnetic Alloy 2605S3A(Iron-based) Technical Bulletin*. [online] Metglas.com. Available at: https://metglas.com/wp-content/uploads/2016/12/2605S3A-Technical-Bulletin.pdf. [Accessed 16 Dec. 2017]

# Chapter 7. The Design and Development of a Flexible Figure-of-Eight Planar Coil Sensor for Angular Displacement Measurements

## 7.1 Introduction

In this chapter the design of a flexible AD sensor is presented. Based on the data obtained in Chapter 6 the square coil topology will be used in the design of this AD sensor. The AD sensor will consist of a FOE sensing coil and a magnetic sensing element. The FOE coil will be fabricated on a flexible substrate and employ two square planar coils, connected in series. The fields produced by the coils are opposite in polarity leading to a continuous magnetic flux path travelling through the magnetic sensing element, i.e. magnetostrictive Metglas 2605S3A.

To further characterise this AD sensor, different configurations have been investigated, which include additional layers of magnetic sensing element being used, and increasing the thickness of the adhesive layer between the magnetic sensing element and the planar coil sensor. The direction of bending was also investigated, as the AD sensor could be bent in two directions, which will incur different stress profiles within the magnetic ribbon, and therefore different permeability changes.

## 7.2 Results and Discussion

### 7.2.1 Preliminary characterisation of the angular displacement sensor

Figure 7.1 shows a TMR scan of the AD sensor without the magnetic ribbon layer, the $H_z$ field is presented. The scan was performed at a lift-off distance of approximately 0.1 mm from the surface of the coil, which was excited by a 0.2 A DC supply. The scan provides the $H_z$ profile generated by the FOE coil.

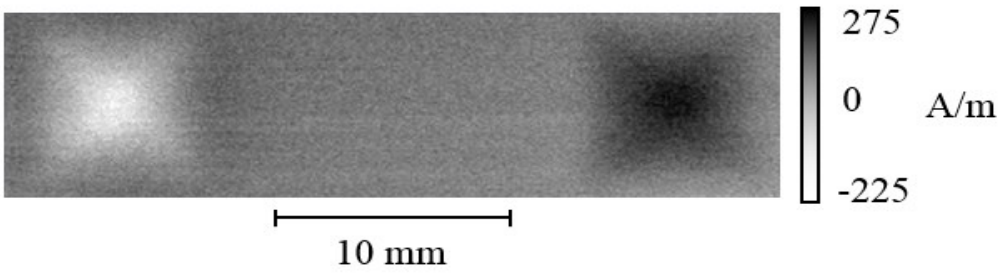


Figure 7.1 – TMR scan of the $H_z$ generated by the figure-of-eight coil, without magnetic sensing element, showing opposite polarities of each end of coil.

The image shows opposite polarities at the two coil segments of the sensor. The opposing polarities generated by the coil segments is a characteristic of the traditional wound FOE coil, and has been replicated in a planar coil configuration.

The AD sensors were first characterised without any magnetic ribbon layers, to investigate their inductance values and how the sensor performs without a magnetic ribbon layer. Ten ribbon-less AD sensors were fabricated and analysed at 80 kHz, taking ten inductance measurements for each sensor and averaging them. The mean inductance and the standard error of the group of ten sensors equalled 1.17 μH, and 3 nH respectively, indicating that the inductance characteristics of FOE coils can be reproduced with a high precision. This is an inherent characteristic of planar coil design, as the inductance of the sensor is determined by the geometrical dimensions and topology of the coil design.

Figure 7.2 shows the response of the ribbon-less AD sensor against displacement induced bending, as detailed in 4.4.2. The ribbon-less AD sensor does not react to the bending; therefore, it will also not function as an AD sensor without the magnetic ribbon layer. It is possible under extreme deformations that mutual inductance linkage occurs between the two coil segments of the FOE coil, however this is very unlikely in a practical situation, due to the extreme bend angle required. Figure 7.2 is representative for both directions of bending, there was minimal difference between the data sets obtained for each direction of bending.

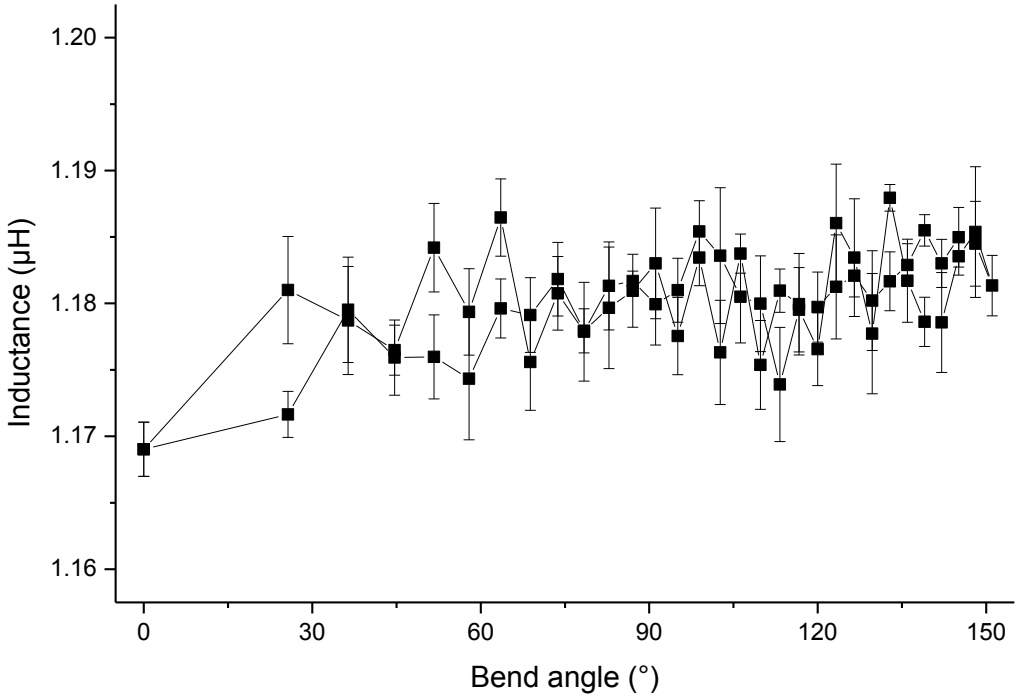


Figure 7.2 – Inductance response of ribbon-less angular displacement sensor to repeated cycles of bending and unbending.

Following the investigation of the ribbon-less AD sensor's characteristics, the sensors were fabricated with different bonding layer to ribbon layer configurations. The configuration with 1 adhesive layer and 1 ribbon layer was characterised first, and will be used for comparison reasons in the investigation of different configurations. This basic configuration will be referred to as the single-sided sensor configuration. Figure 7.3 shows the response of the single-sided sensor to both directions of bending, with respect to displacement, as described in 4.4.2. In this figure, the inductance response of the sensor has been plotted against the displacement which induces bending in the AD sensor. This offers insight into how equation (4-1) was used to extrapolate a bend angle from the displacement of the stage. This displacement induces the bending that the AD sensor undergoes, and Figure 7.3 and Figure 7.4 show the data plotted against displacement, and extrapolated angle, respectively.

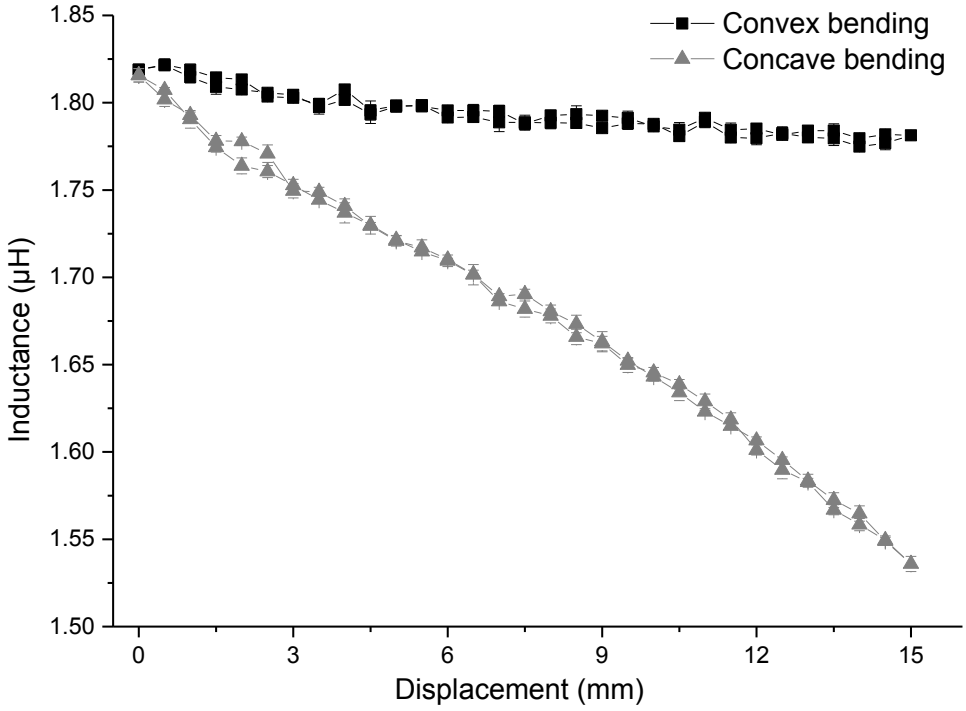


Figure 7.3 – Single-sided sensor response to displacement, with 1 ribbon and 1 adhesive layer.

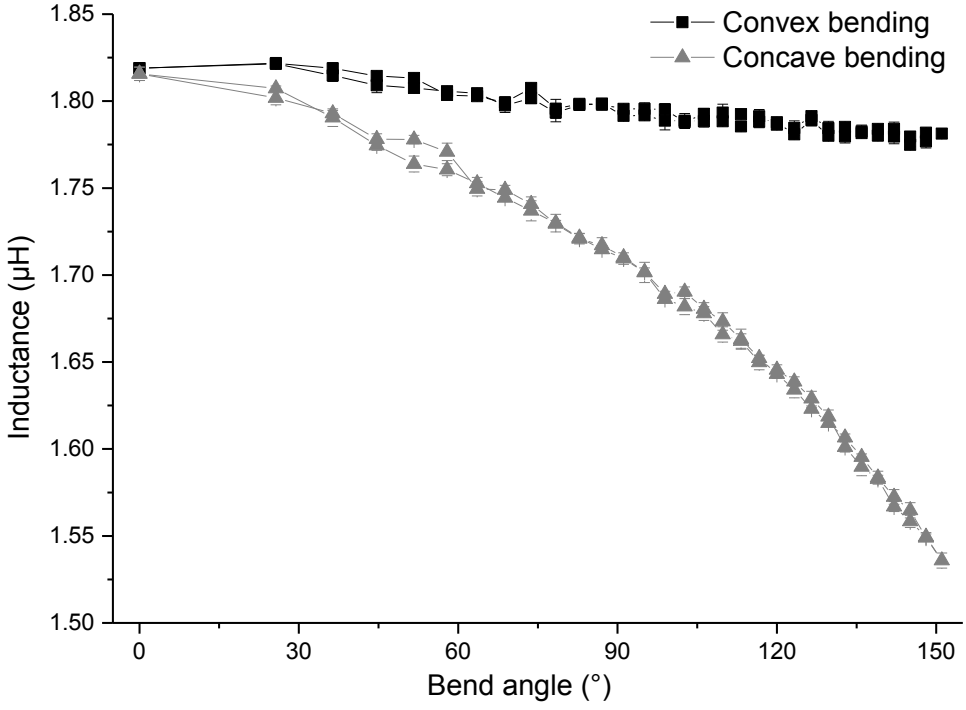


Figure 7.4 – Single-sided sensor response to extrapolated bend angle, with 1 ribbon and 1 adhesive layer.

It can be seen in Figure 7.3 that the direction of bending has a significant impact on the performance of the single-sided sensor, as the inductance change observed differs significantly. An inductance change of approximately 25 nH was observed for the convex direction of bending, whereas an inductance change of approximately 300 nH was observed for the concave direction of bending. The hysteresis and measurement uncertainty are comparable between the two traces, indicating that the direction of bending has a minimal impact on the sensor hysteresis and measurement uncertainty. Figure 7.4 was plot against extrapolated bend angle, obtained through equation (4-1). Figure 7.4 shows that due to the nonlinear nature of equation (4-1), the distribution of data points has been skewed towards larger angles, therefore although the sensor response appears linear against the displacement, it cannot be considered as a linear sensor response against bend angle.

There is a difference in inductance change seen between the two different directions of bending. The different bending directions mirror each other, and develop different stresses in the ribbon, which causes the difference in inductance response. Considering a beam, deforming under a uniform stress, two types of stresses are developed in the beam, separated by a neutral axis, as shown in Figure 7.5. [1]

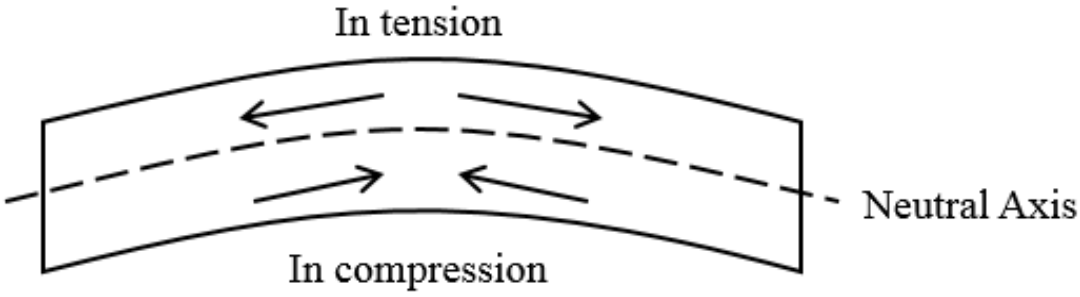


Figure 7.5 – Bending stresses developed in a beam, showing regions of different stresses developed, separated by neutral axis.

The neutral axis is located where the bending stress is zero. Considering the construction of the AD sensor, seen in Figure 4.12, it can be represented by a composite beam. To simplify the solving for the neutral axis, the polyester film will be assumed to be a homogenous material, and the contribution of the adhesive layer to the solution has been assumed to be negligible. Another consideration is the Kapton layer which the sensor is attached to for the experiment, seen in Figure 4.14. This layer has been removed from calculations to simplify the analysis. To solve for the location of the neutral axis of the AD sensor, an equivalent area method has been used.

The equivalent area method is used to describe and analyse composite beams which are composed of materials with different Young's moduli. Figure 7.6 shows how the method is used in an example of a composite beam composing of steel and aluminium. The transform is carried out to represent the stiffness of the second material, which can be increased or decreased. [2]

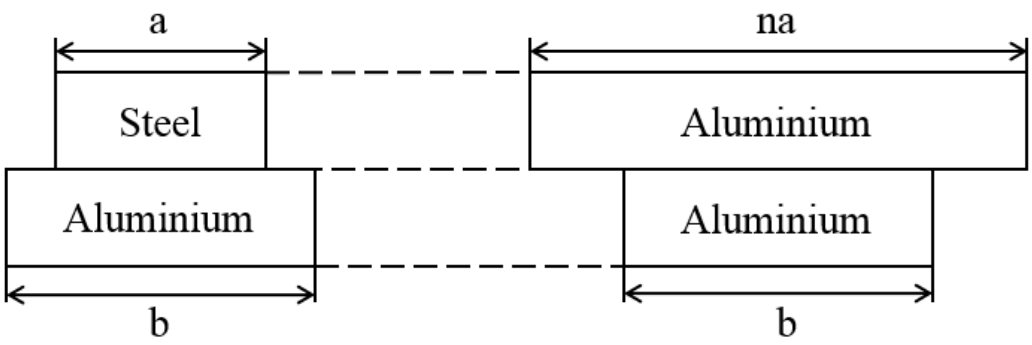


Figure 7.6 – Example of equivalent area method for a composite beam. (Image not to scale)

In this example, the steel layer has a larger young's modulus than the aluminium. The transform is used to create a new equivalent cross section of the beam, which can be assumed to be made from a single material. In this example the transform aims to create an equivalent cross section which is constructed from aluminium. To achieve this, the steel layer is multiplied by a scaling factor, n, which is defined as

$$n = \frac{E'_t}{E'_d} \tag{7-1}$$

The variable $E'_t$ is the Young's modulus of the target component, which will be transformed. In this example $E'_t$ will be the Young's modulus of steel. The variable $E'_d$ is the Young's modulus of the desired component, which is the Young's Modulus of aluminium for this example. [3]

The length of the steel component is multiplied by the scaling factor, and the equivalent cross section of the beam is obtained, composed entirely of aluminium. It should be noted that the transform must only affect the area in the horizontal direction, and the height should remain unchanged. After the equivalent area has been obtained, the neutral axis is calculated. Figure 7.7 shows the components required for calculating the neutral axis of a cross section, assuming the cross section is composed of one material only.

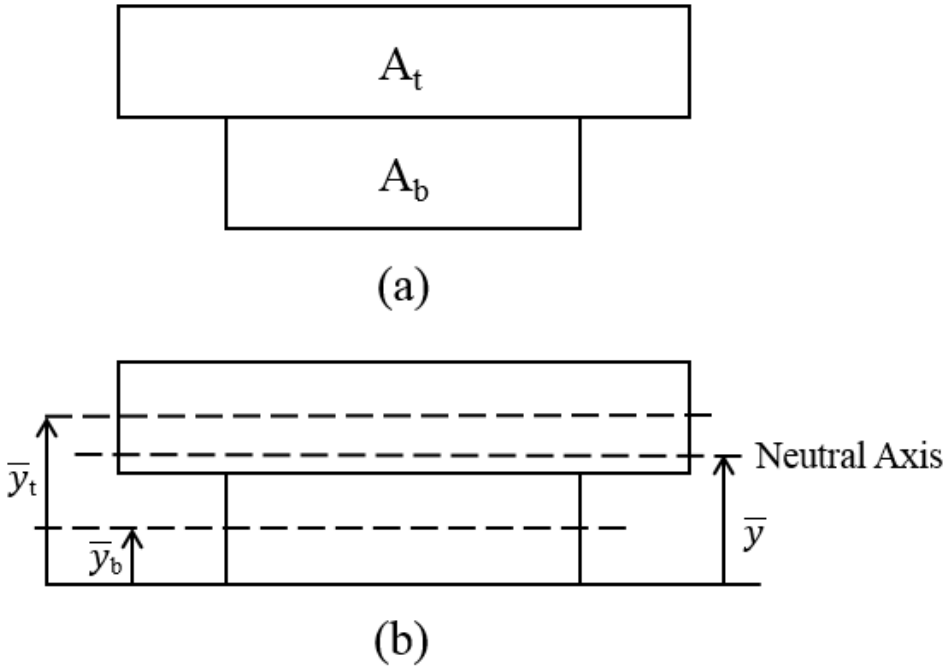


Figure 7.7 – Components for neutral axis calculation using equivalent area method. (a) Equivalent area of composite beam; (b) center for the top and bottom cross sections, and the location of the neutral axis.

The location of the neutral axis, $\overline{y}$, can be calculated by solving the following equation

$$\overline{y} = \frac{A_t \overline{y}_t + A_b \overline{y}_b}{A_t + A_b} \tag{7-2}$$

The parameters $A_t$ and $A_b$ represent the area of the top and bottom sections of the total cross section, respectively. The parameters $\overline{y}_t$ and $\overline{y}_b$ represent the distance from the bottom of the total cross section to the center of the top and bottom section, respectively, as shown in Figure 7.7. The dimensions of the sensor are shown in Figure 4.12, and the Young's modulus for the ribbon tested is assumed to be 100 GPa [4]. Quick-Teck, the manufacturer of the FOE coil, has quoted a Young's modulus of 1 GPa for the polyester substrate used. Substituting the parameters with values of the bend sensor, the neutral axis is calculated to be approximately 13 μm from the top surface of the ribbon.

Figure 7.8 shows the neutral axis superimposed on the single-sided sensor prior to the equivalent area transformation, it also shows that the neutral axis was calculated to be within the ribbon layer. Concave bending yielded superior results compared with convex bending, as seen in Figure 7.4. Figure 7.8 shows the single-sided AD sensor as a composite beam schematic, with the neutral axis location shown in Figure 7.8 (a). Considering Figure 7.5, concave bending would have seen a region of tensile stressing in close proximity to the sensing coil, which is on the top surface of the sensor substrate, as shown in Figure 7.8 (b). For convex bending, this region undergoes compressive stressing, as shown in Figure 7.8 (c). This difference in stressing induced in the region close to the sensing coils are seen to contribute largely to the sensor's performance. The sensor operates in a superior manner when tensile stresses are developed in close proximity to the sensing coils.

Another aspect which could impact the sensor performance is the transfer of strain, it is possible in the convex direction of bending the adhesive is not transferring the strains efficiently to the ribbon layer. This could offer an additional explanation which may explain the difference in sensor performance, depending on the direction of bending. It is likely that the difference in sensor response is due to several contributing factors, however for this work the transfer of strains will not be investigated in depth.

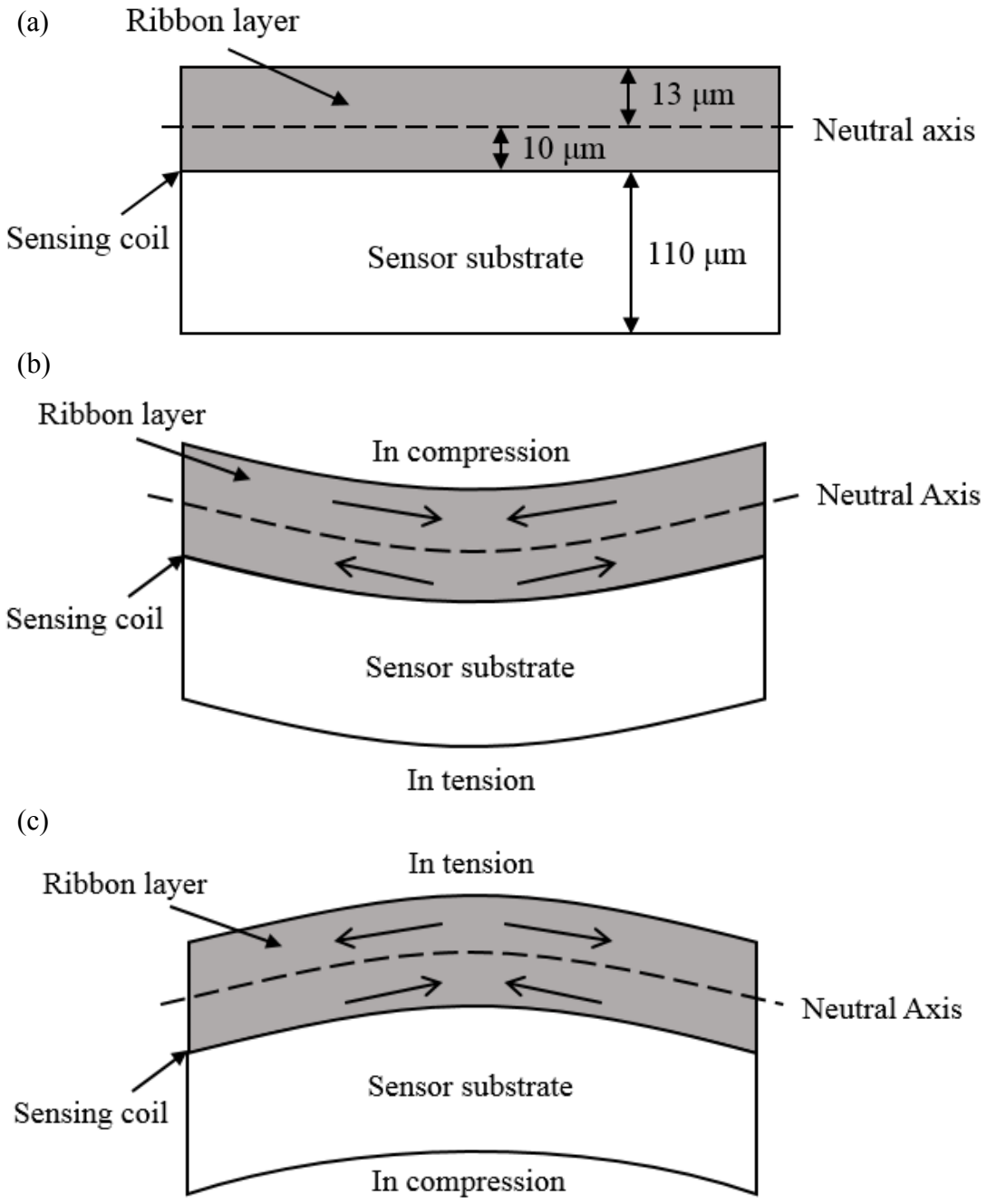


Figure 7.8 – Composite beam schematic for the single-sided sensor. (a) Neutral axis position calculated for single-sided sensor; (b) stresses induced through concave bending; (c) stresses induced through convex bending. (Image not to scale)

Figure 7.9 shows the frequency response of the single-sided sensor's inductance, it shares similar characteristics to the planar coils reported in the previous chapters, where a stable response was seen above 20 kHz. Figure 7.9 shows that the frequency independency was not affected by the FOE design of the sensor, this allows for the sensor to be integrated in different applications with ease, due to the stable inductance value over the observed frequency span.

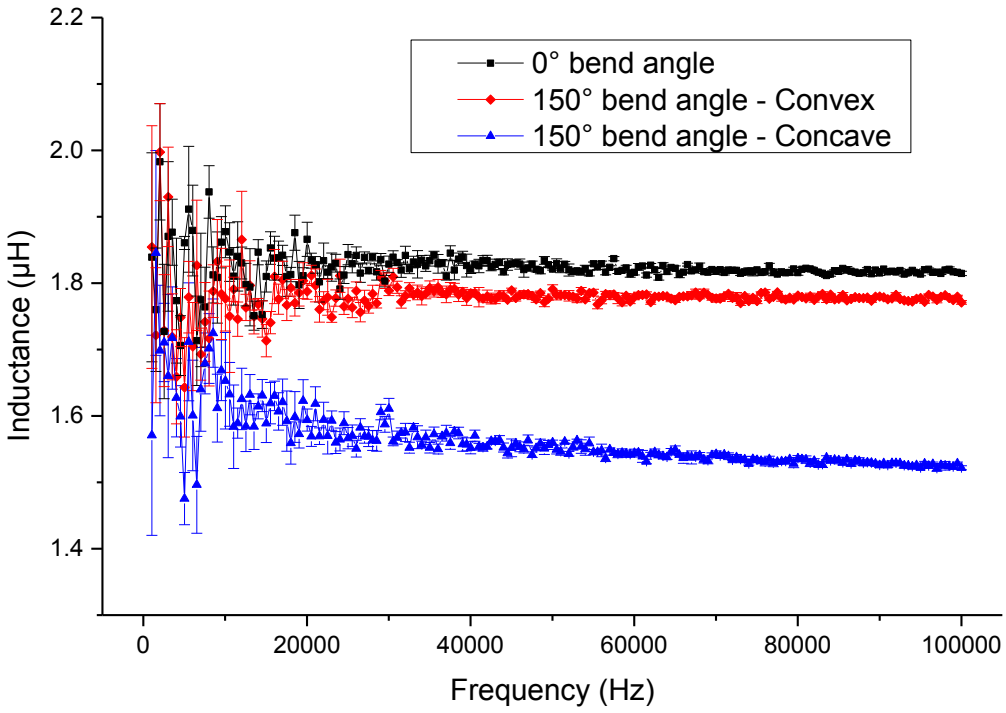


Figure 7.9 – Inductance change for single-sided sensor, with configuration of 1 ribbon layer and 1 adhesive layer, due to applied displacement over the full span of observed frequencies.

### 7.2.2 Investigation of single-sided sensor response to additional ribbon layers

The following figures show inductance responses of different single-sided sensor configurations of various layers of ribbon. Additional layers of bonding adhesive were used to attach the layers of ribbon. Figure 7.10 and 7.11 show the inductance response of the different sensor configurations, in both directions of bending, convex and concave respectively. It can be seen in Figure 7.10 that additional ribbon layers increase the inductance of the single-sided sensor, however the effects of adding additional ribbon layers was not linear.

The difference in sensor inductance between configurations of 2 layers and 3 layers of ribbon was much smaller than that seen between 1 layer and 2 layers of ribbon. This can be due to the increased displacement between the top surface of the sensor and the outer layer of ribbon due to the additional adhesive layers. Figure 7.10 also shows that the relative change of inductance with bend angle is not significantly affected by adding ribbon layers for convex bending.

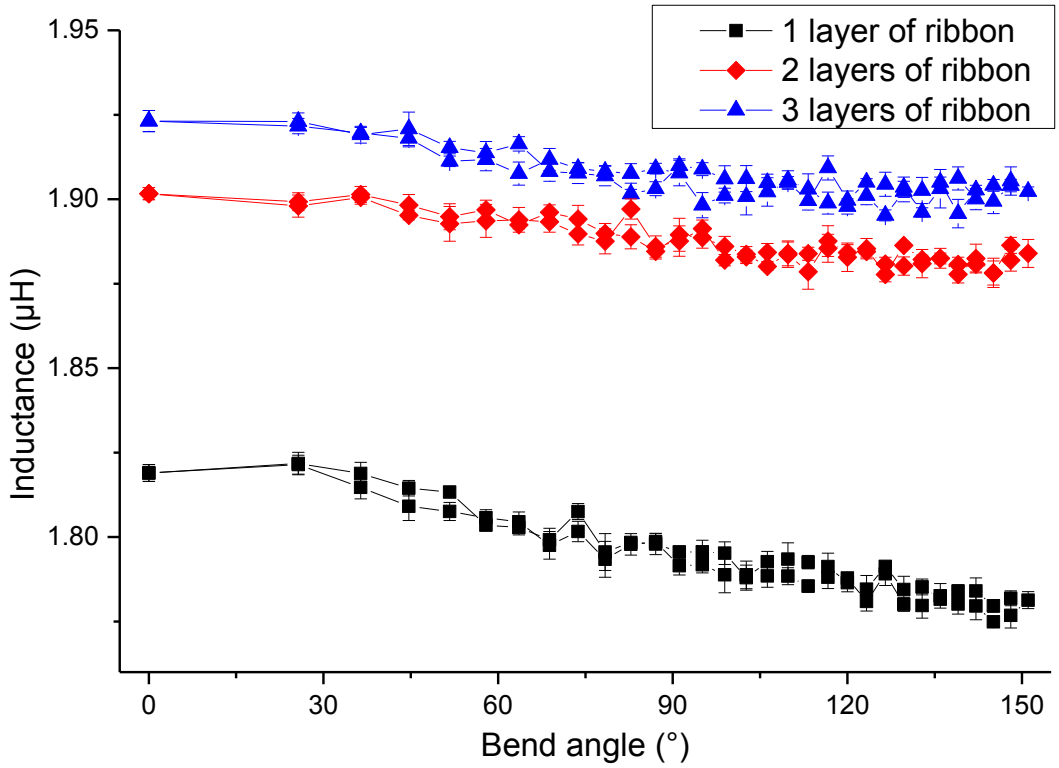


Figure 7.10 – Single-sided sensor response, with varying layers of ribbon, convex direction of bending.

Figure 7.11 shows the single-sided sensor response in the concave direction of bending. In all three configurations the inductance response was vastly superior in the concave direction of bending. It can also be seen that the difference in inductance between the different configurations was nonlinear. The effect of adding ribbon layers to the inductance of the sensor diminishes as the number of layers are increased. Through these observations it can be predicted that there is a point where adding further layers of ribbon will not affect the inductance of the sensor. The frequency response for the sensors tested here are shown in Appendix C.

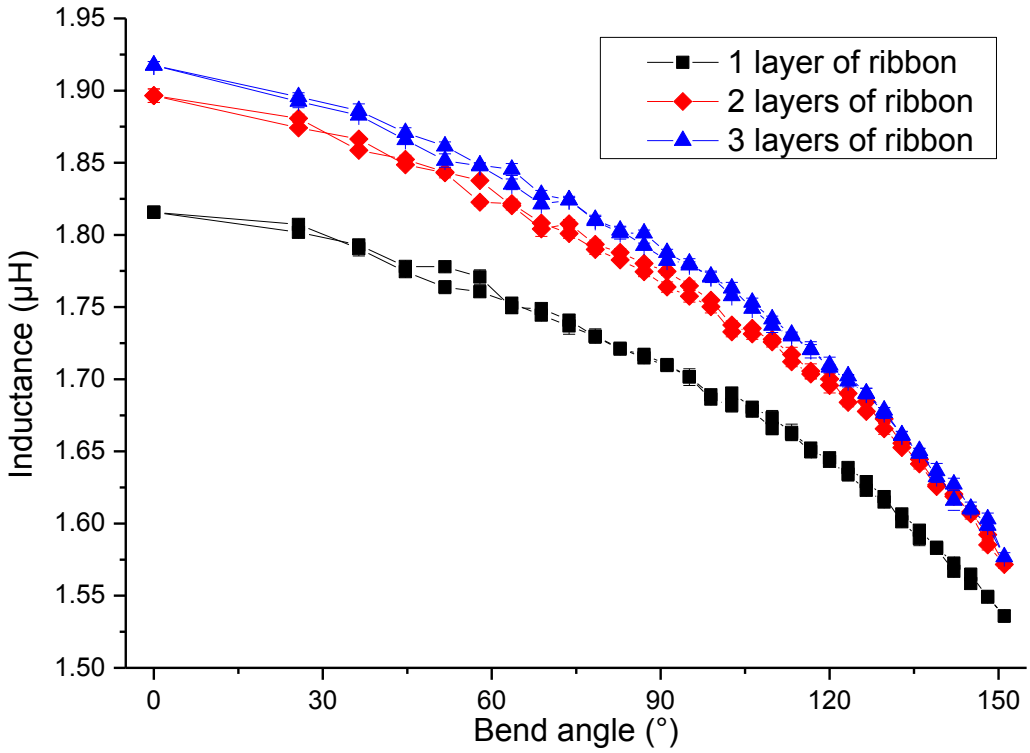


Figure 7.11 – Single-sided sensor response, with varying layers of ribbon, concave direction of bending.

Nonlinear fitting was performed for the sensor response in the concave direction of bending, as this was the superior operating mode for the sensor. An exponential decay function was used to best describe the sensor response shown in Figure 7.11. The various exponential decay functions generated for the different sensor configurations have been differentiated to obtain the rate of change, which has been plotted in Figure 7.12. By comparing the sensitivity responses shown in Figure 7.12, the single-sided sensor with 3 layers of ribbon possesses the highest sensitivity at large bend angles, followed closely by the sensor with 2 layers of ribbon. By introducing further additional ribbon layers the sensitivity was seen to decrease. The sensitivity of all three single-sided sensors tested are similarly matched below 40 degrees but then the single ribbon sensor diverges from the other two at higher bend angles. All three traces shown in Figure 7.12 show an increasing rate of change with increased bend angle, which is also seen in Figure 7.11. In general, this investigation indicates that additional ribbon layers can be added to increase the sensor's inductance, along with the sensitivity of the sensor, at the expense of increased sensor thickness. Increases to the sensor's inductance and sensitivity was limited, with little benefit beyond two ribbon layers.

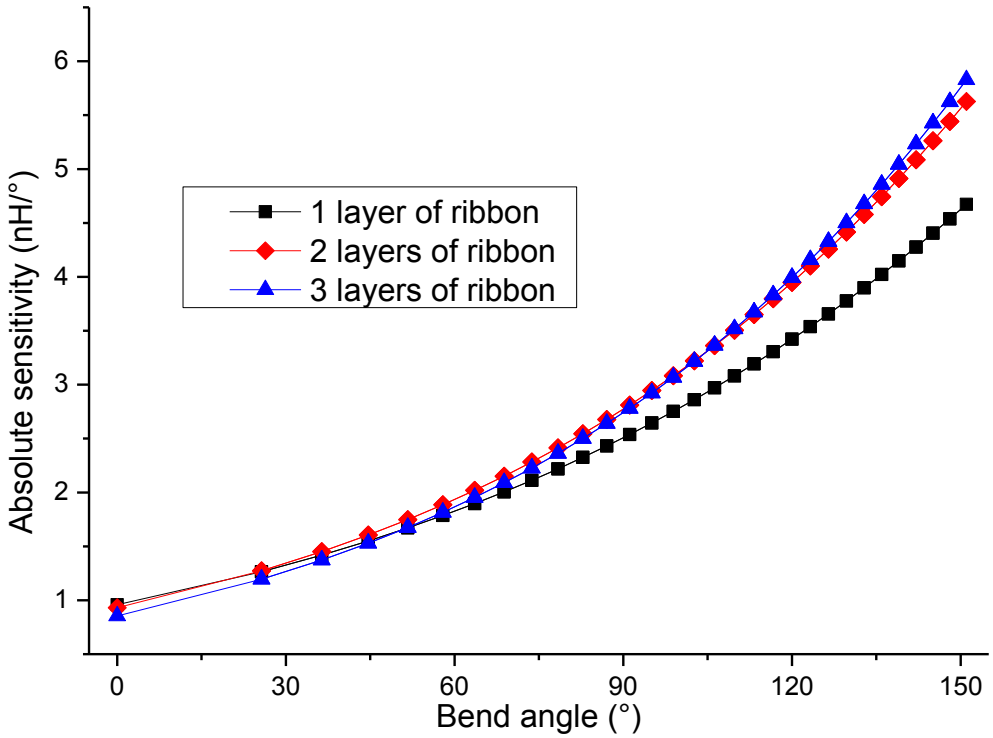


Figure 7.12 – Rate of inductance change of single-sided sensor, with varying layers of ribbon, concave direction of bending.

To analyse the differences in sensitivity between the different sensors fabricated in this investigation, two factors should be considered. The first is related to the addition of ribbon layers, and how the magnetic interaction between the FOE coil and the ribbon layers is affected. By examining Figure 7.11, it can be seen that at 0 degrees, the inductance is increased greatly by adding additional ribbon layers. This effect is due to the interaction between the magnetic flux of the sensing coil and the additional ribbon layers, however as the number of ribbon layers increase, there is less magnetic flux which can interact with the added ribbon layers. This, combined with an effective increase in distance between the additional ribbon layers and the sensing coil, results in a diminishing effect of adding ribbon layers.

As an increase was seen in the sensitivity, it can be concluded that the inductance increase at zero degrees bend angle is not the only factor affecting the sensor response. By adding additional layers of ribbon, the neutral axis is shifted. Assuming the additional adhesive layers do not contribute to the neutral axis calculations, the effect of adding ribbon layers equates to increasing the thickness of the ribbon layer, seen in

Figure 7.8. The neutral axis location was calculated for the sensor configuration with two ribbon layers, to show how the neutral axis shifted. The assumptions previously made for calculating the neutral axis were applied, in addition the two ribbon layers were assumed as one ribbon layer with their combined thickness. Figure 7.13 shows the neutral axis position calculated for the sensor.

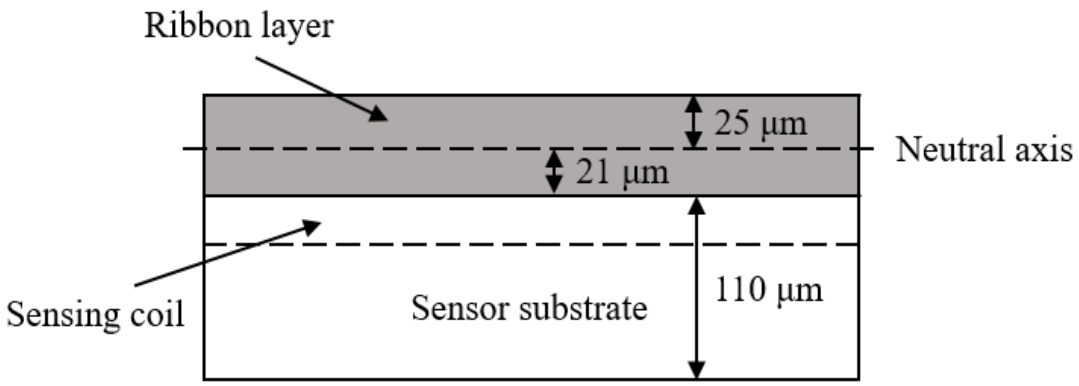


Figure 7.13 – Neutral axis position calculated for single-sided sensor with two ribbon layers. (Image not to scale)

It can be seen that as the ribbon layer's thickness is increased, a larger region is formed which undergoes tensile stressing, when concave bending is applied. This increases the sensitivity of the sensor as the inductance change is larger by this shift in the neutral axis. It can be concluded that through adding ribbon layers, the inductance and sensitivity of the single-sided sensor is increased, at the cost of a larger size profile of the sensor. The investigation only considered a maximum of three ribbon layers, however due to the difference between the sensor with two and three layers of ribbon being quite small, it may not be effective to consider having more than two layers of ribbon.

### 7.2.3 Investigation of single-sided sensor response to additional adhesive layers

In this section the effects of additional adhesive layers are presented, it should be noted that for the configurations discussed in this section there is only one ribbon layer, and a varying number of bonding adhesive layers. Different bonding methods may add varying thickness to the sensor, it is important to understand how the performance of the AD sensor differs due to a change in the bonding layer's height. The addition of adhesive layers will also help understand how increased separation can affect the neutral axis and the sensor's performance. Figure 7.14 shows the inductance response of the single-sided sensor when the direction of bending is convex. It was shown that additional adhesive layers decrease the inductance of the sensor, as the magnetic ribbon layer was displaced further away from the surface of the sensor. The added adhesive layers did not have a large impact on the trends of the sensors.

Figure 7.15 shows the sensors' inductance response in the concave direction of bending, there was minimal difference between the inductance responses of the sensor, other than the inductance difference caused by the added layers of adhesive. The inductance offset between the traces was close to linear, with near equal spacing between each trace, as opposed to those seen in Figure 7.11. This was only valid as the displacement caused by a few additional layers of adhesive was small, if the displacement between the ribbon and the surface of the coil becomes too large, the inductance will reduce dramatically and eventually no inductance linkage will exist between the coil and the ribbon. The frequency response for the sensors tested here are shown in Appendix C.

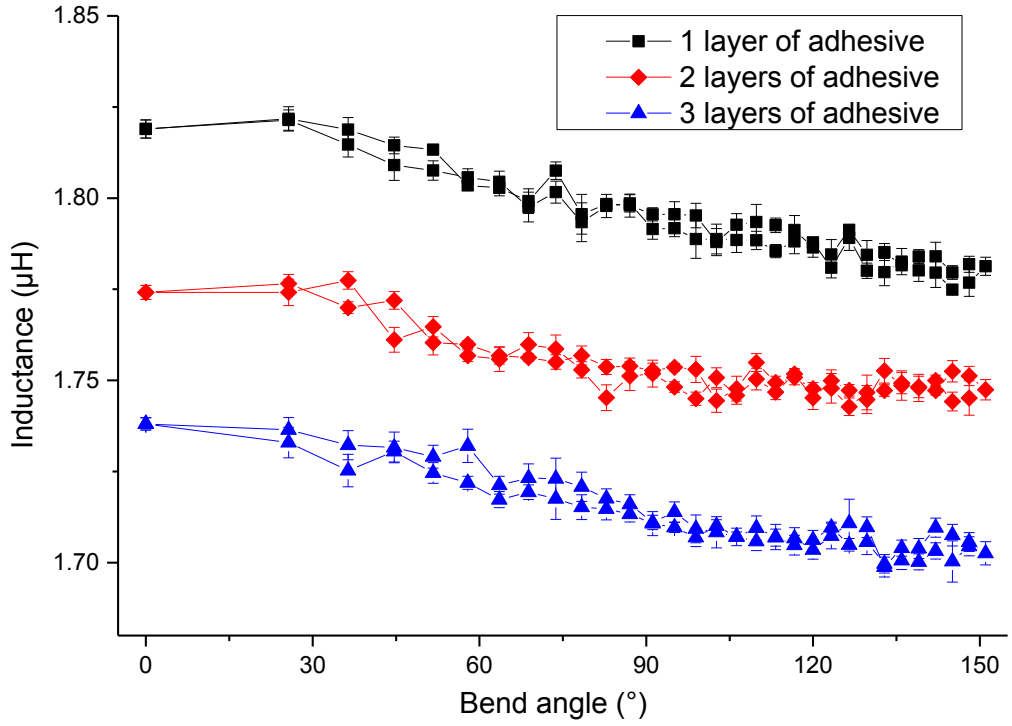


Figure 7.14 – Single-sided sensor response, with varying layers of adhesive, convex direction of bending.

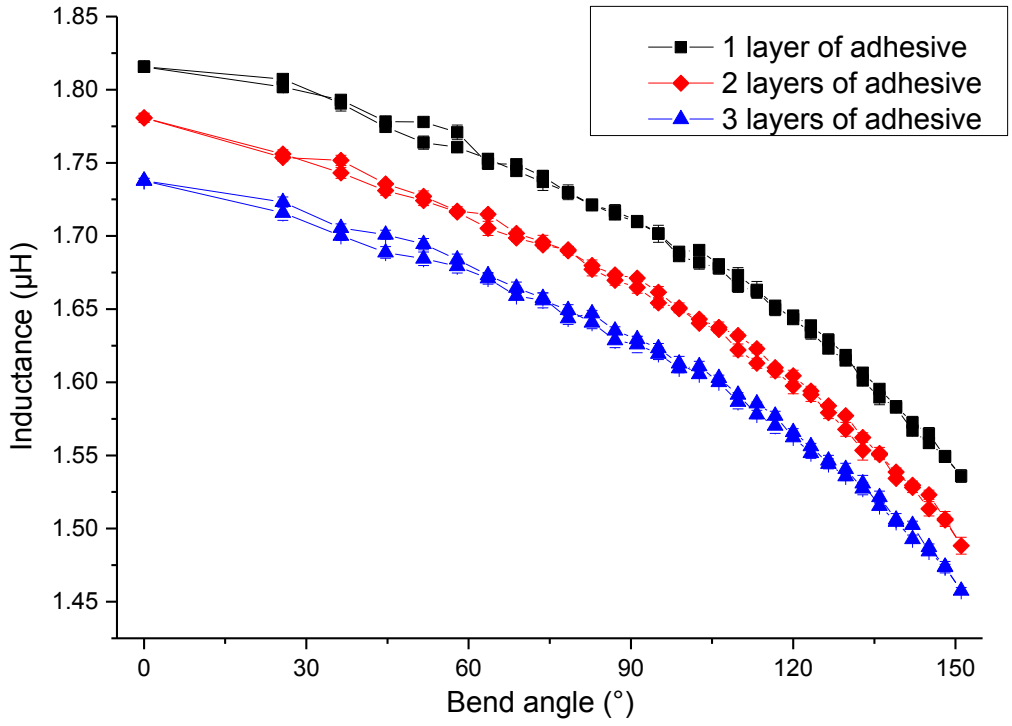


Figure 7.15 – Single-sided sensor response, with varying layers of adhesive, concave direction of bending.

Nonlinear fitting was performed for the sensor response in the concave direction of bending, as this was the superior operating mode for the single-sided sensor. An exponential decay function was used to best describe the sensor response shown in Figure 7.15, which is similar to that seen in Figure 7.11. The various exponential decay functions generated for the different sensor configurations have been differentiated to obtain the rate of change, which has been plotted in Figure 7.16. By analysing the sensitivity responses shown in Figure 7.16, the sensitivity trends shown are quite similar compared to the ones seen in Figure 7.12. The shapes of the trends differed between Figure 7.12 and Figure 7.15, however this is not a large difference between the sensors with varying layers of adhesive, as opposed to the significant differences by adding layers of ribbon. Due to the investigation not considering the adhesive layer in neutral axis calculations, it has not been considered for this particular investigation of varying adhesive layers. This investigation indicates that additional adhesive layers reduce the inductance of the sensor, whilst affecting the sensitivity response slightly. This corresponds to the findings detailed in Chapter 5.

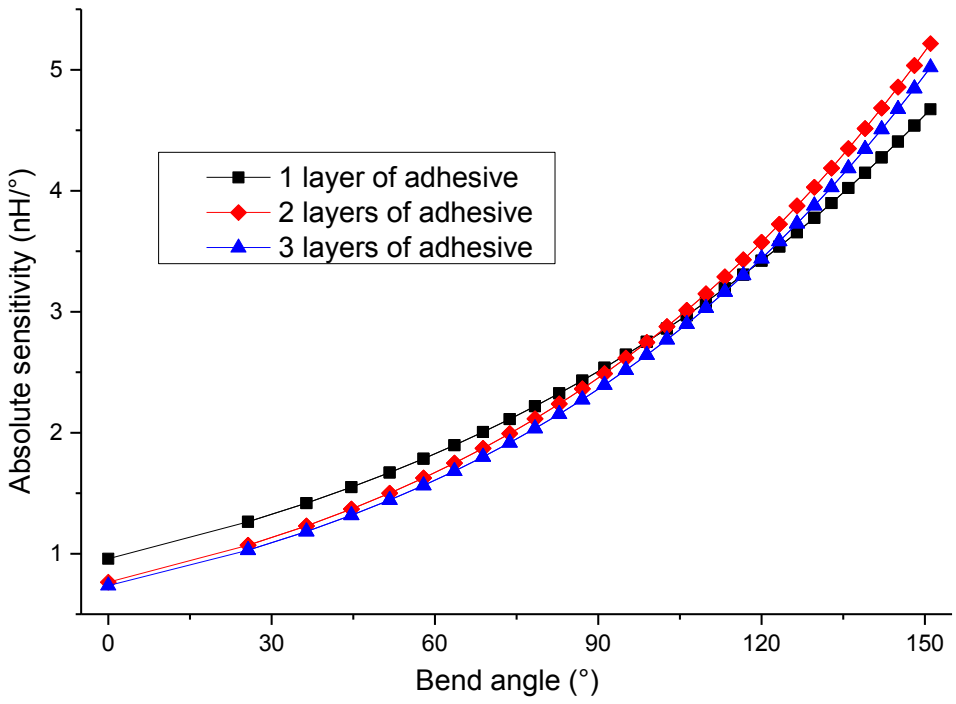


Figure 7.16 – Rate of inductance change of single-sided sensor, with varying layers of adhesive, concave direction of bending.

### 7.2.4 Investigation of sensor response with double-sided configuration

The effects of sandwiching the planar coil between two ribbon layers have been investigated. A layer of ribbon was attached to both the top surface and the bottom surface of the sensor coil. The ribbon attached to the bottom surface was then attached to the Kapton support layer, as detailed in Figure 4.14; this configuration will be referred to as double-sided. Figure 7.17 shows the double-sided sensor response when convex bending was applied, it should be noted that the type of bending applied was with respect to the top surface of the sensor, detailed in Figure 4.16.

This configuration increases the inductance of the sensor significantly; the inductance has increased by over threefold compared to all of the single-sided sensor configurations previously reported. The figure also shows a large change in inductance for the convex direction of bending, this was not seen in any other single-sided configuration tested. Figure 7.17 exhibits a large hysteresis, which was not present in the response for any other single-sided sensor configurations tested. In addition, the double-sided sensor exhibits an inductance response that is more linear compared to the inductance responses exhibited by single-sided sensor configurations tested.

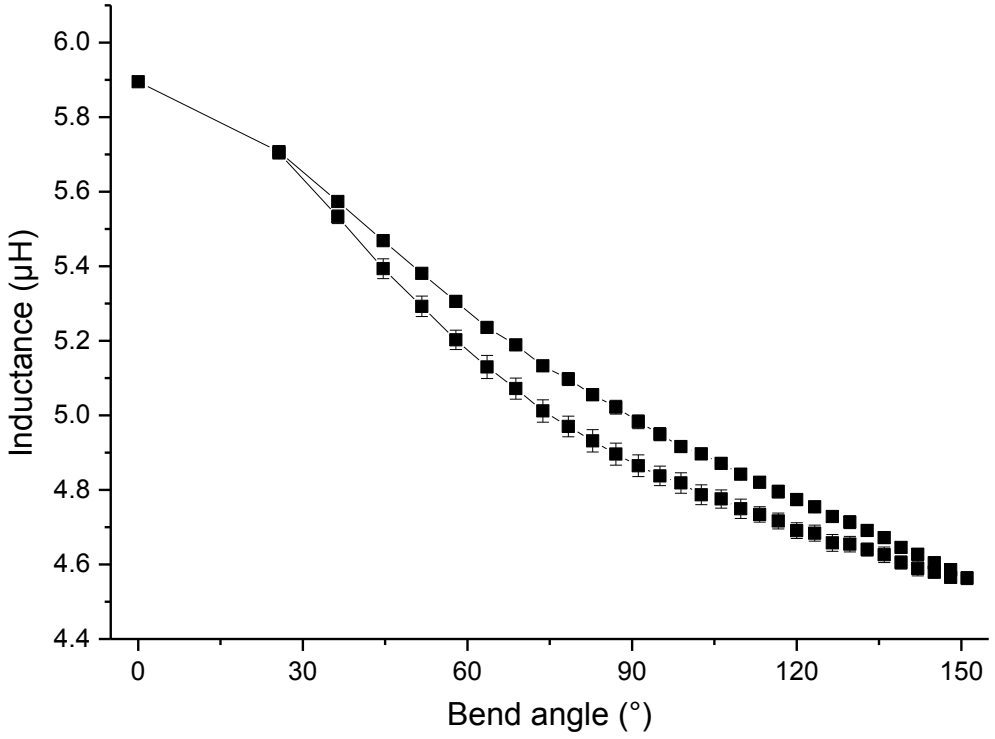


Figure 7.17 – Double-sided sensor response, convex direction of bending.

Figure 7.18 shows the double-sided sensor response when concave bending was applied. The inductance change observed in Figure 7.18 was smaller than observed in Figure 7.17, this is the first instance where convex bending has yielded a larger inductance change than concave bending. Figure 7.18 displays hysteresis that is much smaller than that seen in Figure 7.17, it also exhibits quite a linear response similar to that seen in Figure 7.17. The double-sided sensor tested does not follow trends previously observed in the single-sided sensors. By employing the double-sided configuration, the AD sensor's characteristics have been altered. Trends previously observed in the single-sided sensor are not representative for the double-sided sensor configuration. The double-sided configuration has increased the inductance of the sensor greatly, and a more linear response was obtained. Both directions of bending resulted in a significant inductance change, however convex bending introduces a large hysteresis, and exhibits a larger overall change in inductance due to bending.

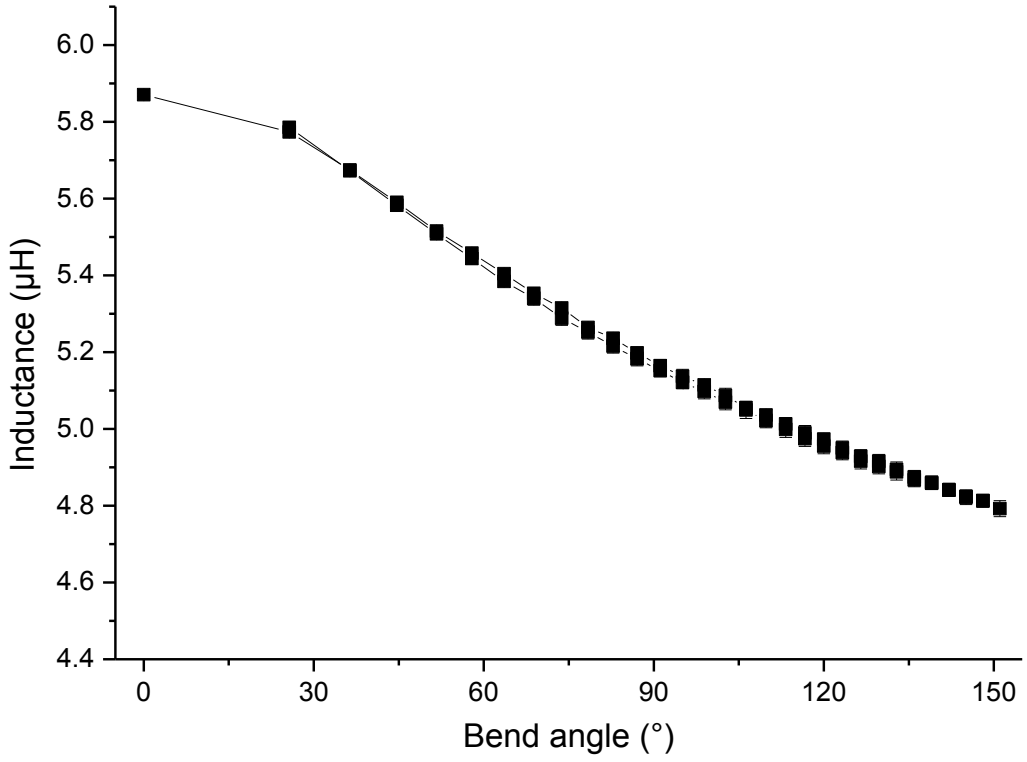


Figure 7.18 – Double-sided sensor response, concave direction of bending.

Linear fitting was performed for both directions of bending for the double-sided sensor. The sensitivity of the double-sided sensor for both convex and concave direction of bending was -12.1 nH/degree and -10 nH/degree respectively. These values are much larger than the sensitivity values reported in Figure 7.12 and Figure 7.16. Convex bending did not yield meaningful response in the single-sided configurations, however it yielded the largest sensitivity for the double-sided configuration.

Convex bending yielded superior results for the double-sided configuration due to the new location of the neutral axis. Considering the double-sided sensor as a composite structure, it has an identical composition mirrored at the centre of the sensor, and therefore the neutral axis can be considered to be located in the centre of the sensor, as seen in Figure 7.19. As the double-sided sensor undergoes convex bending, the topside of the sensor undergoes tensile stressing. It has been previously established in this chapter that a superior sensor response is obtained when the region in close proximity to the sensing coil undergoes tensile stressing. For the double-sided configuration this occurs when convex bending is applied, and an improved sensor response can be seen by comparing Figure 7.17 and Figure 7.18.

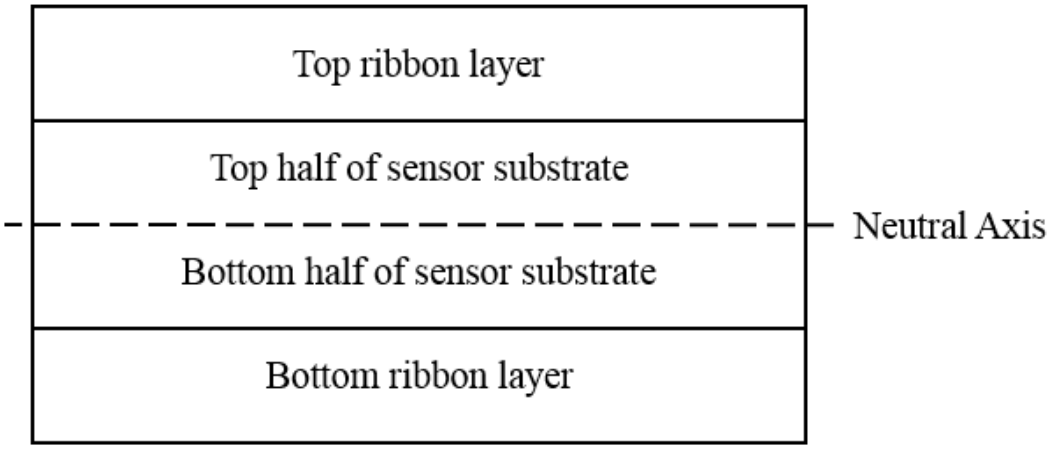


Figure 7.19 – Basic composite beam schematic of double-sided sensor configuration, with location of neutral axis. (Image not to scale)

Concave bending also yielded meaningful results for the double-sided configuration, this is due to the near symmetrical construction, with an exception that the sensing coil is located on the top surface of the sensor. When the double-sided sensor undergoes concave bending, the tensile stresses are developed in the bottom ribbon layer, which is further away from the sensing coil and this may explain why an inferior response was obtained for this type of bending. To compensate for this, a future design could implement sensing coils on both the top and bottom surfaces of the sensor substrate, which should produce an identical response for both directions of bending.

Figure 7.20 shows the frequency response of the double-sided sensor's inductance, a general negative trend can be seen for the inductance value with increased frequency, this was only seen for concave bending in Figure 7.9, and was of a smaller effect. By fitting over the traces of Figure 7.19, the inductance was shown to decrease at a rate of approximately -2.5 nH/kHz.

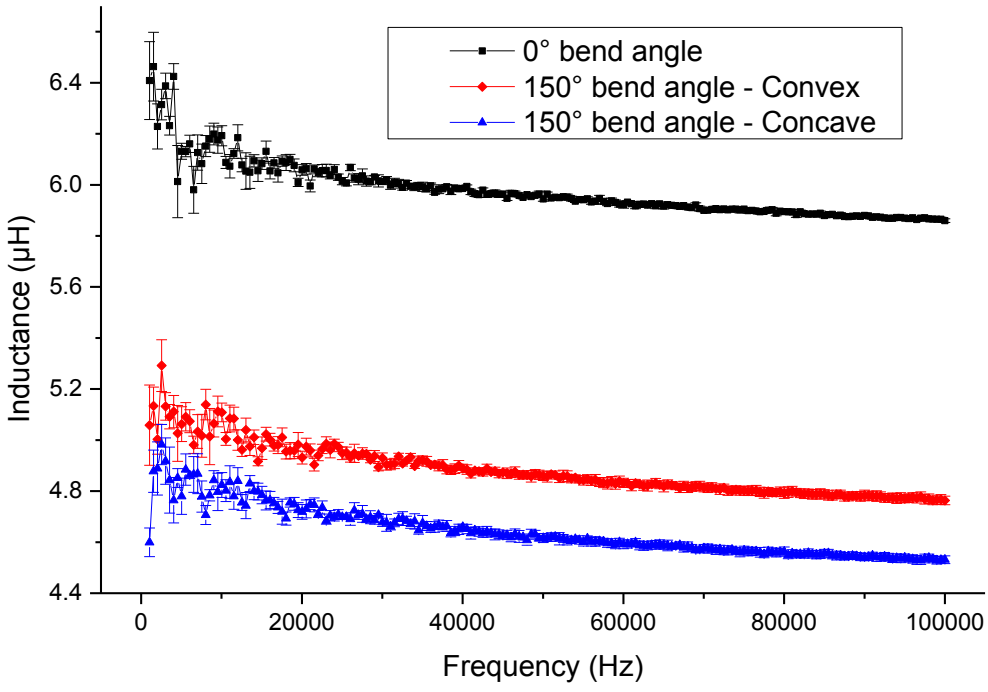


Figure 7.20 – Inductance change for the double-sided sensor, due to applied displacement over the full span of observed frequencies.

In this section the characteristics of the double-sided sensor has been investigated, and the results indicate that it performs very differently to the single-sided sensors tested prior. The addition of another ribbon layer can contribute to the changes, as each ribbon layer has an intrinsic stress profile after it has been cut to the shape of the sensor's sensing area. This can be different for both ribbon layers, and affect the sensor's performance. The effects of this phenomenon can be negated by annealing the ribbon after it has been cut to the desired size.

Another factor to consider is how the adhesive layer affects the stresses applied to the ribbon; as the bottom surface of the sensor was attached to the Kapton layer, as shown in Figure 4.13. The composite beam structure is not entirely symmetrical around the centre of the sensor, which will contribute to the differences in the response obtained from the two directions of bending applied.

### 7.2.5 Investigation of variation between sensor samples

In this section, several sensors have been fabricated to investigate the variation in sensor performance, this will indicate how different samples of the same material can influence the sensor. For this investigation five sensors were fabricated for the single-sided configuration with one ribbon and one adhesive layer, as reported in 7.2.1. In addition to this, five more sensors were fabricated with the double-sided configuration, as reported in 7.2.4. To avoid confusion, the five single-sided sensors with the topology reported in 7.2.1 have been labelled as Sensor 1A, 2A… whereas the double-sided sensors with the topology reported in 7.2.4 have been labelled as Sensor 1B, 2B…

Figure 7.21 shows the response of various single-sided sensors, due to the weak response exhibited through convex bending for this configuration, only the concave bending responses are shown. The single-sided sensors exhibit similar responses, with a slight deviation in their inductance value. There was minimal hysteresis seen in these sensor responses.

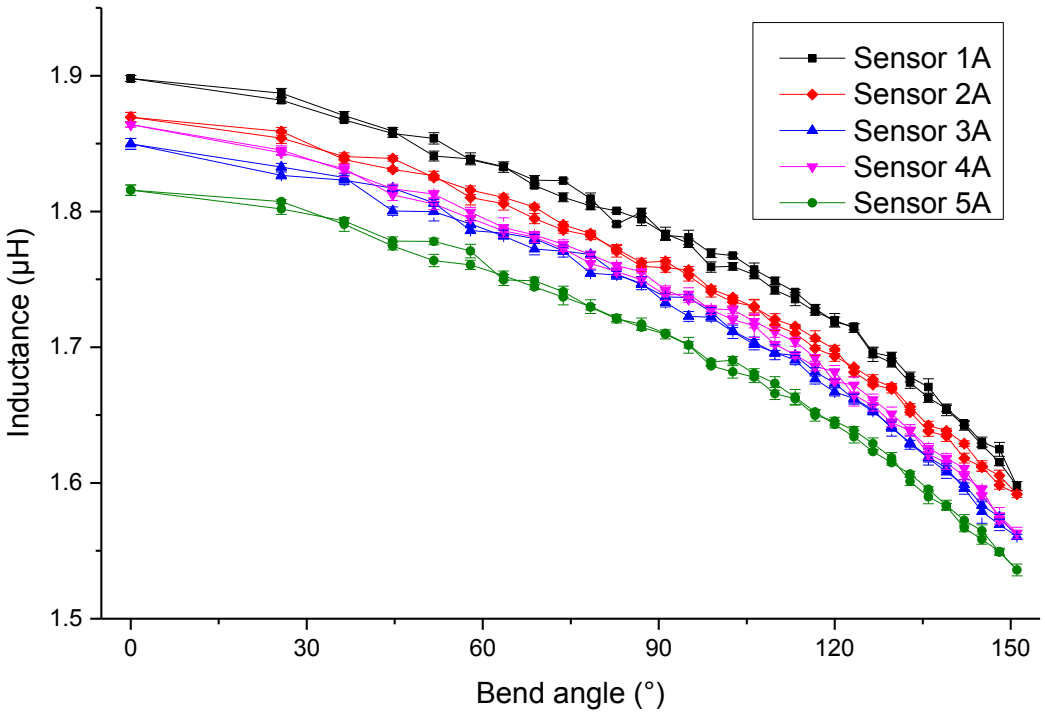


Figure 7.21 – Response of various single-sided sensors, concave direction of bending.

To quantify the different sensor responses seen in Figure 7.21, the data at five bend angles were chosen to be analysed. The bend angles chosen were at approximately 0º, 30º, 60º, 90º, and 120º. At these points the data points from the five traces were averaged and the standard error was obtained. Table 7.1 shows these quantitative measures obtained for Figure 7.21.

Table 7.1. Averaged inductance values and standard error values of the 5 single-sided sensors tested, obtained at different bend angles, from 5 measurements per sensor.

| Bend angle (º) | *Average inductance value (μH)* | *Standard error (μH)* |
|---|---|---|
| 0 | 1.859 | ±0.013 |
| 30 | 1.831 | ±0.012 |
| 60 | 1.775 | ±0.012 |
| 90 | 1.698 | ±0.012 |
| 120 | 1.570 | ±0.011 |

Table 7.1 shows that at the 5 bend angles investigated, the standard error was small relative to the average inductance value. The standard error is approximately ±0.7% of the average inductance value at the bend angle points shown in Table 7.1.

Figure 7.22 shows the inductance change obtained for each trace in Figure 7.21. The inductance value at each point was compared with the maximum inductance, observed at 0º bend angle, and the change in inductance against bend angle was obtained. The data obtained indicates that the single-sided sensors have a predictable response which does not deviate greatly between different sensor samples.

Th single-sided configuration has demonstrated a response which was reproducible, as consistently seen in all sensor prototypes tested. The difference in inductance between the single-sided sensors may be attributed to the different samples of ribbon used, due to the different stress profiles of the ribbon samples. As the sensor prototypes exhibit reproducible responses, it may be possible to calibrate to account for deviations in the inductance of different sensors.

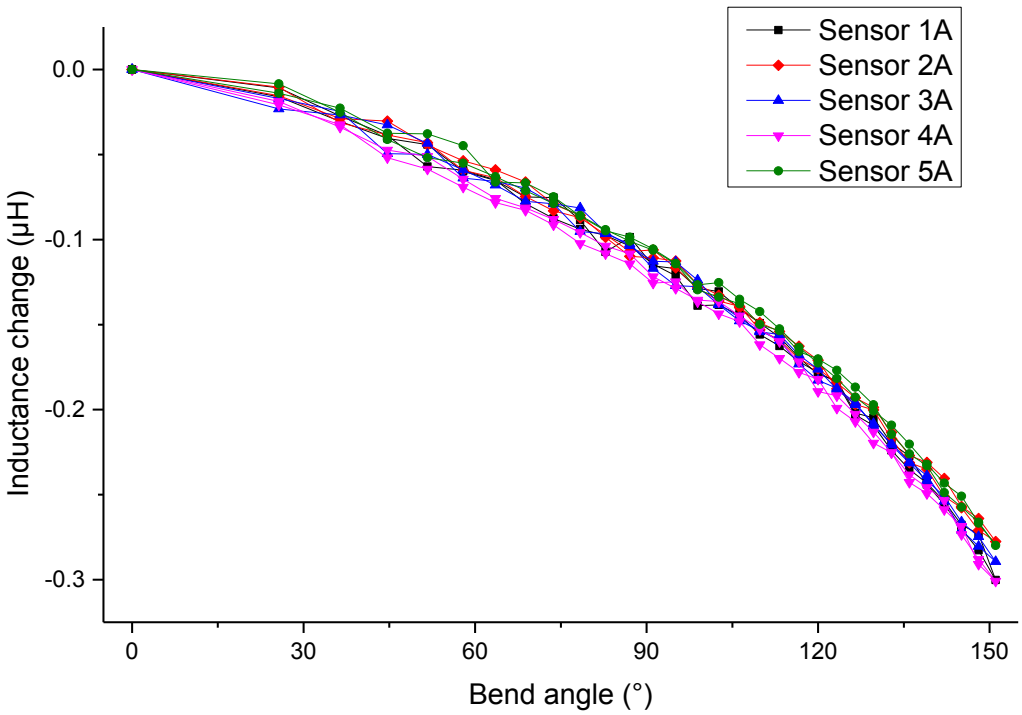


Figure 7.22 – Inductance change in the responses of various single-sided sensors, concave direction of bending.

Figure 7.23 and 7.24 shows the inductance response of the sensors with double-sided configuration, as detailed in 7.2.4, with convex and concave bending applied respectively. In Figure 7.23 and Figure 7.24, large deviations in the inductance of the sensors is shown, a difference of approximately 1 µH can be seen between the response of sensor 1B and 2B. As the double-sided sensors tested are the same for both directions of bending, the deviations between the traces are expected to be the same in both Figure 7.23 and Figure 7.24. In Figure 7.24, smaller hysteresis is seen for the traces compared with Figure 7.23, which corresponds to the findings in 7.2.4. Compared with Figure 7.21, a significant increase can be seen for the inductance deviation between traces.

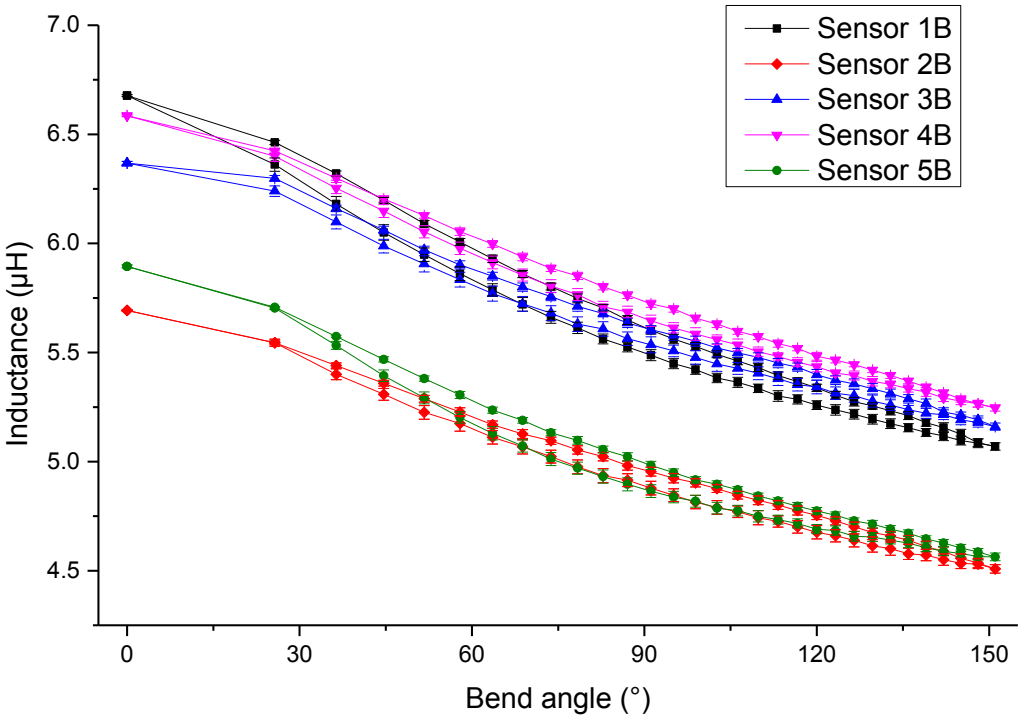


Figure 7.23 – Response of various double-sided sensors, convex direction of bending.

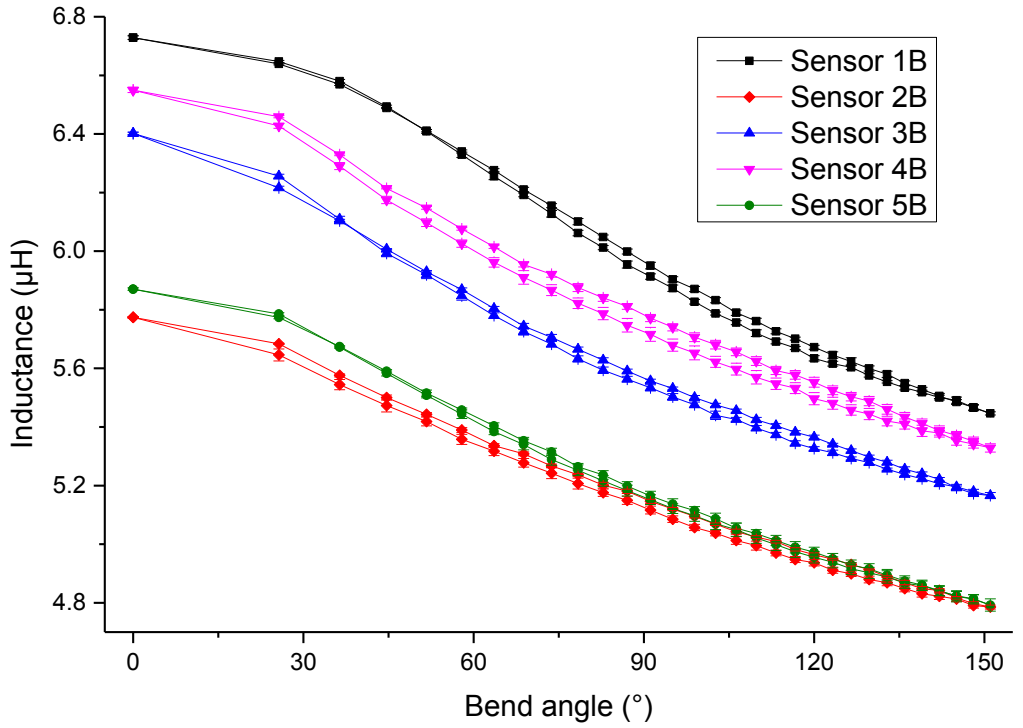


Figure 7.24 – Response of various double-sided sensors, concave direction of bending.

To analyse the uncertainty for the traces shown in Figure 7.23 and Figure 7.24, quantitative measures were obtained. The average inductance value and standard error value were obtained for 5 bend angles, for both Figures 7.23 and Figure 7.24. This will help better understand the effects caused by different directions of bending, and how the double-sided configuration compares with the single-sided configuration tested prior. Table 7.2 shows the quantitative measures obtained for the double-sided configuration for both directions of bending.

Table 7.2. Averaged inductance values and standard error values of the 5 double-sided sensors tested, obtained at different bend angles, from 5 measurements per sensor per direction of bending applied.

| Bend angle (º) | *Direction of bending* | *Average inductance value (μH)* | *Standard error (μH)* |
|---|---|---|---|
| 0 | Convex | 6.244 | ±0.128 |
| | Concave | 6.265 | ±0.126 |
| 30 | Convex | 5.926 | ±0.177 |
| | Concave | 6.045 | ±0.127 |
| 60 | Convex | 5.485 | ±0.173 |
| | Concave | 5.657 | ±0.113 |
| 90 | Convex | 5.163 | ±0.164 |
| | Concave | 5.333 | ±0.098 |
| 120 | Convex | 4.910 | ±0.103 |
| | Concave | 5.103 | ±0.136 |

Table 7.2 shows that for the double-sided configuration, convex bending generated larger standard errors, this is predominantly due to the large hysteresis seen in Figure 7.23. A larger change in inductance can be seen for the convex direction of bending. At 0º bend angle the inductance values are similar, however with increased bend angle, the inductance decreases more rapidly when convex bending was applied. This indicates that the sensitivity for the convex direction of bending is larger than concave direction of bending, which corresponds to the findings of 7.2.4. This was contrary to the findings for the single-sided configurations, where convex bending generated very weak responses.

Figure 7.25 and 7.26 show the inductance change obtained for each trace in Figure 7.23 and Figure 7.24, respectively. The inductance value at each bend angle was compared with the maximum inductance observed for the trace, at 0º bend angle, and the change in inductance was obtained. The difference in inductance change between sensor configurations will provide insight to how the inductance responses obtained for the double-sided configuration compares with the single-sided configuration.

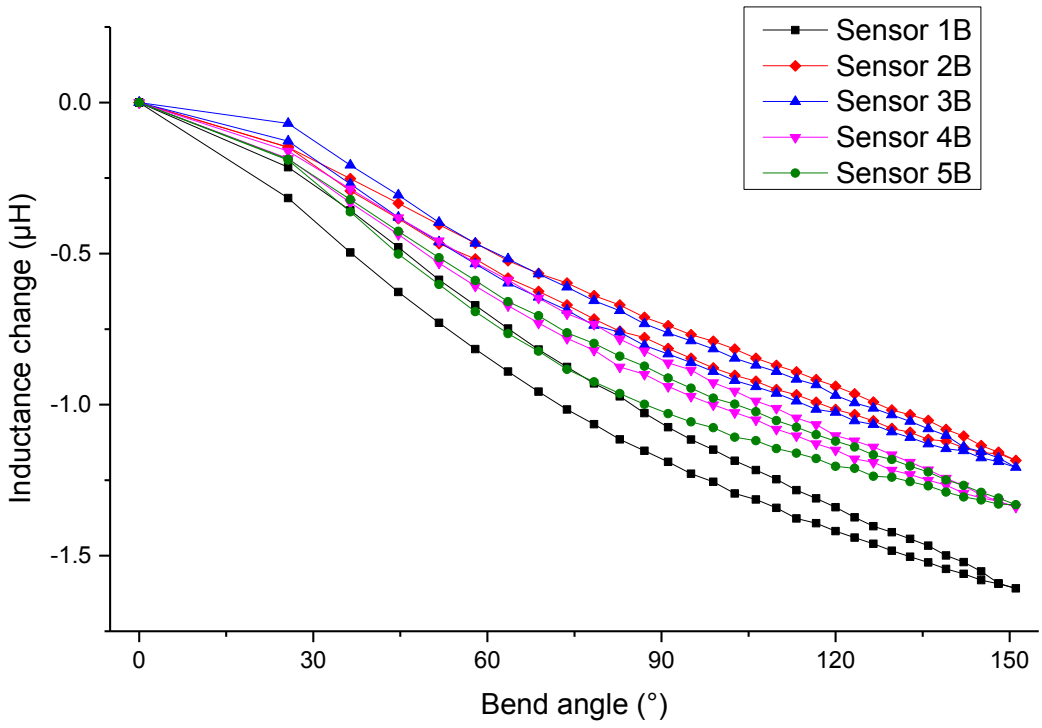


Figure 7.25 – Inductance change in the responses of various double-sided sensors, convex direction of bending.

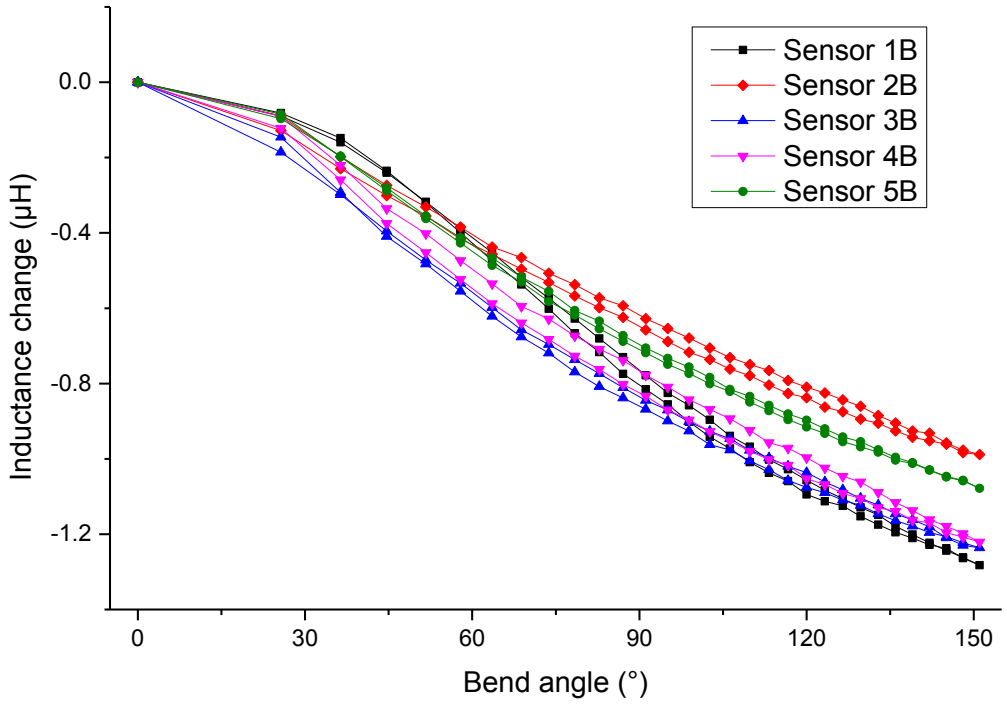


Figure 7.26 – Inductance change in the responses of various double-sided sensors, concave direction of bending.

Comparing Figure 7.25 and Figure 7.26, a large disparity in overall inductance change was observed for both directions of bending. The responses shown for double-sided sensors have not been reproducible. A difference of approximately 500 nH is seen in Figure 7.25 at 120º bend angle. Similarly, a difference of approximately 400 nH is seen in Figure 7.26 at 120º bend angle. This was a large difference of approximately 25% and may make it difficult to calibrate the double-sided sensors. It should be noted that the double-sided configuration generated more linear responses than the single-sided sensor configuration.

However, by comparing the responses shown by the different configurations and different directions of bending, the single-sided configuration bending in the concave direction can be considered superior. The sensor responses are less spread out, and they are more consistent. For the double-sided configuration, the convex bending responses were the most inconsistent.

The responses exhibited by the single-sided sensor showed small tolerances of ~5 %. This was superior to commercially available flex sensors based on resistive technology which typically quote ~±25 % tolerance values, as detailed in Table 3.1. The thickness of the single-sided sensor is also comparable to resistive flex sensors, which vary from 130 μm to 470 μm, as shown in Table 3.1. The resistive flex sensors have been chosen for comparison as they are widely available, and are commonly used. The AD sensor presented in this work is also less cumbersome than current magnetic solutions. [5]

The resolution of the AD sensor presented in this work, in its single-sided configuration with concave bending applied, is calculated to be ~5 degrees, accounting for the measurement inaccuracy. Resistive solutions have been demonstrated to achieve 1 degree resolution, at the cost of decreased sensor durability For a durable sensor, suitable for wearable technologies, the sensor will have a decreased resolution. [5-6]

The AD sensor developed in this work can therefore be considered to be a viable alternative, with a resolution that can be improved by further sensor optimisation. For example, the ribbon may be annealed to remove stresses and improve consistency between ribbon samples. All ribbon samples used in this work were in the as cast state and therefore subject to random stresses and those induced through cutting. Improvements in ribbon preparation will potentially reduce the inconsistency between sensor responses.

The durability of the AD sensor presented has not been investigated in depth, as it is beyond the scope of the work. It is important to note that amorphous ribbons have demonstrated high tensile strengths and will not fail under the low stresses applied through bending. The primary concern regarding the ribbon lies in the oxidation of the iron-based magnetic ribbon, which will have a severe impact on the sensor's performance. The adhesive layer may also affect the durability of the AD sensor, as it may lose its bond strength, after extended amount of bend cycles applied. The durability of the AD sensor should therefore be dependent on the adhesive layer and ensuring oxidation does not occur to the magnetic ribbon. This may be achieved through a design where the ribbon is secured to the surface of the ribbon through sealing. The seal will provide protection for the ribbon from oxidation, and will serve as a more durable method for constructing the AD sensor.

Bend sensors have been receiving an increasing amount of interest recently [6]. This investigation has presented a possible alternative solution using an inductive based sensor. The sensor response reported, shows a decrease in inductance in both directions of bending, whereas resistive flex sensors demonstrate both an increase and decrease in resistance depending on direction of bending [6]. The AD sensor presented in this work should therefore be considered for applications where the bending occurs in only one direction, and the sensor should be configured so concave bending is induced, assuming a single-sided configuration is employed.

## 7.3 Summary

In this chapter, an investigation of a novel bend sensor based on a FOE coil has been presented. The coil was fabricated on a flexible substrate, and a magnetostrictive ribbon was used as the sensing element. Changes in the ribbon's permeability caused by bending resulted in an inductance change in the coil. Bending was applied to the sensor through displacement, by placing the sensor between two displacement stages, it was possible to induce uniform bending.

Angles were determined by extrapolating the sensor displacements using a derived expression. Two directions of bending were investigated, as the sensor could be used in either direction of bending.

Various sensor configurations were tested, the layers of adhesive and ribbon were varied, and a double-sided configuration was also fabricated. By increasing the number of adhesive layers, the initial inductance of the sensor was decreased, but the sensor's inductance response was not affected greatly. However, if the displacement between the ribbon and the surface of the sensor becomes too great, the inductance response will be affected adversely, this should be considered when designing such a sensor. The sensor's inductance and sensitivity can be increased by increasing the number of ribbon layers. This comes at the expense of an increased sensor thickness.

The double-sided configuration exhibited larger hysteresis errors than the single-sided configurations, along with larger inductance and sensitivity. This has been explained by analysing the location of the neutral axis, by assuming the sensor as a composite

beam. The findings were that the region of ribbon in the closest proximity to the sensing coil should be undergoing tensile stressing for the optimal sensor response.

Additional sensors were fabricated to investigate the variance between the sensors, it was observed that the variation was much larger for the double-sided configuration. Considering the larger hysteresis errors and low reproducibility of the double-sided configuration, it can be considered inferior when compared to the single-sided configuration.

This work has achieved the design of an inductive AD sensor which is based on planar coil technology, and utilises magnetostrictive ribbon. The single-sided sensor has demonstrated superior accuracy whilst maintaining a thin profile and mechanical flexibility. The AD sensor presented has the potential to form the basis of the next generation of bend sensors.

## 7.4 References for Chapter 7


[1] Rattan, S. (2011). *Strength Of Materials*. New York: Tata McGraw-Hill, pp.129-132.

[2] Hibbeler, R. and Yap, K. (1994). *Mechanics of materials*. 2nd ed. Harlow: Pearson, pp.321-325.

[3] Megson, T. (1996). *Structural and stress analysis*. 1st ed. London: Arnold, pp.308-313.

[4] Metglas. (n.d.). *Magnetic Alloy 2605S3A(Iron-based) Technical Bulletin*. [online] Metglas.com. Available at: https://metglas.com/wp-content/uploads/2016/12/2605S3A-Technical-Bulletin.pdf. [Accessed 16 Dec. 2017]

[5] Szelitzky, E., Kuklyte, J., Mândru, D., O'Connor, N. (2014). Low cost angular displacement sensors for biomechanical applications—A review. *Journal of Biomedical Engineering and Technology*, 2(2), pp.21–28.

[6] Saggio, G., Riillo, F., Sbernini, L. and Quitadamo, L. (2015). Resistive flex sensors: a survey. *Smart Materials and Structures*, 25(1), p.013001.

# Chapter 8. Conclusions

This research concerned the development of a flexible angular displacement sensor which could be used as a superior alternative to currently available options. The aim was for the sensor to have a small size, with good accuracy, and easy to use. This was achieved by adopting the novel approach using an inductive sensing planar coil to detect changes caused by the Villari effect in amorphous ferromagnetic ribbon.

In this work three investigations of planar coils were completed, which culminated in the fabrication of a flexible angular displacement angle sensor. Chapter 5 and 6 were conducted to obtain a better understanding of planar coil characteristics, and to aid in the design of the sensor. This body of work has presented insight into the characteristics of different planar coil topologies.

Four different types of planar coil topologies were investigated, two of which were spiral, and the other two non-spiral. The spiral topologies investigated were square coil and circular coil, the non-spiral topologies investigated were meander coil and mesh coil. These coils were characterised, and their stress sensing capabilities were investigated. It was discovered that the spiral coil topologies had much larger inductance values, and exhibited superior stress sensing capabilities. The square coil topology performed better than the circular coil topology when comparing their responses with the smallest pitch value.

3D modelling was performed in this work to demonstrate the feasibility of employing 3D FEM to aid the design process for planar coil sensors. The results show good agreement, the FEM findings deviated within 10% of the experimental findings, and can successfully predict trends. This indicates that 3D FEM could be used for future development of planar coil sensors. Further detail will be provided in Chapter 9.

Due to the square coil's superior response in tensile stress sensing, it was used in the design of a figure-of-eight coil, which was investigated for its characteristics as a bend sensor. The figure-of-eight coil is easily mass produced with reproducible inductance values. The basic angular displacement sensor was constructed from a flexible figure-of-eight coil, a magnetostrictive ribbon layer, and an adhesive layer. This configuration exhibited good repeatability, and minimal hysteresis errors. Different

configurations were tested to investigate the effects of altering the number of ribbon layers and adhesive layers.

The investigation found that increasing the number of adhesive layers, i.e. increasing ribbon to coil separation, incrementally reduces the inductance of the sensor, however this was only true for a small increase in the number of adhesive layers. By increasing the number of ribbon layers the sensor's inductance increased, along with its sensitivity. However, the thickness of the sensor was increased, and the relationship was not linear between inductance and number of ribbon layers. The configuration of one ribbon layer and one adhesive layer on both sides of the sensor was investigated. This configuration yielded larger inductance values and larger hysteresis errors.

Multiple bend sensors were fabricated with the same configuration to investigate the reproducibility of the sensor response, it was discovered that the basic single-sided sensor configuration, of one ribbon layer and one adhesive layer attached to the top surface of the sensor, was superior compared to other configurations tested. The sensors' inductance response showed an accuracy of approximately 5%, which was good compared to a commercially available resistive flex sensor, with typical tolerances of ±25%.

The single-sided angular displacement sensor reported in Chapter 7 is accurate, with a small size profile, and easy to manufacture. These properties make it extremely suitable for wearable technology, which is vital for fields such as medical instrumentation, medical rehabilitation, and virtual reality. The possibility of producing the sensors on different materials also present many opportunities for the future development of this sensor.

In this work, planar coil sensors have been developed, and characterised for designing an angular displacement sensor which utilises planar coil technology and the Villari effect. This new approach for angular displacement sensing has produced superior accuracy compared with the most common sensor currently used, the resistive flex sensor. With a thin size profile and similar composition of a polymer substrate and a sensing element, the angular displacement sensor presented in this work maintains mechanical flexibility, and demonstrated a marked improvement over current angular displacement sensing solutions.

# Chapter 9. Recommended Future Works

To advance the angular displacement sensing method described in this work, the following actions should be considered and undertaken;

## 9.1 Heat Treatment of Magnetic Ribbon

The Metglas magnetic ribbons used in the investigations have been used in their as cast state. By annealing the material improvements can be made on the consistency of the bend sensor's performance and it will reduce the deviation seen between sensors with different samples of magnetic ribbon. This is due to the relaxation of internal stresses within the ribbon during the annealing process, which will normalise the characteristics of the ribbon samples.

Annealing should be carried out to decrease disparity between different sensor samples. The investigation detailed in 7.2.5 should be repeated for single-sided sensor configuration with annealed ribbon samples. This should result in an improvement of the accuracy seen in the sensor's response.

## 9.2 The Development of a Simplified Sensor Interrogation Method

In this body of work, an impedance analyser was used to interrogate the different coils. It will not be feasible to employ this interrogation method for wearable technology applications, due to cost, size, and weight restraints. An alternative interrogation method is required for this sensor, which will be cheaper, smaller, and lighter than the impedance analyser. As the coil behaves as an inductor, it is possible to integrate the inductor as part of a tank circuit. This tank circuit can then be implemented as part of an oscillator, for example, producing an output which is frequency modulated. The output signal can then be transferred wirelessly if desired by the user.

The angular displacement sensor should be integrated as part of an LC tank circuit, and it should be integrated into an oscillating circuit. The signal generated by the oscillator will differ depending on the sensor's inductance. Using demodulation techniques in LabVIEW, a simplified sensor interrogation method can be achieved.

# Appendix A. Planar Coil Displacement Separation Characteristics

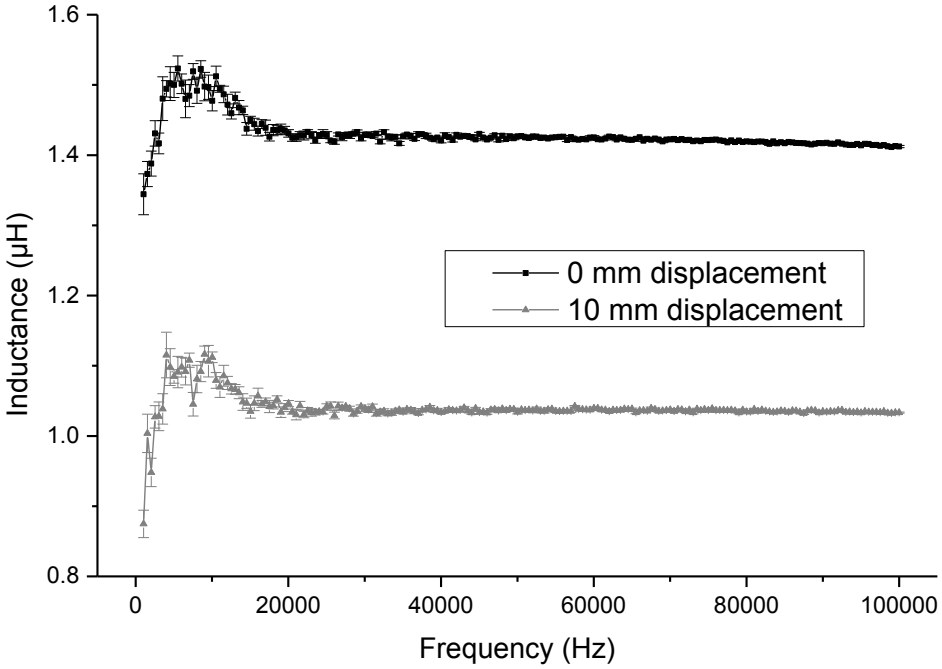


Figure A.I – Inductance change due to displacement over full span of observed frequencies for square topology with pitch of 0.75 mm.

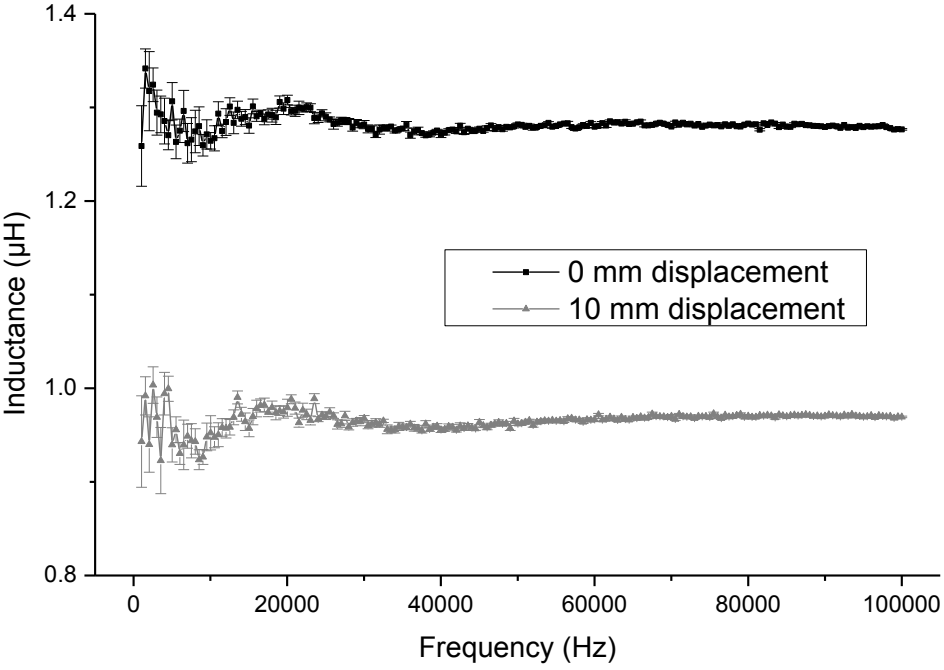


Figure A.II – Inductance change due to displacement over full span of observed frequencies for square topology with pitch of 1.0 mm.

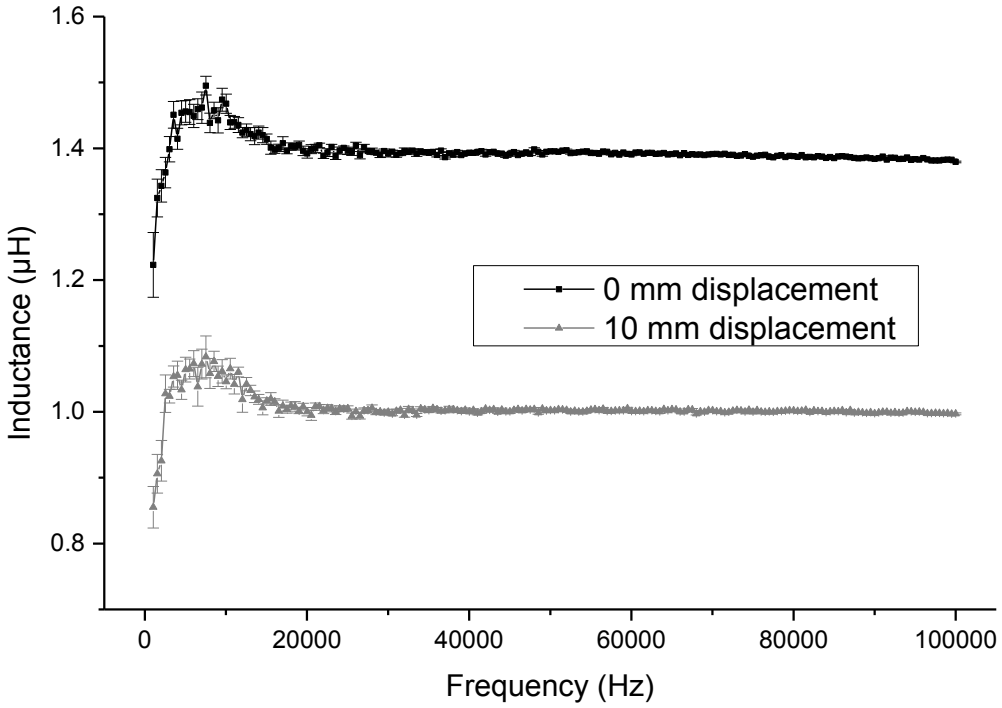


Figure A.III – Inductance change due to displacement over full span of observed frequencies for circular topology with pitch of 0.75 mm.

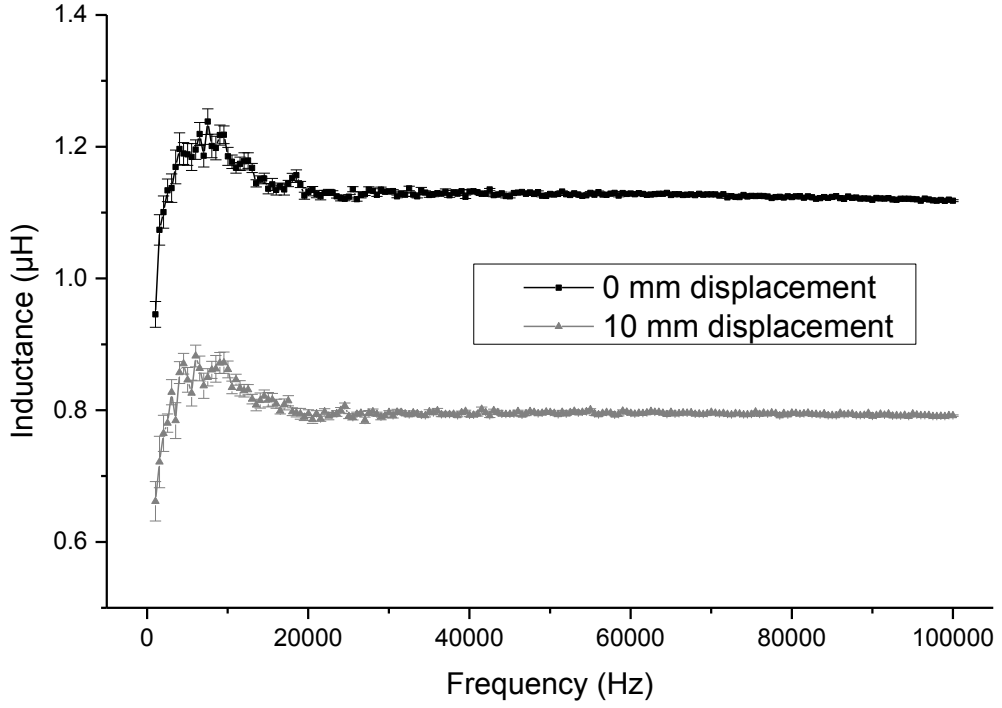


Figure A.IV – Inductance change due to displacement over full span of observed frequencies for circular topology with pitch of 1.0 mm.

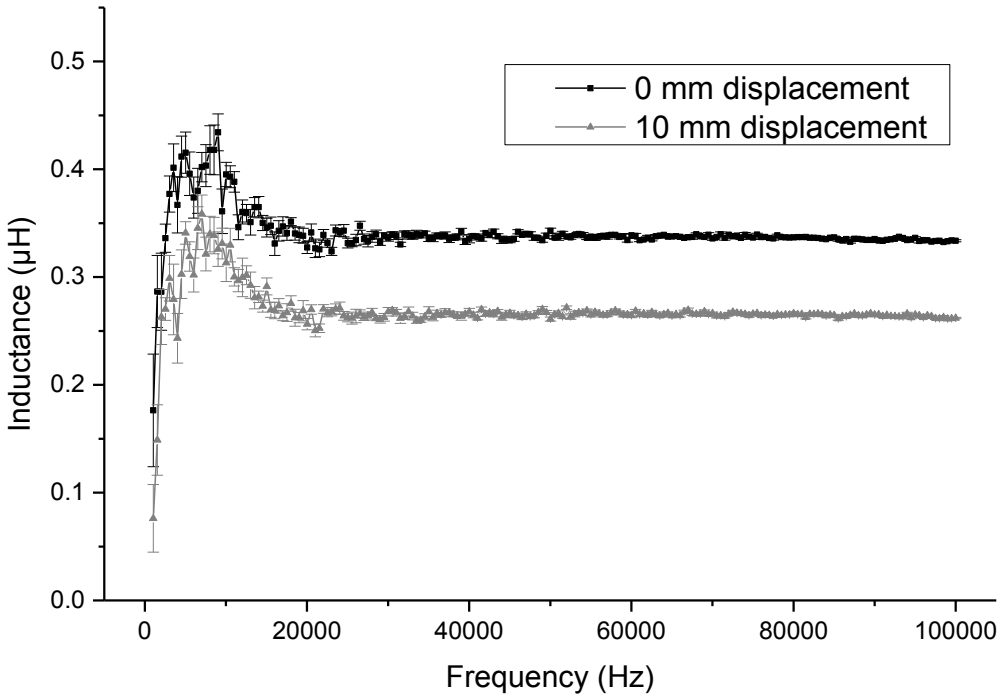


Figure A.V – Inductance change due to displacement over full span of observed frequencies for meander topology with pitch of 0.75 mm.

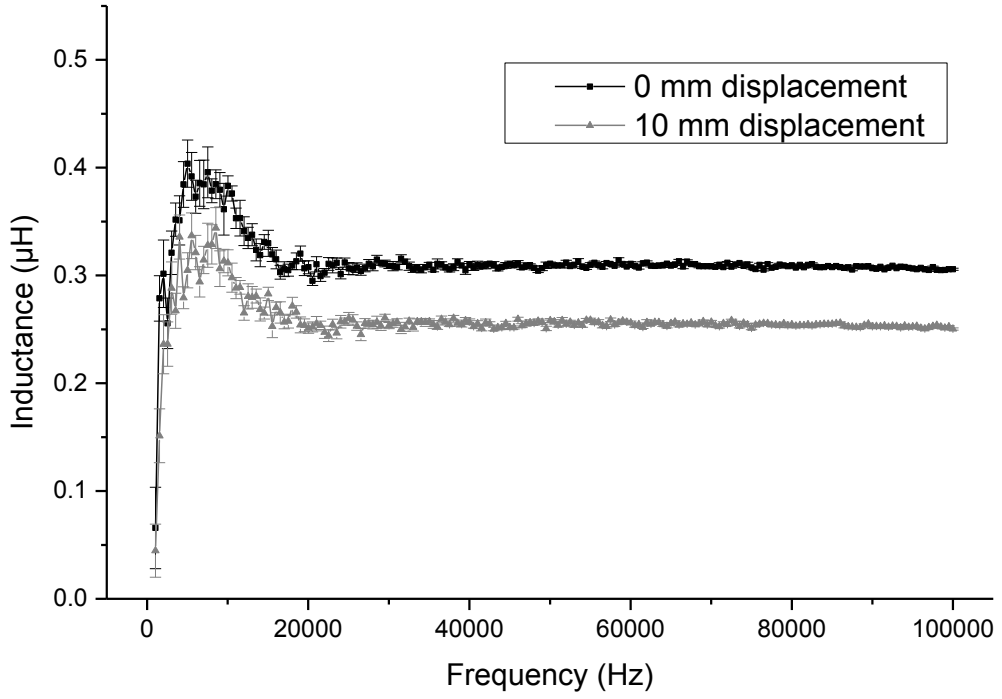


Figure A.VI – Inductance change due to displacement over full span of observed frequencies for meander topology with pitch of 1.0 mm.

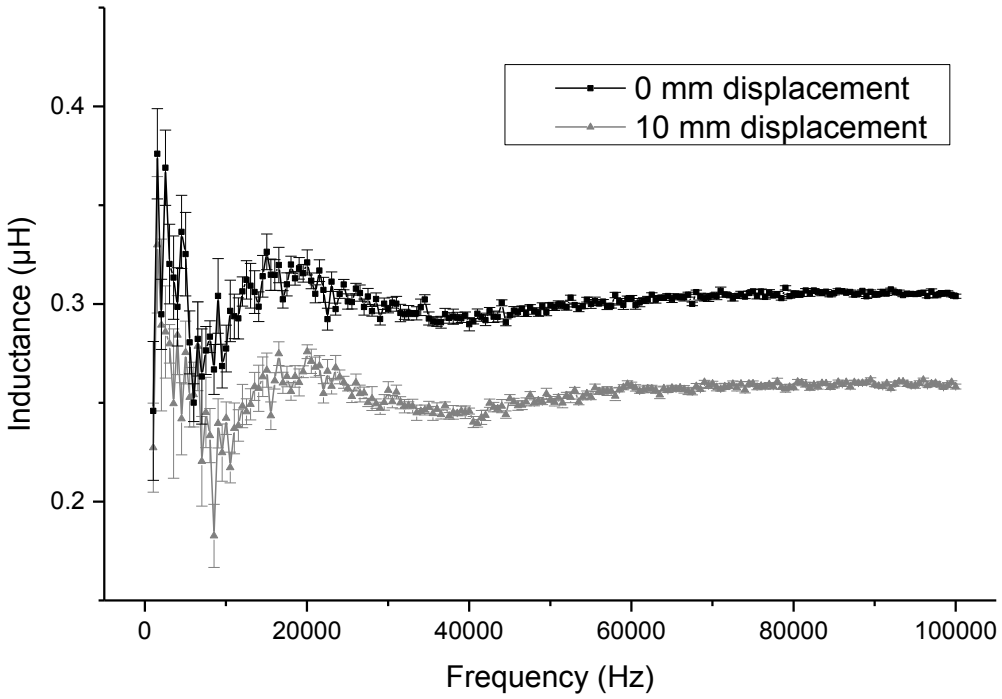


Figure A.VII – Inductance change due to displacement over full span of observed frequencies for mesh topology with pitch of 2.5 mm.

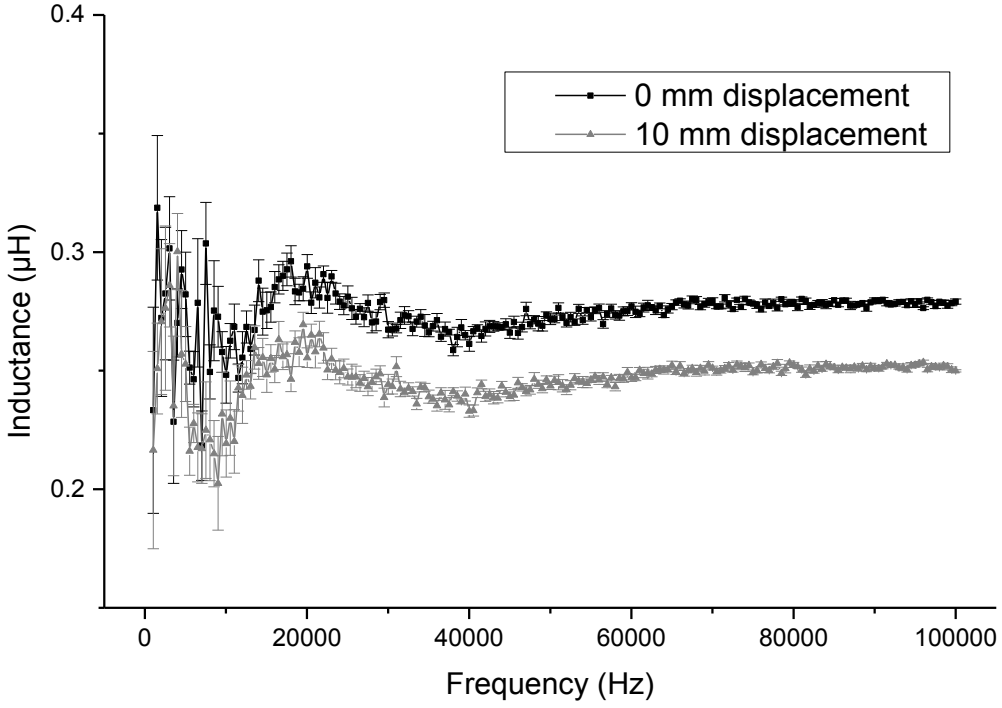


Figure A.VIII – Inductance change due to displacement over full span of observed frequencies for mesh topology with pitch of 3.5 mm.

# Appendix B. Planar Coil Stress Sensing Responses

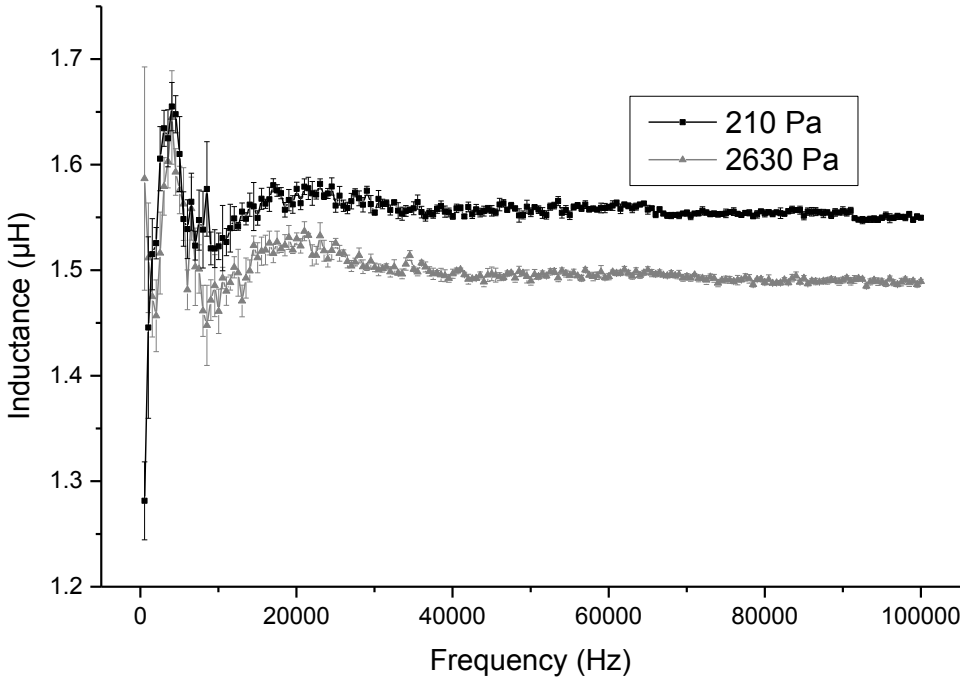


Figure B.I – Inductance change due to applied stress over the full span of observed frequencies, for square topology with pitch of 0.75 mm.

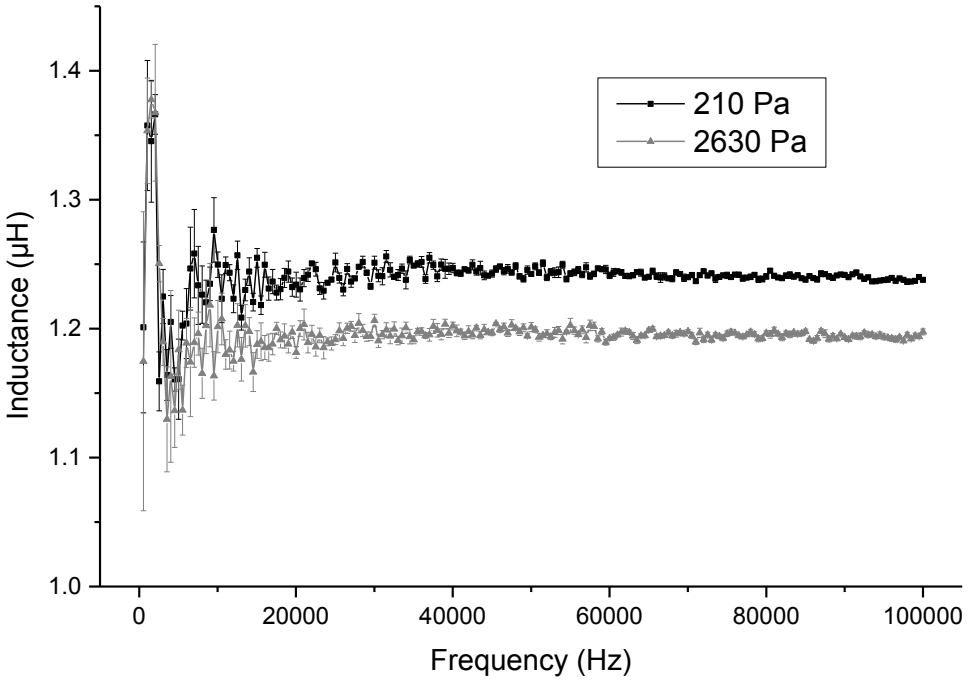


Figure B.II – Inductance change due to applied stress over the full span of observed frequencies, for square topology with pitch of 1.0 mm.

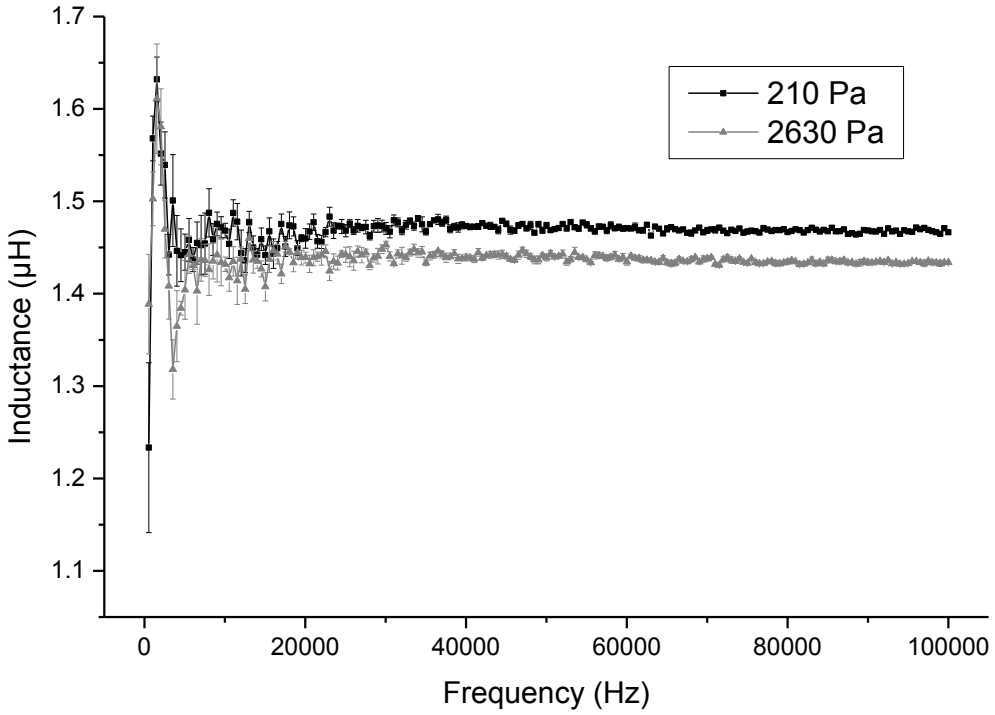


Figure B.III – Inductance change due to applied stress over the full span of observed frequencies, for circular topology with pitch of 0.75 mm.

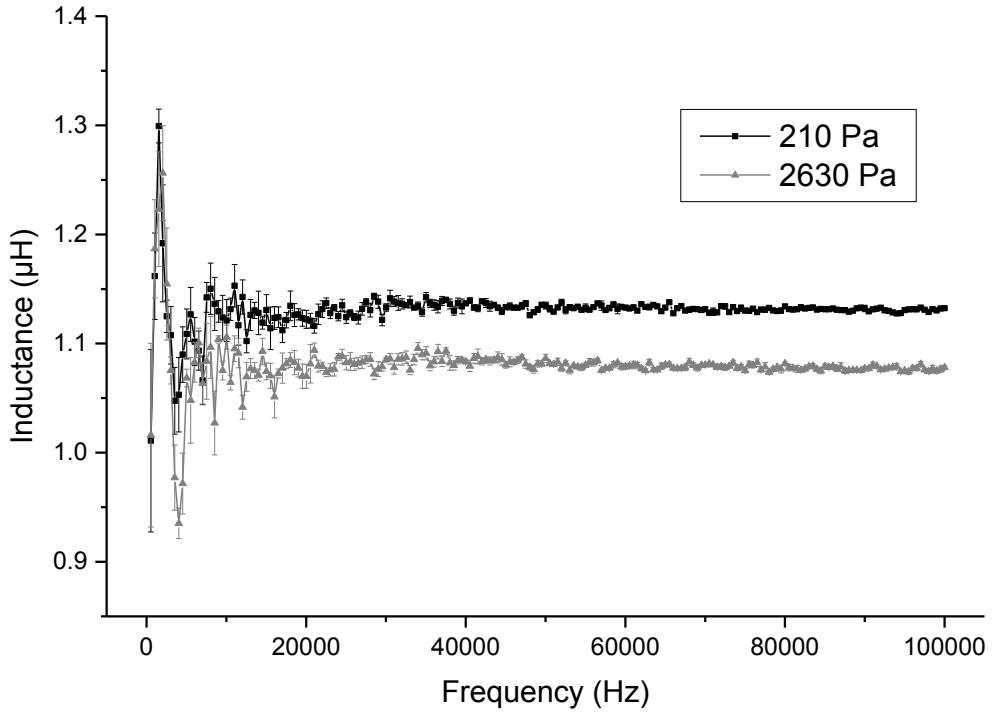


Figure B.IV – Inductance change due to applied stress over the full span of observed frequencies, for circular topology with pitch of 1.0 mm.

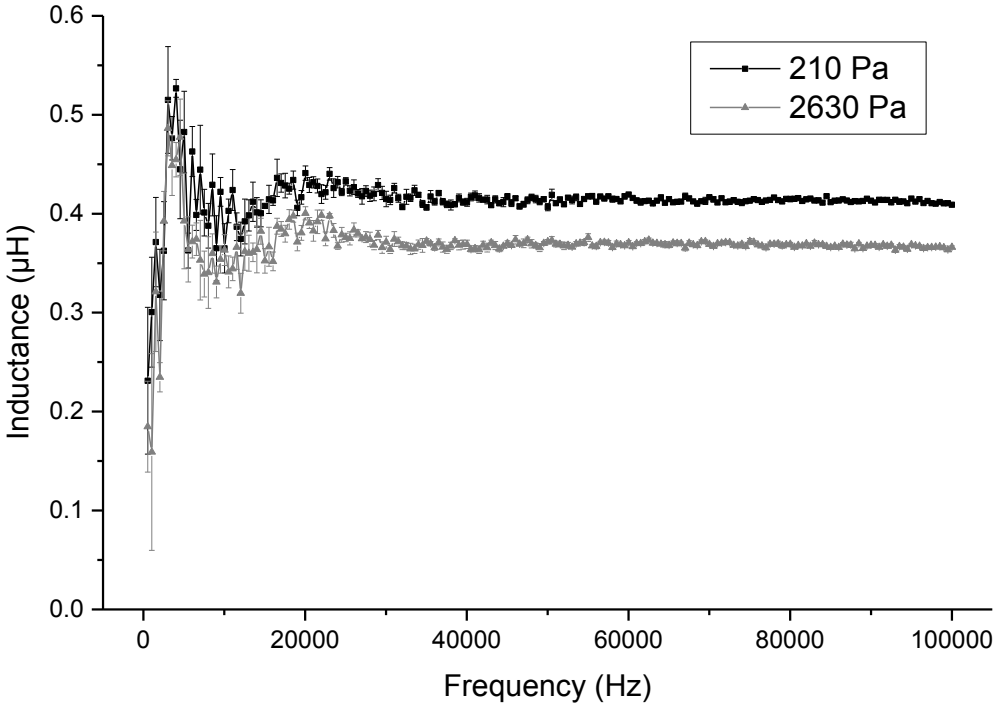


Figure B.V – Inductance change due to applied stress over the full span of observed frequencies, for meander topology with pitch of 0.75 mm.

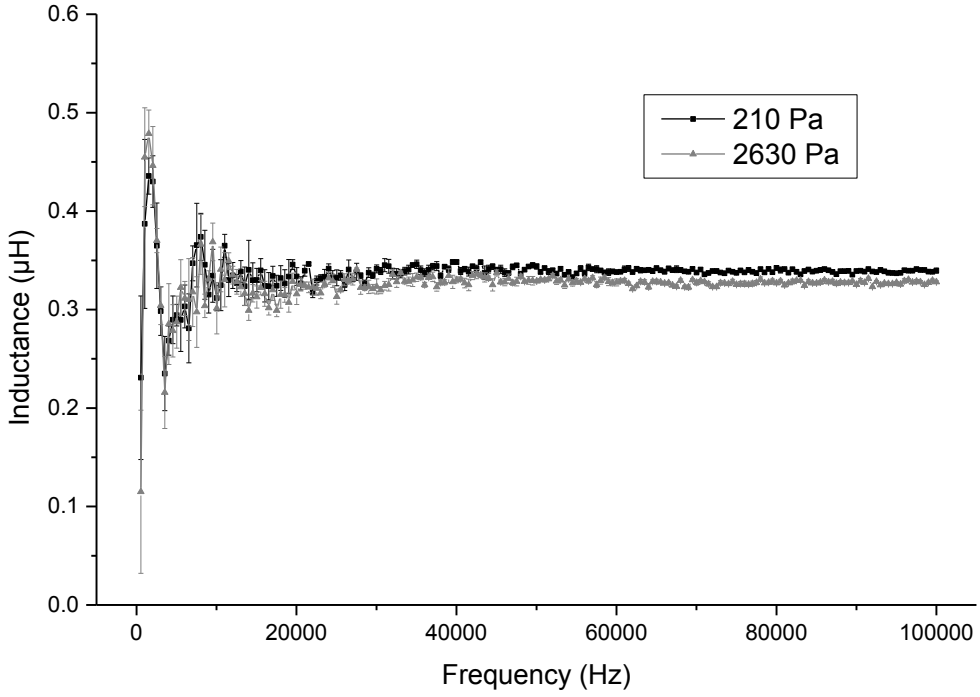


Figure B.VI – Inductance change due to applied stress over the full span of observed frequencies, for meander topology with pitch of 1.0 mm.

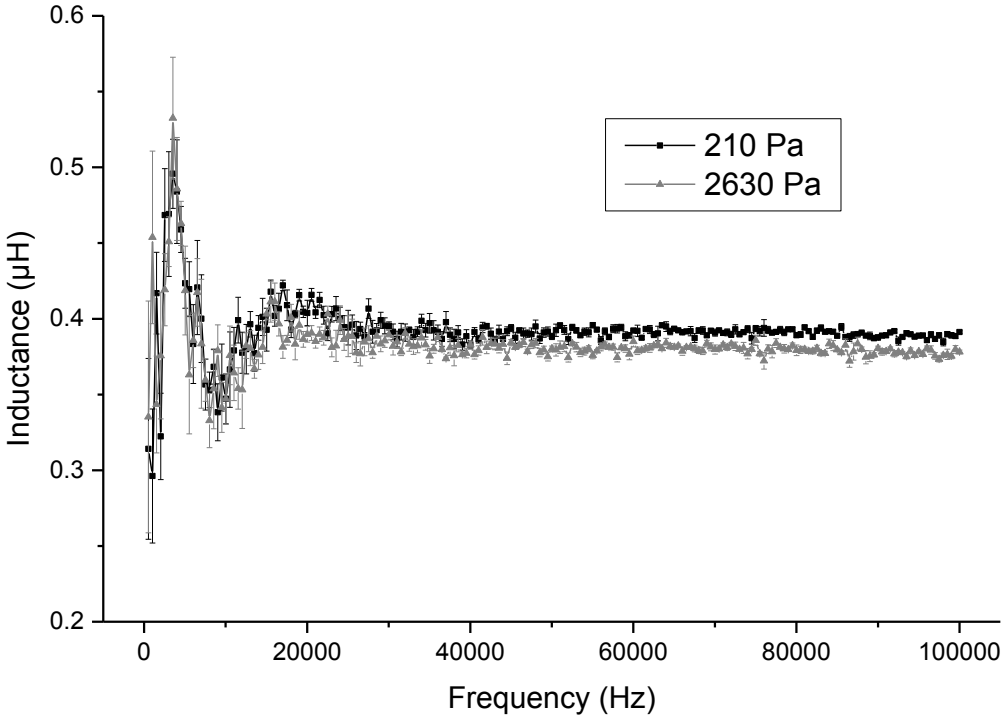


Figure B.VII – Inductance change due to applied stress over the full span of observed frequencies, for mesh topology with pitch of 2.5 mm.

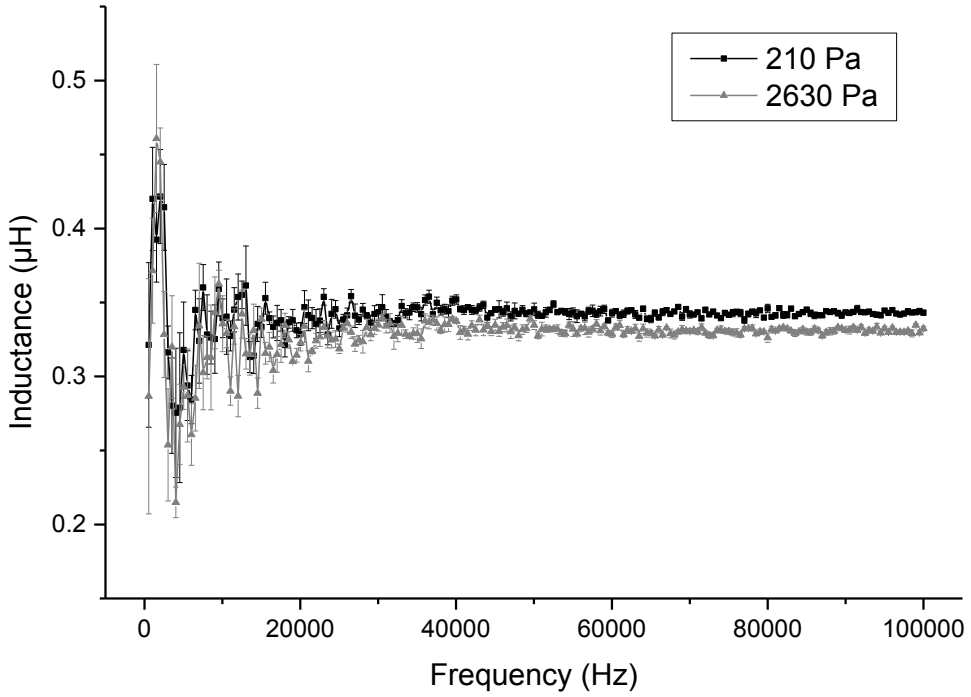


Figure B.VIII – Inductance change due to applied stress over the full span of observed frequencies, for mesh topology with pitch of 3.5 mm.

# Appendix C. Figure-of-Eight Angular Displacement Sensor Responses

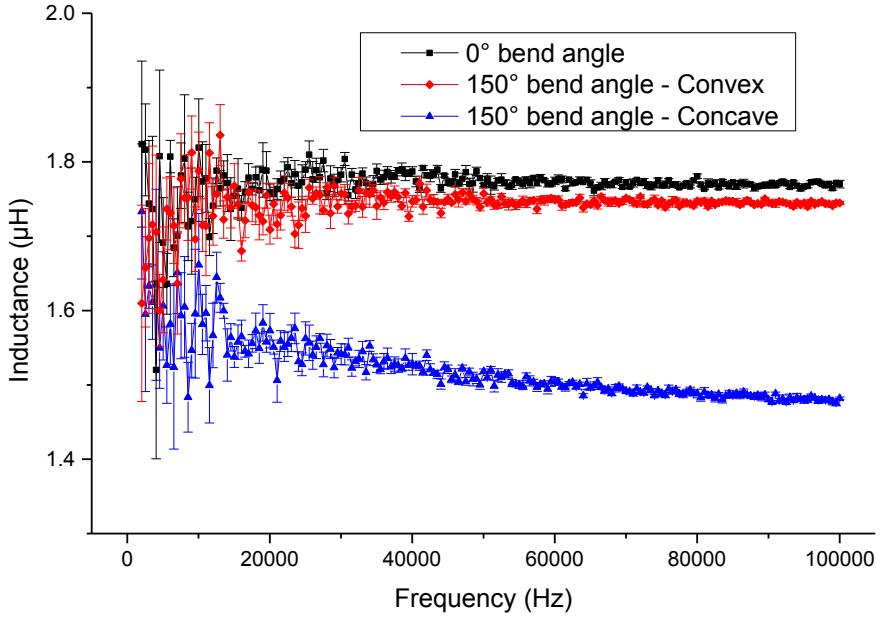


Figure C.I – Inductance change for sensor with configuration of 2 adhesive layers due to applied displacement over the full span of observed frequencies

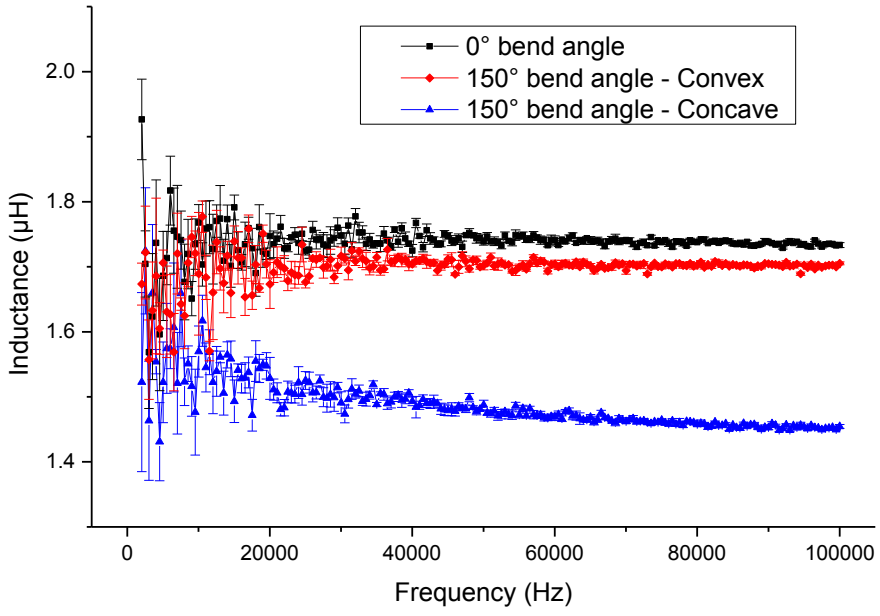


Figure C.II – Inductance change for sensor with configuration of 3 adhesive layers due to applied displacement over the full span of observed frequencies

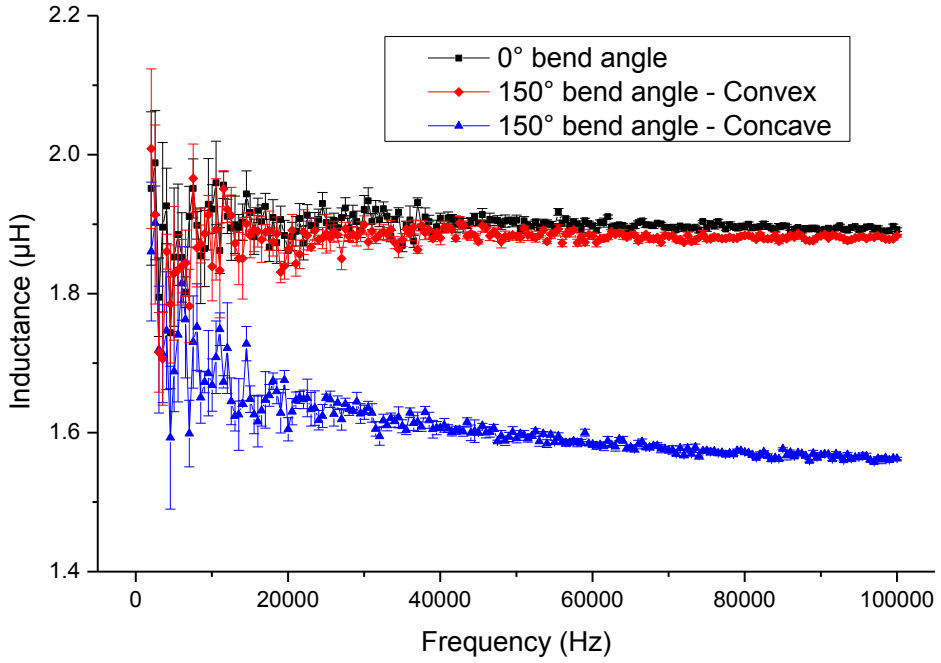


Figure C.III – Inductance change for sensor with configuration of 2 ribbon layers due to applied displacement over the full span of observed frequencies

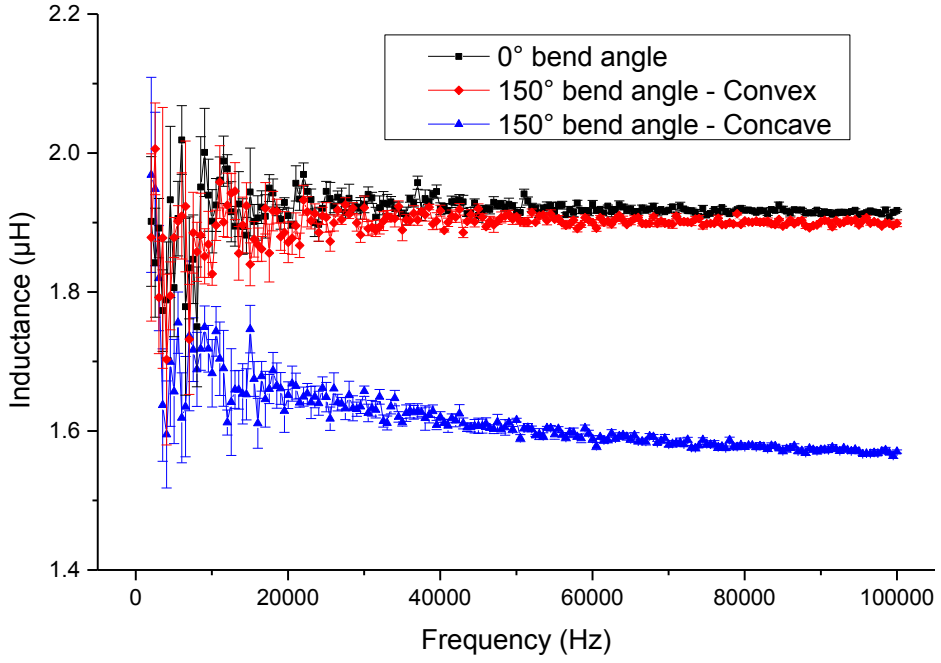


Figure C.IV – Inductance change for sensor with configuration of 3 ribbon layers due to applied displacement over the full span of observed frequencies